Russian Journal of Earth Sciences

Vol. 23
Issue 6

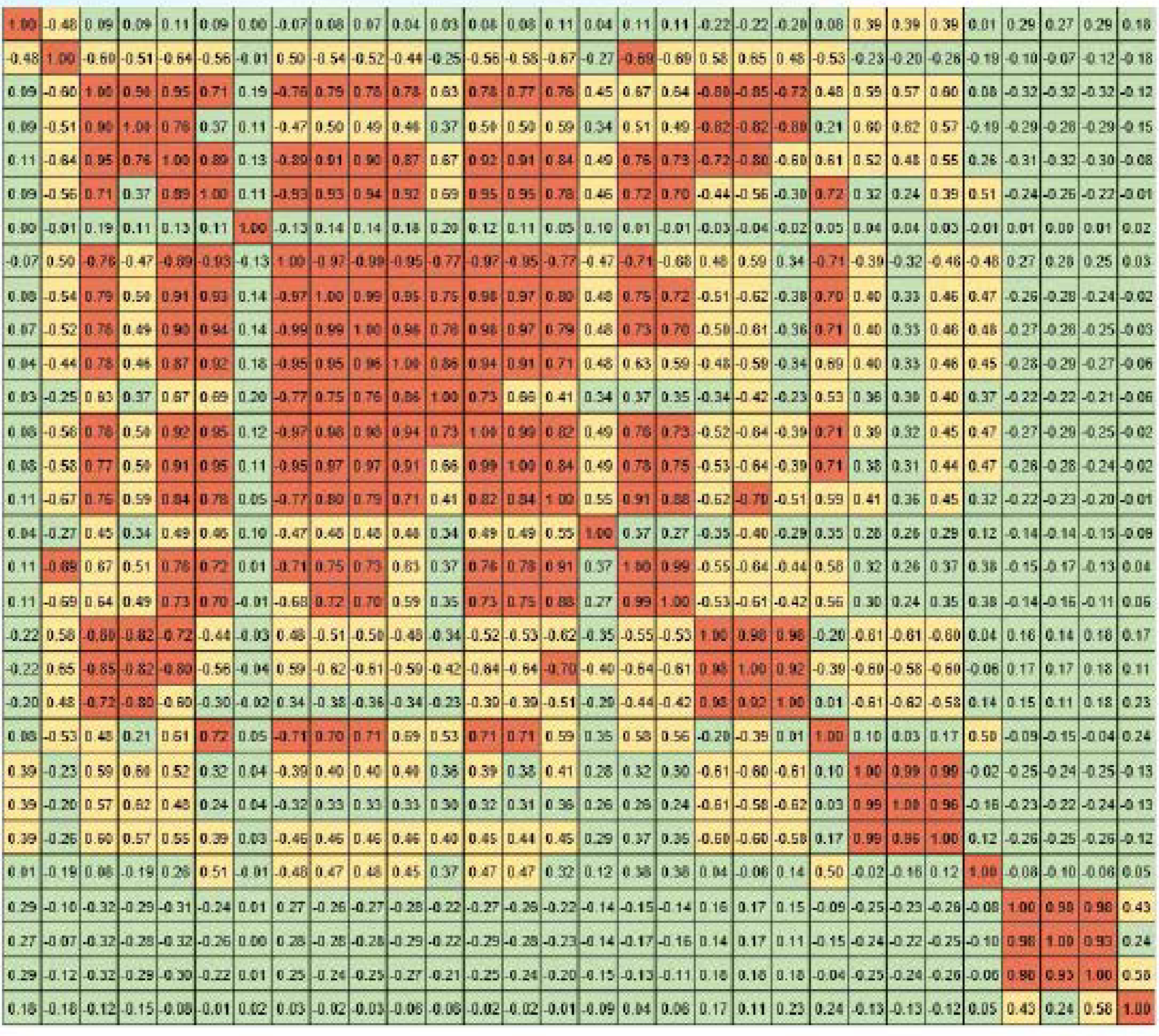

RUSSIAN JOURNAL *of* EARTH SCIENCES

Regression Derivatives and Their Application in the Study of Magnetic Storms

S. Agayan[1], **Sh. Bogoutdinov**[1,2], **R. Sidorov**[*,1], **A. Soloviev**[1,2], **D. Kamaev**[3], **A. Aleksanyan**[4], and **B. Dzeranov**[1]

[1] Geophysical Center of the Russian Academy of Sciences, Moscow, Russia
[2] Schmidt Institute of Physics of the Earth of the Russian Academy of Sciences, Moscow, Russia
[3] Research and Production Association "Typhoon", Obninsk, Russia
[4] Obninsk Institute for Nuclear Power Engineering, Obninsk, Russia
[*] **Correspondence to:** Roman Sidorov, r.sidorov@gcras.ru.

Abstract: Discrete Mathematical Analysis (DMA) is a data analysis method that uses fuzzy mathematics and fuzzy logic. DMA involves the active participation of the researcher in the study of records, offering technologies and algorithms for analyzing records through the properties of interest to the researcher. In the present work, such properties are related to regression derivatives, and the results obtained are applied to magnetic records. The possibilities of the method in the morphological analysis of geomagnetic storms are demonstrated on the example of three strongest storms that have occurred since the beginning of the current 25th solar cycle.

Keywords: Proximity measure, regression derivation, regression smoothing, measures of activity. multi-scale measures of activitys.

Citation: Agayan, S., Sh. Bogoutdinov, R. Sidorov, A. Soloviev, D. Kamaev, A. Aleksanyan, and B. Dzeranov (2023), Regression Derivatives and Their Application in the Study of Magnetic Storms, *Russian Journal of Earth Sciences*, 23, ES6001, EDN: PHVZCV, https://doi.org/10.2205/2023es000889

Research Article

Received: 25 October 2023
Accepted: 28 December 2023
Published: 30 December 2023

1. Introduction

The systematic study of geomagnetic storms as extreme phenomena of geomagnetic activity with a certain morphology began approximately in the middle of the 20th century, although the perturbations of the Earth's external magnetic field were studied even earlier. Today, this is a vast area of research. There are numerous studies related to the geomagnetic storms. Issues under considerations include the onset and evolution of a storm [*Akasofu and Chapman*, 1963]. Another group of studies is related to the dependence of magnetic storm evolution and its phases from different types of solar wind [*Yermolaev et al.*, 2014; *Zhang*, 1992]. Some researchers conducted studies of characteristic morphological features of geomagnetic storms and their occurrence over a solar cycle [*Pandey and Dubey*, 2009; *Yokoyama and Kamide*, 1997], as well as different aspects of magnetosphere dynamics [*Boroev and Vasiliev*, 2017; *Lazutin*, 2012] and the disturbances which take place during the storm phases [*Gromova et al.*, 2016; *Mishin et al.*, 2007; *Yermolaev et al.*, 2012].

Until recent years, a researcher when working with magnetograms could rely only on statistical methods of spectral-temporal analysis. Recently new methods of records analysis have appeared. They are connected with development of artificial intelligence, fuzzy mathematics and allow a researcher to have more active position, to express his experience and his knowledge. This is particularly related to analysis of magnetograms. Research of data and methods of their analysis using fuzzy mathematics has now taken shape as an independent direction, which includes methods of fuzzy regression and analysis of fuzzy time series. We can highlight the main stages of development of this direction.

Research of data and methods of their analysis using fuzzy mathematics has now taken shape as an independent direction, which includes methods of fuzzy regression and analysis of fuzzy time series [*Batyrshin et al.*, 2007; *Kacprzyk et al.*, 2007; *Kovalev*, 2007;

Pedrycz and Smith, 1999; Tanaka et al., 1982; Yarushkina, 2004; Yarushkina et al., 2007]. We can highlight the main stages of development of this direction.

At the initial stage, studies of the fuzzy regression model were carried out. The second stage is the development of soft computing methods, within which a huge number of studies have carried out studies of the effectiveness of soft computing for time series analysis. The third stage was the transition from the analysis of time series using fuzzy mathematics methods to the analysis of fuzzy time series. The development of fuzzy database methods has made it possible to move to the stage of extracting rules from fuzzy (granular) time series. The proposed work should be attributed to the direction of using fuzzy mathematics methods for the analysis of discrete time series, that is, to the second stage.

This work should be viewed precisely from these positions: it proposes a methodology for formalizing the logic of a researcher studying a record, and its implementation within the framework of Discrete Mathematical Analysis (DMA) – a new approach to data analysis, focused on the researcher and occupying an intermediate position between hard mathematical methods and soft intellectual [Agayan et al., 2016, 2021a, 2018].

The DMA solution scenario consists of two parts. The first is informal: it explains the researcher's logic, introduces the necessary concepts, and explains the schemes and principles of the solution. The second is of a formal nature: with the help of the DMA apparatus, all concepts receive strict definitions within the framework of Fuzzy Mathematics (FM) and Fuzzy Logic (FL) (since the researcher does not think in numbers, but in fuzzy concepts), and schemes and principles become algorithms.

The result of this work in theoretical terms should be considered the construction for the original record $f = f(t)$ and the property P specified relative to it, of interest to the researcher, a two-dimensional function $\mu P_f = \mu P_f(t,s)$, expressing on the scale of the segment $[-1,1]$ in at a given node t, a measure of the manifestation of property P on a record f at a given scale of its consideration $s \geq 0$ [Agayan et al., 2016, 2021b, 2020; Oshchenko et al., 2020; Soloviev et al., 2017].

Similar to wavelet analysis, the μP_f measure visualizes what is happening at f and allows us to better understand the nature of the process behind it. Formal analysis of μP_f, including the extraction of useful information about f, can be performed using Image Processing, as well as morphological and cluster DMA methods [Agayan et al., 2021a, 2020, 2022].

This is the motivation for the research presented in this paper. It continues the DMA study of records that form one of the foundations of the MAGNUS functionality, designed for collecting, processing, storing and analyzing geomagnetic information [Gvishiani et al., 2016a]. Before that, the authors were engaged in approaches to recognizing disturbances with knownmorphology on geomagnetic data, aimed at search for artificial disturbances. With the creation of MAGNUS, the DMA-based approaches were integrated into it. For example, using the local indicators, the analysis of St. Patrick's Day Storm was performed [Gvishiani et al., 2016b]. The developed anomalousness measure [Soloviev et al., 2017] was applied to geomagnetic activity studies [Agayan et al., 2016], in Sq variation analysis [Soloviev et al., 2019], and in the global geomagnetic storm analysis at different latitudes during different phases [Oshchenko et al., 2020]. The preceding research, also related to the DMA apparatus, was intended to demonstrate the possibilities of activity measures in the analysis of the structure of a magnetic storm [Agayan et al., 2021b]. This study continues this approach.

From a practical point of view, the main result of this work should be considered a multiscale morphological geomagnetic analysis of magnetic storms associated with their properties based on regression discrete derivatives.

2. Notations and Conventions

We will consider the observation period T of a record (time series) f to be a finite regular set of nodes on the real line $\mathbb{R}$ with sampling parameter h:

$$T = \{t\} = \{t_1 < \cdots < t_N\};\ t_{i+1} - t_i = h,\ i = 1, \ldots, N-1,$$

and the record of f itself as a function on T: $f : t \to \mathbb{R}$. Let $\mathrm{F}(T)$ denote the N-dimensional space of records on T.

Analysis by a researcher of a record involves consideration of its values not only in a separate node, but also simultaneous consideration of its values in some of its neighborhood. This is why the segment T needs to be localized at each of its nodes t. This can be done using the fuzzy structure δ_t on T, acting as a neighborhood of node t and expressing the proximity of nodes t normalized in $\bar{t}$: $\delta_t(\bar{t}) \in [0,1]$ – measure of proximity of $\bar{t}$ to t:

$$\delta_t \in \mathrm{Fuzzy}\,T : (\delta_t(\bar{t})) \wedge \left(|\bar{t} - t| < \left|\bar{\bar{t}} - t\right|\right) \to \delta_t(\bar{\bar{t}}) \le \delta_t(\bar{t}). \tag{1}$$

We will consider the proximity measure δ on T to be a set of fuzzy structures δ_t: $\delta = \{\delta_t, t \in T\}$.

Example 1. *$\delta = \delta(p,r)$; s – scale parameter, r – viewing radius (Figure 1)*

$$\delta_t(\bar{t}) = \delta(p,r)(\bar{t}) = \begin{cases} \left(1 - \frac{|\bar{t}-t|}{r}\right)^s & \\ 0 & \end{cases},\ \mathit{if} \left|\bar{\bar{t}} - t\right| \begin{matrix} \le r \\ > r \end{matrix}\ . \tag{2}$$

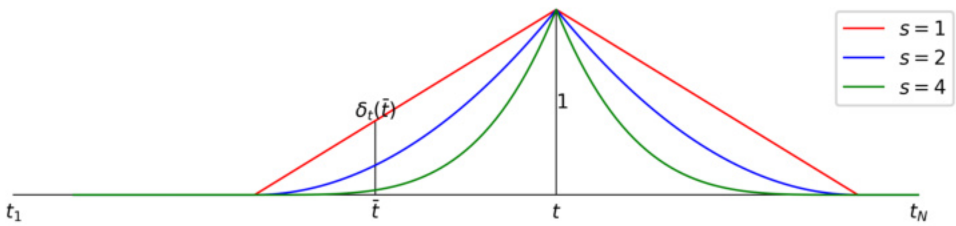

Figure 1. Proximity of $\delta(p,r)$ to node t for different s.

The parameters s and r are chosen by the researcher: the parameter r (view radius) is responsible for the boundaries of the review, and the parameter s (the scale of the review) is for the accuracy of consideration within the boundaries of the review.

3. Records Exploration Using Fuzzy Mathematics

The study of a record f by a researcher presupposes some property of P that interests him: it is the dynamics of the execution of P for f on T that the researcher needs, in particular, the zones in T where P is most pronounced on f and which he considers anomalous (P-anomalous) for f.

The DMA has a recording research program that allows us to formalize and algorithmize the above. It is implemented in the language of FM and FL, contains several stages and includes, in particular, the construction on T of a fuzzy structure (measure) $\mu P_f(t)$, which expresses at node t the degree of manifestation of property P on record f. The measure μP_f should be understood as a fuzzy formalization of the property P on the record f. Its construction involves two stages.

The first stage is called straightening of property P, consists of constructing a quantitative expression of P on record f, which is called straightening of P by f and is denoted by P_f: $P_f : T \to \mathbb{R}^+$, $P_f(t) \leftrightarrow$ "quantity of property P on record f at node t".

Straightening P_f serves as the basis for the qualitative expression of property P on record f in the form of a fuzzy structure μP_f on T, a measure of property P on f: $\mu P_f \leftrightarrow$ "quality (degree of manifestation) of property P on record f at node t".

The measure μP_f is a membership function on T to the fuzzy concept "manifestation of P on f", its construction constitutes the second stage of the DMA research program for studying records. In DMA, μP_f is also called a measure of the activity (anomaly) of property P on a record f.

A fundamental scheme for DMA emerges (Figure 2), which forms the basis of his approach to records.

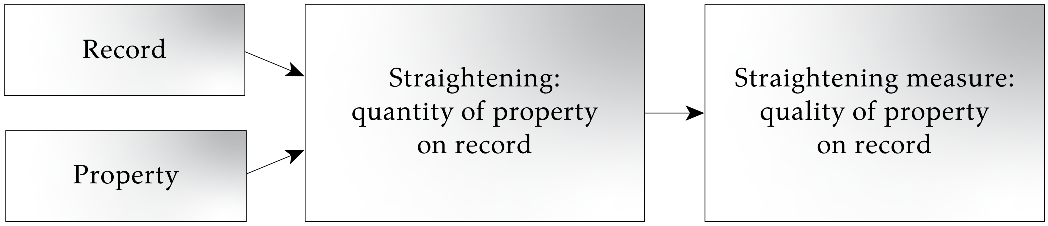

Figure 2. Scheme of DMA emerges.

4. Straightening (Quantity of Properties)

DMA leaves to the researcher the choice of both the property P itself and the construction of its quantitative expression P_f on the record f. Nevertheless, reality has shown the stability of this choice: a circle of basic straightenings has been determined that most researchers would like to deal with. Behind each of them is a fundamental mathematical concept. Let us present the most important of them: energy E (dispersion, continuity), scatter O (Cauchy fundamentality, variation), ruggedness L (frequency, length). Within the framework of this work, two more constructions related to regression derivatives will be added to them.

All listed properties P and their straightenings P_f are local: the quantity of the property $P_f(t)$ is obtained only after localizing $T(t)$ of the space T at node t, which is done using the measure δ_t by fuzzification of T: $T \to T(t) = T(t|\delta_t) = \{(\bar{t}, \delta_t(\bar{t})), \bar{t} \in T\}$.

Definition 1. *Let $\mathsf{F}(T)$ be the space of functions on T.*

1. *Construction of straightening of the property $P \leftrightarrow$ non-negative functional on T, parameterized by T:*
$$P : \mathsf{F}(T) \times T \to \mathbb{R}^+.$$
2. *Straightening the record f based on the construction $P \leftrightarrow$ is a non-negative function:*
$$P_f : t \to P(f, t).$$

The value $P(f,t) = P_f(t)$ is understood as a quantitative assessment of the behavior of record f at node t when P looks at its dynamics. This view is local in all interesting cases, so that everywhere below the straightening construction P is connected to some fixed localization δ_t (1), therefore $P(f,t) = P_f(t|\delta_t)$.

Example 2.

1. *Energy (dispersion)*
$$E_f(t|\delta_t) = \frac{\sum_{\bar{t}\in T} \left| f(\bar{t}) - M_f(t|\delta_t) \right| \delta_t(\bar{t})}{\sum_{\bar{t}\in T} \delta_t(\bar{t})},$$
where
$$M_f(t|\delta_t) = \frac{\sum_{\bar{t}\in T} f(\bar{t})\delta_t(\bar{t})}{\sum_{\bar{t}\in T} \delta_t(\bar{t})}.$$

2. *Length (ruggedness)*

$$L_f(t|\delta_t) = \frac{\sum_{\bar{t},\bar{\bar{t}}\in T:|\bar{t}-\bar{\bar{t}}|=h} \left|f(\bar{t}) - f(\bar{\bar{t}})\right| \delta_t(\bar{t})\delta_t(\bar{\bar{t}})}{\sum_{\bar{t},\bar{\bar{t}}\in T:|\bar{t}-\bar{\bar{t}}|=h} \delta_t(\bar{t})\delta_t(\bar{\bar{t}})}.$$

5. Measure of Straightening (Quality of Property)

As mentioned above, the measure μP_f of straightening P_f is a function of membership on T to the fuzzy concept "manifestation of property P on record f". In DMA there are several designs of transitions from P_f to μP_f. Let us present one of them using fuzzy comparison.

Definition 2. *Fuzzy comparison $n(b,a)$ of non-negative numbers a and b measures the degree of superiority of a over b:*

$$n(b,a) = \mathrm{mes}(b < a) \in [-1,1].$$

Comparison n should be understood as a fuzzy binary relation on the half-axis $\mathbb{R}^+$, consistent with its natural order. There are many fuzzy comparisons; let's choose one of them, further considering that $n(b,a) = (a-b)(a+b)^{-1}$. It can be extended (ambiguously) to compare a with the finite collection $B = \{b\} \subset \mathbb{R}^+$. Any such extension $n(B,a)$ will be a membership function on $\mathbb{R}^+$ for the fuzzy concept "to be large modulo B", therefore $n(B,a)$ is also treated as a measure of the maximum of a modulo B and is denoted by $\mathrm{mes}\max_B a$:

$$n(B,a) = \mathrm{mes}(B < a) = \mathrm{mes}\max_B a \in [-1,1].$$

Example 3. *Binary extension*

$$n(B,a) = \frac{\sum_{b\in B} n(b,a)}{|B|}.$$

Example 4. *Let ψ be a non-negative function on T, then the measure* $\mathrm{mes}\max_{\mathrm{Im}\,\psi}\psi(t)$ *shows to what extent ψ is large at node t. In this case, it is denoted by* $\mathrm{mes}\max\psi(t)$*), and the image of* $\mathrm{Im}\,\psi$ *is omitted in the index.*

Figures 3a and 4a show two reliefs, and Figures 3b and 4b show their measures of maximum. The latter make it possible to divide nodes into anomalous and moderate: node t is anomalous (moderate) if $|\mathrm{mes}\max\psi(t)| \geq 0.5$ (< 0.5). Anomalous nodes (large – red, small – magenta), in contrast to moderate ones (large – green, small – blue), do not always exist: there are no abnormally large nodes, for example, on the second relief (Figure 4a), which, of course, right. Note that the traditional probabilistic-stochastic approach to anomaly for ψ based on the distribution function of its image $\mathrm{Im}\,\psi$ is softer and always effective.

We return to the property P for writing f: it is natural to consider the quality $\mu P_f(t)$ of its manifestation at node t to be the degree of maximum of its quantity $P_f(t)$:

$$\mu P_f(t) = \mathrm{mes}\max P_f(t).$$

The quality of manifestation $\mu P_f(t)$ can also be interpreted as the degree of interest of the researcher in the record f at node t in connection with the property P.

Definition 3. *The fuzzy quantity $\mu P_f(t)$ on T is called a measure of property P for f.*

The measure of a property is dimensionless and does not depend on the nature of the property, because it does not express the property itself, but the degree (quality) of its manifestation. Thus, the transition $P_f(t) \to \mu P_f(t)$ translates the analysis of the record f into the language of FL and FM: measures of the property μP_f for different straightenings P_f take values on a single scale of the segment $[-1,1]$ and can be combined in any compositions and

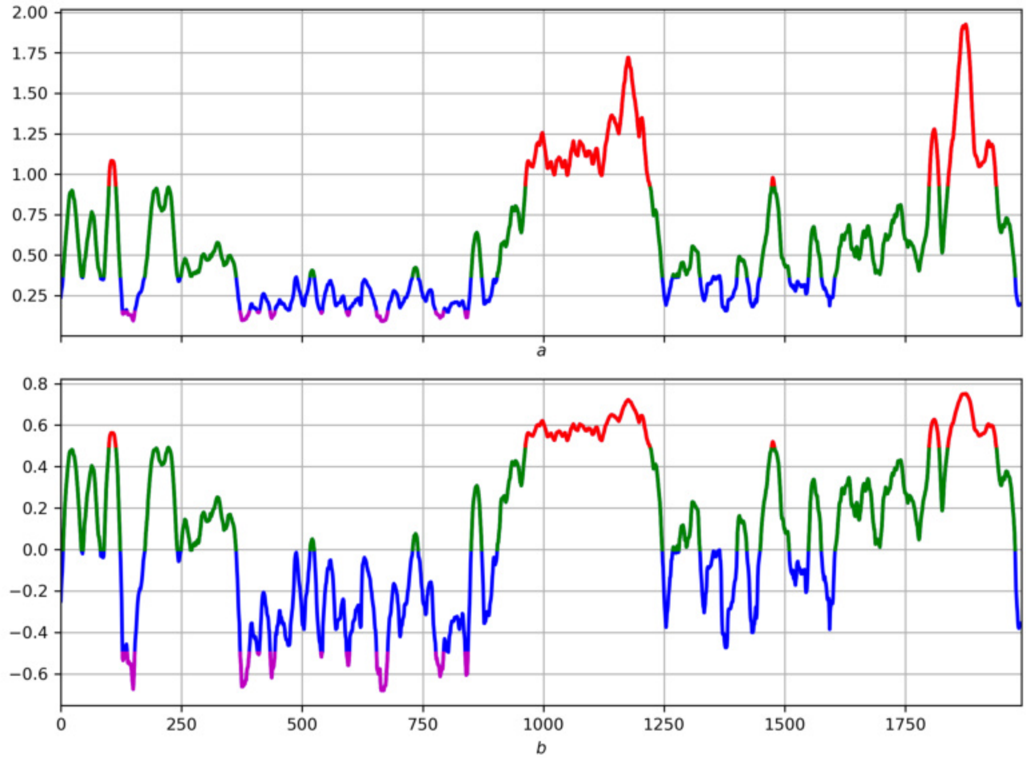

Figure 3. *a* – synthetic function; *b* – maximality measure.

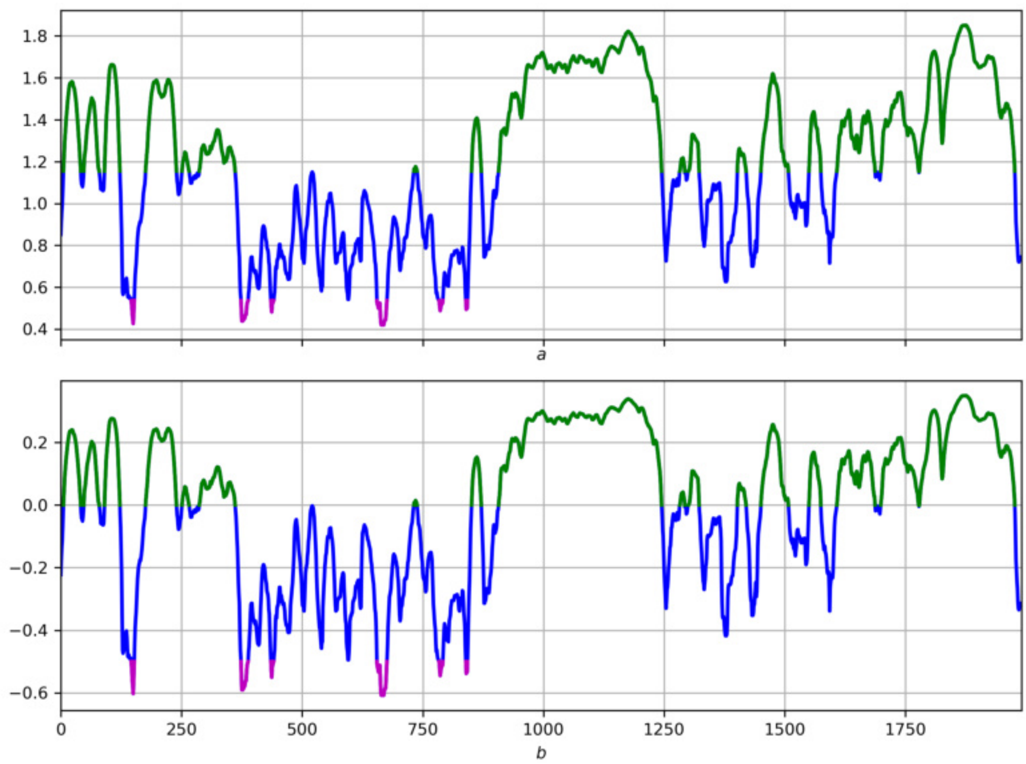

Figure 4. *a* – synthetic function; *b* – maximality measure.

in any quantities using numerous fuzzy logic operations and all kinds of averaging, which are denoted by $*$. These combinations are correct not only from a technical (syntactic) point of view, but also semantically, since all measures of straightening express the same essence – the quality of manifestation of the corresponding property.

It becomes possible to give meaning to a complex approach to record f from a set of straightenings $\mathfrak{P} = \{P\}$

$$\mu(\mathfrak{P})_f(t) = *_{P\in\mathfrak{P}}(\mu P_f(t)).$$

It is precisely this construction that, in the general case, models the researcher's view of the record f (a complex property on f). In many ways, such modeling is an art; it consists of selecting basic straightenings $\mathfrak{P}$ and connecting them correctly $* - *(\mathfrak{P})$. It is definitely not possible without understanding the measures μP_f on the record f for the basic straightening P_f.

This article is devoted to such an understanding in relation to the properties associated with discrete regression differentiation, and in this sense continues the research of the authors in the works [*Agayan et al.*, 2016, 2021b, 2019]. But before we get into that, let's take a quick look at the anomaly-related phase of the DMA research program.

If a fuzzy property is expressed on the scale of the segment $[-1, 1]$, then falling into the segment $[0.5, 1]$ can naturally be considered a strong (anomalous) manifestation of it.

Definition 4. *Node t is P-anomalous for record f if $\mu P_f(t) > 0.5$.*

The Figure 5 shows the triad: record → straightening → straightening measure for the ruggedness property L, anomalous nodes are marked in red.

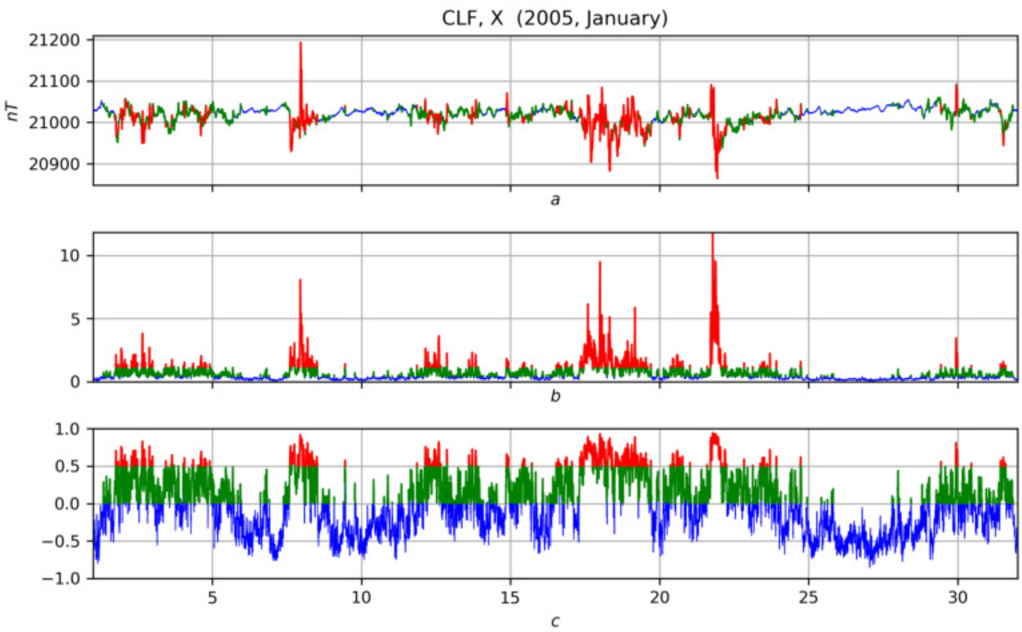

Figure 5. Triad: a – record f; b – straightening L_f; c – straightening measure μL_f.

The set of all anomalous nodes in T cannot be considered the final answer to P-anomaly: an anomalous node surrounded by calm nodes loses its anomaly and, conversely, a calm node surrounded by anomalous ones cannot in any way be considered completely calm.

In DMA, a functional clustering algorithm FDPS has been created that is capable of stably identifying the bases of hills on stochastic non-negative reliefs. Figure 6 compares its performance with simple level selection.

The result FDPS$(T, \mu P_f)$ of the FDPS algorithm on the space T with respect to the measure μP_f is the answer about the P-anomaly of the record f.

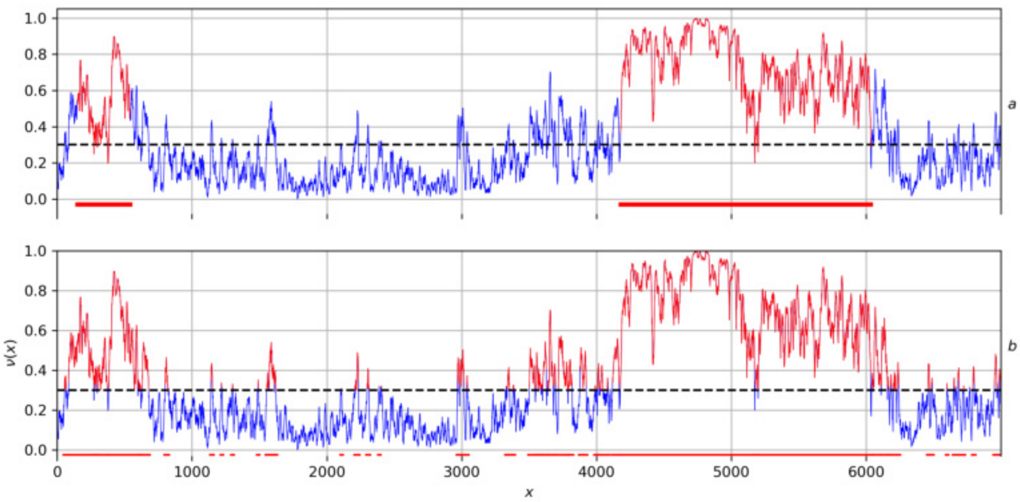

Figure 6. a – anomalies identified by the FDPS algorithm with $r = 23.26$; b – anomalies identified by level. The dotted line is the specified level $\alpha = 0.3$.

6. Regression Differentiation and Regression Smoothing

Continuous case: let the function f be integrable on an interval I containing zero internally. Then for a sufficiently small $\Delta > 0$ the segment $[-\Delta, \Delta]$ is contained in I. Let us denote by f_Δ the restriction of f to the segment $[-\Delta, \Delta]$: $f_\Delta = f_{[-\Delta,\Delta]}$ and calculate the projection $\operatorname{pr} f_\Delta$ of the function f_Δ in space $L^2[-\Delta, \Delta]$ into the two-dimensional subspace of linear functions $\operatorname{Lin}[-\Delta, \Delta]$. In [*Agayan et al.*, 2019] proven:

State 1. *If a function f has a tangent at zero, then as $\Delta \to 0$ the linear projection $\operatorname{pr} f_\Delta$ tends to it.*

The projection $\operatorname{pr} f_\Delta$ is nothing more than a linear regression of f on $[-\Delta, \Delta]$, and therefore the tangent is the limit position of local continuous regressions. This approach to differentiation in the continuous case can be extended to the discrete case, since discrete regressions are as effective and fundamental as continuous ones.
Discrete case. The limit transition $\bar{t} \to t$ in T is performed by the proximity measure δ_t (1) by fuzzification $T(t|\delta_t) = \{(\bar{t}, \delta_t(\bar{t})), \bar{t} \in T\}$. The above statement gives grounds to consider the tangent $l_\delta f(t) \leftrightarrow l_\delta f(t)(\bar{t}) = a_t \bar{t} + b_t$ for recording f at node f to be a linear regression constructed from the fuzzy image $\operatorname{Im}_\delta f(t) = \{(f(\bar{t}), \delta_t(\bar{t})), \bar{t} \in T\}$. Omitting the standard things associated with linear regressions, we present the formulas for a_t and b_t:

$$a_t = \frac{\begin{vmatrix} \sum_{\bar{t}\in T} \bar{t}\delta_t(\bar{t}) f(\bar{t}) & \sum_{\bar{t}\in T} \bar{t}\delta_t(\bar{t}) \\ \sum_{\bar{t}\in T} \delta_t(\bar{t}) f(\bar{t}) & \sum_{\bar{t}\in T} \delta_t(\bar{t}) \end{vmatrix}}{\begin{vmatrix} \sum_{\bar{t}\in T} \bar{t}^2\delta_t(\bar{t}) & \sum_{\bar{t}\in T} \bar{t}\delta_t(\bar{t}) \\ \sum_{\bar{t}\in T} \bar{t}\delta_t(\bar{t}) & \sum_{\bar{t}\in T} \delta_t(\bar{t}) \end{vmatrix}}, \quad b_t = \frac{\begin{vmatrix} \sum_{\bar{t}\in T} \bar{t}^2\delta_t(\bar{t}) & \sum_{\bar{t}\in T} \bar{t}\delta_t(\bar{t}) f(\bar{t}) \\ \sum_{\bar{t}\in T} \bar{t}\delta_t(\bar{t}) & \sum_{\bar{t}\in T} \delta_t(\bar{t}) f(\bar{t}) \end{vmatrix}}{\begin{vmatrix} \sum_{\bar{t}\in T} \bar{t}^2\delta_t(\bar{t}) & \sum_{\bar{t}\in T} \bar{t}\delta_t(\bar{t}) \\ \sum_{\bar{t}\in T} \bar{t}\delta_t(\bar{t}) & \sum_{\bar{t}\in T} \delta_t(\bar{t}) \end{vmatrix}}.$$

Definition 5.

1. *The angular coefficient a_t is called the regression derivative of f at t and is denoted by $D_\delta f(t)$.*
2. *The function $t \to a_t$ is called the regression derivative f and is denoted by $D_\delta f \in \mathrm{F}(T)$.*
3. *The functional correspondence $f \to D_\delta f$ is a linear operator $\mathrm{F}(T)$ and is called regression differentiation D_δ.*

Definition 6.

1. *The value* $l_\delta f(t)(t) = a_t t + b_t$ *of the regression tangent* $l_\delta f(t)$ *of record* f *at node* t *is called the regression value of* f *at* t *and is denoted by* $R_\delta f(t)$*.*
2. *The function* $t \to R_\delta f(t)$ *is called regression smoothing* f *and is denoted by* $R_\delta f \in \mathsf{F}(T)$*.*
3. *The functional correspondence* $f \to R_\delta f$ *is a linear operator* $\mathsf{F}(T)$ *and is called regression smoothing* R_δ*.*

Everywhere the measure δ is assumed to be from the family $\delta(s,r)$ (2). We denote the corresponding differentiation and smoothing by $D(s,r)$ and $R(s,r)$. Numerous studies provide grounds for the following conclusions:

1. Smoothing $D(s,r)$, not inferior to the usual averaging $M(s,r) = M_{\delta(s,r)}$ in universality, surpasses it in results (Figures 7–8).

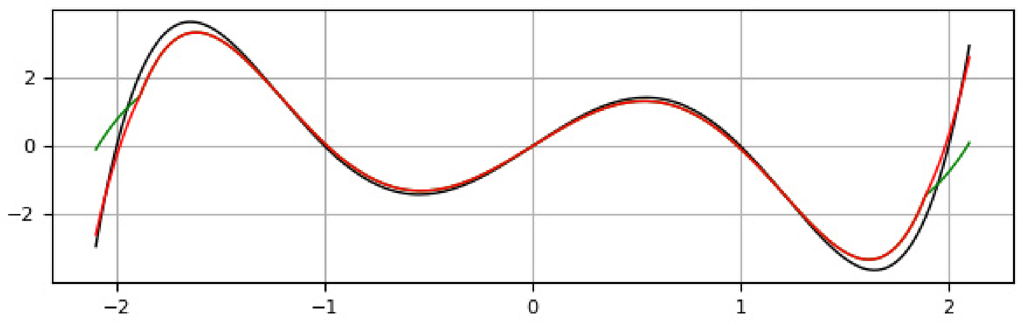

Figure 7. Regular grid. Black color – original function, green color – moving average, red color – regression smoothing.

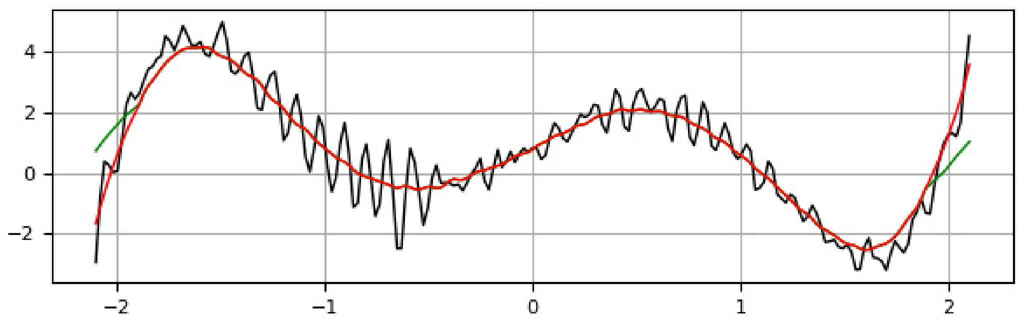

Figure 8. Regular grid. Black color – original function, green color – moving average, red color – regression smoothing.

2. The operator $R(s,r)$ is closely related to stochastic trends: areas of positive (negative) sign for $D(s,r)f$ correspond to increasing (decreasing) trends for f (Figures 9–10).

7. Multi-scale property analysis

Combining the property measure μP_f with a parametric family of different-scale localizations $\delta(s,r)$ (2) gives the spectrum of manifestation of property P on a record f in the interval of scales S:

$$\mu P_f(t,s) = \mu P_f(t|\delta_t(t,s)).$$

The function μP_f is defined on the product $T \times S$, takes values on the scale of the segment $[-1,1]$ and at each point (t,s) there is a measure $\mu P_f(t,s)$ of the manifestation of property P on the record f at node t at the scale of its consideration s, that is, relative to the localization $\delta_t(t,s)$.

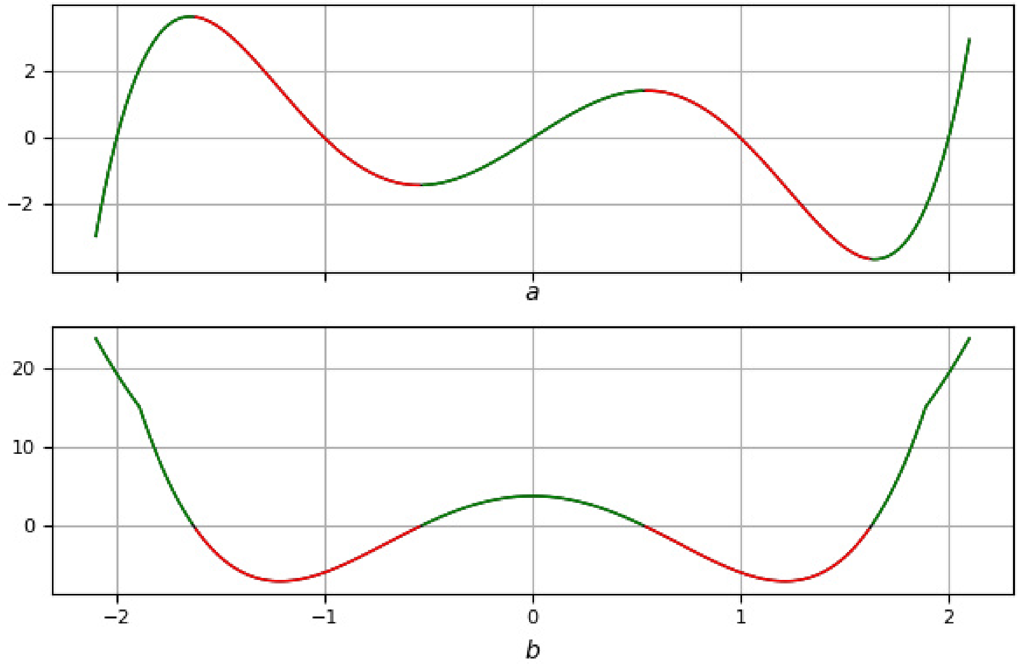

Figure 9. *a* – original function, *b* – its regression derivative. Red indicates decreasing zones, green indicates increasing zones.

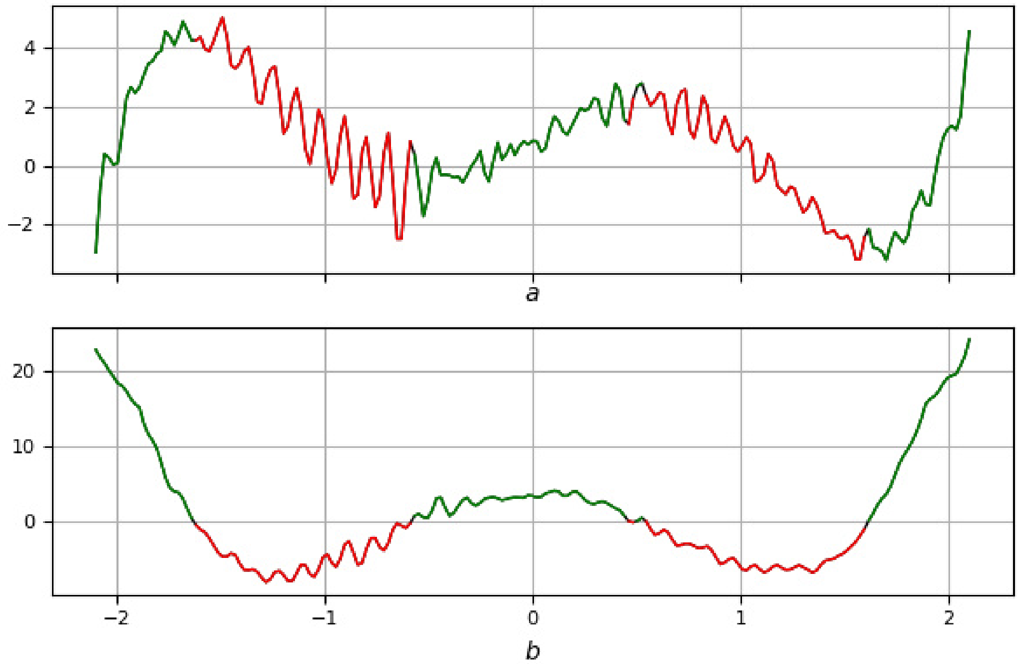

Figure 10. *a* – original function, *b* – its regression derivative. Red indicates decreasing zones, green indicates increasing zones.

Thus, the one-dimensional notation of f on T is associated with the two-dimensional function μP_f on $T \times S$. This redundancy makes it possible to better see what is happening at f and understand the nature of the process behind it.

Like the wavelet spectrum, the two-dimensional relief $\mu P_f(t,s)$ provides a visual representation of the dynamics of the emergence, evolution and disappearance of P-anomalies on f at different scales and in time. Formal analysis of the measure μP_f, which consists of extracting useful information from the record f, can be performed using the same methods as for the wavelet spectrum, in particular, Image Processing. Morphological and cluster DMA methods are also suitable. This is the motivation for conducting research at different scales.

8. Work Objectives (Statement and Goals)

One of the most important when analyzing any record is the "discontinuity-discontinuity" connection. In turn, the main design of their quantitative expression (straightening) is associated with the idea of smoothing: one or another smoothing of a record is considered its ideal scenario, the deviation from which quantitatively expresses "discontinuity-continuity" (small deviation ↔ continuity, large deviation ↔ discontinuity).

Thus, when constructing the straightening "energy" E_f, the ideal scenario for recording f was considered to be its averaging $M_\delta f$, and the energy itself $E_f(t) = EM_\delta f(t)$ was a local deviation at node t from its "correct" value $M_\delta f(t)$.

Similarly, if the ideal scenario for f is its regression smoothing $R_\delta f$, then the deviation $ER_f = |f - R_\delta f|$ will be a new straightening for f, quantitatively expressing for it the properties of continuity and discontinuity:

$$ER_f(t) = ER_f(t|\delta_t) = \frac{\sum_{\bar{t}\in T} |f(\bar{t}) - R_\delta f(t)\delta_t(\bar{t})}{\sum_{\bar{t}\in T} \delta_t(\bar{t})}.$$

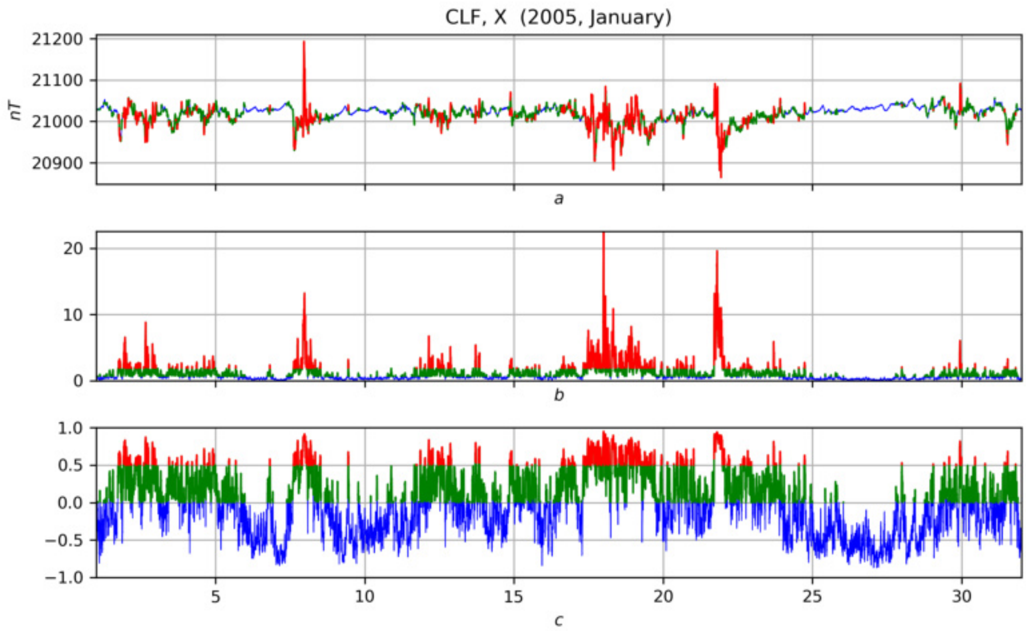

Figure 11. Triad: a – record f; b – straightening ER_f; c – maximality measure μER_f.

A multi-scale study of the μER_f measure for magnetic storms f is the first task of this work (Figure 11). The second task is a similar study for magnetic storms f of the measure of their local growth μD_f, based on regression differentiation D_δ (Figure 12):

$$\mu D_f(t) = \mu|D_f|(t)\,\mathrm{sgn}\,D_f(t),$$

where $\mu|D_f|(t)$ is a measure of the maximum modulus $|D_\delta f(t)|$ in the positive scale of the interval $[-1,1]$:

$$\mu|D_f|(t) = \frac{\sum_{\bar{t}\in T} \frac{|D_\delta f(t)|}{|D_\delta f(t)|+|D_\delta f(\bar{t})|}}{|T|}.$$

The study, in addition to the phenomenological geomagnetic analysis of measures, involves their simplest statistical analysis. It is associated with the division H of the segment $[-1,1]$ into four segments:

$$H \leftrightarrow [-1,1] = [-1,-0.5] \vee [-0.5,0] \vee [0,0.5] \vee [0.5,1].$$

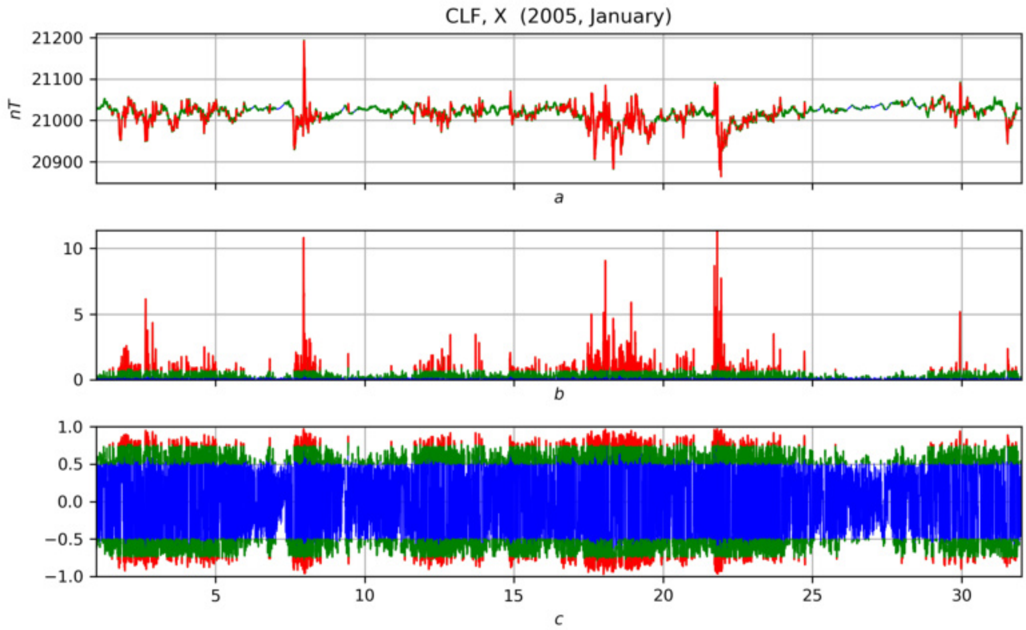

Figure 12. Triad: a – record f; b – straightening D_f; c – maximality measure μD_f.

If the measure $P_f(t,s)$ falls into these intervals, it means, respectively, from left to right, very weak, weak, moderate and strong manifestation of property P on the record f at node t at scale s.

The general picture on $T \times S$ of such a qualitative understanding of the situation in (t,s) is given by the histogram $H(\mu P_f)$, constructed from the partition H for the measure μP_f. It represents a four-dimensional coding f, is carried out in the work and serves as the basis for further studies of records, including their correlation and classification.

9. Application to Geomagnetic Storm Analysis

The capabilities of the technique can be displayed by analyzing magnetic observatory data registered during geomagnetic storms. From more than 50 storms that occurred during the current 25th magnetic activity solar cycle, we selected three storms that took place in November 2021 and during spring of 2022. The information on these storms, including their duration and peak values of geomagnetic activity indices Kp and Dst, is given in Table 1. According to NOAA magnetic storm intensity scale [*NOAA*, 2023], two of these three storms (the 2nd and 3rd) are moderate in their intensity (G2), and the first one is intense (G3). This also argees with their intensity classification using the Dst index: the first storm, having a Dst minimum value of −105 nT, refers to intense storms (however it is just 5 nT lower than the intense storm range threshold), and two other storms are moderate. This table actually gives the information about time spans for two storm phases, these are the main phase (MP) and the recovery, or relaxation phasre (RP). The main phase onset can generally be assumed as an exact moment of a whole magnetic storm onset; however, before some storms the sudden commencements take place several hours prior to a storm onset, and in this case, depending on a particular research goals, the sudden commencement time moment can be a point in time that can be considered the beginning of a storm. For convenience, we use the Dst index data [*ISGI*, 2023] to identify the timestamps of storm onsets and ends, as well as the Dst minimum values at the end of main storm phases. Dst index abrupt decrease to slightly negative values was considered a storm onset, and its increase during the storm recovery phase above -30 nT was defined as its end. The corresponding dashed marking lines with captions were superimposed on magnetic data plots for Dst index data (Figure 13).

Table 1. Information on seismic stations used

MP Start, UTC	Peak (MP End), Peak (UTC)	Peak Dst, nT	RP End, UTC	Duration, Hrs	Kp max
04.11.2021 06:00	04.11.2021 13:00	–105	05.11.2021 04:00	22	8–
13.03.2022 14:00	14.03.2022 00:00	–83	14.03.2022 08:00	18	6+
14.04.2022 15:00	14.04.2022 21:00	–86	15.04.2022 03:00	12	6o

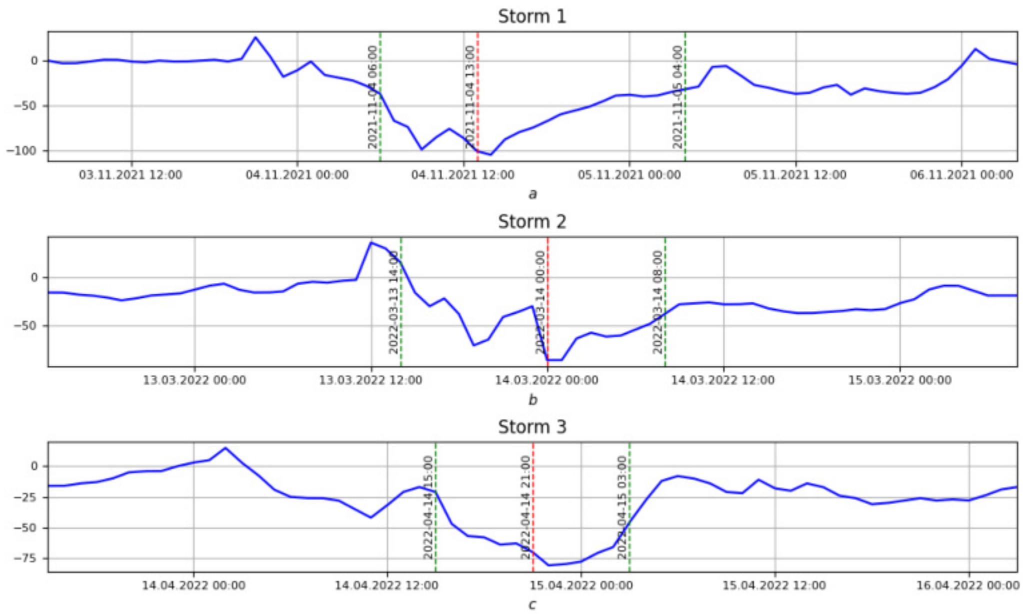

Figure 13. Dst index data for the selected storms (see Table 1). Dashed lines mark the storm onsets, peaks and ends.

To test the general capabilities of the method, data from two magnetic observatories were selected: the Borok observatory (IAGA-code BOX, Russia) and the Alma Ata observatory (AAA, Kazakhstan). The information on these observatories is given in Table 2 and includes their names, geographic coordinates (ϕ, λ) and geomagnetic coordinates (ϕ_M, λ_M). The geomagnetic coordinates were calculated for the corresponding time periods using the web service designed at the World Data Center for Geomagnetism, Kyoto [*WDC*, 2023]. Both observatories are members of INTERMAGNET network [*Intermagnet*, 2023], so we use their names as given on the INTERMAGNET website. As these two observatories differ by latitude, they were chosen in order to see how the method works in geomagnetic conditions at different latitudes. We analyzed the X component as it is most exposed to the external magnetic field during a geomagnetic storm. It is often hard to identify the time limits of storm evolution phases using only magnetic observatory data, even cleared from possible artificial disturbances and converted into complete component values, due to intense magnetic activity variations.

Table 2. Information on seismic stations used

IAGA Code	Name	ϕ, λ	ϕ_M, λ_M (2021)	ϕ_M, λ_M (2022)
AAA	Alma Ata	43.25° N, 76.92° E	34.83° N 153.22° E	34.88° N 153.20° E
BOX	Borok	58.07° N, 38.23° E	53.61° N 123.20° E	53.64° N 123.14° E

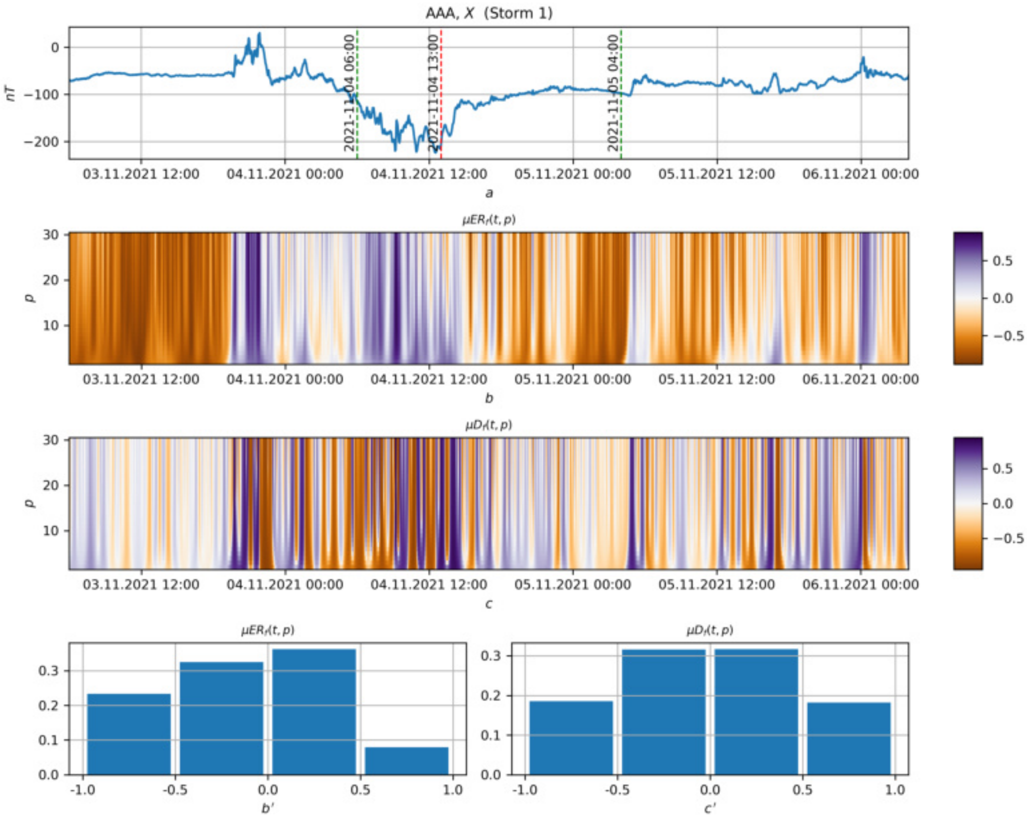

Figure 14. *X* component recorded at AAA magnetic observatory during Storm 1 (*a*); the activity measure plots (*b*–*d*) and their corresponding histograms (*b′*-*d′*).

The first storm (November 4–5, 2021, Figures 14, 15) was the one of the fist intense storms since the beginning of the new 25th solar cycle. The studied interplanetary magnetic field (IMF) and solar wind data extracted from NASA/GSFC's OMNI data set through OMNIWeb [*OMNI*, 2023] generally shows that, despite the fact that the initial interplanetary field state did not look very suitable for a storm generation, the overall energy driven by the coronal mass ejection produced an intense impact of the magnetohydrodynamic shockwave on the Earth's magnetosphere by the end of November 3. As the *Bz* magnetic field component abruptly turned southward, indicating the moment of the shockwave arrival, the particle speed and proton density in the plasma flux also rapidly increased 1.5 times and more than 3 times, respectively. The resulting sudden commencement signal, reaching 40 to 55 nT, is clearly seen on the records of magnetic observatories on November 3 at approximately 19:50 UTC, and also can be identified on the Dst plot (Figure 13). During November 4, the planetary K-index increased to almost 8 points, which corresponds to strong geomagnetic disturbance. By the end of the main storm phase, the total storm magnitude, as found out by the Dst peak value, was about −105 nT. During November 5, the Kp-index took values from 2 to 4 points (4 points also corresponds to a disturbed geomagnetic situation). The storm recovery phase lasted till November 5, 04:00 UTC.

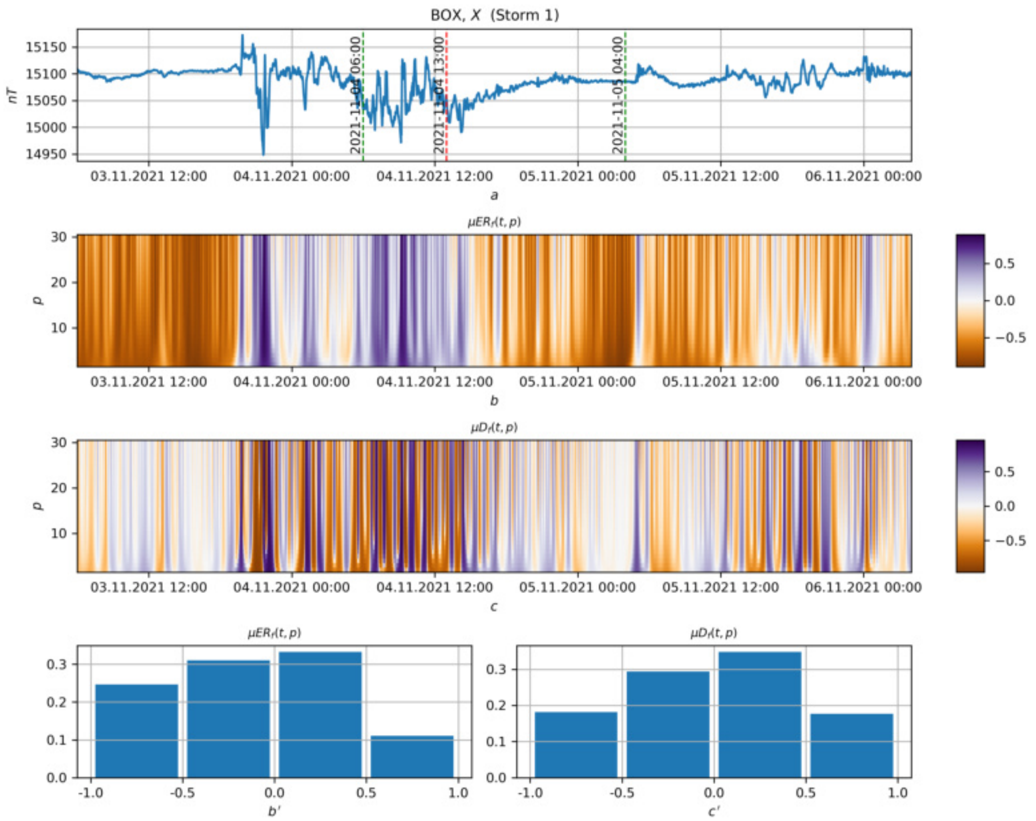

Figure 15. X component recorded at BOX magnetic observatory during Storm 1 (a); the activity measure plots (b–d) and their corresponding histograms (b'–d').

The activity measures for this storm for both BOX and AAA observatories (Figures 16–17) were built not only for the above mentioned storm phases, but also for some time period prior to the MP onset and for some period after the storm recovery. Their plots display some general similarities. However, the particular storm periods are reflected in a different way. The $\mu ER_f(t,p)$ measure plot clearly displays more high-magnitude elements of the storm signal, such as the sudden commencement beginning and its abrupt decrease, as well as the most intense oscillations on the X component during the main storm phase. The particularity of the behavior of this measure is that most of the anomalous fragments highlighted by it as positive are bounded by abrupt increases and decreases and correspond to changes of physical conditions of the magnetic field of the Earth and its interaction with the solar wind. Therefore, the storm sudden commencement and the main phase are clearly marked as fragments within the values are strongly positive. On the contrary, the calm periods of the X component correspond mostly to negative μER_f values (an example is the storm recovery phase fragment). The next measure, μDR_f, related to derivative and therefore to an overall signal variability, emphasizes smaller oscillations of the initial signal; however, relatively large-scale abrupt fragments are reflected in a way close to the μER_f result. Certainly, the μDR_f values appear to be lower for less variable fragments This can be a tool to highlight the structure of oscillation sequences related to the storm phases. It's important to note that the initial X component magnetic records for AAA and BOX observatories are quite different in their range: the AAA data for the MP ending period has a minimum of more than 200 nT compared to the conditions before the storm (Figure 14a), whereas the corresponding BOX data (Figure 15a) decrease is only about 100 nT. Moreover, the BOX data has disturbances higher in their amplitude

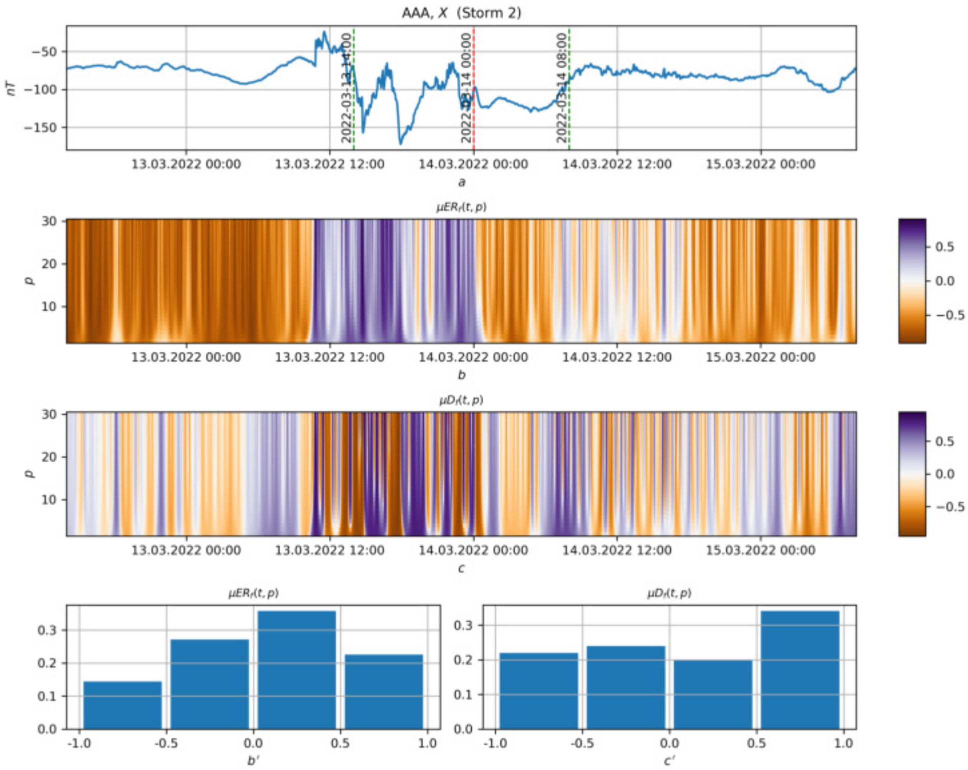

Figure 16. X component recorded at AAA magnetic observatory during Storm 2 (a); the activity measure plots (b–c) and their corresponding histograms (b'–c').

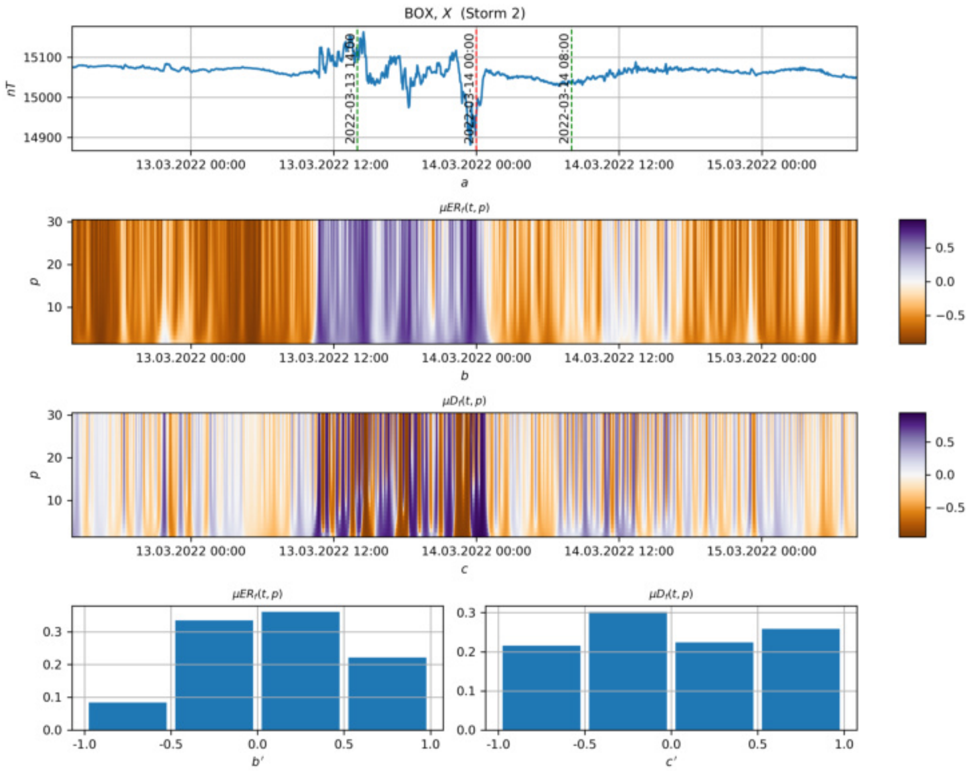

Figure 17. X component recorded at BOX magnetic observatory during Storm 2 (a); the activity measure plots (b–c) and their corresponding histograms (b'–c').

than the corresponding ones in the AAA data. The reason for both is in the geographical location of these observatories (see Table 2) and, in particular, in the latitudinal distance of these observatories from the equatorial ring current and the auroral zone: the Dst current system contributes more to the overall dynamics of geomagnetic variations at the AAA observatory, whereas the auroral disturbandes, including the ones occurring during the recovery phase of the storm, have a stronger impact on the BOX variation data. The next storm that occurred in March 2022 (Figures 16–17) was quite similar to the previous one in the initial interplanetary conditions as, according to IMF and plasma data, the coronal mass ejection also caused a large shockwave impact on the magnetosphere, which resulted in a sudden commencement in the middle of March 13. However, due to a series of intense IMF *Bz* direction alternations, the storm evolution began several hours later at about 19:00 UTC. By the end of the relatively short and intense main phase, the Dst value for this storm reached a minimum of −83 nT (on March 14, 01:00 UTC). The measure plots for both observatories again have similarities: both μER_f plots show large positive values related to the sudden commencement moment and the following fragment related to intense alternations of $\underline{Bz}$ and solar wind characteristics during the storm phase that influenced the geomagnetic field registered on the Earth's surface. Both μDR_f and μER_f show the oscillations possibly related to auroral disturbances, however, μDR_f reflects more small-scale details for this phase.

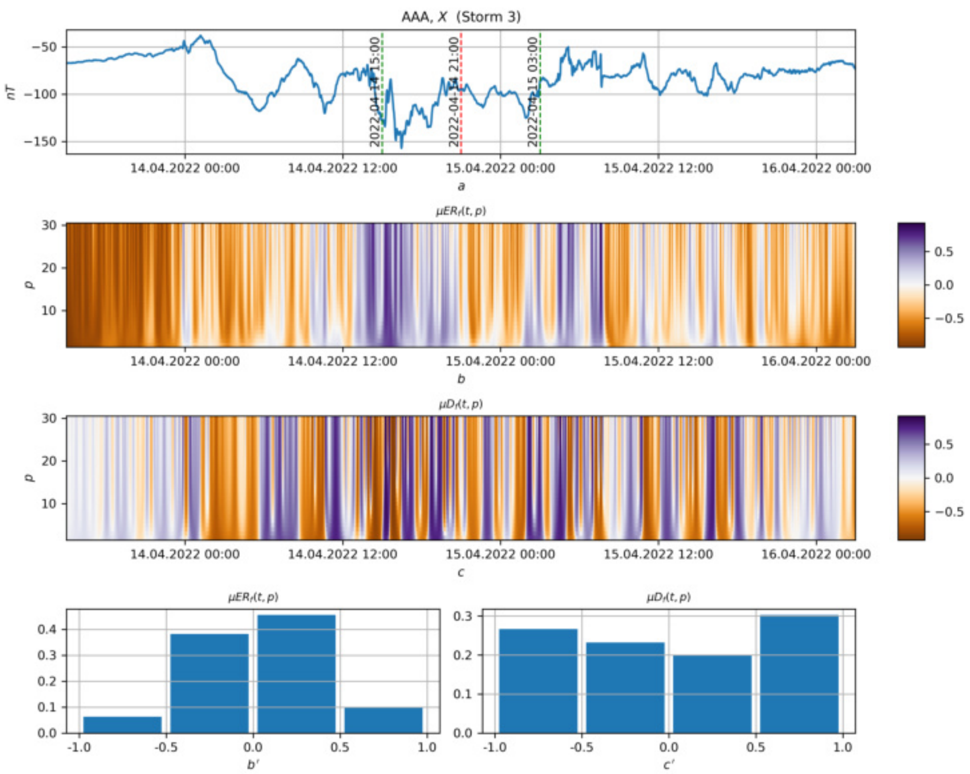

Figure 18. *X* component recorded at AAA magnetic observatory during Storm 3 (*a*); the activity measure plots (*b*–*c*) and their corresponding histograms (*b′*–*c′*).

On the eve of the third storm that occurred in April 2022 (Figures 18–19), the IMF *Bz* component turned southward on April 13, however, initially the solar wind energy was lower than that of two previous storms, and its impact on the Earth's magnetosphere was too low to produce an abrupt sudden commencement signal. Nevertheless, during the storm evolution, the energy driven by the solar wind plasma resulted in a total storm magnitude of −80 nT, according to Dst index data. Like in the previous cases, the closeness of BOX geomagnetic (as well as geographic) latitude to the auroral oval results in multiple oscillations caused by related disturbances due to the auroral current system behaviour. Unlike the BOX data, the AAA X data appears to have more long-period disturbances, which are a result of several generations of a storm. As seen from Figures 18–19 (b, c), the behavior of each measure is similar to its behavior for previous storms; nevertheless, the μER_f again indicates both large- and small-scale morphological features of the storm more clearly than the other indicator.

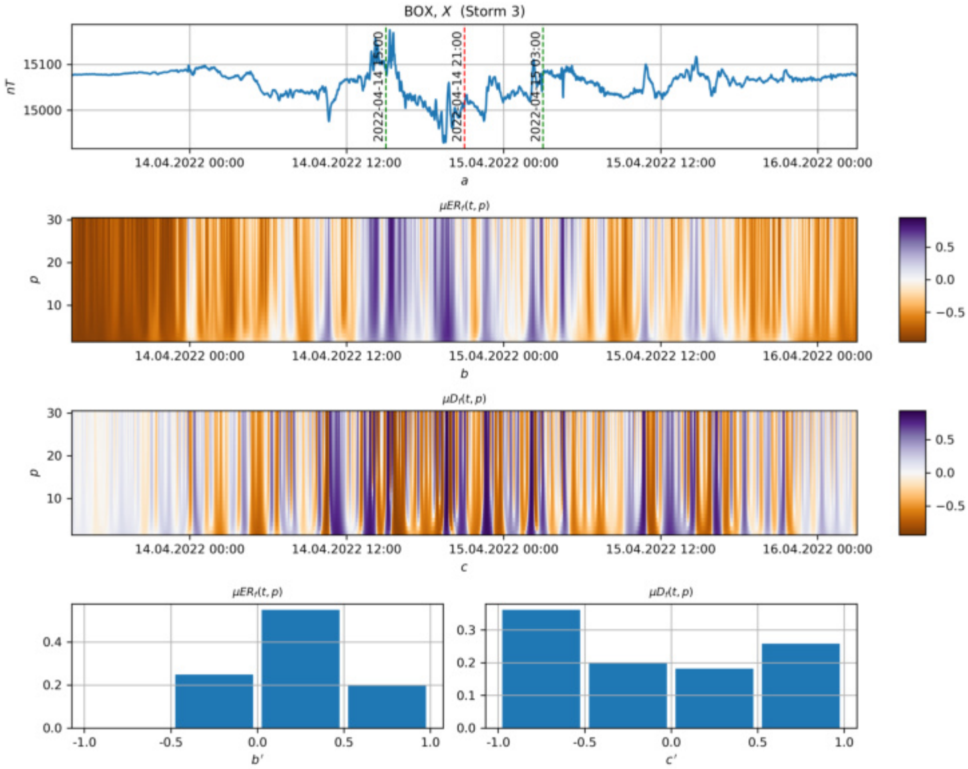

Figure 19. X component recorded at BOX magnetic observatory during Storm 3 (a); the activity measure plots (b–c) and their corresponding histograms (b'–c').

The histograms for μER_f, representing an additional quantitative geomagnetic activity assessment, display the distribution of energy levels within the interval $[-1, 1]$. As seen, maximal μER_f occurrence is related to the $[-0.5, 0.0]$ interval; therefore, the most fragments that respond to the energy indicator are related to slightly negative values. Strong positive correlation is seen between the histograms for different observatories during the same storm. This confirms that the chosen method allows assessing geomagnetic activity regardless of geomagnetic latitude and even predicting the expected levels of disturbances to a certain extent. Notably, this strong correlation is seen for histograms related to different storms. This suggests a reliable connection of the indicator with the physical processes of interactions between the magnetosphere and the solar wind during a geomagnetic storm.

The indicators also provide an opportunity for spectral decomposition of geomagnetic variations, as the p increase results in adding more high-frequency details to the measure plots.

10. Discussion and Conclusion

In this work, to record $f = f(t)$ and the local property P relating to it, a fuzzy measure (spectrum) $\mu P_f = \mu P_f(t, s)$ of the manifestation of P on f in time t and scale of consideration s is constructed. Thus, the one-dimensional record $f(t)$ is associated with the two-dimensional function $\mu P_f(t, s)$. This redundancy makes it possible to better see what is happening at f and understand the nature of what is behind it. The authors suggest further improvement of the transition $f \to \mu P_f$. But the main thing for them today is the similarity of the spectrum of properties and the wavelet spectrum. More precisely, when the property of P is the correlation of the record f with one or another wavelet ψ: $P = \mathrm{cor}_\psi$, then the measure constructed for it is similar to the wavelet spectrum, but more contrasting (Figures 20–21). So in this sense, the property measure generalizes wavelets.

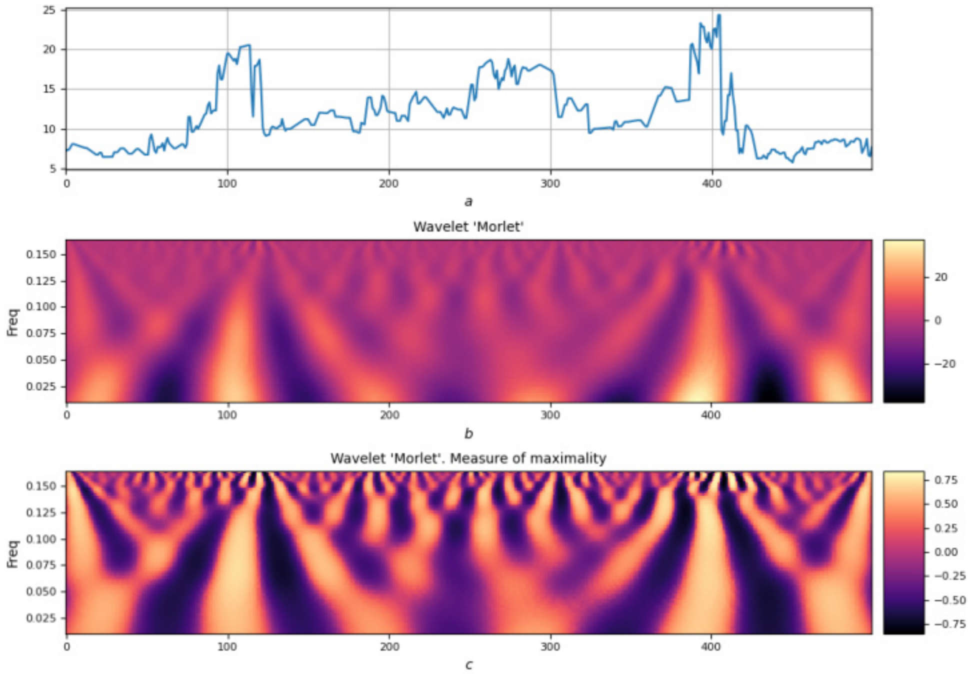

Figure 20. *a* – synthetic record (units in both axes are dimensionless); *b* – wavelet spectrum (Morlet); *c* – maximality measure.

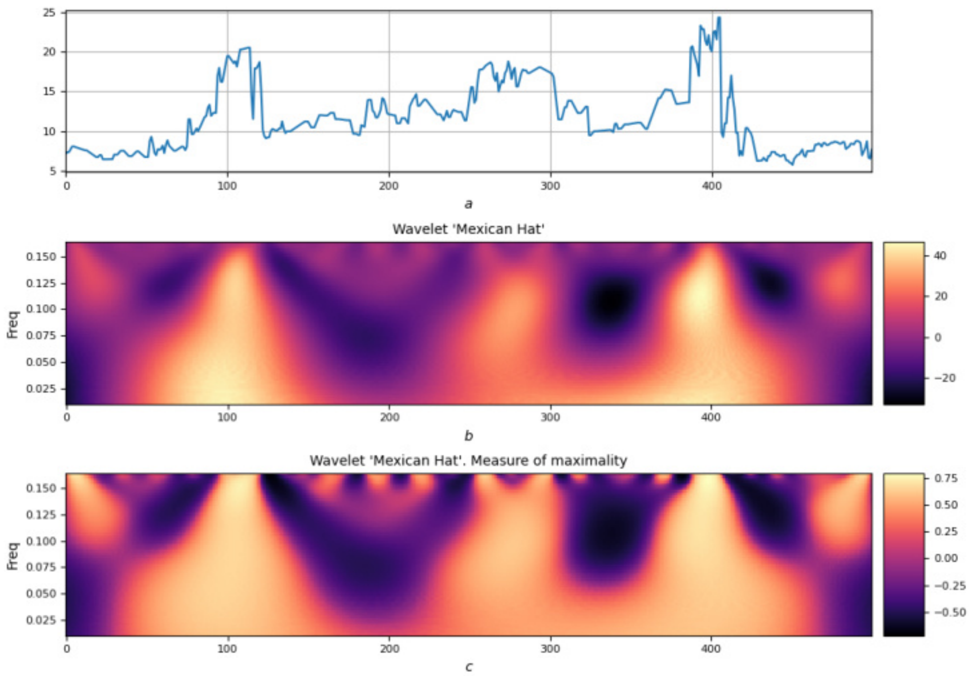

Figure 21. *a* – synthetic record (units in both axes are dimensionless); *b* – wavelet spectrum (Mexican Hat); *c* – maximality measure.

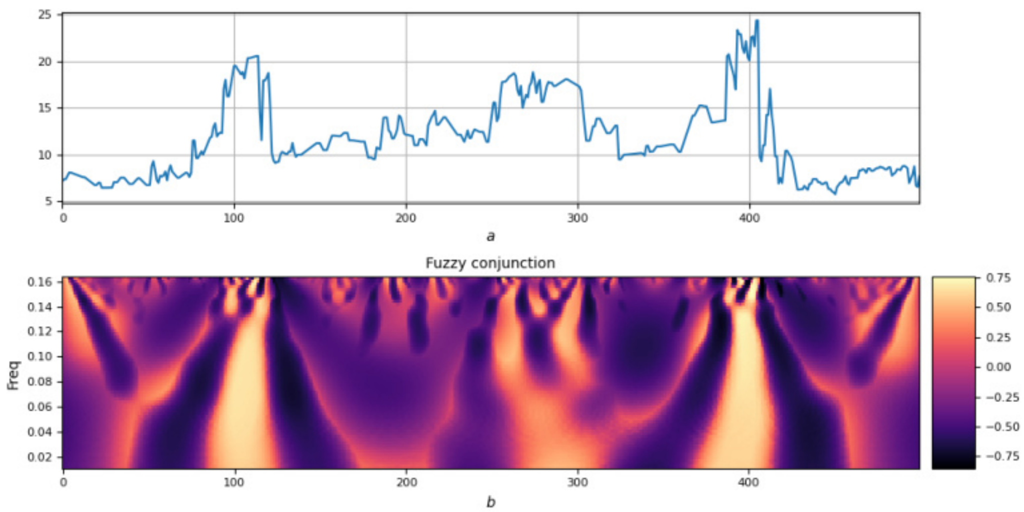

Figure 22. *a* – synthetic record (units in both axes are dimensionless); *b* – connection of measures (Figures 20*c* and 21*c*): fuzzy conjunction.

There is one more important circumstance: property measures, being fuzzy structures, can be combined using fuzzy logic operations into new measures (spectra). In projection onto wavelets, this is a completely new thing for them: the wavelet spectrum obtained by such a combination of two traditional wavelet spectra does not have a basis wavelet. Figure 22 shows the conjunction of the wavelet spectra from Figures 20 and 21.

The authors are interested in the possibilities of fuzzy logic in wavelet theory.

Acknowledgments. This work was conducted in the framework of budgetary funding of the Geophysical Center of RAS, adopted by the Ministry of Science and Higher Education of the Russian Federation (grant number 075-00443-24-00). The results presented in this paper rely on data collected at magnetic observatories. We thank the national institutes that support them and INTERMAGNET for promoting high standards of magnetic observatory practice (http://www.intermagnet.org/). This work employed facilities and data provided by the Shared Research Facility "Analytical Geomagnetic Data Center" of the Geophysical Center of RAS (http://ckp.gcras.ru/).

References

Agayan, S., S. Bogoutdinov, A. Soloviev, and R. Sidorov (2016), The Study of Time Series Using the DMA Methods and Geophysical Applications, *Data Science Journal*, *15*, https://doi.org/10.5334/dsj-2016-016.

Agayan, S., S. Bogoutdinov, D. Kamaev, V. Kaftan, M. Osipov, and V. Tatarinov (2021a), Theoretical Framework for Determination of Linear Structures in Multidimensional Geodynamic Data Arrays, *Applied Sciences*, *11*(24), 11,606, https://doi.org/10.3390/app112411606.

Agayan, S., S. Bogoutdinov, R. Krasnoperov, and R. Sidorov (2021b), A Multiscale Approach to Geomagnetic Storm Morphology Analysis Based on DMA Activity Measures, *Applied Sciences*, *11*(24), 12,120, https://doi.org/10.3390/app112412120.

Agayan, S. M., S. R. Bogoutdinov, and R. I. Krasnoperov (2018), Short introduction into DMA, *Russian Journal of Earth Sciences*, *18*(2), 1–10, https://doi.org/10.2205/2018es000618.

Agayan, S. M., A. A. Soloviev, S. R. Bogoutdinov, and Y. I. Nikolova (2019), Regression Derivatives and Their Application to the Study of Geomagnetic Jerks, *Geomagnetism and Aeronomy*, *59*(3), 359–367, https://doi.org/10.1134/s0016793219030022.

Agayan, S. M., V. N. Tatarinov, A. D. Gvishiani, S. R. Bogoutdinov, and I. O. Belov (2020), FDPS algorithm in stability assessment of the Earth's crust structural tectonic blocks, *Russian Journal of Earth Sciences*, *20*(6), 1–14, https://doi.org/10.2205/2020es000752.

Agayan, S. M., S. R. Bogoutdinov, B. A. Dzeboev, B. V. Dzeranov, D. A. Kamaev, and M. O. Osipov (2022), DPS clustering: New results, *Applied Sciences*, *12*(18), 9335, https://doi.org/10.3390/app12189335.

Akasofu, S.-I., and S. Chapman (1963), The development of the main phase of magnetic storms, *Journal of Geophysical Research*, *68*(1), 125–129, https://doi.org/10.1029/jz068i001p00125.

Batyrshin, I. Z., A. O. Nedosekin, and A. A. Stetsko (2007), *Fuzzy hybrid systems. Theory and practice*, 207 pp., Fizmatlit.

Boroev, R. N., and M. S. Vasiliev (2017), Relationship between Indexes of Geomagnetic Activity on the Main Phase of a Magnetic Storm for Various Types of Solar Wind, *Science and Education*, *1*, 67–70, in Russian.

Gromova, L. I., N. G. Kleimenova, A. E. Levitin, S. V. Gromov, L. A. Dremukhina, and N. R. Zelinskii (2016), Daytime geomagnetic disturbances at high latitudes during a strong magnetic storm of June 21–23, 2015: The storm initial phase, *Geomagnetism and Aeronomy*, *56*(3), 281–292, https://doi.org/10.1134/s0016793216030051.

Gvishiani, A., A. Soloviev, R. Krasnoperov, and R. Lukianova (2016a), Automated Hardware and Software System for Monitoring the Earth's Magnetic Environment, *Data Science Journal*, *15*, https://doi.org/10.5334/dsj-2016-018.

Gvishiani, A. D., R. V. Sidorov, R. Y. Lukianova, and A. A. Soloviev (2016b), Geomagnetic activity during St. Patrick's Day storm inferred from global and local indicators, *Russian Journal of Earth Sciences*, *16*(6), 1–8, https://doi.org/10.2205/2016es000593.

Intermagnet (2023), International Real-time Magnetic Observatory Network, https://intermagnet.org, accesed on 1 November 2023.

ISGI (2023), International service of geomagnetic indices, https://isgi.unistra.fr, accesed on 1 November 2023.

Kacprzyk, J., A. Wilbik, and S. Zadrożny (2007), Linguistic Summarization of Time Series by Using the Choquet Integral, in *Lecture Notes in Computer Science*, pp. 284–294, Springer Berlin Heidelberg, https://doi.org/10.1007/978-3-540-72950-1_29.

Kovalev, S. M. (2007), Hybrid fuzzy-temporal models of time series in problems of analysis and identification of weakly formalized processes, in *Integrated Models and Soft Computing in Artificial Intelligence. Proceedings of the IVth International Scientific and Practical Conference (Kolomna, May 28-30, 2007), Moscow: Fizmatlit.*, vol. 1, pp. 26–41.

Lazutin, L. L. (2012), *Global and polar magnetic storms*, 214 pp., Moscow State University, in Russian.

Mishin, V. M., M. Foerster, T. I. Saifudinova, A. D. Bazarzhapov, Y. A. Karavaev, L. A. Sapronova, and S. I. Solovyev (2007), Spontaneous substorms and ordered type of magnetospheric disturbances during the superstorm of November 20, 2003, *Geomagnetism and Aeronomy*, *47*(4), 429–441, https://doi.org/10.1134/s0016793207040032.

NOAA (2023), National Oceanic and Atmospheric Administartion, https://www.noaa.gov, accesed on 1 November 2023.

OMNI (2023), OMNIWeb Plus, https://omniweb.gsfc.nasa.gov, accesed on 01 November 2023.

Oshchenko, A. A., R. V. Sidorov, A. A. Soloviev, and E. N. Solovieva (2020), Overview of anomality measure application for estimating geomagnetic activity, *Geophysical research*, *21*(4), 51–69, https://doi.org/10.21455/gr2020.4-4.

Pandey, S. K., and S. C. Dubey (2009), Characteristic features of large geomagnetic storms observed during solar cycle 23, *Indian Journal of Radio & Space Physics*, *38*(6), 305–312.

Pedrycz, W., and M. Smith (1999), Granular correlation analysis in data mining, in *FUZZ-IEEE'99. 1999 IEEE International Fuzzy Systems. Conference Proceedings (Cat. No.99CH36315)*, IEEE, https://doi.org/10.1109/fuzzy.1999.790078.

Soloviev, A., S. Agayan, and S. Bogoutdinov (2017), Estimation of geomagnetic activity using measure of anomalousness, *Annals of Geophysics*, *59*(6), https://doi.org/10.4401/ag-7116.

Soloviev, A., A. Smirnov, A. Gvishiani, J. Karapetyan, and A. Simonyan (2019), Quantification of Sq parameters in 2008 based on geomagnetic observatory data, *Advances in Space Research*, *64*(11), 2305–2320, https://doi.org/10.1016/j.asr.2019.08.038.

Tanaka, H., S. Uejima, and K. Asai (1982), Linear Regression Analysis with Fuzzy Model, *IEEE Transactions on Systems, Man, and Cybernetics*, *12*(6), 903–907, https://doi.org/10.1109/tsmc.1982.4308925.

WDC (2023), World Data Center for Geomagnetism, Kyoto, https://wdc.kugi.kyoto-u.ac.jp, accesed on 1 November 2023.

Yarushkina, N. G. (2004), *Fundamentals of the theory of fuzzy and hybrid systems*, 320 pp., Finansy i statistika.

Yarushkina, N. G., T. R. Yunusov, and T. V. Afanasyeva (2007), Terminal-server traffic modeling based on fuzzy time series trend analysis, *Program products and systems*, (4), 15–19.

Yermolaev, Y. I., I. G. Lodkina, N. S. Nikolaeva, and M. Y. Yermolaev (2012), Recovery phase of magnetic storms induced by different interplanetary drivers, *Journal of Geophysical Research: Space Physics*, *117*(A8), A08,207, https://doi.org/10.1029/2012ja017716.

Yermolaev, Y. I., I. G. Lodkina, N. S. Nikolaeva, and M. Y. Yermolaev (2014), Influence of the interplanetary driver type on the durations of the main and recovery phases of magnetic storms, *Journal of Geophysical Research: Space Physics*, *119*(10), 8126–8136, https://doi.org/10.1002/2014ja019826.

Yokoyama, N., and Y. Kamide (1997), Statistical nature of geomagnetic storms, *Journal of Geophysical Research: Space Physics*, *102*(A7), 14,215–14,222, https://doi.org/10.1029/97ja00903.

Zhang, G.-L. (1992), Interplanetary disturbance structures and geomagnetic storm, in *AIP Conference Proceedings*, AIP, https://doi.org/10.1063/1.41724.

MODELING THE HORIZONTAL VELOCITY FIELD OF THE EARTH'S CRUST IN A REGULAR GRID FROM GNSS MEASUREMENTS

Alexander I. Manevich[*,1,2], **Iliya V. Losev**[1], **Alina M. Avdonina**[1], **Roman V. Shevchuk**[1,3], **Vladimir I. Kaftan**[1], **and Viktor N. Tatarinov**[1,3]

[1] Geophysical Center RAS, Moscow, Russia
[2] National University of Science and Technology MISIS, College of Mining, Moscow, Russia
[3] Schmidt Institute of the Physics of the Earth RAS, Moscow, Russia
[*] **Correspondence to:** Alexander I. Manevich, a.manevich@gcras.ru.

Abstract: There are numerous methods for modeling velocity fields of the Earth's crust. However, only a few of them are capable of modeling data beyond the contour of the geodetic network (extrapolating). Spatial modeling based on a neural network approach allows for the adequate modeling of the field of recent crustal movements and deformations of the Earth's crust beyond the geodetic network contour. The study extensively examines the hyperparameter settings and justifies the applicability of the neural network model for predicting crustal movement fields using the Ossetian geodynamic polygon as an example. The presented results, when compared to classical modeling methods, demonstrate that the neural network approach confidently yields results no worse than classical methods. The results of modeling for the Ossetian polygon can be used for geodynamic zoning, identification zones of extension and compression, computing the tectonic component of stresses, and identifying areas of high-gradient displacements.

Keywords: velocity fields, resent crustal movements, spatial modeling, regular grid, extrapolation, interpolation, artificial neural networks.

Citation: Manevich, A. I., I. V. Losev, A. M. Avdonina, R. V. Shevchuk, V. I. Kaftan, and V. N. Tatarinov (2023), Modeling the Horizontal Velocity Field of the Earth's Crust in a Regular Grid from GNSS Measurements, *Russian Journal of Earth Sciences*, 23, ES6002, EDN: IXIPOZ, https://doi.org/10.2205/2023es000885

RESEARCH ARTICLE

Received: 30 November 2023
Accepted: 24 December 2023
Published: 30 December 2023

1. Introduction

Recent crustal movements (RCM), especially in seismically active areas within zones of active tectonic faults, can lead to natural disasters and accidents at hazardous industrial facilities. These facilities include linear main gas and oil pipelines, hydraulic structures, radiation hazardous sites, chemical plants, etc. [*Batugin et al.*, 2022; *Tatarinov et al.*, 2019]. Each year, new technologies and protective measures are developed. They are aimed at reducing the number of accidents and the associated social, economic, and environmental consequences. The exploration of new territories, the complexification of mineral extraction conditions, and industrial technological processes result in stricter industrial safety requirements. According to regulatory requirements, deformation monitoring of the geological environment is an integral and crucial part of the system ensuring the safety of engineering structures. Deformation monitoring involves periodic geodetic observations, accompanied by analysis, interpretation of observation results, and an ensuing evaluation of the geological environment's condition.

The most common measurement tools for monitoring RCM are Global Navigation Satellite Systems (GNSS). GNSS tools are used to measure displacements of points at geodynamic sites in the vicinity of engineering objects. However, due to various circumstances, ensuring the sufficiency and reliability of the initial data is not always possible. The insufficiency of data for studying RCM parameters is caused by the following reasons [*Bogusz et al.*, 2013; *Manevich et al.*, 2022; *Shen et al.*, 1996, 2015]:

- limited availability of dense networks and a sufficient number of points for continuous instrumental observations operating over a long period.

- complex organization of measurements in both field campaigns and continuous observations.
- inability to establish a proper structure for geodynamic sites due to economic, physical-geographical, and social conditions.
- difficulty in accessing instrumental measurement data at geodynamic sites (both governmental and academic).
- a low number of highly accurate continuously operating GNSS stations with open access to measurement data.

Figure 1 presents an example of the Ossetian geodynamic polygon [Mironov et al., 2021]. It is evident that the GNSS network contour is disproportionately elongated in the southwest-northeast direction. Due to complex physical geographical conditions, approximately 3/4 of the entire territory lies outside the measurement network's contour. Consequently, obtaining surface movement values for this area is unattainable. This affects the assessment of internal deformations. This happens because the triangles along the edges are comparable in area to the entire polygon's contour, while those along the diagonal are too distant from an equilateral Figure 1. The configuration of the finite elements is not optimal for deformation analysis. This deteriorates the accuracy of deformation component calculations and complicates their geometric interpretation [Dokukin et al., 2010; Wu et al., 2003].

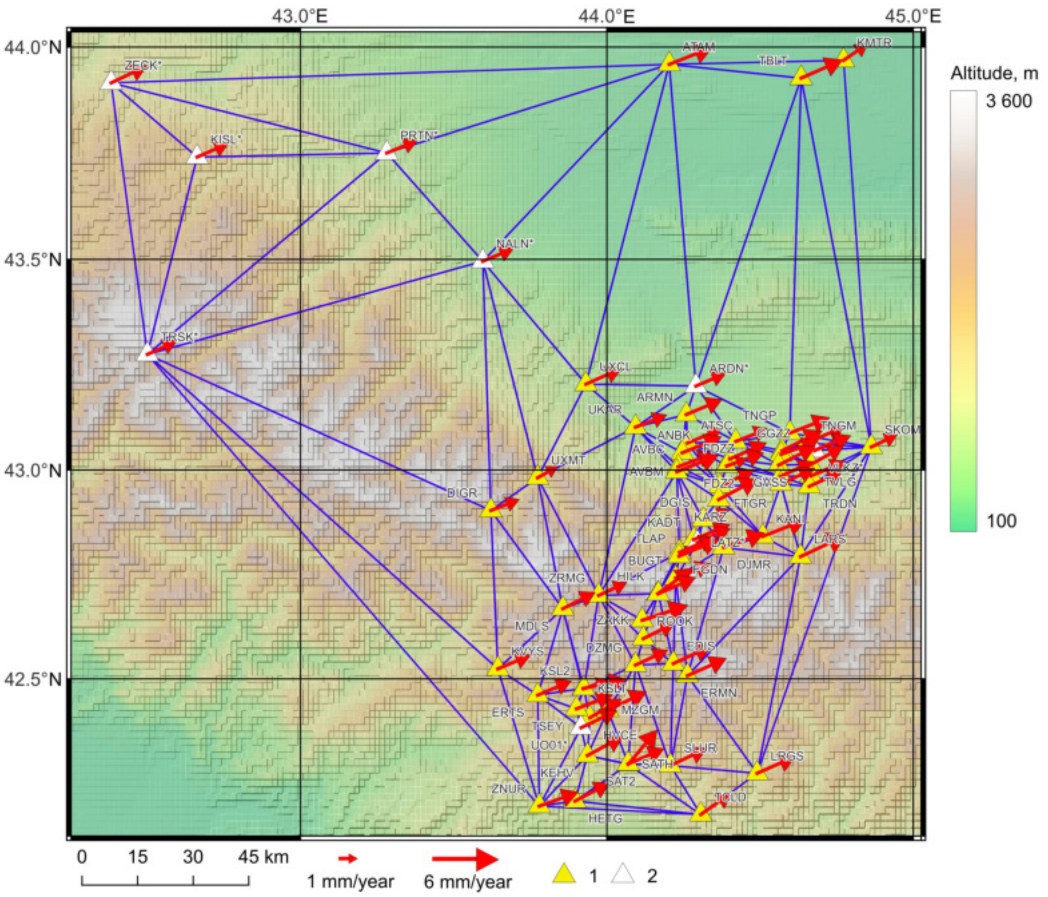

Figure 1. Geodynamic polygon of the Ossetia [Mironov et al., 2021]. 1 – periodically measured geodetic points; 2 – continuously operating geodetic points.

In geodynamics, the parameters of planned surface deformations are determined at specific points, assuming that sections of the Earth's crust are uniformly deformed. Typically, the geodetic network is divided into triangles, and the obtained deformation tensor components are associated with their geometric centers. There is an approach in deformation field calculations that does not involve triangular finite elements. This approach utilizes points falling within a defined survey radius, assigning them weighting coefficients based on their distance from the deformation reference point. One of the most prevalent methods for computing the deformation tensor field is outlined in the study by [*Shen et al.*, 1996], and it is implemented in the software packages grid_strain and grid_strain3 [*Teza et al.*, 2008]. The assessment of observation point weights is performed according to a prescribed analytical function [*Shen et al.*, 1996, 2015]. The weight of the displacement values is inversely proportional to the mathematical expectation of the measure of crustal deformation heterogeneity between the interpolated point and the observation point. However, using such a weighting function can pose a problem in incorrectly assessing observation point weights as these functions fail to account for the crustal heterogeneities. Unjustified weight assignments can lead to significant distortions in the results. Thus, it is crucial to have robust justifications when selecting a specific weighting function.

The primary uncertainty in deformation field calculations stems from the lack of a physical understanding of the deformed geological environment. This leads to subsequent uncertainties in interpreting its deformation. Distance weighting methods create complex geometric shapes with difficult interpretation. The triangular network method of calculation strictly associates a physically defined area within the finite element on the geodetic network, enabling a clear interpretation of its deformation derived from precise displacement values at its vertices. Another perspective method is to interpolate the data onto a regular grid to obtain uniformly distributed data throughout the entire study area.

The interpolation model allows obtaining regular data at grid nodes across the entire study area. Therefore, in deformation monitoring based on GNSS measurements, there is a pressing issue of analyzing data when there is an insufficient quantity available. Moreover, computations based on irregular geodetic network data may lead to a significant loss of accuracy in determining displacements and deformation components. This is consequently increasing the unreliability of the derived estimations and predictions [*Dokukin et al.*, 2010; *Wu et al.*, 2003]. To obtain regular (grid) data on surface deformations, it is necessary to employ methods of mathematical modeling of displacement fields. For instance, in [*Aleshin et al.*, 2022; *Allmendinger et al.*, 2011; *Esikov*, 1979], it is noted that due to the complexity of calculating deformation parameters, it is advisable to choose regions where more complex deformed conditions should be specified within the finite element (where deformation is typically assumed to be uniformly distributed), thereby enhancing the order of approximation of the data. There are numerous methods for modeling field movements (which will be discussed below). However, only some of them can model data beyond the geodetic network contour (extrapolate data). Artificial neural networks constitute one such family of methods, showing extensive promise in this area of research. Therefore, the goal of this study is to study the potential for modeling the field of recent horizontal crustal movements on a regular data grid. This is done based on GNSS measurements using a neural network approach and substantiating the parameters of the neural network algorithm for this specific task.

2. Materials and Methods

2.1. Interpolation models

The main methods for modeling recent Earth's surface movements are discussed below. These methods can be divided into two major groups:

- deterministic methods: These methods involve the physical description of a specific model for the movements of a geological process or phenomenon. These models are commonly used for modeling displacement fields during earthquakes [*Lei and Loew*, 2021; *Okada*, 1992], fault slip displacements [*Aki*, 1968; *IAEA-TECDOC-1987*, 2021; *Moss and Ross*, 2011; *Nurminen et al.*, 2020; *Youngs et al.*, 2003], surface subsidence due to mining operations [*Kuzmin*, 2020; *Mazurov*, 2016; *Petrov et al.*, 2021], and so on.
- interpolation and extrapolation methods: These methods do not rely on physical representations of the environment. They are universal for generating gridded data

for movement and deformation fields regardless of the studied geological process or phenomenon. These methods include geostatistical methods [*Bogusz et al.*, 2013; *Ghiasi and Nafisi*, 2015], distance-weighting methods [*Bogusz et al.*, 2013; *Shen et al.*, 1996, 2015], spline and polynomial methods [*Bogusz et al.*, 2013; *Sandwell*, 1987], machine learning methods [*Aleshin et al.*, 2022; *Grishchenkova*, 2017; *Manevich et al.*, 2021; *Manevich and Tatarinov*, 2017; *Tatarinov et al.*, 2018], and others.

Spline functions are the most frequently used methods, serving as a reliable and effective tool for approximating and interpolating various geophysical data, including surface movements [*Bogusz et al.*, 2013; *Markovich*, 2020; *Sandwell*, 1987]. Several types of spline functions are known to be applied in the field of surface movement interpolation. Primarily, cubic spline functions are utilized to create smooth surfaces from a set of unevenly distributed points in space. The physical interpretation of the cubic spline corresponds to the application of force to an elastic material (like a rod or layer), approximating it to a model of elastic crustal deformation. The spline interpolation method minimizes the surface's curvature function, which passes through all original points within the accuracy of their average errors. At the original data points, the curvature of the function is at a minimum, while between the points, the function's surface is close to linear. All original data points contribute to the modeled value [*Bogusz et al.*, 2013].

Another method commonly used in practice is the Shen method [*Shen et al.*, 1996]. This approach employs GNSS stations within a specified survey radius, assigning them weighting coefficients based on their distance from the reference point of deformation. The technique has been implemented in several software packages for deformation analysis, such as grid_strain and grid_strain3 [*Teza et al.*, 2008], SSPX [*Cardozo and Allmendinger*, 2009], Geostrain [*Goudarzi et al.*, 2015], PyStrain [*Dimitrios et al.*, 2019], among others. The assessment of observation point weights is performed according to a prescribed analytical function [*Shen et al.*, 1996]. The weight of the displacement value is inversely proportional to the mathematical expectation of the degree of crustal deformation heterogeneity between the interpolated point and the observation station. In essence, the approach emphasizes that the closer the GNSS station is to the studied point, the more significant its contribution.

In modeling recent crustal movement fields, classical spatial interpolation methods are regularly employed, such as the inverse distance method, kriging, and the natural neighbour method [*Bogusz et al.*, 2013; *Ghiasi and Nafisi*, 2015; *Matheron*, 1970; *Shen et al.*, 2015; *Srivastava and Isaaks*, 1989; *Wackernagel*, 1994]. Their application is justified by their ease of implementation in GIS environments and the ability to finely tune parameters. However, it is essential to select the search radius correctly when using these methods. If the search radius is set too large, the modeled data will be excessively smoothed and averaged. Conversely, if the radius is set too small, the nearest neighbour effect may be observed, where the modeled value is increasingly similar to the nearest known point. It is important to note that the Shen method, to some extent, resembles the inverse distance method but employs a different weighting function.

The next method is based on formulating multiple regression equations, where the regressors are not statistically derived coefficients but a set of geological-geophysical parameters of the studied area. It is worth noting that in modern GIS packages, this approach is referred to as geographic weighted regression, essentially denoting the same process. One of the initial mentions of using this approach for predicting recent crustal movements can be traced back to the work of [*Kolmogorova and Karataev*, 1975]. However, its application is also seen in recent crustal movement research [*Markovich*, 2020]. This method works well for building regional models of recent crustal movements over large territories. The large scale allows the utilization of a more extensive array of geological-geophysical parameters, the variability of which is less significant for local areas.

The focus should also be on machine learning methods. The most prominent among them is the artificial neural network (ANN) method. Experience in its application is known for predicting ground subsidence caused by mining activities [*Boubou et al.*, 2010; *Grishchenkova*, 2017], modeling post-seismic deformations [*Yamaga and Mitsui*, 2019], forecasting landslide movements [*Yang et al.*, 2019], volcanic deformations [*Anantrasirichai et al.*, 2018], and slow tectonic movements fields [*Manevich et al.*, 2021; *Manevich and Tatarinov*, 2017; *Tatarinov et al.*, 2018].

The algorithm represents a layered system of interconnected and interacting simple processors (neurons). Each network neuron deals only with the signals it receives and those it sends to other neurons. When connected in a sufficiently large network, these individually simple neurons together are capable of performing rather complex tasks. The network involves interconnections between neurons, and the strength of these connections is expressed by specific weighting coefficients. The complete matrix of these weighting coefficients, along with the input and output signals of the neurons essentially constitutes the decision-making apparatus of this method. Neurons interacting with each other are organized in layers (involving input, hidden, and output layers). The task of neurons in the input layer is to receive, normalize, and transmit information to the hidden layers. Further calculations of signals transmitted to subsequent hidden layers or the output layer take place in the hidden layers of the artificial neural network. The output layer transforms the final signals into output information for the user of the artificial neural network.

To train an artificial neural network (essentially tuning the synaptic weight coefficients), datasets are formed with known predictable data. Then the network is iteratively trained by comparing its predicted value with the actual value until they match within a certain (user-defined) margin of error. Once the training is completed, the network can use its weight coefficient matrix for prediction. Let's take a closer look at the training process of the artificial neural network. There is a set of data entering the input layer of the network:

$$\sum y_n = \begin{pmatrix} y_1 \\ y_2 \\ \cdots \\ y_n \end{pmatrix} \rightarrow \overline{y_n} = \begin{pmatrix} \overline{y_1} \\ \overline{y_2} \\ \cdots \\ \overline{y_n} \end{pmatrix},$$

where $y_1, y_2, \ldots, y_n$ – input data; $\overline{y_1}, \overline{y_2}, \ldots, \overline{y_n}$ – normalized input data, for distribution into ANN layers.

To work with the incoming data within the network, it's necessary to process them by normalizing them, which means representing numerical parameters not in absolute units, but in some dimensionless units characterizing their relative values. Then the signals are passed to the hidden layer, being multiplied by the respective weight coefficients (initially set randomly).

$$S_n = \overline{y_n} \times W_{ij} = \begin{pmatrix} \overline{y_1} \\ \overline{y_2} \\ \cdots \\ \overline{y_n} \end{pmatrix} \times \begin{pmatrix} w_{11} & \cdots & w_{i1} \\ \cdots & \cdots & \cdots \\ w_{1j} & \cdots & w_{ij} \end{pmatrix},$$

where W_{ij} – full matrix of synapse weighting coefficients; $w_{11}, w_{12}, \ldots, w_{ij}$, – weighting coefficients of synapses; i – number of the hidden layer; j – synapse number in the layer.

In each neuron of the hidden layer, the incoming signals are summed, followed by the activation (through a specially chosen function) of a new signal – $F_{\text{act}}(\sum S_n)$. This procedure is repeated for all hidden layers.

On the output layer, the signals are summed for the last time, and the outgoing value is activated and denormalized (if necessary). This represents the forecasted value. The forecast is compared with the true value (the training error is calculated), and if the error is above the specified training accuracy, the synaptic weight coefficients are adjusted, and the entire procedure is repeated. Otherwise, the training is considered complete, and the matrix of weight coefficients is saved and can be used for forecasting.

Thus, in neural network-based forecasting of surface displacements caused by mining operations, their function is represented in the additive form of a set of polynomials $\widehat{K}_n$, summed in the neuron of the output layer:

$$K = \sum_{i=1}^{n} \widehat{K}_n = \begin{cases} \widehat{K}_1 = \beta_{11} f_1 + \cdots + \beta_{gl} f_g + \beta_{12} f_1 f_2 + \cdots + \beta_{gl} f_1 f_g + \cdots \\ \cdots \\ \widehat{K}_n = \beta_{n1} f_1 + \cdots + \beta_{nl} f_g + \beta_{n2} f_1 f_2 + \cdots + \beta_{nl} f_1 f_g + \cdots \end{cases}, \tag{1}$$

where β – coefficients of the polynomial functions; f – set of geological factors; n – all possible combinations of polynomial functions $\widehat{K}$ formed by the internal relationships of the artificial neural network; g – quantity of geological factors taken into account; l – number of the neural network layer.

The ellipsis at the end of expression (1) indicates the continuation of the polynomial function, limited only by the dimensionality of the neural network. This type of model is essentially a regression model and serves for the interpolation and extrapolation of values of surface displacement parameters. Thus, it is possible to formulate a computational model that more accurately corresponds to the real object – the geodynamic polygon. Finding a natural dependency of kinematic parameters in the form of a simple analytical relationship is difficult. On the other hand, the computational neural network model is multifactorial (contains a large number of regressors). This is can be formulated as a system of multiple (linear/non-linear) polynomials, the dimensionality of which is constrained by the structure of the artificial neural network model [*Kolmogorov*, 1957].

Currently, there are numerous methods for predicting surface displacement, including deterministic methods, spline functions, polynomial functions, multiple regression, the Shen method, the overlaid triangulation method, kriging, the inverse distance method, and artificial neural networks. However, deterministic methods effectively address only a narrow range of tasks related to modeling movements resulting from a specific process or phenomenon (coseismic deformations, subsidence of the Earth's surface, etc.). Some methods, due to their application, are challenging to interpret as they form intersecting geometric constructions (the inverse distance method, the overlaid triangulation method, the Shen method), while deformation is strictly related to a specific geometrically defined process. Classical methods of geographical interpolation that depend on reference points (kriging, the inverse distance method) do not allow for data extrapolation. Methods of machine learning, particularly artificial neural networks, show a good perspective in this regard [*Boubou et al.*, 2010; *Grishchenkova*, 2017; *Manevich et al.*, 2021; *Manevich and Tatarinov*, 2017; *Tatarinov et al.*, 2018], and their application will be further discussed.

2.2. GNSS data

To test the proposed approach, two regions with different geological conditions and initial data were selected. We use data from several scientific groups that conducted GNSS measurements in the Caucasus region. The initial data for the Caucasus region were derived from GNSS measurements in the Ossetian sector of the Greater Caucasus, as presented in the publication by [*Mironov et al.*, 2021]. These measurements were obtained during field campaigns conducted from 2008 to 2020, as documented in [*Milyukov et al.*, 2015, 2017]. Geodetic points were established to monitor recent crustal movement of the Earth's crust in this region, crossing the Greater Caucasus Range through the territories of the Ossetia. The measurement network was designed to cover this area, and GNSS measurements were conducted at designated geodetic points. The data collection and processing methodology is detailed in [*Milyukov et al.*, 2017; *Mironov et al.*, 2021]. We used the consolidated measurement results presented in the study by [*Mironov et al.*, 2021], which includes displacement data from 60 GNSS points.

2.3. Modeling the horizontal velocity field of the Earth's crust based on discrete irregular geodetic data

2.3.1. ANN structure

The calculations used Python 3, and the results were visualized with the QGIS 3 environment [*Manevich et al.*, 2023]. The Scikit-learn library [*Pedregosa et al.*, 2011] was employed for neural network modeling, which is widely used for such computations. The artificial neural network (ANN) model was specified as a multilayer perceptron using the mlp.regressor function. The following parameters were used for the ANN model: optimizer – adam; activation function – hyperbolic tangent (as it is required for the output data to have both positive and negative values); learning rate – empirically determined and varied from 0.00005 to 0.0001; number of training iterations – from 100,000 to 1,000,000. The architecture of the ANN was as follows:

- quantity of input neurons – equal to the number of features in the model (in this case, six);
- quantity of hidden layers – options with 1 to 3 hidden layers, with 5, 10, and 15 neurons in each layer, were studied;
- quantity of output neurons – 1, for predicting each component of movement separately.

Relatively simple ANN models were employed, which is atypical for machine learning algorithms. This is due to the volume of the data used. Local geodynamic polygons rarely have more than 100 measurement points for such a small amount of data. Constructing complex models leads to a decrease in learning quality and improper tuning of algorithm hyperparameters. In this case, a three-layer perceptron is more than sufficient to address tasks with such a low volume of data. The ANN algorithm was compared with classical interpolation methods – the inverse distance weighting method (with a power parameter $p = 4$), cubic spline, and B-splines (methods implemented in SAGA GIS).

2.3.2. Feature engineering

The input data for the neural network included features characterizing the contrast and intensity of tectonic movements in the research area [*Agayan et al.*, 2020, 2022; *Faber and Domej*, 2021; *Gvishiani et al.*, 2016, 2020], as well as the geographical coordinates of the training and prediction points. These features primarily consisted of geomorphological characteristics associated with morphometric analysis of the terrain. Geological and geophysical data were not applied in this model. Despite their potential, they introduce a number of uncertainties. Spatial data created manually by humans (such as geological maps or tectonic faults) are not formalized data. Therefore, during the algorithm's training process, it adapts to models created by the author based on the original data, rather than creating new relationships between the data. Geophysical fields, such as results from seismic tomography, magnetic and gravitational anomalies, have proven efficiency in applying machine learning methods in Earth sciences as a whole [*Agayan et al.*, 2022; *Aleshin et al.*, 2022; *Dzeboev et al.*, 2019; *Gvishiani et al.*, 2022, 2023; *Sun et al.*, 2022]. In the considered task, they can reflect the deep structure of the Earth's crust and serve as informative features during algorithm training. However, these data are not always available for the areas of interest where research is conducted. Global models of geophysical fields do not always have sufficient detail for their application. In geodynamic polygons with an area of up to 2500 km^2, one cell of the geophysical field dataset can be larger in area than a triangular finite element. Meanwhile, relief data is available with detail down to 30 meters or less (SRTM, ALOS JAXA, ETOPO datasets, and others).

Features were defined within cells. For a geodetic point, the data of which constitute the training set, a hexagonal cell with a radius of the circumscribed circle R is constructed (Figure 2a). The resulting cells are overlaid on the parameter field (feature) for which the value needs to be obtained. Using zonal statistics, the necessary feature is computed in each cell from those mentioned above (average elevation in the cell, range of minimum and maximum elevations, etc.). When forecasting data on a regular grid, the procedure is constructed similarly. The regular grid of cells for which the forecast will be performed is divided (Figure 2b). The necessary features are computed for each cell, which are then input into the neural network. The forecast result, the displacement components, will be assigned to the centroid of each of the original cells. The following data were used as features:

- coordinates of the cell centroid, in meters, in the universal transverse Mercator projection;
- mean elevation of the terrain in the cell;
- range of elevations in the cell (difference between maximum and minimum values);
- mean density of lineaments in the cell;
- range of lineament density in the cell (difference between maximum and minimum values).

We used the ETOPO1 model as input data [*Amante and Eakins*, 2009]. Lineaments were calculated using the method proposed in [*Sedrette and Rebai*, 2016]. The measure of the dynamic activity index of faults density was determined by using the linear density, which is obtained in a circular vicinity within each cell of the grid. The length of the segment of each line crossed by the circular neighborhood is multiplied by the line weight factor. Then all the length values are summed up and divided by the area of the circle. This process is repeated for all cells in the grid.

The models presented here use a simple feature space. Our goal was to create a simple model, with accessible input data, that can be applied by the widest range of researchers. In addition, simple models are more interpretable than models with complex architecture. The detailed analysis and design of features, their comparison and performance evaluation is an independent study, such as in [*Agayan et al.*, 2022].

2.3.3. Prediction grid and data preprocessing

Equally important is the stage of data preparation and normalization before feeding them into the neural network's input layer. Proper preprocessing of data enables the algorithm to enhance its efficiency and extract valuable information from the data.

A key feature of data preparation is that the displacements need to be transformed into the "no-net-translation" format [*Kaftan and Tatarinov*, 2021] i.e., into the internal displacements of the network. If displacements are provided in the global reference system (as in the work by [*Mironov et al.*, 2021] (Figure 1), it is necessary to subtract from them the mean arithmetic value or the velocity of tectonic plate movement to obtain internal displacements of the geodetic network. This is the format in which the ANN best models the variability of the RCM.

The procedure of declustering data in the context of motion field modeling is discussed. In the preparation of raw data, a situation of overlapping cells can often arise. In this case, the feature values in the cells may be close, while the displacement values can differ significantly. It is necessary to be more attentive to the preparation of raw data and the results of GNSS measurements themselves. Exclude questionable points or points that may be influenced by active exogenous processes or points with poor satellite measurement conditions. In other cases, opposite movements may be caused by local tectonic processes in the research area (such as fault coast displacements) and are important information that should not be removed from the training set. Therefore, in our approach, it is not recommended to apply data declustering, and in cases where two points are in the same location and have different motion indicators, preference is given to the point with the most stable position and a high-quality type of geodetic center. If this parameter is indeterminate, then the point with the longest measurement period is preferred.

The size of the finite element is determined empirically, in accordance with the physical representation of the studied section of the Earth's crust. The Earth's physical crust is not a continuum, so it is not possible to divide the cell into infinitely small elements. When it comes to crustal deformations, the sizes of the sections should be such that changes in their shape and volume can be interpreted. Normalization of feature data is performed according to standard relationships:

$$\overline{x_j} = \frac{x_j - x_{j0}}{\lambda_j}, \tag{2}$$

where $\overline{x_j}$ – transformed (normalized) value; x_j – the value of the original feature; x_{j0} – the center of variation for the numerical series of the n feature; λ_j – range for the numerical series of the n feature; j – number of values in the numerical series of the n feature.

Different statistics of the original data (minimum, maximum, difference modulus, arithmetic mean, median, zero value, etc.) can be taken as the range and center of variation, depending on empirically determined efficiency. In our study, the arithmetic mean values of the original data sample were taken as the range and center of variation. As a result of data normalization, all features are brought into a consistent system of dimensions, making them numerically comparable and enhancing the efficiency of the neural network's recognition.

The limit prediction radius was determined by the distance at which the feature values in the cells did not change within the range of the original cells. That is, provided that the features in the training sample are distributed the same as in the modeled set.

3. Results

3.1. Methodology for assessing the effectiveness of modeling

For a comprehensive assessment of the effectiveness of modeling methods, it is necessary to plan a series of computational experiments aimed at evaluating the accuracy of forecasting methods in interpolation and extrapolation tasks. One of the best methodologies for assessing performance in data science is cross-validation [*Sun et al.*, 2022]. Cross-validation is a method for evaluating a model to determine how successfully the applied statistical analysis in the model can perform on an independent dataset. Cross-validation methods are successfully applied to assess modeling effectiveness in various Earth sciences [*Agayan et al.*, 2022; *Aleshin et al.*, 2022; *Sun et al.*, 2022], including forecasting recent crustal movement fields [*Bogusz et al.*, 2013].

In this case, the cross-validation method will be applied as follows. The test data set will consist of one point in each iteration of the calculation. All other data will be included in the training data set. In other words, in each iteration of the calculation, surface movements for one point will be calculated based on all other data in the training set. When assessing the quality of the forecast, we average the obtained quality metrics for all test sets.

Earth surface movement data have several characteristic features – they can be multidirectional (have positive or negative signs) and each displacement vector has its own azimuth characterizing the direction of movement. There are a number of errors in forecasts that need to be considered at a detailed and even point level. For example, it is an estimation not only of the absolute magnitude of the predicted displacement/velocity of the RCM, but also of its sign, i.e. its direction. It may happen that one method shows the smallest absolute bias, but recognizes fewer directions of RCM velocities. In this case, the second quality metric will be more correct. Since the directions of movements allow to carry out deformation analysis on compression-tension of the area, which is more important. That is why the development of a program of computational experiments is necessary and it will allow a more correct comparison of the proposed methods. Therefore, the metrics for evaluating the quality of the algorithms' predictions were chosen as follows:

Mean absolute error (MAE) shows the mean absolute deviation of the predicted offsets from the true offsets. The use of absolute deviation is due to the fact that displacement values can be both positive and negative. MAE is determined by formula (3):

$$\mathrm{MAE} = \frac{1}{n}\sum_{i=1}^{n}|U_i - a_i|, \tag{3}$$

where n – quantity of points in the used sample (training, test, control); U_i – the value of measured displacement/velocity; a_i – the value of predicted displacement/velocity.

In addition to quantification, it is necessary to recognize the direction of the motion vector (negative or positive). To evaluate the quality of this aspect, accuracy metrics are defined by formula (4). This evaluation is based on the error matrices of the recognized displacement/velocity classes (Table 1). The accuracy metric allows for estimating the vector of the geodetic point movement direction in the 90° sector. If both components are

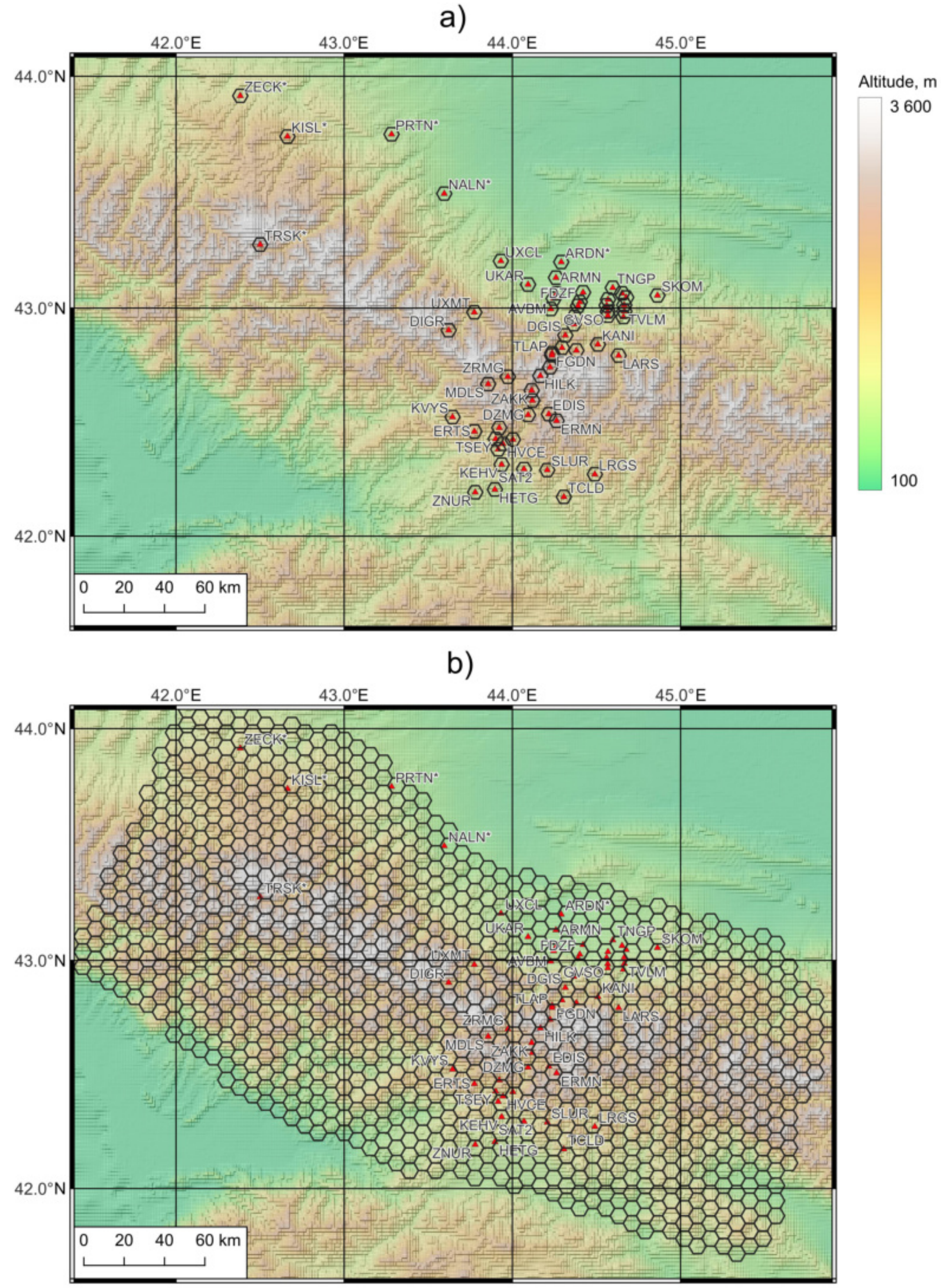

Figure 2. An example of dividing the geodynamic polygon of the Ossetia into cells with $R = 10$ km. a – training set; b – interpolation model with regular cells.

recognized correctly, the modeled value falls into the same direction sector as the true displacement value:

$$\text{accuracy} = \frac{\text{TP+FN}}{\text{TP+FP+FN+TN}}, \tag{4}$$

Table 1. Error matrix (a – the true mark motion vector displacement/velocity, $\hat{a}$ – predicted mark motion vector displacement/velocity)

	$a = 1$	$a = 0$
$\hat{a} = 1$	True Positive (TP)	False Positive (FP)
$\hat{a} = 0$	False Negative (FN)	True Negative (TN)

To evaluate the efficiency of the algorithms, the original data samples are grouped and labeled. All GNSS points are classified into points inside the geodetic network contour (interpolation task) and points outside the geodetic network contour (extrapolation task) (Figure 3). Quality metrics are calculated and compared separately for the groups shown. The points in the control data sample are also classified and analyzed separately from the data used in the modeling.

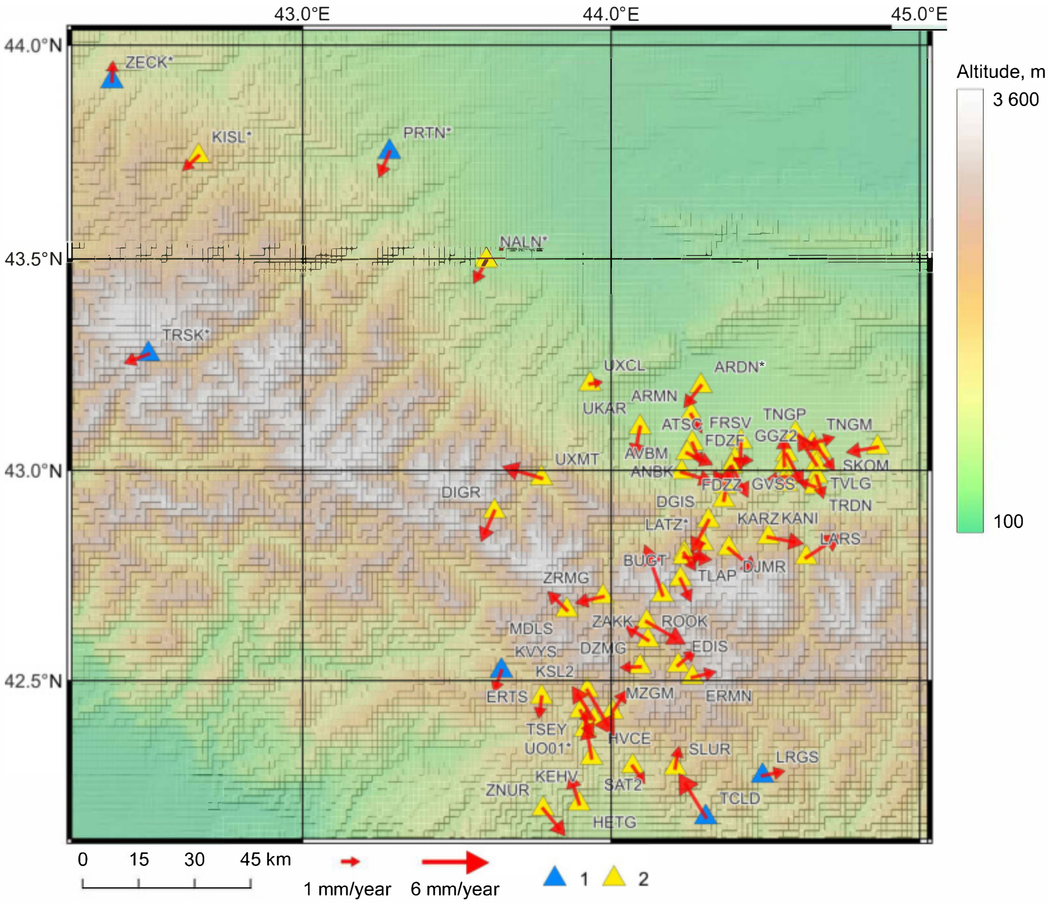

Figure 3. Vectors of geodetic point movements in the internal reference frame and illustration of GNSS point positions outside 1) and inside 2) the geodetic network contour of the Ossetian geodynamic polygon.

Thus, for each data set (from one polygon) the following quality metrics will be calculated:

- MAE – mean absolute deviation of predicted components from the true velocities of motions V_e, V_n in the test sample;

- MAE_extr – mean absolute deviation of predicted components from the true velocities of motions V_e, V_n in the test sample outside in geodetic network (extrapolation points);
- ACC – accuracy of recognizing the direction of the predicted components of motion velocities V_e, V_n (the mean accuracy value is taken for the components V_e, V_n);
- ACC_extr – accuracy of recognizing the direction of the predicted components of motion velocities Ve, Vn in the test sample outside in geodetic network (extrapolation points, the mean accuracy value is taken for the components V_e, V_n);
- ACP – accuracy of recognizing the direction of the predicted velocity vector **V** (the accuracy value is taken for the components V_e, V_n recognized correctly at the same time);
- ACP_extr – accuracy of recognizing the direction of the predicted velocity vector **V** in the test sample outside in the geodetic network (extrapolation points, the accuracy value is taken for the components V_e, V_n recognized correctly at the same time).

These 6 metrics are calculated for each of the algorithms and a comparative evaluation of the modeling performance is performed based on them.

3.2. Results of the Application of ANN for Modeling the RCM field

As a result of the modeling, the components of the RCM were obtained on a regular grid with a step of 10 km (Figure 4). As a result of the modeling, the quality metrics of the cross-validation study on the full dataset and on the extrapolation, dataset were calculated (Table 2).

We analyze the table of the obtained quality metrics of the recent motion field modeling algorithms. The MAE, ACC, ACP rows show the results of calculations of quality metrics for a complete enumeration of the data set. Thus, such a set included points are assigned to the interpolation task and the extrapolation task together. The metrics obtained in this iteration of calculations are very important because they allow to compare the algorithm of artificial neural networks with other algorithms within the framework of the classical problem of interpolation of Earth surface movements. The MAE_extr, ACC_extr, ACP_extr lines contain the results of data extrapolation beyond the geodetic network contour. At the same time, due to the fact that the data are located quite grouped, the estimation for extrapolation points is obtained by classical algorithms. Let us consider in detail the results of quality metrics calculations.

It should also be noted that the level of the mean absolute deviation of the modeled values (both by the ANN algorithm and by classical algorithms) is at or below the RMS of GNSS station velocity definitions (1–3 mm). This result indirectly demonstrates the reliability of the modeled values in the cross-validation sample, as the absolute error of their determination is comparable to the RMS of their definitions.

The following results were obtained for the Ossetian geodynamic polygon. For the full data sample, the metric MAE is between 1.22–2.2 mm. The largest absolute error is obtained when using ANN5,6 architectures and the smallest when using ANN1,9,10 architectures. The classical methods show a range of MAE metric of 1.37–1.65 mm, which on average corresponds to the ANN algorithms. The situation is similar to the mean absolute error on the extrapolation sample (MAE_extr metric). The situation is different with the metric of mean absolute deviations on the extrapolation sample MAE_extr, it lies in the range of 1.04–3.6 mm. The largest absolute error is obtained when using ANN5,6 ANN architecture, and the smallest when using algorithms of inverse distance methods, B-spline, and ANN3,10 architectures. The single-layer and three-layer ANN architectures show lower error on average. The classical algorithms yield a metric range of 1.04–1.63 mm, broadly similar to the full data sample. In terms of mean absolute deviation metrics, ANN1,3,10 architectures show the best results.

For the full data sample, the ACC metric is between 35–56%. The lowest recognition accuracy is obtained using ANN6,11 and the highest recognition accuracy is obtained using ANN3,12 architectures. The classical methods show a range of ACC metric of 43–54%, which is on average higher than the ANN algorithms whose range is 35–56%.

The situation is repeated on the extrapolation dataset. The overall recognition accuracy of ACC_extr lies in the range of 25–66%. The lowest recognition accuracy is obtained using ANN architecture ANN1,6,8,11 and the highest recognition accuracy is obtained using architectures ANN3,4,12, inverse distance method IDP and B-spline. Generally, the ANN architectures show about 40% accuracy in recognizing the direction of the motion components V_e, V_n.

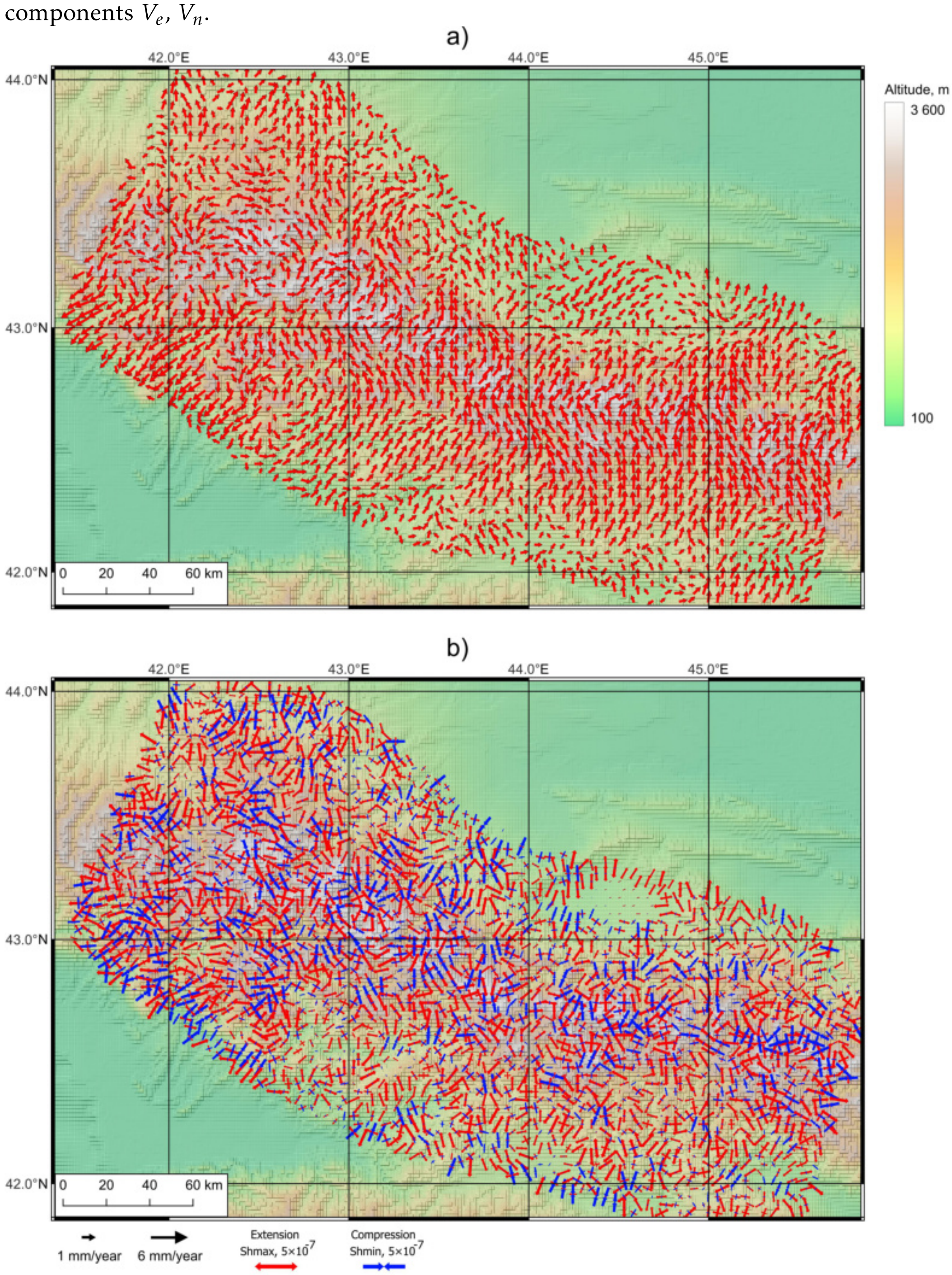

Figure 4. Neural network model of recent crustal movements and deformations of the Ossetian geodynamic polygon: a – field of velocities vectors; b – velocities and orientation axes of main deformations.

For the full data sample, the ACP metric ranges from 8–37%, while the ACP_extr metric ranges from 0–33%. Otherwise, the ACP and ACP_extr metrics show similar results, with the difference that the recognition accuracy is defined in the 90° sector. The lowest recognition accuracy is obtained using the CBSP algorithm and ANN5,6 architectures, while the highest recognition accuracy is obtained using the IDP inverse distance method and ANN3,12 architectures. The classical methods show an ACP metric range of 12–29%, which is on average lower than that of the ANN algorithms, whose range is 12–37%. The situation is similar to the extrapolation dataset. The lowest recognition accuracy is obtained using the CBSP algorithm and ANN1,2,5,6,7,10,11 architectures, while the highest recognition accuracy is obtained using ANN3,4,12 architectures, IDP and B-spline inverse distance methods.

Among the considered ANN architectures, it is worth highlighting the ANN12 algorithm, which shows the highest and most stable recognition accuracy in terms of ACC and ACP metrics, at the same time having one of the lowest MAE values. If we take a closer look at the results of the cross-validation analysis of ANN1–3 architectures (where single-layer ANNs are also considered), we can see that this result is consistent. It is useful to take it into account when planning the ANN architecture in modeling tasks, where the accuracy of recognition of the direction of the motion vector, rather than approximation to its numerical value, is a higher priority. The most stable of the listed architectures seems to be the ANN8 and ANN11 algorithm. It should be emphasized that a detailed selection of hyperparameters and ANN architecture can improve the above quality metrics. Moreover, the given tables do not give grounds for conclusions about which of the methods or algorithms is unambiguously worse or better. However, in this context, they show the most important thing – the proposed neural network approach confidently shows results not worse than classical methods. Having at the same time the possibility of modeling a wider area. Thus, we can make sure of its adequacy for the use of recent crustal movement field modeling tasks outside the contour of geodetic networks.

Figure 4 illustrates the results of modeling the recent crustal movement field by the algorithm with ANN11 architecture. The figures clearly show that the ANN algorithm makes it possible to obtain the necessary amount of data on a regular grid outside the contour of the geodetic network. Neural network extrapolation allows to obtain data with greater detail of the studied area, where there is a large number of local and large regional tectonic structures. Thus, the analysis of cross-validation results gives encouraging results. We can say that the ANN algorithms within the geodetic network contour model of the RCM field are no worse than classical methods. This conclusion allows us to cautiously conclude that the ANN algorithm in the conditions of limited radius of the modeling area shows itself reasonable and its application is possible for modeling the motion fields outside the contour of the geodetic network. Within the framework of this paper, we did not set ourselves the task of geodynamic interpretation of the obtained motion fields. However, it should be noted that the results of modeling for the Ossetian polygon can be used for geodynamic zoning. At the same time, we can identify zones of tension and compression and calculate the tectonic component of stresses, as well as zones of high-gradient displacements, etc.

4. Discussion

Neural network extrapolation allows us to obtain data with more detail of the studied area, where there are many local and regional tectonic structures. We note the high prospect of using this approach for disparate GNSS data obtained in different epochs of observations. GNSS measurements in the Caucasus, which were started in the 1990s [*Reilinger et al.*, 1997; *Shevchenko et al.*, 1999], are of high interest. Now, they have almost a thirty-year history [*Ismail-Zadeh et al.*, 2020; *Karapetyan et al.*, 2020; *Mironov et al.*, 2021; *Reilinger et al.*, 2006; *Sokhadze et al.*, 2018; *Tibaldi et al.*, 2021]. Measurements of recent crustal movements in the Caucasus are very heterogeneous, as a large number of scientific groups have worked in these regions [*Tibaldi et al.*, 2021]. This makes it difficult to spatially compare the results of their measurements, as they cover different, not completely overlapping areas. The application of machine learning methods will make it possible to model these data onto a single regular grid and obtain digital models of displacements and deformations of the Caucasus territory on a unified scale.

Table 2. Quality metrics of the cross-validation study for data from the Ossetian geodynamic polygon (gradient coloring from red to green corresponds to the reduction of the algorithm's prediction error)

Quality metrics	ANN1	ANN2	ANN3	ANN4	ANN5	ANN6	ANN7	ANN8	ANN9	ANN10	ANN11	ANN12	IDP	MSP	CBSP
MAE, mm	1.22	1.47	1.32	1.51	2.20	2.11	1.40	1.44	1.35	1.28	1.40	1.63	1.43	1.37	1.65
MAE_extr, mm	1.43	1.86	1.25	1.72	2.28	3.60	1.53	1.82	1.94	1.17	1.53	2.37	1.26	1.04	1.63
ACC, %	41.7	45.8	56.3	43.8	37.5	35.4	43.8	35.4	45.8	43.8	35.4	56.3	54.2	43.8	47.9
ACC_extr, %	25.0	41.7	66.7	58.3	41.7	25.0	41.7	25.0	41.7	33.3	25.0	50.0	58.3	50.0	33.3
ACP, %	16.7	20.8	37.5	16.7	8.3	12.5	16.7	12.5	20.8	16.7	16.7	33.3	29.2	20.8	12.5
ACP_extr, %	0.0	0.0	33.3	33.3	0.0	0.0	16.7	0.0	16.7	0.0	0.0	33.3	33.3	33.3	0.0

Gradient coloring

Minimal error Maximum error

Decoding of abbreviations: Decoding of abbreviations: ANN1 – ANN algorithm, 1 hidden layer, 5 neurons in the hidden layer; ANN2 – ANN algorithm, 1 hidden layer, 10 neurons in the hidden layer; ANN3 – ANN algorithm, 1 hidden layer, 15 neurons in the hidden layer; ANN4 – ANN algorithm, 2 hidden layers, 5 neurons in the hidden layer; ANN5 – ANN algorithm, 2 hidden layers, 10 neurons in the hidden layer; ANN6 – ANN algorithm, 2 hidden layers, 15 neurons in each hidden layer; ANN7 – ANN algorithm, 3 hidden layers, 5 neurons each in the hidden layer; ANN8 – ANN algorithm, 3 hidden layers, 10 neurons each in the hidden layer; ANN9 – ANN algorithm, 3 hidden layers, 15 neurons in each hidden layer; ANN10 – ANN algorithm, 4 hidden layers, 10 neurons per hidden layer; ANN11 – ANN algorithm, 5 hidden layers, 10 neurons each in the hidden layer; ANN12 – ANN algorithm, 1 hidden layer, 50 neurons in the hidden layer; IDP – inverse weighted distance method, degree coefficient $p = 4$; MSP – B-spline; CBSP – cubic spline.

Above we demonstrated a simple application of the algorithm, but, as it was shown in [*Agayan et al.*, 2022], the synthesis of complex geomorphological and geophysical features has great prospects for modeling geodynamic processes, especially on a regional scale. Let us form a feature correlation matrix for the territory of the Greater and Lesser Caucasus, which can also take into account geomorphological and geophysical data. For the scale of studying the whole territory of the Caucasus, a cell size of 50 km was chosen, which allows us to apply large-scale geophysical data (Figure 5).

As is known, the areas of the newest tectonic uplifts in relief often coincide with the places of prevailing denudation, the plunging ones – with the areas of accumulation. Undoubtedly, there is a strong dependence between tectonic movements, the volume of uplifted or lowered matter and the intensity of exogenous denudation, which leads to compensation of tectonic processes. At the same time, if complete compensation does not occur, tectonic movements are directly reflected in the field of absolute heights [*Simonov*, 1998]. In addition to using the main functions of this field (e.g., DEM construction), it can be used to obtain such an important morphometric parameter as surface curvature (horizontal and vertical). The areas of recent crustal movements are reflected not so much in the height field, curvature and steepness of slopes, but also in the density and depth of dissection. The TRI (terrain ruggedness index) [*Różycka et al.*, 2017], a measure of vertical ruggedness in a given neighborhood. It can be considered the most suitable for calculating dismemberment parameters and does not change the geomorphological meaning of this term. In addition, dissection parameters are an expression of the interaction between tectonic movements and erosion processes. In addition to the above, there are more than a hundred [*Negi et al.*, 2023] morphometric indices that directly and indirectly reflect tectonic movements. However, many of them are criticized by geomorphologists, who note that the most important criterion for the correct choice of an index and its meaning should be an indication of the existing geometric or physical image of the most different values within this index.

In addition to these geomorphological indicators, we used geophysical data on the crustal structure of the Greater and Lesser Caucasus for the correlation matrix. We used Bouguer gravity anomalies and the Moho boundary dataset from the Structure and density of sedimentary basins in the Southern part of the East European platform study [*Kaban* *et al.*, 2021]. As a result, the following indicators were analyzed: the X and Y coordinates of the cell centroid in meters, in the universal transverse Mercator projection; the elevation of the relief in the cell; the density of lineaments in the cell [*Sedrette and Rebai*, 2016]; Bouguer anomalies, Moho surface depth, sediment thickness [*Kaban et al.*, 2021]; surface curvature and TRI terrain dissection index [*Różycka et al.*, 2017]. For each of the indices, we calculated the arithmetic mean, minimum, maximum and range of values within a cell. We calculated the correlation matrix and correlation strength thresholds. The matrix presents Pearson's pairwise correlation coefficient:

$$r = \frac{\sum((x_i - \overline{x}) \times (y_i) - \overline{y})}{\sqrt{\sum(x_i - \overline{x})^2 \times}}.$$

The lower threshold of the correlation relationship was determined using Student's criterion (formula (5)), and the correlation strength intervals using formula (6):

$$r_0 = \frac{t}{\sqrt{t^2 + n - 2}}, \tag{5}$$

$$r_{\text{int}} = \frac{1 - r_0}{3}. \tag{6}$$

Thus, for the set of cells used (691 cells in each of the indicators and the confidence interval of 0.95), the intervals of correlation strength were determined: a weak correlation in the interval 0.0746–0.3831, medium correlation in the interval 0.3831–0.6915, strong correlation in the interval 0.6915–1. The correlation strength was presented as a discrete color scale (Figure 6).

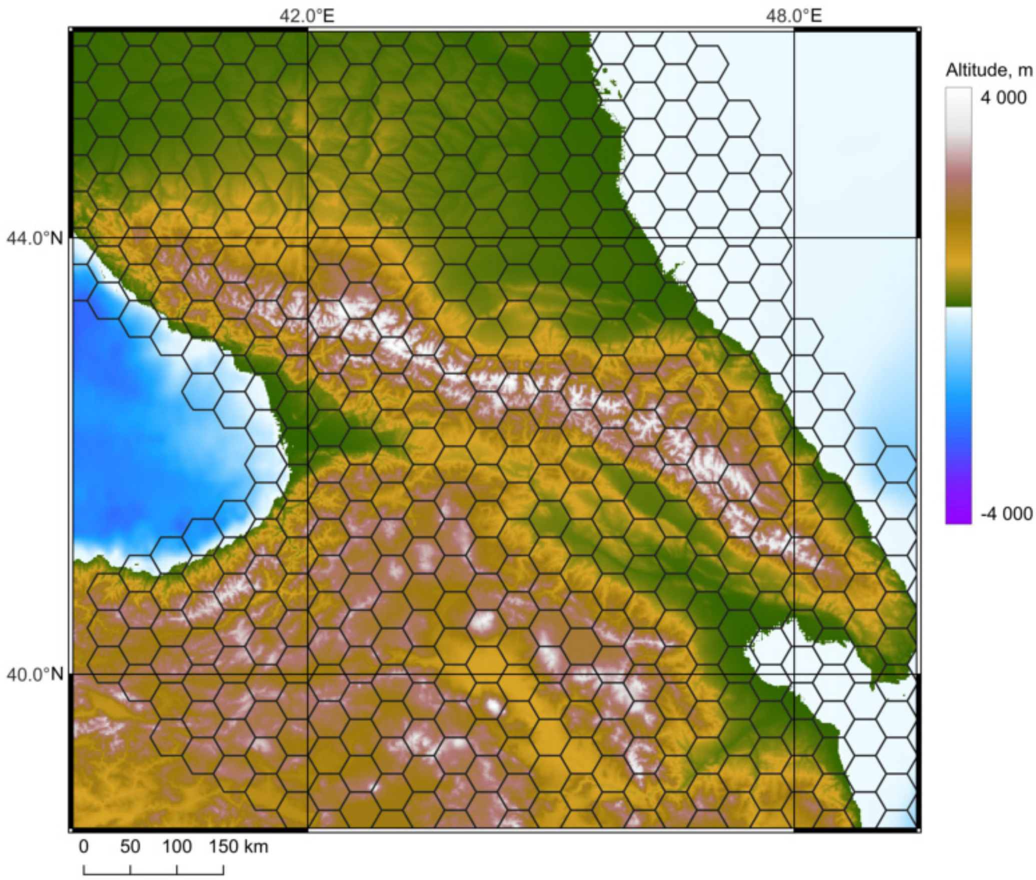

Figure 5. Example of splitting the Caucasus region into cells with $R = 50$ km.

	1	2	3	4	5	6	7	8	9	10	11	12	13	14	15	16	17	18	19	20	21	22	23	24	25	26	27	28	29	30
1	1.00	-0.48	0.09	0.09	0.11	0.09	0.00	-0.07	0.08	0.07	0.04	0.03	0.08	0.08	0.11	0.04	0.11	0.11	-0.22	-0.22	-0.20	0.08	0.39	0.39	0.39	0.01	0.29	0.27	0.29	0.18
2	-0.48	1.00	-0.60	-0.51	-0.64	-0.56	-0.01	0.50	-0.54	-0.52	-0.44	-0.25	-0.56	-0.58	-0.67	-0.27	-0.69	-0.69	0.58	0.65	0.48	-0.53	-0.23	-0.20	-0.26	-0.19	-0.10	-0.07	-0.12	-0.18
3	0.09	-0.60	1.00	0.90	0.95	0.71	0.19	-0.76	0.79	0.78	0.78	0.63	0.78	0.77	0.76	0.45	0.67	0.64	-0.80	-0.85	-0.72	0.48	0.59	0.57	0.60	0.08	-0.32	-0.32	-0.32	-0.12
4	0.09	-0.51	0.90	1.00	0.76	0.37	0.11	-0.47	0.50	0.49	0.46	0.37	0.50	0.50	0.59	0.34	0.51	0.49	-0.82	-0.82	-0.80	0.21	0.60	0.62	0.57	-0.19	-0.29	-0.28	-0.29	-0.15
5	0.11	-0.64	0.95	0.76	1.00	0.89	0.13	-0.89	0.91	0.90	0.87	0.67	0.92	0.91	0.84	0.49	0.76	0.73	-0.72	-0.80	-0.60	0.61	0.52	0.48	0.55	0.26	-0.31	-0.32	-0.30	-0.08
6	0.09	-0.56	0.71	0.37	0.89	1.00	0.11	-0.93	0.93	0.94	0.92	0.69	0.95	0.95	0.78	0.46	0.72	0.70	-0.44	-0.56	-0.30	0.72	0.32	0.24	0.39	0.51	-0.24	-0.26	-0.22	-0.01
7	0.00	-0.01	0.19	0.11	0.13	0.11	1.00	-0.13	0.14	0.14	0.18	0.20	0.12	0.11	0.05	0.10	0.01	-0.01	-0.03	-0.04	-0.02	0.05	0.04	0.04	0.03	-0.01	0.01	0.00	0.01	0.02
8	-0.07	0.50	-0.76	-0.47	-0.89	-0.93	-0.13	1.00	-0.97	-0.99	-0.95	-0.77	-0.97	-0.95	-0.77	-0.47	-0.71	-0.68	0.48	0.59	0.34	-0.71	-0.39	-0.32	-0.46	-0.48	0.27	0.28	0.25	0.03
9	0.08	-0.54	0.79	0.50	0.91	0.93	0.14	-0.97	1.00	0.99	0.95	0.75	0.98	0.97	0.80	0.48	0.75	0.72	-0.51	-0.62	-0.38	0.70	0.40	0.33	0.46	0.47	-0.26	-0.28	-0.24	-0.02
10	0.07	-0.52	0.78	0.49	0.90	0.94	0.14	-0.99	0.99	1.00	0.96	0.76	0.98	0.97	0.79	0.48	0.73	0.70	-0.50	-0.61	-0.36	0.71	0.40	0.33	0.46	0.48	-0.27	-0.28	-0.25	-0.03
11	0.04	-0.44	0.78	0.46	0.87	0.92	0.18	-0.95	0.95	0.96	1.00	0.86	0.94	0.91	0.71	0.48	0.63	0.59	-0.48	-0.59	-0.34	0.69	0.40	0.33	0.46	0.45	-0.28	-0.29	-0.27	-0.06
12	0.03	-0.25	0.63	0.37	0.67	0.69	0.20	-0.77	0.75	0.76	0.86	1.00	0.73	0.66	0.41	0.34	0.37	0.35	-0.34	-0.42	-0.23	0.53	0.36	0.30	0.40	0.37	-0.22	-0.22	-0.21	-0.06
13	0.08	-0.56	0.78	0.50	0.92	0.95	0.12	-0.97	0.98	0.98	0.94	0.73	1.00	0.99	0.82	0.49	0.76	0.73	-0.52	-0.64	-0.39	0.71	0.39	0.32	0.45	0.47	-0.27	-0.29	-0.25	-0.02
14	0.08	-0.58	0.77	0.50	0.91	0.95	0.11	-0.95	0.97	0.97	0.91	0.66	0.99	1.00	0.84	0.49	0.78	0.75	-0.53	-0.64	-0.39	0.71	0.38	0.31	0.44	0.47	-0.26	-0.28	-0.24	-0.02
15	0.11	-0.67	0.76	0.59	0.84	0.78	0.05	-0.77	0.80	0.79	0.71	0.41	0.82	0.84	1.00	0.55	0.91	0.88	-0.62	-0.70	-0.51	0.59	0.41	0.36	0.45	0.32	-0.22	-0.23	-0.20	-0.01
16	0.04	-0.27	0.45	0.34	0.49	0.46	0.10	-0.47	0.48	0.48	0.48	0.34	0.49	0.49	0.55	1.00	0.37	0.27	-0.35	-0.40	-0.29	0.35	0.28	0.26	0.29	0.12	-0.14	-0.14	-0.15	-0.09
17	0.11	-0.69	0.67	0.51	0.76	0.72	0.01	-0.71	0.75	0.73	0.63	0.37	0.76	0.78	0.91	0.37	1.00	0.99	-0.55	-0.64	-0.44	0.58	0.32	0.26	0.37	0.38	-0.15	-0.17	-0.13	0.04
18	0.11	-0.69	0.64	0.49	0.73	0.70	-0.01	-0.68	0.72	0.70	0.59	0.35	0.73	0.75	0.88	0.27	0.99	1.00	-0.53	-0.61	-0.42	0.56	0.30	0.24	0.35	0.38	-0.14	-0.16	-0.11	0.06
19	-0.22	0.58	-0.80	-0.82	-0.72	-0.44	-0.03	0.48	-0.51	-0.50	-0.48	-0.34	-0.52	-0.53	-0.62	-0.35	-0.55	-0.53	1.00	0.98	0.98	-0.20	-0.61	-0.61	-0.60	0.04	0.16	0.14	0.18	0.17
20	-0.22	0.65	-0.85	-0.82	-0.80	-0.56	-0.04	0.59	-0.62	-0.61	-0.59	-0.42	-0.64	-0.64	-0.70	-0.40	-0.64	-0.61	0.98	1.00	0.92	-0.39	-0.60	-0.58	-0.60	-0.06	0.17	0.17	0.18	0.11
21	-0.20	0.48	-0.72	-0.80	-0.60	-0.30	-0.02	0.34	-0.38	-0.36	-0.34	-0.23	-0.39	-0.39	-0.51	-0.29	-0.44	-0.42	0.98	0.92	1.00	0.01	-0.61	-0.62	-0.58	0.14	0.15	0.11	0.18	0.23
22	0.08	-0.53	0.48	0.21	0.61	0.72	0.05	-0.71	0.70	0.71	0.69	0.53	0.71	0.71	0.59	0.35	0.58	0.56	-0.20	-0.39	0.01	1.00	0.10	0.03	0.17	0.50	-0.09	-0.15	-0.04	0.24
23	0.39	-0.23	0.59	0.60	0.52	0.32	0.04	-0.39	0.40	0.40	0.40	0.36	0.39	0.38	0.41	0.28	0.32	0.30	-0.61	-0.60	-0.61	0.10	1.00	0.99	0.99	-0.02	-0.25	-0.24	-0.25	-0.13
24	0.39	-0.20	0.57	0.62	0.48	0.24	0.04	-0.32	0.33	0.33	0.33	0.30	0.32	0.31	0.36	0.26	0.26	0.24	-0.61	-0.58	-0.62	0.03	0.99	1.00	0.96	-0.16	-0.23	-0.22	-0.24	-0.13
25	0.39	-0.26	0.60	0.57	0.55	0.39	0.03	-0.46	0.46	0.46	0.46	0.40	0.45	0.44	0.45	0.29	0.37	0.35	-0.60	-0.60	-0.58	0.17	0.99	0.96	1.00	0.12	-0.26	-0.25	-0.26	-0.12
26	0.01	-0.19	0.08	-0.19	0.26	0.51	-0.01	-0.48	0.47	0.48	0.45	0.37	0.47	0.47	0.32	0.12	0.38	0.38	0.04	-0.06	0.14	0.50	-0.02	-0.16	0.12	1.00	-0.08	-0.10	-0.06	0.05
27	0.29	-0.10	-0.32	-0.29	-0.31	-0.24	0.01	0.27	-0.26	-0.27	-0.28	-0.22	-0.27	-0.26	-0.22	-0.14	-0.15	-0.14	0.16	0.17	0.15	-0.09	-0.25	-0.23	-0.26	-0.08	1.00	0.98	0.98	0.43
28	0.27	-0.07	-0.32	-0.28	-0.32	-0.26	0.00	0.28	-0.28	-0.28	-0.29	-0.22	-0.29	-0.28	-0.23	-0.14	-0.17	-0.16	0.14	0.17	0.11	-0.15	-0.24	-0.22	-0.25	-0.10	0.98	1.00	0.93	0.24
29	0.29	-0.12	-0.32	-0.29	-0.30	-0.22	0.01	0.25	-0.24	-0.25	-0.27	-0.21	-0.25	-0.24	-0.20	-0.15	-0.13	-0.11	0.18	0.18	0.18	-0.04	-0.25	-0.24	-0.26	-0.06	0.98	0.93	1.00	0.58
30	0.18	-0.18	-0.12	-0.15	-0.08	-0.01	0.02	0.03	-0.02	-0.03	-0.06	-0.06	-0.02	-0.02	-0.01	-0.09	0.04	0.06	0.17	0.11	0.23	0.24	-0.13	-0.13	-0.12	0.05	0.43	0.24	0.58	1.00

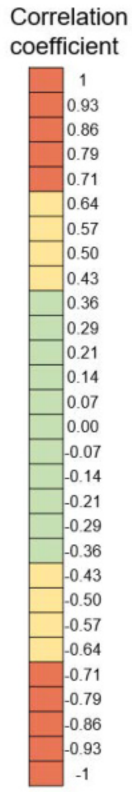

Figure 6. Correlation matrix of geomorphological and geophysical features of the Caucasus region: 1 – X coordinates; 2 – Y coordinates; 3 – arithmetic mean value of relief in a cell; 4 – minimum value of relief in a cell; 5 – maximum value of relief in a cell; 6 – range of relief values in a cell (max–min); 7 – arithmetic mean value of curvature in a cell; 8 – minimum value of curvature in a cell; 9 – maximum value of curvature in the cell; 10 – range of curvature values in the cell (max–min); 11 – arithmetic mean value of TRI index in the cell; 12 – minimum value of TRI index in the cell; 13 – maximum value of TRI index in the cell; 14 – range of TRI index values in the cell (max–min); 15 – arithmetic mean value of lineament density in the cell; 16 – minimum value of lineament density in the cell; 17 – maximum value of lineament density in the cell; 18 – range of lineament density values in the cell (max–min); 19 – arithmetic mean of Bouguer anomalies in the cell; 20 – minimum value of Bouguer anomalies in the cell; 21 – maximum value of Bouguer anomalies in the cell; 22 – range of Bouguer anomalies in the cell (max–min); 23 – arithmetic mean of Moho surface values in the cell; 24 – minimum value of Moho surface in the cell; 25 – maximum value of Bouguer anomalies in the cell; 26 – range of Moho surface values in the cell (max–min); 27 – arithmetic mean of precipitation power values in the cell; 28 – minimum value of precipitation power in the cell; 29 – maximum value of precipitation power in the cell; 30 – range of precipitation power values in the cell (max–min).

The correlation matrix of geomorphological and geophysical features was analyzed (Figure 6). 200 out of 435 values of correlation of features have weak correlation. This is a good indicator from the point of view of data analysis, because the features must be non-collinear, otherwise, the generalization ability of the neural network algorithm is reduced due to the high variance of the data. Medium and strong correlations are found within the feature groups of relief, curvature, TRI index and lineament density. This is true since all these indices were calculated from the same initial data. The exceptions are certain calculated indices, such as the average value of curvature in a cell (absolutely not correlated with any data), the minimum values of TRI index in a cell and the minimum values of lineament density in a cell. Similarly, medium and strong correlations are formed within groups of the same geophysical indicator features (Bouguer anomalies, Moho boundary and sediment thickness). Other groups of geophysical attributes have on average weak correlation relations. In general, the best results show signs related to sediment thickness –

weak correlation with all other parameters. Mostly weak and average correlations have signs of Moho boundary and Bouguer anomaly. They are more strongly correlated with geomorphological features.

In general, weak correlations between features characterize these indicators as reflecting different properties of the geological environment and are independent datasets for the conditions of the Caucasus region. However, the application of such a dataset is only possible on a small scale with a specified cell size of 50 km. Since the geophysical models used have low spatial resolution and the chosen radius allows to cover the area with some degree of variability. Cells with a smaller radius would perform worse under these conditions.

5. Conclusions

Spatial modeling based on the neural network approach allows to model adequately the fields of recent crustal movements and deformations outside the geodetic network contour. The paper details the settings of hyperparameters and the justification of the applicability of the neural network model for the tasks of forecasting crustal velocity fields. The results presented in comparison with classical modeling methods show that the neural network approach shows results not worse than classical methods. However, the ANN algorithm has an important property – it can extrapolate data beyond the contour of the geodetic network. Comparison of quality metrics of classical methods and neural network approach shows the adequacy of ANN results, which allows us to apply them in the tasks of large-scale modeling of the RCM field. Neural network extrapolation allows us to obtain data with greater detail of the studied area, where there are a lot of local and regional tectonic structures.

The possibility of designing and applying more complex features for the neural network based on geomorphological and geophysical data is considered. As a discussion, we note the prospect of first of all using geomorphological indicators as a feature space for modeling the RCM field. In the presented models, the objective was not to construct a complex feature space. On the contrary, the aim was to create a simple model, with available input data, that can be applied by the widest range of researchers. In addition, simple models are more interpretable than models with complex architecture.

The application of such an approach to disparate GNSS data obtained in different epochs of observations is very promising. Of high interest are the GNSS measurements in the Caucasus, which are very heterogeneous, since a large number of scientific groups worked in these regions. The application of machine learning methods will allow the modeling of these data on a single regular grid and obtaining digital models of displacements and deformations of the Caucasus territory on a unified scale. The use of geomorphological indicators as a feature space for modeling the RCM field is a promising approach. Since it is the relief that reflects tectonic movements, both recent and modern, which is especially pronounced in the tectonically active region of the Caucasus.

Acknowledgments. The research was supported by Russian science foundation "System Seismic Hazard Assessment of the Central Part of the Greater Caucasus (Ossetian sector)" (project #23-17-00176). This work employed facilities and data provided by the Shared Research Facility "Analytical Geomagnetic Data Center" of the Geophysical Center of RAS (http://ckp.gcras.ru/).

References

Agayan, S. M., V. N. Tatarinov, A. D. Gvishiani, S. R. Bogoutdinov, and I. O. Belov (2020), FDPS algorithm in stability assessment of the Earth's crust structural tectonic blocks, *Russian Journal of Earth Sciences*, *20*, ES6014, https://doi.org/10.2205/2020ES000752.

Agayan, S. M., I. V. Losev, I. O. Belov, V. N. Tatarinov, A. I. Manevich, and M. A. Pasishnichenko (2022), Dynamic Activity Index for Feature Engineering of Geodynamic Data for Safe Underground Isolation of High-Level Radioactive Waste, *Applied Sciences*, *12*(4), 2010, https://doi.org/10.3390/app12042010.

Aki, K. (1968), Seismic displacements near a fault, *Journal of Geophysical Research*, *73*(16), 5359–5376, https://doi.org/10.1029/JB073i016p05359.

Aleshin, I., K. Kholodkov, I. Malygin, R. Shevchuk, and R. Sidorov (2022), Geomagnetic Survey Interpolation with the Machine Learning Approach, *Russian Journal of Earth Sciences*, *22*, https://doi.org/10.2205/2022ES000818.

Allmendinger, R. W., N. Cardozo, and D. M. Fisher (2011), *Structural Geology Algorithms: Vectors and Tensors*, Cambridge University Press, https://doi.org/10.1017/CBO9780511920202.

Amante, C., and B. W. Eakins (2009), ETOPO1 1 Arc-Minute Global Relief Model: Procedures, Data Sources and Analysis.

Anantrasirichai, N., J. Biggs, F. Albino, P. Hill, and D. Bull (2018), Application of Machine Learning to Classification of Volcanic Deformation in Routinely Generated InSAR Data, *Journal of Geophysical Research: Solid Earth*, *123*(8), 6592–6606, https://doi.org/10.1029/2018jb015911.

Batugin, A., V. Ogadzhanov, S. Han, S. Shevchuk, S. Kostikov, and A. Oborin (2022), Exploring the Nature of Seismic Events in the Underground Gas Storages Area of the Volga Federal District, *Russian Journal of Earth Sciences*, *22*, https://doi.org/10.2205/2022ES000819.

Bogusz, J., A. Kłos, P. Grzempowski, and B. Kontny (2013), Modelling the Velocity Field in a Regular Grid in the Area of Poland on the Basis of the Velocities of European Permanent Stations, *Pure and Applied Geophysics*, *171*(6), 809–833, https://doi.org/10.1007/s00024-013-0645-2.

Boubou, R., F. Emeriault, and R. Kastner (2010), Artificial neural network application for the prediction of ground surface movements induced by shield tunnelling, *Canadian Geotechnical Journal*, *47*(11), 1214–1233, https://doi.org/10.1139/T10-023.

Cardozo, N., and R. W. Allmendinger (2009), SSPX: A program to compute strain from displacement/velocity data, *Computers & Geosciences*, *35*(6), 1343–1357, https://doi.org/10.1016/j.cageo.2008.05.008.

Dimitrios, G. A., X. Papanikolaou, A. Ganas, and D. Paradissis (2019), StrainTool: A software package to estimate strain tensor parameters (Version v1.0).

Dokukin, P. A., V. I. Kaftan, and R. I. Krasnoperov (2010), Influence of triangle shape in geodetic network on the results of definition of Earth surface deformations, *Izvestia vuzov. Geodesy and aerophotosurveying*, *5*, 6–11 (in Russian).

Dzeboev, B. A., A. A. Soloviev, B. V. Dzeranov, J. K. Karapetyan, and N. A. Sergeeva (2019), Strong earthquake-prone areas recognition based on the algorithm with a single pure training class. II. Caucasus, M ≥ 6.0. Variable EPA method, *Russian Journal of Earth Sciences*, *19*(6), https://doi.org/10.2205/2019ES000691.

Esikov, N. P. (1979), *Tectonophysical aspects of analysis of recent Earth's surface movements*, Nauka, Novosibirsk.

Faber, R., and G. Domej (2021), 3D Computer-Assisted Geological Mapping: Testing WinGeol's FaultTrace for semi-automatic structural geological assessment, *Russian Journal of Earth Sciences*, *21*(1), https://doi.org/10.2205/2020ES000757.

Ghiasi, Y., and V. Nafisi (2015), The improvement of strain estimation using universal kriging, *Acta Geodaetica et Geophysica*, *50*(4), 479–490, https://doi.org/10.1007/s40328-015-0103-y.

Goudarzi, M. A., M. Cocard, and R. Santerre (2015), GeoStrain: An open source software for calculating crustal strain rates, *Computers & Geosciences*, *82*, 1–12, https://doi.org/10.1016/j.cageo.2015.05.007.

Grishchenkova, E. N. (2017), Development of a Neural Network for Earth Surface Deformation Prediction, *Geotechnical and Geological Engineering*, *36*(4), 1953–1957, https://doi.org/10.1007/s10706-017-0438-y.

Gvishiani, A. D., B. A. Dzeboev, and S. M. Agayan (2016), FCaZm intelligent recognition system for locating areas prone to strong earthquakes in the Andean and Caucasian mountain belts, *Izvestiya, Physics of the Solid Earth*, *52*(4), 461–491, https://doi.org/10.1134/s1069351316040017.

Gvishiani, A. D., A. A. Soloviev, and B. A. Dzeboev (2020), Problem of Recognition of Strong-Earthquake-Prone Areas: a State-of-the-Art Review, *Izvestiya, Physics of the Solid Earth*, *56*(1), https://doi.org/10.1134/S1069351320010048.

Gvishiani, A. D., M. N. Dobrovolsky, B. V. Dzeranov, and B. A. Dzeboev (2022), Big Data in Geophysics and Other Earth Sciences, *Izvestiya, Physics of the Solid Earth*, *58*(1), https://doi.org/10.1134/S1069351322010037 (in Russian).

Gvishiani, A. D., V. Y. Panchenko, and I. M. Nikitina (2023), System analysis of big data for Earth sciences, *Herald of the Russian Academy of Sciences*, *93*(6), 518–525, https://doi.org/10.31857/S0869587323060087 (in Russian).

IAEA-TECDOC-1987 (2021), An Introduction to Probabilistic Fault Displacement Hazard Analysis in Site Evaluation for Existing Nuclear Installation.

Ismail-Zadeh, A., S. Adamia, A. Chabukiani, T. Chelidze, and other (2020), Geodynamics, seismicity, and seismic hazards of the Caucasus, *Earth-Science Reviews*, *207*, 103,222, https://doi.org/10.1016/j.earscirev.2020.103222.

Kaban, M. K., A. Gvishiani, R. Sidorov, A. Oshchenko, and R. I. Krasnoperov (2021), Structure and Density of Sedimentary Basins in the Southern Part of the East-European Platform and Surrounding Area, *Applied Sciences*, *11*(2), 512, https://doi.org/10.3390/app11020512.

Kaftan, V. I., and V. N. Tatarinov (2021), An Analysis of Possibilities of GNSS Local Strain Monitoring Networks in Earthquake-Prone Areas, *Journal of Volcanology and Seismology*, *15*(6), 379–386, https://doi.org/10.1134/S074204632106004X.

Karapetyan, J. K., R. S. Sargsyan, K. S. Kazaryan, B. V. Dzeranov, B. A. Dzeboev, and R.-K. Karapetyan (2020), Current state of exploration and actual problems of tectonics, seismology and seismotectonics of Armenia, *Russian Journal of Earth Sciences*, *20*(2), https://doi.org/10.2205/2020es000709.

Kolmogorov, A. N. (1957), On the representation of continuous functions of many variables by superposition of continuous functions of one variable and addition, *Doklady Akademii Nauk SSSR*, *114*(5), 953–956 (in Russian).

Kolmogorova, P. P., and G. I. Karataev (1975), Prediction of the velocities of modern vertical movements of the Earth's crust by the correlation model from statistical geological and geophysical data, in *Methodical issues of the study of modern movements of the Earth's crust*, pp. 182–203, IGM SB RAS (in Russian).

Kuzmin, Y. O. (2020), Topical issues of use of geodetic measurements at geodynamic monitoring of objects of oil and gas complex, *Vestnik SSUGT (Siberian State University of Geosystems and Technologies)*, *25*(1), 43–54, https://doi.org/10.33764/2411-1759-2020-25-1-43-54.

Lei, Q., and S. Loew (2021), Modelling coseismic displacements of fracture systems in crystalline rock during large earthquakes: Implications for the safety of nuclear waste repositories, *International Journal of Rock Mechanics and Mining Sciences*, *138*, 104,590, https://doi.org/10.1016/j.ijrmms.2020.104590.

Manevich, A., V. Kaftan, R. Shevchuk, and D. Urmanov (2021), Modelling the horizontal velocity field of the Nizhne-Kansk massif according to GNSS Observations, *ENVIRONMENT. TECHNOLOGIES. RESOURCES. Proceedings of the International Scientific and Practical Conference*, *1*, 162–169, https://doi.org/10.17770/etr2021vol1.6545.

Manevich, A. I., and V. N. Tatarinov (2017), Application of artificial neural networks for forecasting modern crustal movements, in *Geoinformation technologies - a tool for increasing the efficiency and safety of mining*, vol. 5, pp. 37–48, Geophisical Center RAS (in Russian).

Manevich, A. I., R. V. Shevchuk, V. I. Kaftan, V. N. Tatarinov, and S. M. Zabrodin (2022), Improvement of the gnss monitoring network of the nizhne-kansky massif using a bedrock pin geodetic center, *Seismic Instruments*, *58*(S2), S267–S280, https://doi.org/10.3103/s0747923922080084.

Manevich, A. I., R. V. Shevchuk, I. V. Losev, V. I. Kaftan, D. I. Urmanov, and A. I. Shakirov (2023), PyGeoStrain: A software package for calculation crustal strain (v1.0).

Markovich, K. I. (2020), Prediction of velocities of modern vertical movements of the earth's crust from geodetic, geophysical and seismological data, *Geodynamics & Tectonophysics*, *11*(2), 365–377, https://doi.org/10.5800/GT-2020-11-2-0480.

Matheron, G. (1970), Random Functions and their Application in Geology, in *Geostatistics*, pp. 79–87, Springer US, https://doi.org/10.1007/978-1-4615-7103-2_7.

Mazurov, B. T. (2016), Geodynamic system (kinematic and deformation model of block movements), *Vestnik SSUGT*, *3*(35), 5–15 (in Russian).

Milyukov, V. K., A. P. Mironov, G. M. Steblov, V. I. Shevchenko, A. G. Kusraev, V. N. Drobyshev, and K. M. Khubaev (2015), The contemporary GPS-derived horizontal motions of the main elements of tectonic structure in the Ossetian segment of Greater Caucasus, *Izvestiya, Physics of the Solid Earth*, *51*(4), 522–534, https://doi.org/10.1134/S1069351315040072.

Milyukov, V. K., A. P. Mironov, G. M. Steblov, A. N. Ovsyuchenko, E. A. Rogozhin, V. N. Drobyshev, A. G. Kusraev, K. M. Khubaev, and K.-M. Z. Torchinov (2017), Satellite geodetic monitoring of the Vladikavkaz active fault zone: First results, *Izvestiya, Physics of the Solid Earth*, *53*(4), 598–605, https://doi.org/10.1134/S1069351317040061.

Mironov, A. P., V. K. Milyukov, G. M. Steblov, V. N. Drobyshev, A. G. Kusraev, and K. M. Khubaev (2021), Crustal Strains in the Ossetian Region of the Greater Caucasus Based on GNSS Measurements, *Izvestiya, Atmospheric and Oceanic Physics*, *57*(11), 1498–1513, https://doi.org/10.1134/S0001433821110074.

Moss, R. E. S., and Z. E. Ross (2011), Probabilistic Fault Displacement Hazard Analysis for Reverse Faults, *Bulletin of the Seismological Society of America*, *101*(4), 1542–1553, https://doi.org/10.1785/0120100248.

Negi, P., A. Goswami, and G. C. Joshi (2023), Geomorphic indices based topographic characterization of Alaknanda catchment, Western Himalaya using spatial data, *Environmental Earth Sciences*, *82*(20), https://doi.org/10.1007/s12665-023-11158-w.

Nurminen, F., P. Boncio, F. Visini, B. Pace, A. Valentini, S. Baize, and O. Scotti (2020), Probability of Occurrence and Displacement Regression of Distributed Surface Rupturing for Reverse Earthquakes, *Frontiers in Earth Science*, *8*, https://doi.org/10.3389/feart.2020.581605.

Okada, Y. (1992), Internal deformation due to shear and tensile faults in a half-space, *Bulletin of the Seismological Society of America*, *82*(2), 1018–1040, https://doi.org/10.1785/BSSA0820021018.

Pedregosa, F., G. Varoquaux, A. Gramfort, V. Michel, B. Thirion, and other (2011), Scikit-learn: Machine Learning in Python, *Journal of Machine Learning Research*, *12*, 2825–2830.

Petrov, V. A., V. A. Minaev, S. A. Ustinov, I. O. Nafigin, and A. B. Lexin (2021), Assessment of Seismogeodynamic Activity of Mining Areas on the Basis of 3D Geoinformation Modeling, *Russian Journal of Earth Sciences*, *21*(6), https://doi.org/10.2205/2021ES000781.

Reilinger, R., S. McClusky, P. Vernant, S. Lawrence, S. Ergintav, R. Cakmak, and other (2006), GPS constraints on continental deformation in the Africa-Arabia-Eurasia continental collision zone and implications for the dynamics of plate interactions, *Journal of Geophysical Research: Solid Earth*, *111*(B5), https://doi.org/10.1029/2005JB004051.

Reilinger, R. E., S. C. McClusky, B. J. Souter, M. W. Hamburger, M. T. Prilepin, A. Mishin, T. Guseva, and S. Balassanian (1997), Preliminary estimates of plate convergence in the Caucasus Collision Zone from global positioning system measurements, *Geophysical Research Letters*, *24*(14), 1815–1818, https://doi.org/10.1029/97gl01672.

Różycka, M., P. Migoń, and A. Michniewicz (2017), Topographic Wetness Index and Terrain Ruggedness Index in geomorphic characterisation of landslide terrains, on examples from the Sudetes, SW Poland, *Zeitschrift für Geomorphologie, Supplementary Issues*, *61*(2), 61–80, https://doi.org/10.1127/zfg_suppl/2016/0328.

Sandwell, D. T. (1987), Biharmonic Spline Interpolation of GEOS-3 and SEASAT Altimeter Data, *Geophysical Research Letters*, *14*(2), 139–142.

Sedrette, S., and N. Rebai (2016), Automatic extraction of lineaments from Landsat Etm+ images and their structural interpretation: Case Study in Nefza region (North West of Tunisia), *Journal of Research in Environmental and Earth Sciences*, *4*, 139–145.

Shen, Z., D. D. Jackson, and B. X. Ge (1996), Crustal deformation across and beyond the Los Angeles basin from geodetic measurements, *Journal of Geophysical Research: Solid Earth*, *101*(B12), 27,957–27,980, https://doi.org/10.1029/96JB02544.

Shen, Z., M. Wang, Y. Zeng, and F. Wang (2015), Optimal Interpolation of Spatially Discretized Geodetic Data, *Bulletin of the Seismological Society of America*, *105*(4), 2117–2127, https://doi.org/10.1785/0120140247.

Shevchenko, V. I., T. V. Guseva, A. A. Lukk, A. V. Mishin, and other (1999), Modern geodynamics of the Caucasus (based on GPS measurements and seismological data), *Izvestiya, Physics of the Solid Earth*, *9*, 3–18 (in Russian).

Simonov, Y. G. (1998), *Morphometric analysis of relief*, SGU Publishing House, Moscow-Smolensk (in Russian).

Sokhadze, G., M. Floyd, T. Godoladze, R. King, E. S. Cowgill, Z. Javakhishvili, G. Hahubia, and R. Reilinger (2018), Active convergence between the Lesser and Greater Caucasus in Georgia: Constraints on the tectonic evolution of the Lesser–Greater Caucasus continental collision, *Earth and Planetary Science Letters*, *481*, 154–161, https://doi.org/10.1016/j.epsl.2017.10.007.

Srivastava, H., and E. Isaaks (1989), *An Introduction to Applied Geostatistics*, Oxford University Press.

Sun, Z., L. Sandoval, R. Crystal-Ornelas, S. M. Mousavi, J. Wang, C. Lin, and other (2022), A review of Earth Artificial Intelligence, *Computers & Geosciences*, *159*, 105,034, https://doi.org/10.1016/j.cageo.2022.105034.

Tatarinov, V. N., A. I. Manevich, and I. V. Losev (2018), A system approach to geodynamic zoning based on artificial neural networks, *Mining science and technology*, (3), 14–25, https://doi.org/10.17073/2500-0632-2018-3-14-25 (in Russian).

Tatarinov, V. N., V. N. Morozov, and A. S. Batugin (2019), An underground research laboratory: new opportunities in the study of the stress-strain state and dynamics of rock mass destruction, *Russian Journal of Earth Sciences*, *19*, ES2002, https://doi.org/10.2205/2019ES000659 (in Russian).

Teza, G., A. Pesci, and A. Galgaro (2008), Grid_strain and grid_strain3: Software packages for strain field computation in 2D and 3D environments, *Computers & Geosciences*, *34*(9), 1142–1153, https://doi.org/10.1016/j.cageo.2007.07.006.

Tibaldi, A., F. L. Bonali, E. Russo, and N. Corti (2021), Active Kinematics of the Greater Caucasus from Seismological and GPS Data: A Review, in *Building Knowledge for Geohazard Assessment and Management in the Caucasus and other Orogenic Regions*, NATO Science for Peace and Security Series C: Environmental Security, pp. 33–57, Springer Netherlands, https://doi.org/10.1007/978-94-024-2046-3.

Wackernagel, H. (1994), *Multivariate Geostatistics*, Springer, Berlin, Germany.

Wu, J., C. Tang, and Y. Chen (2003), Effect of triangle shape factor on precision of crustal deformation calculated, *Journal of Geodesy and Geodynamics*, *23*(3), 26–30.

Yamaga, N., and Y. Mitsui (2019), Machine Learning Approach to Characterize the Postseismic Deformation of the 2011 Tohoku-Oki Earthquake Based on Recurrent Neural Network, *Geophysical Research Letters*, *46*(21), https://doi.org/10.1029/2019gl084578.

Yang, B., K. Yin, S. Lacasse, and Z. Liu (2019), Time series analysis and long short-term memory neural network to predict landslide displacement, *Landslides*, *16*(4), 677–694, https://doi.org/10.1007/s10346-018-01127-x.

Youngs, R. R., W. J. Arabasz, R. E. Anderson, A. R. Ramelli, J. P. Ake, D. B. Slemmons, and other (2003), A Methodology for Probabilistic Fault Displacement Hazard Analysis (PFDHA), *Earthquake Spectra*, *19*(1), 191–219, https://doi.org/10.1193/1.1542891.

Russian Journal of Earth Sciences

The Present State of the Kola Peninsula Broadband Seismic Network

A. G. Goev*,[1], A. V. Fedorov[2], I. S. Fedorov[2], V. E. Asming[2], I. M. Aleshin[3,4], and N. A. Yudochkin[1]

[1] Sadovsky Institute of Geosphere Dynamics RAS, Moscow, Russia
[2] Kola Branch, Federal Research Centre "Geophysical Survey" RAS, Apatity, Russia
[3] Schmidt Institute of the Physics of the Earth RAS, Moscow, Russia
[4] Geophysical Center RAS, Moscow, Russia
* **Correspondence to:** Andrey Goev, goev@idg.ras.ru.

Abstract: This paper provides information about the main parameters of spatial broadband seismic network in the Kola region (the northeastern part of the Fennoscandian Shield). Since 2021 the seismic network has been expanded by five seismic stations and currently consists of nine stations located on the territory of the Russian Federation. Configuration of the network allows to broaden the scope of research of the Kola region lithospheric structure significantly. The prospects of integrating the newly installed stations into the automated regional seismic monitoring network are considered. The analysis of seismic noise in the places of installation of new seismic stations was carried out. It was shown that the data provided by the new broadband stations increases the accuracy of seismic events location in the research area.

Keywords: Arctic, Kola region, Fennoscandia, seismic network, location, technogenic seismicity, earthquakes.

Citation: Goev, A. G., A. V. Fedorov, I. S. Fedorov, V. E. Asming, I. M. Aleshin, and N. A. Yudochkin (2023), The Present State of the Kola Peninsula Broadband Seismic Network, *Russian Journal of Earth Sciences*, 23, ES6003, EDN: FICDWW, https://doi.org/10.2205/2023es000872

1. Introduction

Arctic Region' exploration requires deepening the knowledge about its geological structure, tectonics and seismicity. The Kola region is one of the key regions of the Arctic zone of the Russian Federation (AZRF) with developed civil and industrial infrastructure and also with the largest mining complex in Europe.

One of the fundamental issues related to deep geodynamics is the genesis of large polymetallic deposits that are currently being mined within Kola Peninsula, and the features of their spatial distribution. A combination of geological and geochemical data links ore genesis to plume-lithospheric processes [*Bayanova et al.*, 2019]. Presumably, determining the characteristics of these mineral deposits' origin will lead to a new vision of the circumstances of their formation.

The Kola Peninsula is an area of low tectonic activity. The main tectonic process, as for the entire Baltic Shield, is considered to be the process of slow and differentiated uplift, accompanied by the emergence of new or revival of former disjunctive dislocations [*Lukk et al.*, 2019]. Natural earthquakes that occasionally occur within the Kola Peninsula are a consequence of this process. Along with natural, technogenic seismic events also occur in the region [*Morozov et al.*, 2022]. It is worth mentioning, that the intensity of technogenic events is comparable to the intensity of the natural events in terms of energy emitted.

Developing the Kola Peninsula seismic network allows to deepen our knowledge of the lithospheric structure of the region. This adds to the understanding of Fennoscandia geological evolution in general [*Thybo et al.*, 2021] and, hopefully, of the numerous ore deposits' origin within the Kola region. In addition, the new seismic data provides the opportunity to research local seismicity, especially in proximity to large mining operations, which is crucial to Kola's mining industry.

Research Article

Received: 5 August 2023
Accepted: 21 September 2023
Published: 30 December 2023

This paper demonstrates the technical capabilities of the extended broadband seismic network within the Kola region. The technical characteristics, the quality of the data obtained, as well as the stations' distribution make it possible to study the lithosphere effectively and locate various seismic events.

2. Characteristics of the Kola Region Seismic Network

Seismic monitoring on the Kola region territory and adjacent areas of Fennoscandia is performed by Kola Branch of the Geophysical Survey of the Russian Academy of Sciences (KB GS RAS). Prior to 2021 the regional seismic monitoring network consisted of 5 seismic stations and a seismic array comprised of 9 short-period seismometers with an aperture of 1 km. Additionally, the data collected by Norwegian and Finnish seismic networks is jointly analyzed by the regional information processing center of the KB GS RAS.

The analysis of the network configuration (Figure 1) prior to 2021 reveals an extremely heterogeneous distribution of seismic stations over the territory under observation. This complicates the ability to research of the lithospheric structure of the Kola region's western part (as well as in the areas containing large ore deposits – "Pechenga" and "Kovdor"). This also hindered the local focal zones' research.

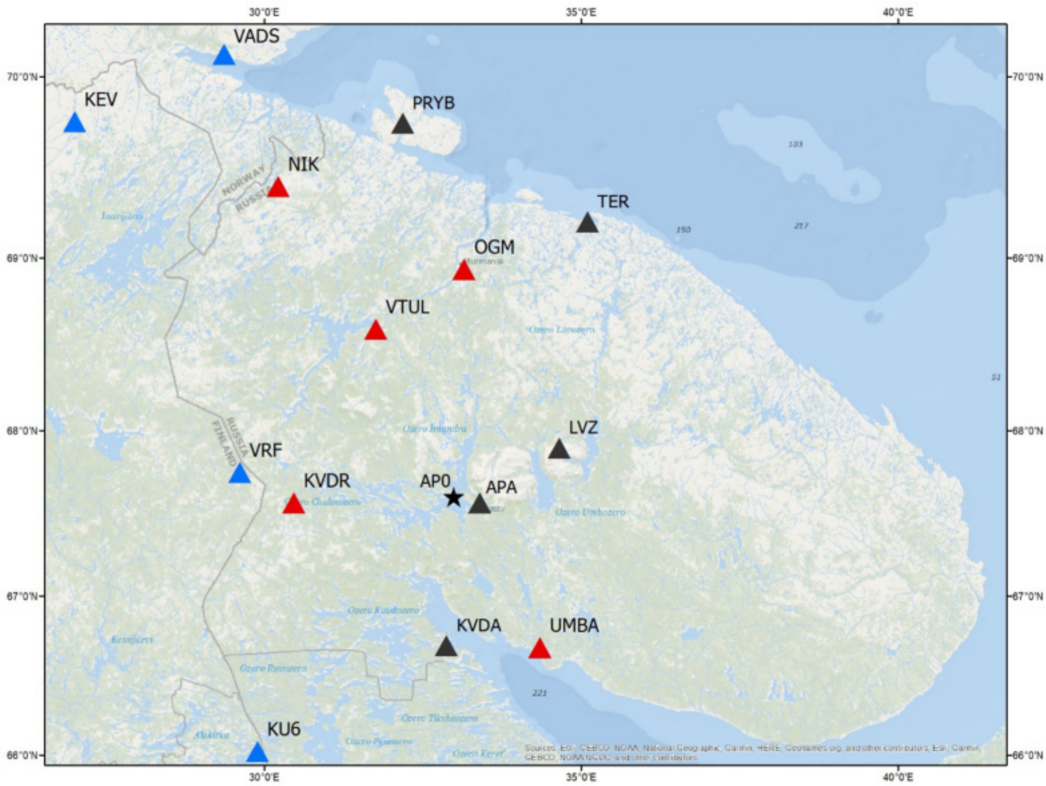

Figure 1. A map seismic stations' distribution within the Kola region. The black triangles represent stations prior to 2021. The black star represents the Apatity seismic array. The red triangles represent the new broadband seismic stations. Blue triangles represent permanent broadband stations of foreign services.

In 2021 the Russian science foundation (RSF) (https://rscf.ru/project/21-17-00161/) project named "Development of a spatial structural-dynamic model of the interaction of near-surface geological forms and geophysical processes with deep inhomogeneities of the earth's crust and upper mantle of the central and arctic parts of the Kola Peninsula" was initiated. It was aimed at studying the lithosphere's structure of the central and Arctic parts of the Kola Peninsula and to investigate possible links between the genesis of deposits and plume-lithospheric processes. As a part of this project, five new broadband stations have been installed – "Nickel" (NIK), "Verkhnetulomsky" (VTUL), "Kovdor" (KVDR), "Ogni

Murmanska" (OGM) and "Umba" (UMBA). The location and technical characteristics of seismic stations are shown in Figure 1 and in Table 1, respectively.

Table 1. Main characteristics of new seismic network

Name	Code	Lat	Lon	freq. range (Hz)	Start time
Nickel	NIK	69.24	30.13	0.03–50	06.2020
Verkhnetulomsky	VTUL	68.35	31.45	0.03–50	06.2021
Teriberka	TER	69.20	35.10	0.03–50	12.2013
Lovozero	LVZ	67.89	34.65	0.002–10	1991
Apatity	APA	67.56	33.40	0.01–50	1991
Kovda	KVDA	66.69	32.87	0.03–100	07.2018
Umba	UMBA	66.67	34.34	0.03–100	05.2021
Kovdor	KVDR	67.56	30.47	0.008–100	12.2021
Ogni Murmanska	OGM	68.93	33.14	0.03–100	10.2022

The seismic network's configuration and equipment used provides the opportunity to study the lithosphere of the Kola region. It makes possible to carry out a comparative analysis of the structure of the Earth's crust and the upper mantle of the largest tectonic elements – the Murmansk, Kola and Belomorsky megablocks (Figure 2). In addition, there is an opportunity to study Khibino-Lovozersky tectonic cluster and the areas of the largest iron ore and copper-nickel deposits of "Kovdor" and "Pechenga" in detail in order to identify their origins. Results of the conducted research are presented in [*Adushkin et al.*, 2021; *Goev*, 2022].

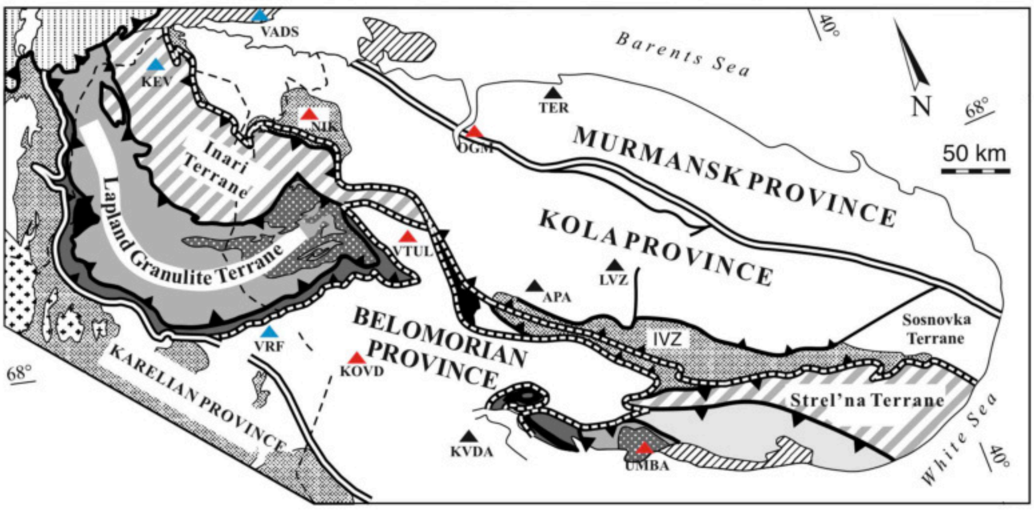

Figure 2. Tectonic scheme of the Kola region according to [*Mudruk et al.*, 2013]. The black triangles represent stations prior to 2021. The red triangles represent new broadband seismic stations. Blue triangles represent permanent broadband stations of foreign services.

The stations installed within the boundaries of the project were placed on sites with varied foundations its terms of soil type, however sites with rocky foundations were prioritized during initial planning. The recording equipment was installed directly on the rocky foundation and equipped with insulated metal cases to reduce low-frequency temperature fluctuations (Figure 3).

To assess the data quality provided by new seismic stations, evaluation of seismic noise was carried out. Data acquired by new seismic stations was analyzed, excluding

Figure 3. The seismic equipment within the insulated metal cases at stations Umba (a), Verkhnetulomsky (b), and Ogni Murmanska (c).

materials from the UMBA station, since its registration capabilities were already discussed in detail earlier in [*Fedorov et al.*, 2022]. The analysis was carried out as follows: using the vertical components of seismograms (Z) of continuous recordings within one month period, the spectral noise density was calculated and probability density graphs were derived according to [*McNamara*, 2004] (Figure 4). These graphs were compared to the model curves of the maximum (NNM curve) and minimum (LM curve) values of seismic noise calculated by the world observation network [*Peterson*, 1993]. The seismic noise levels found in the records of the new stations do not exceed the values of the NHNM high noise model.

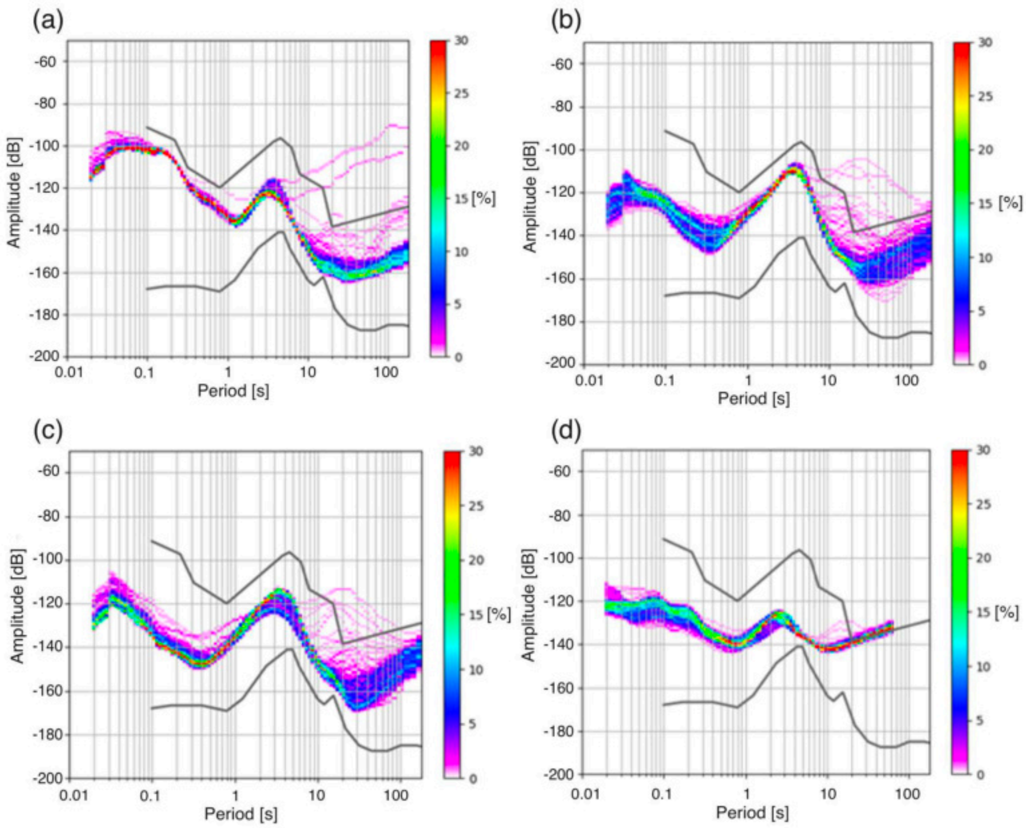

Figure 4. Power spectral density and Probability Density Function [*McNamara*, 2004] for the following station: a – KVDR, b – NIK, c – VTUL, d – OGM. Gray curves represent max and min values according to [*Peterson*, 1993].

3. Seismic Events Location Methods

Since 2016 for continuous seismic monitoring in the western sector of the Russian Federation's Arctic zone the KB GS RAS is using NSDL – an automated software package designed to detect and locate seismic events [*Fedorov et al.*, 2019]. NSDL processes data obtained by a total of 19 seismic stations of the international network located within the Kola Peninsula, in northern Norway, eastern Finland and the Spitsbergen archipelago. Data processing happens in close to real time mode. Seismic stations located on the Spitsbergen archipelago and the Kola Region are processed separately in specially allocated subsystems of the NSDL [*Asming et al.*, 2018].

The NSDL system is structurally divided into two functional parts. The first, called NSS, detects and locates regional seismic events using the data of individual stations. The second, called NAS, associates results obtained from individual stations.

The NSS program is able to analyze the data of individual seismic station (in almost real time), detect seismic events and make preliminary estimation of the epicenter coordinates using the difference in the arrival times of P- and S-waves, and their polarization.

The NAS program associates the results of data processing done by the NSS program. The program correlates the arrival time of seismic waves with registered events, locates hypocenters and compiles a database of events. The results of the NSS programs are submitted to the NAS input. These are lists of seismic events found at one station and lists of all detected phases with their azimuthal estimates obtained in cohesion with wave polarization. Association and location of hypocenters of seismic events in the NAS program is implemented by a method similar to the Generalized Beamforming method [*Ringdal and Kvaerna*, 1989]. The final catalogue is formed during the next processing stage after automated results has been reviewed by a geophysicist.

To evaluate the quality of the KB GS RAS monitoring system's automation with the inclusion of new stations installed within the frames of the RSF project, one month of data was picked – January 2023. The following chapter presents the analysis results of the automated data processing done with the new stations' data and a comparison of the results of the automated catalogues calculated by the regional network with the new stations included and excluded in the data processing.

4. Discussion

According to the automated data processing procedures described in the previous chapter, each new station was subjected to a single-station processing procedure at the first stage. The quantity of events detected by each station is presented in Table 2. The automated detector selected events with epicentral distances of 1500 km or less from the station.

Table 2. The quantity of detected seismic events during single-station processing of new stations

Station code	NIK	VTUL	KVDR	OGM
Event Number	5948	1835	611	1789

In the great majority of cases, the detected events reflect drilling and blasting operations. The results of the automated processing of singular stations were selectively validated. The average percentage of false positives detected was 22%, which is generally an acceptable result, coinciding with the results of the regional network's processing in prior years [*Fedorov et al.*, 2019].

Due to the difference in conditions, the number of detected seismic events of different stations (Table 2) varies significantly. First of all, this difference is attributed to varied levels of seismic noise (Figure 4). Additionally, the number, remoteness and intensity of ongoing drilling and blasting operations varies from station to station which also affects the number of false positives. Analysis of the data recorded by the KVDR station revealed that due to high seismic noise, this station mainly registers seismic events from the area of the

"Zhelezny" mine of the "Kovdor" deposit nearby, where industrial blasts are carried out once a week. Most of the seismic events detected by the NIK station are also the result of drilling and blasting operations. Due to the large number of technogenic interference, this station demonstrates the highest percentage of false positives – 28%. It should be noted, that at the stage of association with the other stations' data, most of the false positives are discarded and impose minimal impact on the final automated catalogue.

VTUL and OGM stations are characterized by lower seismic noise, much lower local technogenic interference and have the lowest percentage of false positives (10% and 12%, respectively). These stations register weak local events and even strong quarry blasts from the area of "Kovdor" and the Khibiny mountain range (130–180 km away).

At the next stage, single-station bulletins and lists of all detected phases of seismic events identified during single-station processing of new stations were combined with similar datasets of the permanent monitoring network.

Figure 5 presents a comparison of the results obtained from the data of automated processing done by the NSDL for the regional monitoring network with new stations included in processing (red circles) and without them (blue circles). The map shows automated results obtained by at least 3 seismic stations from January 1 to January 31 period of 2023 for the Kola region.

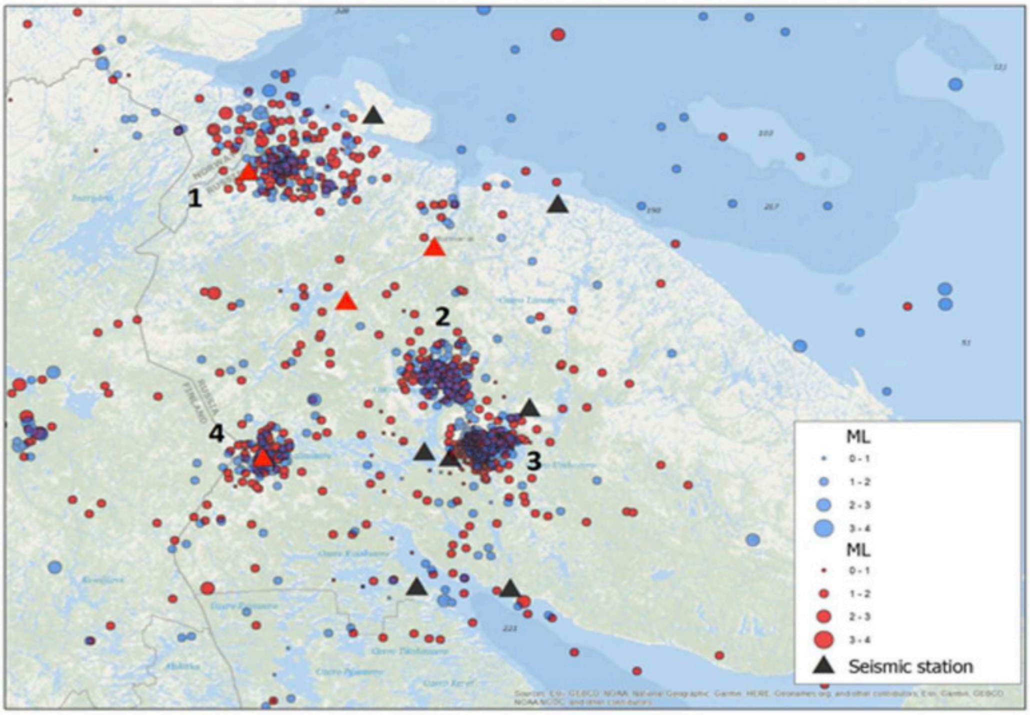

Figure 5. Comparison of the automated data processing results. Blue circles represent seismic events detected by stations of the regional monitoring network without new stations, red circles – with new stations included. The numbers indicate the areas of natural and technogenic seismicity: 1 – Mines near Zapolyarny and Kirkenes (Norway); 2 – Olenegorsky; 3 – Deposits of the Khibiny pluton; 4 – Kovdor.

The analysis of Figure 5 and Table 3 demonstrated that the inclusion of four new stations into the local monitoring network grants an increase in the number of seismic events detected and increases the accuracy of epicenters' location calculation.

5. Conclusions

The prospects of expanding the automated regional seismic monitoring network of the Kola region with five newly installed broadband stations in the region starting from 2021 were presented in this paper. It is shown that incorporating new stations into the

Table 3. Comparison of the number of detected seismic events in the main seismic zones of the Kola region according to the regional network with and without new stations

The seismogenic zone Number	Event Number with new stations	Event Number without new stations
1	214	142
2	92	72
3	1051	934
4	70	51

regional network will increase the density of stations in the western part of the Kola region and significantly improve the area coverage of the network.

Seismic noise levels were assessed for each individual station. It is shown that seismic background noise levels do not exceed the level of the high noise model for all new stations.

The automated data processing of the Kola regional monitoring network with the new seismic stations included in it was tested. The data of one month period was selected for this experiment (from January 1 to January 31, 2023). Comparison of the results of automated processing over the network with new stations and without them revealed an increase in accuracy of epicenters location calculations within key seismogenic zones of the Kola region.

Acknowledgements. The research on newly obtained data integration to the GS RAS system and analysis of the seismic activity was supported by the Ministry of Science and Higher Education of the Russian Federation (GS RAS #075-01271-23 and IDG RAS #122040400015-5). New seismic stations installation and data processing was done in accordance with Russian Science Foundation grant #21-17-00161. The data used in the paper was obtained with large-scale research facilities "Seismic infrasound array for monitoring Arctic cryolitozone and continuous seismic monitoring of the Russian Federation, neighbouring territories and the world" (https://ckp-rf.ru/usu/507436/, http://www.gsras.ru/unu/). Government contracts #075-01349-23-00 (the Geophysical Center of the Russian Academy of Sciences) and #075-01030-23-00 (the Schmidt Institute of Physics of the Earth of the Russian Academy of Sciences), approved by the Ministry of Education and Science of the Russian Federation.

References

Adushkin, V. V., A. G. Goev, I. A. Sanina, and A. V. Fedorov (2021), The Deep Velocity Structure of the Central Kola Peninsula Obtained using the Receiver Function Technique, *Doklady Earth Sciences*, *501*(2), 1049–1051, https://doi.org/10.1134/S1028334X21120011.

Asming, V., A. Fedorov, A. Alenicheva, and Z. Jevtjugina (2018), Usage of the NSDL location system for the detailed study of the Spitsbergen archipelago seismicity, *Bulletin of the Kola Scientific Center RAS*, *10*(3), 120–131, https://doi.org/10.25702/KSC.2307-5228.2018.10.3.120-131 (in Russian).

Bayanova, T., A. Korchagin, A. Mitrofanov, P. Serov, N. Ekimova, E. Nitkina, I. Kamensky, D. Elizarov, and M. Huber (2019), Long-Lived Mantle Plume and Polyphase Evolution of Palaeoproterozoic PGE Intrusions in the Fennoscandian Shield, *Minerals*, *9*(1), 59, https://doi.org/10.3390/min9010059.

Fedorov, A. V., V. E. Asming, Z. A. Jevtjugina, and A. V. Prokudina (2019), Automated Seismic Monitoring System for the European Arctic, *Seismic Instruments*, *55*(1), 17–23, https://doi.org/10.3103/S0747923919010067.

Fedorov, I. S., S. V. Asming, A. G. Goev, and S. G. Volosov (2022), Expansion of the seismological monitoring network on the Kola Peninsula, *Russian Journal of Seismology*, *4*(1), 63–72, https://doi.org/10.35540/2686-7907.2022.1.05.

Goev, A. G. (2022), Some Features of the Mantle Transition Zone on the Kola Peninsula, *Doklady Earth Sciences*, *506*(2), 804–808, https://doi.org/10.1134/S1028334X22600402.

Lukk, A. A., V. G. Leonova, and A. Y. Sidorin (2019), Revisiting the Origin of Seismicity in Fennoscandia, *Izvestiya, Atmospheric and Oceanic Physics*, *55*(7), 743–758, https://doi.org/10.1134/S000143381907003X.

McNamara, D. E. (2004), Ambient Noise Levels in the Continental United States, *Bulletin of the Seismological Society of America*, *94*(4), 1517–1527, https://doi.org/10.1785/012003001.

Morozov, A. N., G. N. Antonovskaya, V. E. Asming, S. V. Baranov, N. V. Boldireva, N. V. Vaganova, Y. A. Vinogradov, Y. V. Konechnaya, N. N. Starkova, A. V. Fedorov, I. S. Fedorov, and S. V. Shibaev (2022), Arctic, in *Earthquakes in Russia in 2020: Annual edition*, pp. 34–38, Geophysical Survey of the Russian Academy of Sciences, Obninsk (in Russian).

Mudruk, S. V., V. V. Balagansky, I. A. Gorbunov, and A. B. Raevsky (2013), Alpine-type tectonics in the Paleoproterozoic Lapland-Kola Orogen, *Geotectonics*, (4), 13–30, https://doi.org/10.7868/s0016853x1304005x (in Russian).

Peterson, J. R. (1993), *Observations and modeling of seismic background noise*, US Geological Survey, https://doi.org/10.3133/ofr93322.

Ringdal, F., and T. A. Kvaerna (1989), Multi-channel processing approach to real time network detection, phase association, and threshold monitoring, *Bulletin of the Seismological Society of America*, *79*(6), 1927–1940, https://doi.org/10.1785/BSSA0790061927.

Thybo, H., N. Bulut, M. Grund, A. Mauerberger, A. Makushkina, I. M. Artemieva, N. Balling, O. Gudmundsson, V. Maupin, L. Ottemøller, J. Ritter, and F. Tilmann (2021), ScanArray-A Broadband Seismological Experiment in the Baltic Shield, *Seismological Research Letters*, *92*(5), 2811–2823, https://doi.org/10.1785/0220210015.

Russian Journal of Earth Sciences

Influence of Rock Watering on Post-Seismic Activity: A Study on the Khibiny Massif

S. V. Baranov[*,1], **P. N. Shebalin**[2], **S. A. Zhukova**[1,3], **A. Yu. Motorin**[1,4], **and I. S. Fedorov**[1]

[1] Kola branch of the Federal Research Center "Geophysical Survey, Russian Academy of Sciences", Apatity, Russia
[2] Institute of Earthquake Prediction Theory and Mathematical Geophysics, Russian Academy of Sciences, Moscow, Russia
[3] Mining Institute of the Kola Federal Research Center, Russian Academy of Sciences, Apatity, Russia
[4] Kirovsk Branch of JSC "Apatit", Kirovsk, Russia
[*] **Correspondence to:** Baranov Sergey Vladimirovich, bars.vl@gmail.com.

Abstract: The article is devoted to the study of the influence of watering of the rock environment on post-seismic activity in the deposits of the Khibiny mountains. Initial data are the results of long-term monitoring of seismicity and observations of water inflows. At a qualitative level, the influence of watering of the environment on the *b*-value of the Gutenberg – Richter distribution of magnitudes of triggered events, as well as on the parameters of the Omori – Utsu law, which describes the post-seismic activity decay rate over time, was studied.

Keywords: Khibiny massif, watering, post-seismic activity, Gutenberg – Richter distribution, Omori – Utsu law.

Citation: Baranov, S. V., P. N. Shebalin, S. A. Zhukova, A. Yu. Motorin, and I. S. Fedorov (2023), Influence of Rock Watering on Post-Seismic Activity: A Study on the Khibiny Massif, *Russian Journal of Earth Sciences*, 23, ES6004, EDN: AROKFS, https://doi.org/10.2205/2023es000880

Introduction

Presently, the issue of the influence of watering of the rock on seismicity can be considered well-studied. There are experimental [*Board et al.*, 1992; *Kartseva et al.*, 2022] and field data [*Hainzl et al.*, 2006, 2013; *Heinicke et al.*, 2017; *Maystrenko et al.*, 2020; *Smirnov et al.*, 2022; *Talwani*, 1997; *Vorobieva et al.*, 2020; *Zoback and Harjes*, 1997] on the influence of moisture content of the geologic material on the parameters of the seismic regime for natural (tectonic) and induced seismicity. The key result of these studies is the increase in seismicity during elevation of pore fluid pressure and the "lubrication" effect due to the increase in the amount of liquid penetrating into the medium caused either by the changes in the reservoir level [*Smirnov et al.*, 2022; *Talwani*, 1997], or by heavy rainfalls [*Hainzl et al.*, 2006, 2013; *Heinicke et al.*, 2017; *Maystrenko et al.*, 2020], or by snowmelt in spring [*Zhukova et al.*, 2023], or by direct liquid injection for extraction of hydrocarbons [*Vorobieva et al.*, 2020; *Zoback and Harjes*, 1997].

Porosity and moisture content of rock play a significant role in this process. At the same time, the increase in seismicity during the growth of moisture content is manifested in both the growth in the number of earthquakes and the reduction of the *b*-value of the Gutenberg – Richter magnitude distribution [*Smirnov et al.*, 2013, 2022; *Zhukova et al.*, 2023], which reflects an increase in the proportion of strong earthquakes.

Thus, the increase in watering of the rock, accompanied by an increase in pore pressure, is a significant factor affecting the seismic regime. Moreover, a number of Russian [*Batugin*, 2006; *Lazarevich et al.*, 2006; *Nikolaev*, 1988; *Rebetskiy*, 2007] and foreign [*Bell and Nur*, 1978; *Manga and Wang*, 2015; *Shapiro*, 2015; *Simpson*, 1986] researchers consider the hypothesis that one of the main triggers of induced earthquakes may be an increase in the pore fluid pressure.

Despite the fact that the influence of watering of the rock mass on the overall seismicity has been discussed in many research, the impact of this factor on the post-seismic activity

Research Article

Received: 3 November 2023
Accepted: 19 December 2023
Published: 30 December 2023

arising from the stress changes caused by an earlier earthquake has been studied less (see, for example, section 1.1.3 in [*Smirnov et al.*, 2020] and references therein). A possible reason for this is that such studies encounter objective difficulties. First, the data of long-term seismic observations and regular monitoring of water inflow in a territory with both seismicity and significant fluctuations in the watering of the medium are required. Second, it is desirable for watering measurements to be carried out at depths comparable to the depths of earthquakes in order to avoid ambiguities associated with the delay in the flow of fluid into the earth's crust, as it happens, for example, in the case of seismicity of reservoirs.

The territory where such a study is possible is the Khibiny massif, located in the center of the Kola Peninsula. Due to its commercial development, seismic monitoring has been carried out at the fields of the Khibiny massif since the late 1980s, and since 2002, regular measurements of water inflow have been carried out at depths comparable to the depths of seismic events (for more details refer to the section "Research area and materials"). In addition, previous studies have revealed a significant influence of watering of the rock on the seismicity of the Khibiny fields [*Kozyrev et al.*, 2021; *Zhukova*, 2015; *Zhukova et al.*, 2023]. In particular, *Zhukova et al.* [2023] showed a significant decrease in b-value during the high watering period of the Khibiny massif, from May to October, compared to the low period from November to April. In this paper, we will find out whether watering of the rock affects the parameters of post-seismic activity.

Post-seismic activity is described by three laws of statistical seismology: Gutenberg – Richter [*Gutenberg and Richter*, 1944], Omori – Utsu [*Utsu et al.*, 1995], and earthquake productivity [*Baranov et al.*, 2022; *Shebalin et al.*, 2020]. The Gutenberg – Richter law specifies the distribution of magnitudes. The Omori – Utsu law describes the decay of triggered events over time. The law of productivity characterizes the ability of seismic events to trigger aftershocks (the number of events triggered by an earlier earthquake obeys an exponential distribution).

The physical mechanism of post-seismic activity is often described by the rate- and state-dependent friction model [*Dieterich*, 1994, 2007] (other models are briefly discussed in [*Smirnov and Ponomarev*, 2020]. Under some assumptions, this model predicts Omori's law with $p = 1$ and gives a physical interpretation of its parameters [*Cocco et al.*, 2010; *Dieterich*, 1994, 2007].

In this article, we will qualitatively study the effect of rock watering in the research area on the distribution of magnitudes of triggered events and on their decay over time.

Research Area and Materials

The Khibiny massif, located in the center of the Kola Peninsula, is the world's largest alkaline intrusion [*Arzamastsev et al.*, 2013]. The complex structure of the massif is characterized by a high level of tectonic stresses, reaching values of 40–60 MPa at depths ranging from −600 to −90 m. In some cases, these stresses exceed the gravitational forces due to the weight of the overlying rocks [*Onokhin*, 1975; *Rebetskiy*, 2007].

Here and further the depths are relative to the zero of the Kronstadt footstock, corresponding to the average level of the Baltic Sea, towards the center of the Earth. Negative value means that the depth is above the reference level.

There are many annular and radial faults in the massif, some of which intersect deposits of apatite-nepheline ores [*Arzamastsev et al.*, 2013; *Shabarov et al.*, 2021]. Because of this, the mining area is a zone of increased seismic activity, saturated with tectonic disturbances. Uplifts of the Khibiny massif at a rate of 0.5 to 2–4 mm per year and periodic earthquakes [*Kremenetskaya and Trjapitsin*, 1995] indicate modern tectonic changes in this region.

For decades, in the course of mining operations, new systems of cracks and cavities are formed in the Khibiny massif, which have a direct impact on the distribution of natural stress fields. This, in turn, leads to the destabilization of the block structure of the massif. The impact of technology and tectonics creates annealing zones, which gradually contribute to the destruction of individual areas of the massif, generally activating seismicity [*Kozyrev* et al., 2022]. Thus, the seismicity of the Khibiny massif is the result of the impact of both tectonic and mining activity.

The study used a catalog of seismic events recorded by the seismic network of Kirovsk Branch (KB) of "Apatit" JSC for 2002–2022. Currently, the network consists of 60 3-component seismic sensors located at the Kirovsk and Rasvumchorr mines with a sampling rate of 1000 Hz (Figure 1). The network determines the hypocenters of seismic events with energy $E \geq 10^3$ J with an accuracy of up to 25 m in the area of increased accuracy and up to 100 m in the area of confident registration [*Korchak et al.*, 2014]. The magnitude of the completeness $M_c = 0$. The epicenters of earthquakes with $M \geq 1.5$ are shown in Figure 2.

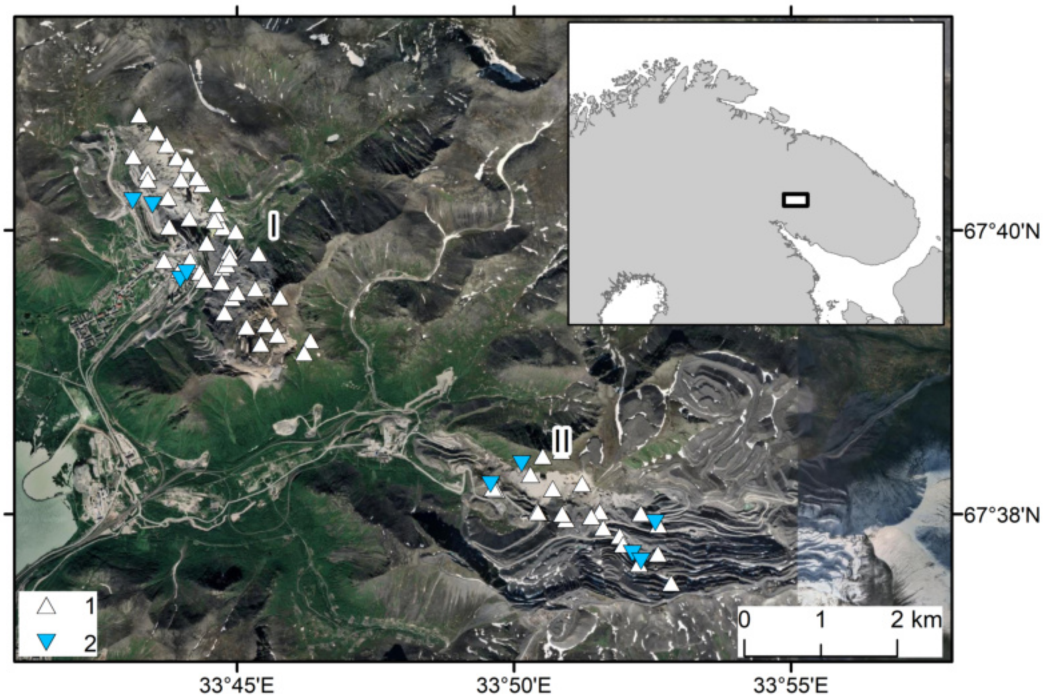

Figure 1. Location of seismic sensors (1) and water inflow measurement points (2). Roman numerals show the territories of the Kirov (I) and Rasvumchorr (II) mines. The rectangle on the insert indicates the location of the area under study.

Data on water inflows at the fields of the Khibiny massif for 2002–2022 were provided by the geological service of the KB "Apatit" JSC. Measurements of water inflow are carried out at underground mines once a day in water collectors located on production levels. Measurements of the volume of water channels at the Central quarry are carried out in ore passes in special dewatering grooves twice a day. The location of the water inflow measurement points is shown in the Figure 1. The depths at which water inflows are measured (Table 1) are comparable to the depths of earthquakes (the average depth of representative seismic events is about −450 m, 95% of them occur at depths from −725 to −100 m).

For the purposes of this article, watering refers to the total water inflow to the mine horizons where measurements are made. This characteristic is actually equivalent to infiltration, which characterizes the amount of water that penetrates into the massif.

The study area (Figures 1, 2) is in the basin of the Bolshoy Vudyavr lake in the highest and well-drained southwestern part of the massif, characterized by high runoff values, unstable seasonal changes in water outflows, as well as mutually close location of water sources, such as the Yuksporyok and Vudyavryok river systems and their tributaries. Fault zones filled with oxidized and crushed rocks have the highest degree of water saturation, their width varies from 2 to 30 meters. Groundwater is replenished by precipitation [*Gimmelfarb et al.*, 1965]. Thus, long-term series of observations of seismicity and water inflows, as well as the unstable and zonal nature of water inflow in the study area, allow us to study the impact of watering of the rock on post-seismic activity.

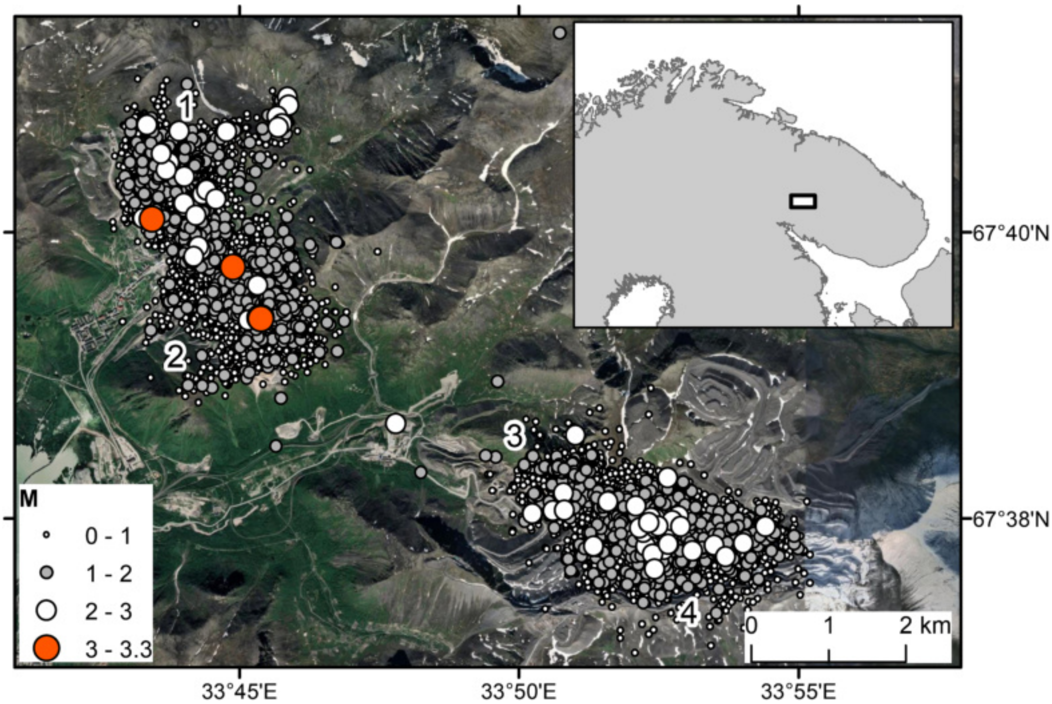

Figure 2. Epicenters of seismic events with $M \geq 1.5$ recorded in the fields of the Khibiny massif during 2002–2022. The figures indicate the following deposits: 1 – Mt. Kukisvumchorr, 2 – Mt. Yukspor (developed by the Kirov Mine); 3 – Apatitovyi Tsirk (Rasvumchorr Mine); 4 – Mt. Rasvumchorr (until 2014 Central, currently Eastern Mine). The rectangle on the insert indicates the location of the area under study.

Table 1. Coordinates and depths (m) of the points at which water inflows are measured (negative values correspond to depths above the average level of the Baltic Sea, chosen as the reference level)

Latitude	Longitude	Depth (m)
	Kirovsk Mine	
67.6616	33.7349	−320
67.6701	33.7187	−90
67.6696	33.7247	−170
67.6609	33.7330	−170
67.6616	33.7349	−252
	Rasvumchorr Mine	
67.6368	33.8263	−310
67.6392	33.8357	−425
67.6323	33.8759	−530
67.6287	33.8690	−430
67.6278	33.8716	−430

Methods

Triggering and triggered events were identified using the nearest neighbor method [*Zaliapin and Ben-Zion*, 2016]. The method is based on application of a proximity function for the space, time, and magnitude [*Baiesi and Paczuski*, 2004]

$$\eta_{ij} = \begin{cases} t_{ij}(r_{ij})^{d_f} 10^{-bm_i}, & t_{ij} > 0, \\ +\infty, & t_{ij} \leq 0, \end{cases} \tag{1}$$

where $t_{ij} = t_j - t_i$ is the time between events, which is positive if the event j occurs after the event i and negative otherwise; $r_{ij} \geq 0$ is the spatial distance between the hypocenters of the events; m_i is the magnitude of the ith event; b is the parameter of the Gutenberg – Richter law [*Gutenberg and Richter*, 1944]; d_f is the fractal dimension of the hypocenter distribution.

For each event in the catalog, its trigger is determined by the minimum value of the proximity function (1), calculated from all previous events relative to the one considered. If this value is less than the specified threshold η_0, then the event in question is considered to have been triggered by a trigger event at which the minimum of the function (1) is reached. Otherwise, the link is broken, and it turns out that the event is background (does not have a trigger). A trigger event can trigger multiple events, while any event can only be triggered by a single trigger.

The η_0 threshold can be determined in a variety of ways (for more details, see [*Bayliss et al.*, 2019; *Shebalin et al.*, 2020; *Zaliapin and Ben-Zion*, 2016]), developed to decluster catalogs of tectonic earthquakes. Here we used the model-independent method [*Shebalin et al.*, 2020] since it is preferable in the case of mining-induced seismicity.

The nearest neighbor method, unlike, for example, the method of *Molchan and Dmitrieva* [1992], does not impose any restrictions on the temporal behavior of triggered shocks (conformance to the Omori – Utsu law). *Pisarenko and Rodkin* [2019] demonstrated that efficiency of the nearest neighbor method for catalog declustering is higher than that of window methods.

The application of the nearest neighbor method to the conditions of mining-induced seismicity of the Khibiny massif is considered in detail in the paper [*Baranov et al.*, 2020], where the following estimates of the seismic regime parameters were obtained: $b = 1.25$, $d_f = 1.5$; threshold estimate $\lg \eta_0 = -6.25$. Using these estimates, for each earthquake with a magnitude $M \geq 1.5$ we will find events triggered by it. The triggered events found in this way represents the post-seismic activity of the area under study.

In order to assess the parameters of post-seismic activity, we will use the approach of [*Baranov and Shebalin*, 2019; *Shebalin and Narteau*, 2017] and stack the triggered events, replacing the magnitudes with the differences $M_\mathrm{a} = M - M_\mathrm{m}$ (M is the magnitude of the triggered event, M_m is the magnitude of its trigger), and arrange events in ascending order of time after the main shock. The use of relative magnitudes M_a brings the triggered events to a comparable form with respect to their triggers.

The use of the stack of triggered events to estimate the parameters of post-seismic activity is more correct compared to averaging the estimates obtained for individual series (this approach was used by *Reasenberg and Jones* [1989], since the distributions of parameters are generally asymmetrical. In addition, the parameters p and c of the Omori – Utsu law are correlated. For example, during fracturing along the formed fault, the relaxation parameter p increases with the increase of axial stresses; the delay in the onset of power-law decay (the parameter c in the Omori – Utsu law) decreases with an increase in axial stresses and increases with an increase in comprehensive compression pressure [*Smirnov et al.*, 2019]. In addition, a number of laboratory and field studies revealed a correlation between the Omori – Utsu and Gutenberg – Richter parameters, indicating implementation of various relaxation mechanisms [*Sharma et al.*, 2023; *Smirnov et al.*, 2019, 2020].

Estimation of the parameter b of the Gutenberg – Richter law using relative magnitudes from the stack has the advantage that the value is estimated for all the series in the range of large magnitudes, which minimizes the influence of the possible inflection of the repeatability graph that occurs due to possible post-seismic plastic deformations at the earthquake source [*Vorobieva et al.*, 2016].

The parameters of post-seismic activity were estimated based on a set of initiated events at the time interval [$t_\mathrm{start} = 0.005$, $t_\mathrm{stop} = 30$] days. The delay after the moment of the trigger event (t_start) is necessary to eliminate the distortion of parameter estimates due to the deficit of weak aftershocks at the beginning of the series [*Holschneider et al.*, 2012; *Narteau et al.*, 2009; *Smirnov et al.*, 2010]. The value $t_{stop} = 30$ days was chosen because during this time the dependence of the total number of triggered events on time (cumulative curve) has a regular form and is well described by the Omori – Utsu law.

The magnitudes of earthquakes follow the Gutenberg – Richter [*Gutenberg and Richter*, 1944] distribution:

$$P(M_a < m) = F(m) = 1 - 10^{-b_a m}.$$

Hereinafter, the notation $b = b_a$ is used to denote the parameter b of the magnitude distribution of triggered events from the stack. The estimation was performed using the maximum likelihood method according to the Aki's formula adapted for discrete magnitudes [*Marzocchi and Sandri*, 2009]:

$$b_a = \frac{\lg_{10} e}{E[M_a] - M_{ca} + \frac{\Delta M}{2}}.$$

Here $M_{ca} = -1.5$ is the magnitude of completeness for the stack of triggered events; $E[M_a]$ is the average sampling magnitude at $M_a \geq M_{ca}$; ΔM is the binning magnitude width of the catalog.

The distribution of estimation error of b-value and its standard deviation σ were calculated using the bootstrap method. The evaluation of the parameter b_a for the stack of triggered events is provided in Figure 3; the resulting b-value $b_a \pm \sigma = 1.21 \pm 0.048$.

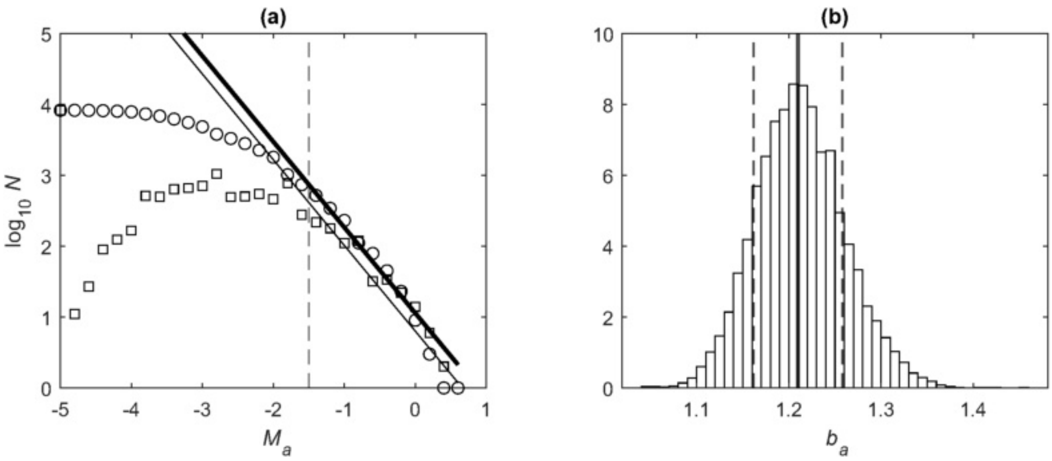

Figure 3. Estimate of b_a-value of the Gutenberg – Richter law for the stack of triggered events. (a) Cumulative (bold line) and differential (thin line) magnitude–frequency curves for the $M_a = M - M_m$; circles denote cumulative values, squares – differential ones; dashed line denotes the level of representative relative magnitude. (b) Probability density of the error; solid vertical line denotes estimation of $b_a = 1.21$; dashed vertical lines are values $b_a \pm \sigma = 1.21 \pm 0.048$ (σ is standard error).

The time decay of post-seismic activity is described by the Omori – Utsu law [*Utsu et al.*, 1995]:

$$n(t) = \frac{K}{(t+c)^p}, \tag{2}$$

where t is the time after the main shock; $n(t)$ is the rate of triggered events (the number of events per unit of time); c is the time delay of power-law decay rate of the triggered events; p is the relaxation parameter, the higher the p, the faster the triggered events decay in time; K is the productivity parameter of the stack (not to be mistaken with the parameter of the law of earthquake productivity). [*Shebalin and Narteau*, 2017] using the data on seismicity in California showed that the value $-\log(c)$ approximates the difference between the maximum and minimum stresses.

The parameters of the Omori – Utsu law were estimated using the Bayes method [*Holschneider et al.*, 2012] in the time interval $t_{start} = 0.005$ to $t_{stop} = 30$ days with uniform prior distribution of parameters c in the interval $[t_{\text{start}}2,\ 2t_{\text{stop}}]$ and p in the interval $[0.5, 2.5]$. Figure 4 demonstrates posterior distributions of the K, c, and p estimates, as well as the empirical and theoretical distribution of the times of the triggered events from the stack. The resulting values given the 95% confidence interval are: $c = 0.012(0.006, 0.018)$, $p = 1.27(1.209, 1.332)$, $K = 74.9(69.97, 79.95)$. The proximity of theoretical and empirical cumulative curves of the aftershock number (Figure 4b) indicates that post-seismic activity in the area under study obeys the Omori – Utsu law. To measure the error of estimating the parameters of the Omori – Utsu law, we use 95% confidence intervals instead of the standard error, since the posterior distribution of Bayesian estimates of parameters is generally asymmetrical.

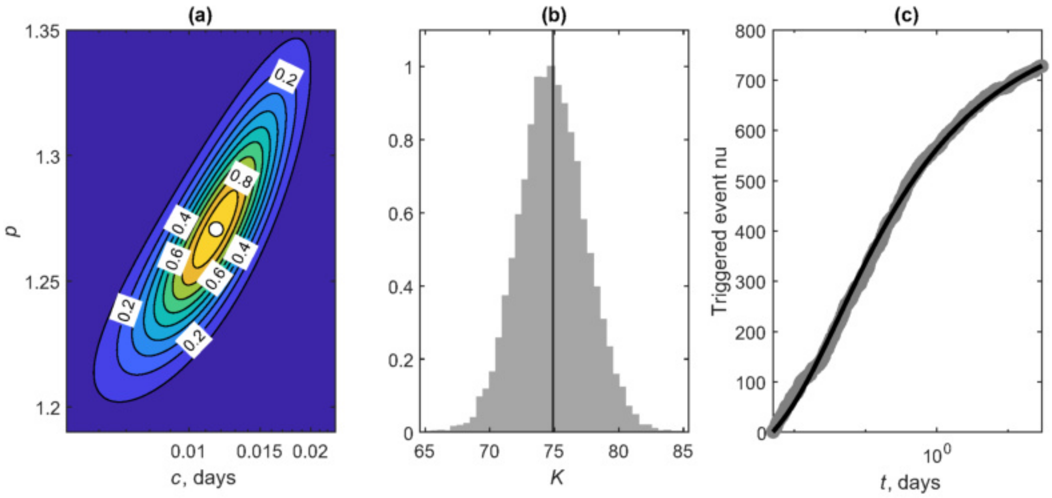

Figure 4. Estimation of the parameters of the Omori – Utsu law for the stack of triggered events. (a) Posterior probabilities of the joint distribution of estimated parameters c and p, white circle denotes the maximum likelihood. (b) Posterior probabilities of the K estimate (gray rectangles), vertical line denotes the maximum likelihood. (c) Distribution of the times of triggered events, gray line denotes the empirical distribution within the triggered aftershock stack, the black line denotes the distribution according to the Omori – Utsu law with estimated values: $c = 0.012(0.006, 0.018)$, $p = 1.27(1.209, 1.332)$, $K = 74.9(69.97, 79.95)$, 95% confidence interval is indicated in the parentheses.

For induced seismicity, estimates of p-value are usually believed to be from 0.5 to 0.8 [*Gupta*, 2002; *Mekkawi*, 2004; *Rastogi et al.*, 1997]. Here we obtained a significantly larger value of $p = 1.27(1.209, 1.332)$. It is possible that the reason for this discrepancy is in geological conditions. The cited papers studied post-seismic activity in reservoir areas in India and Egypt. Here we are considering post-seismic activity that occurs during mining in a tectonically loaded crystalline rock mass (Khibiny Mountains), tectonic (horizontal) stresses significantly exceed gravitational (vertical) ones.

To demonstrate the influence of watering of the rock on the parameters of post-seismic activity, we estimated the monthly variations of the the b_{a} of the Gutenberg – Richter distribution and the K, c, and p of the Omori – Utsu law. By comparing the parameter estimates with the average monthly values of water inflow, we will be able to conclude whether the watering of the rock affects the post-seismic activity.

Results

The period of increased watering in the study area (water inflow above the average value) occurs in May to October (Figure 5a), while from November to April low watering is observed. The increase in watering in May and June is caused by the intense melting of the snow accumulated during the winter. From July to October, the elevated watering of the massif is maintained due to atmospheric precipitation. Approximately from the second half of October, the air temperature in the Khibiny becomes negative and the watering of the massif starts to decrease.

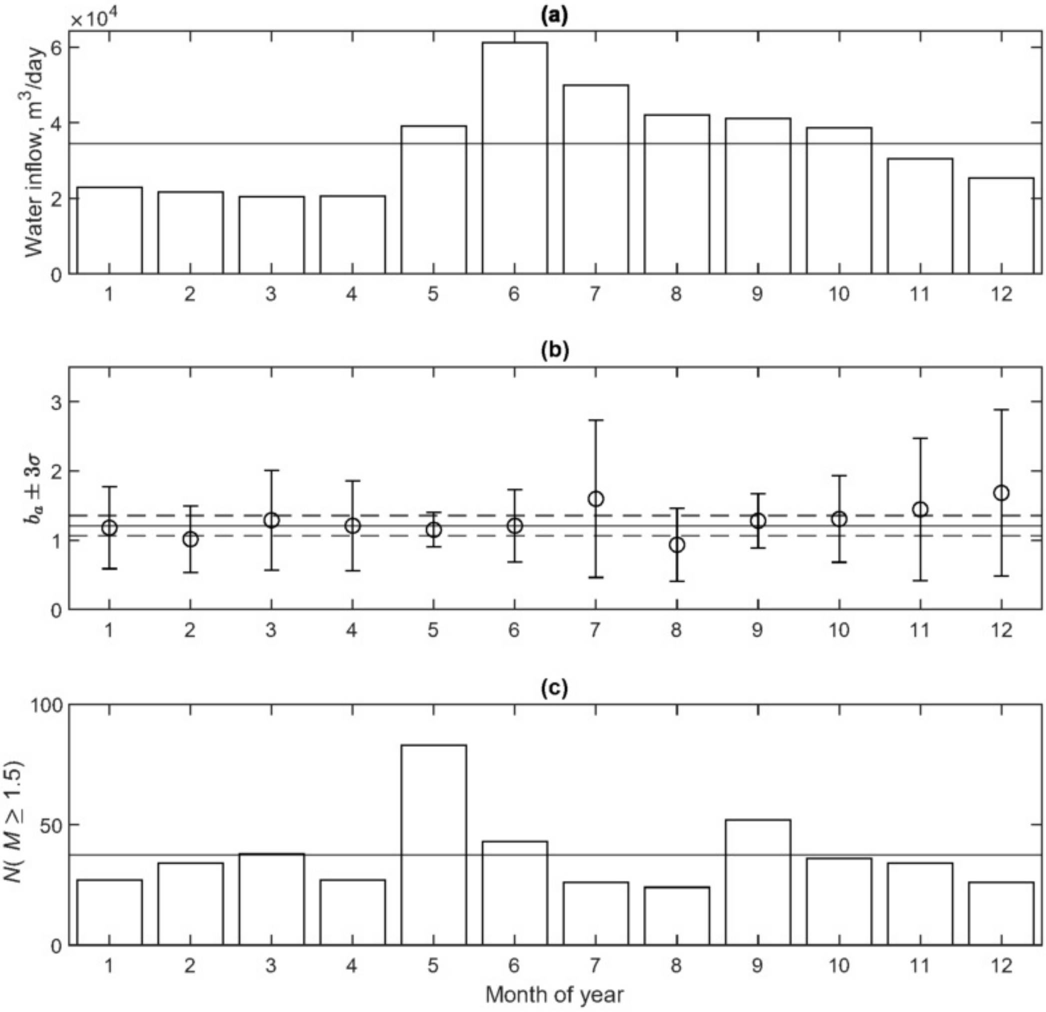

Figure 5. Monthly average variation in the rock watering level and b_a-values for the stack of triggered events at the fields of the Khibiny massif. (a) The average water inflow (m^3/day), the horizontal line denotes the average value; (b) The $b_a \pm 3\sigma$ (the error bars denote triple standard errors σ), horizontal line denotes the b_a, estimated from all the data, dashed lines are $b_a \pm 3\sigma$; (c) The number of earthquakes with $M \geq 1.5$ considered as triggers, horizontal line denotes the monthly average value (37.5).

Comparing seasonal variations in the water inflow level (Figure 5a) and the values of the b_a of the Gutenberg – Richter distribution (Figure 5b) estimated based on the stack of triggered events, we can state that the observed fluctuations of b_a are less than the estimation errors. Thus, we cannot state that the influence of watering of the rock on the distribution of the relative magnitudes of the triggered events ($M_a = M - M_m$) is significant. At the same time, there is a significant increase in the number of earthquakes with a magnitude $M \geq 1.5$ in May (2.2 times higher compared to the annual average value of 37.5), when the increase in watering (Figure 5c) associated with melting of snow accumulated through the winter occurs.

Let us consider the influence of the rock watering on the parameters K, c, and p of the Omori – Utsu law, determining decay of post-seismic activity over time (Figure 6). Estimates of the K-value of the Omori – Utsu law (2) (Figure 6a) show a significant increase in May, when the melting of snow accumulated over the winter causes an increase in watering of the rock. In June, the value of K decreases, but still lingers above the average annual value.

Then the value of K decreases below the annual average and then significantly increases in September. From October until January K is lower, and from November until April it does not exceed the annual average. This means that during the period of low watering of the rock from October until April the values of the parameter K do not exceed the average annual value.

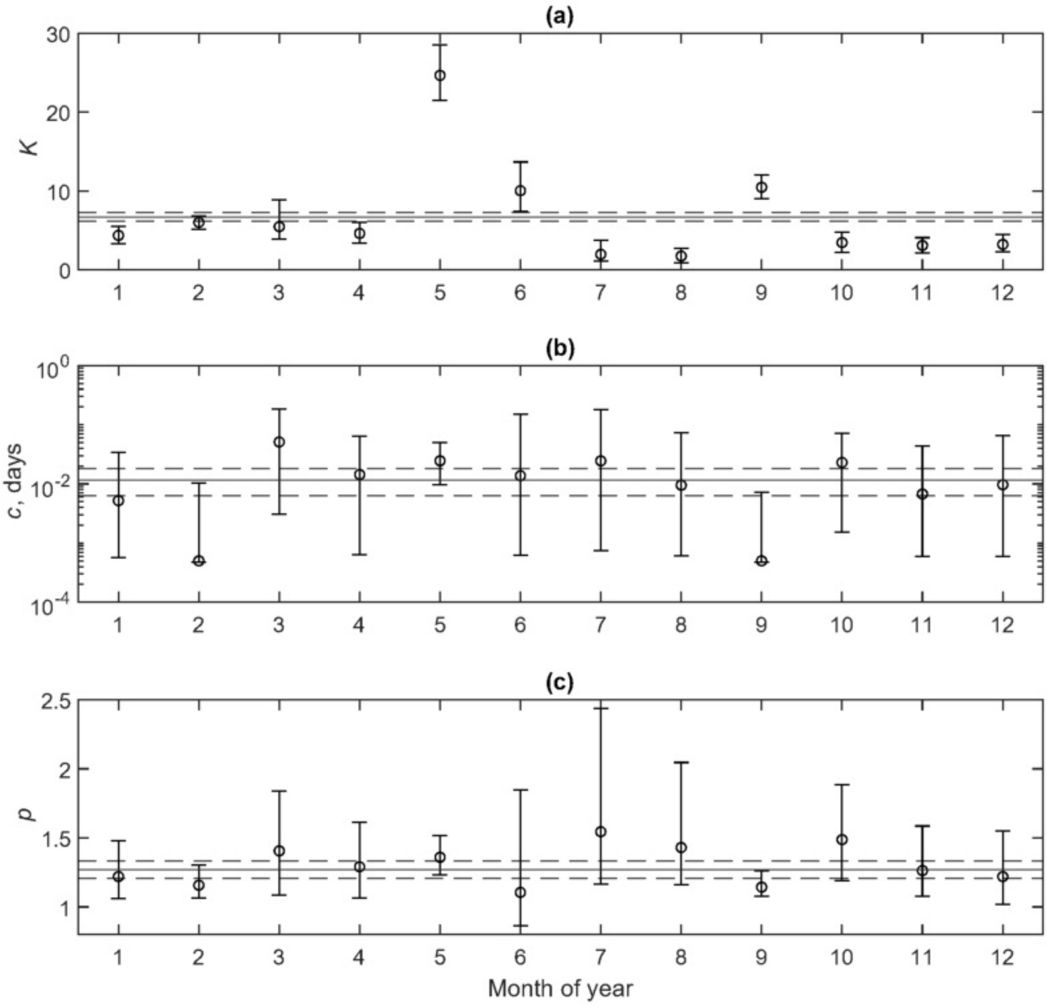

Figure 6. Estimates of the parameters of the Omori – Utsu law (error bars are the 95% confidence intervals) for triggered events at the Khibiny massif calculated by months of the year. (a) The K-values, horizontal line denotes the annual average K, dashed lines are limits of the 95% confidence interval. (b) The c-values, horizontal line denotes the c estimated using all the data, dashed lines are limits of the 95% confidence interval. (c) The p-value, horizontal line denotes the p estimated using all the data, dashed lines are limits of the 95% confidence interval.

The highest deviation of the estimates of c (Figure 6b) and p (Figure 6c) from the values obtained using all the data occur in June, when the maximum value of water inflow is observed (Figure 5a). However, these deviations do not exceed the estimation errors. In the remaining months, the variations in the estimates of these parameters are also within the 95% confidence intervals, so we cannot consider them significant. Thus, there is no significant dependence of the relaxation rate (p) and the delay in the onset of power-law decay (c) on the watering of the rock.

Discussions

Using the data of long-term monitoring of seismicity and observations of water inflows in the fields of the Khibiny massif, it was revealed that the values of the parameter b_a of the distribution of magnitudes of triggered events ($M_a = M - M_m$) virtually do not change in different periods of watering of the massif. In [*Zhukova et al.*, 2023] it was demonstrated that the influence of watering on the b-value of the distribution of magnitudes of all seismic events is significant (Figure 7). The b significantly decreases in May (the beginning of high watering period) and maintains its lowered value virtually throughout the entire high-watering period until the end of September.

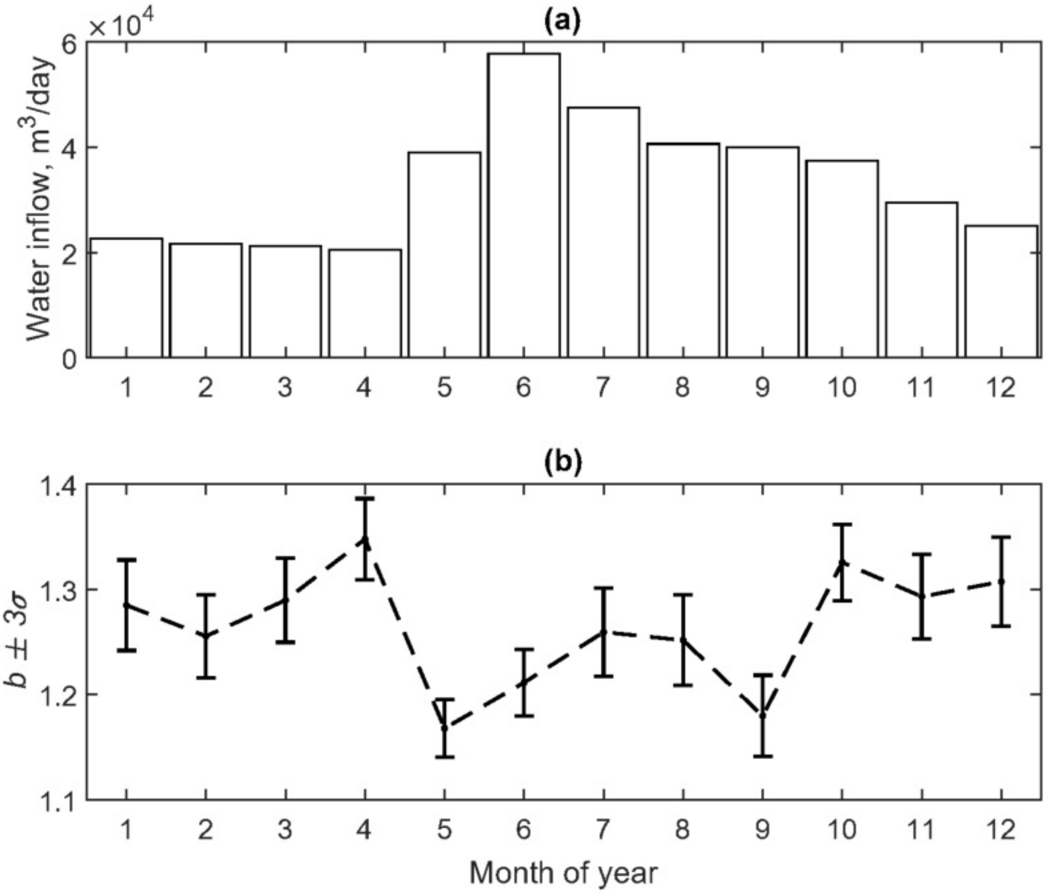

Figure 7. Monthly variations in watering and the b-value for all earthquake with $M \geq 0$ at the deposits of the Khibiny massif for 2002–2020 [*Zhukova et al.*, 2023]. (a) Average water inflow m^3/day; (b) b-values (error bars denote the values of a triple standard error 3σ).

The decrease in the b-value is illustrated even more clearly by the estimates obtained for the periods of high (May–October) and low (November–April) periods of watering of the geologic material. For the period of high watering, $b \pm 3\sigma = 1.30 \pm 0.017$ (σ is standard error); for the period of low watering, $b \pm 3\sigma = 1.22 \pm 0.014$ [*Zhukova et al.*, 2023]. These estimates are separated from each other by more than 3σ, which indicates the significance of the differences.

Despite the fact that the watering of the rock affects the distribution of the magnitudes of all seismic events, the influence of this factor on the distribution of the relative magnitudes of the triggered events ($M_a = M - M_m$) is not observed. Since b-value determines the ratio of weak and strong earthquakes, the proportion between the weak and strong events in the relative magnitudes M_a is maintained in the area under study. This allows to obtain the estimate of the parameter b_a for all the data regardless of the level of watering of the rock environment. This estimate is necessary during the assessment of post-seismic danger, for example, during the calculation of the parameters of the dynamic Bath's law [*Baranov et al.*, 2022; *Motorin and Baranov*, 2022].

As it was noted in the Introduction section, the physical mechanism of emergence of post-seismic activity is described by the *Dieterich* [1994] rate-and-state model, the key point of which is the dependence of the friction coefficient on the slip speed and the state of the fault. An increase in the moisture content of the medium directly affects the state of the fault, decreasing the friction coefficient and increasing the pore pressure. Below, we will try to explain the behavior of the parameters of the Omori – Utsu law using this model. At the same time, we are aware of the limitations of this explanation, since from rate-and-state model it follows that that the relaxation parameter $p = 1$ [*Dieterich*, 1994]. In our case, the estimates of p in most of the cases are greater than 1 (Figure 4a, Figure 6c). Moreover, according to the field [*Sharma et al.*, 2023; *Smirnov and Ponomarev*, 2020] and laboratory [*Smirnov et al.*, 2019] data, a correlation is found between the parameters of the Omori – Utsu law and changes in stresses, indicating the limitations of the model.

Assuming that the rate of tectonic deformation is the same before and after the trigger earthquake and is not equal to zero, the parameters K and c of the Omori – Utsu law using the rate- and state-dependent friction model are estimated as the following [*Cocco et al.*, 2010]

$$K = \frac{r t_a}{1 - \exp\left(-\frac{S}{A\sigma}\right)}, \tag{3}$$

$$c = \frac{t_a \exp\left(-\frac{S}{A\sigma}\right)}{1 - \exp\left(-\frac{S}{A\sigma}\right)}, \tag{4}$$

where r is the rate of background seismicity; t_a is the relaxation time, determining the duration of the aftershock series; S is the change in the Coulomb stresses due to the main shock; $A\sigma$ is the constitutive parameter of the rate- and state-dependent law governing fault friction.

According to the formula (3), productivity K depends on the stress jump, rate of background seismicity, and the value of $A\sigma$. Meanwhile, the parameters r, $A\sigma$ and t_a are strongly correlated [*Cocco et al.*, 2010]. It is difficult to understand how the increase in watering affects the K and c of the Omori – Utsu law using the equations (3) and (4) directly, because the different values $r, A\sigma$ and t_a can result in the same values of K and c. However, if it is reasonable to assume that $S \gg A\sigma$ [*Cocco et al.*, 2010], then the denominator in the formula (3) is approximately equal to 1. Then $K \sim r t_a$. It means that, as the rate of background seismicity (r) and/or relaxation time (t_a) grows, the value of K also increases.

Miller [2020] demonstrated by numerical simulation that the relaxation time has to grow with an increase in watering. A growth in the background seismicity rate during the increase in watering of the rock at the fields of Khibiny massif was also demonstrated in [*Zhukova et al.*, 2023], an illustration is provided in Figure 8. Thus, the observed increase in the parameter K of the Omori – Utsu law with an increase in the watering of the rock in May and June is explained by the rate- and state-dependent model and caused by the growth in background seismicity and relaxation time.

The behavior of the c-value of the Omori – Utsu law, characterizing the delay in the onset of power-law decay of post-seismic activity, does not depend on the level of watering of the rock (Figure 6b). According to (4), c-value depends on the Coulomb stresses jump, relaxation time and the $A\sigma$. During the increase in the rock watering, the $A\sigma$ should decrease due to the growth of the pore pressure and reduction of friction. It would be difficult to unequivocally assume what would the change in the Coulomb stresses S be in this case ($S = \Delta\tau - \mu\Delta\sigma$, $\Delta\tau(\Delta\sigma)$ is the change in the shear (effective normal) stress, μ is the effective friction coefficient). *Miller* [2020] demonstrated that t_a should increase with the increase in watering. It means that theoretically the value of c can both decrease and increase. If we assume that $S \gg A\sigma$ then we will obtain that c is positive and near 0 as it is demonstrated in the Figure 6b.

A similar interpretation of the c-value behavior can be drawn based on the paper by *Shebalin and Narteau* [2017], there they showed that $c \approx \exp[-(\sigma_1 - \sigma_3)]$ for $p = 1$ ($\sigma_1 - \sigma_3$) is the difference between the maximum and minimum stresses). In the Khibiny massif, tectonic (horizontal) stresses at the depths ranging from −600 to −90 m are 40–60 MPa and exceed gravitational (normal) stresses fivefold, and in some cases more than by an order

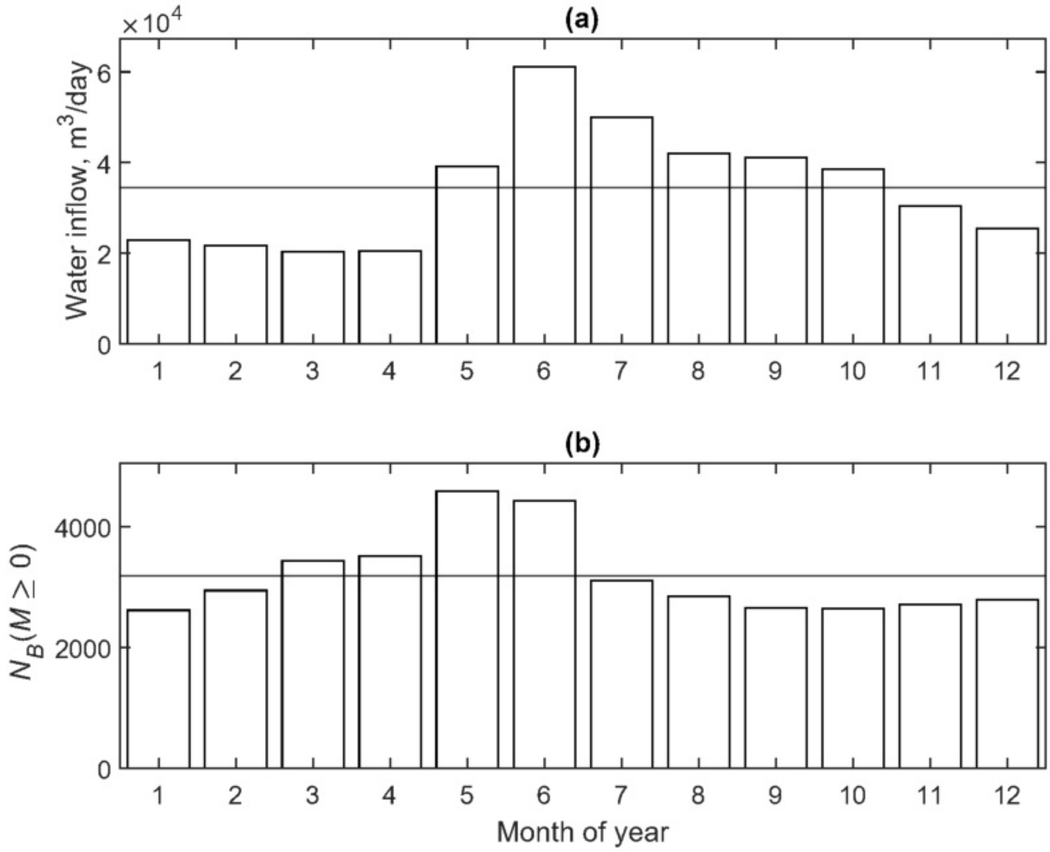

Figure 8. Monthly average variations in the level of watering of the rock environment and the total number of representative background events. (a) Average watering (m^3/day), the horizontal line represents the average value; (b) The number of background earthquakes with $M \geq 0$, the horizontal line is the average value (3188).

of magnitude [*Onokhin*, 1975; *Rebetskiy*, 2007]. (Average depth of representative seismic events in the research area is about −450 m, 95% of them occur at depths from −725 to −100 m.) This means that the c-value should be positive and close to 0. We should note that there is no reason to expand the independence of the c-value on the watering level to all the cases. It is possible that for the other values of stress differences the behavior of this parameter would be different.

We cannot apply similar reasoning to explain the behavior of the p-value of the Omori – Utsu law, characterizing the time decay of post-seismic activity, as the rate-and-state model predicts this law for $p = 1$. And in the Khibiny massif, the p-value in most of the cases is significantly higher than 1 (Figure 4a, Figure 6c).

Miller [2020] using a simple model of crustal permeability, has numerically demonstrated that the decay rate of aftershocks reflects the ability of area tectonics to re-seal cracks resulting from a trigger and triggered earthquakes. Re-sealing of the crack over time reduces the subsequent flow of fluid and therefore the formation of aftershocks. Thus, approximately the same values of p in different periods of watering of the Khibiny massif indicate that the tectonics of the Khibiny are able to quickly re-seal cracks due to earthquakes. (This property is determined by the specifics of tectonics and does not depend on the level of rock watering.) This is also supported by the high level of tectonic stresses in the massif, reaching values of 40–60 MPa at the depths of −600 to −90 m.

In conclusion, we note that the influence of the rock watering on the time decay parameters of post-seismic activity is a complex process with various relaxation mechanisms. The rate and state friction model qualitatively explains only some of the revealed effects. At the same time, the identification of patterns of the influence of watering on post-seismic activity based on field and laboratory data will allow us to obtain a universal model of post-seismic activity and broaden scientific knowledge of transient regimes of seismicity.

Acknowledgements. The study was funded by the Russian Science Foundation (project No. 22-27-20125).

References

Arzamastsev, A. A., L. V. Arzamastseva, A. M. Zhirova, and V. N. Glaznev (2013), Model of formation of the Khibiny-Lovozero ore-bearing volcanic-plutonic complex, *Geology of Ore Deposits*, *55*(5), 341–356, https://doi.org/10.1134/S1075701513050024.

Baiesi, M., and M. Paczuski (2004), Scale-free networks of earthquakes and aftershocks, *Physical Review E*, *69*(6), 066,106, https://doi.org/10.1103/PhysRevE.69.066106.

Baranov, S., C. Narteau, and P. Shebalin (2022), Modeling and Prediction of Aftershock Activity, *Surveys in Geophysics*, *43*(2), 437–481, https://doi.org/10.1007/s10712-022-09698-0.

Baranov, S. V., and P. N. Shebalin (2019), Global Statistics of Aftershocks Following Large Earthquakes: Independence of Times and Magnitudes, *Journal of Volcanology and Seismology*, *13*(2), 124–130, https://doi.org/10.1134/S0742046319020027.

Baranov, S. V., S. A. Zhukova, P. A. Korchak, and P. N. Shebalin (2020), Productivity of Mining-Induced Seismicity, *Izvestiya, Physics of the Solid Earth*, *56*(3), 326–336, https://doi.org/10.1134/S1069351320030015.

Batugin, A. S. (2006), On the Mechanism of Earthquakes of 25.04.97 and 27.04.97 in the North of Kuzbass, *Gornaya Kniga, Gorny'j informacionno-analiticheskij byulleten'*, *11*, 185–189 (in Russian).

Bayliss, K., M. Naylor, and I. G. Main (2019), Probabilistic identification of earthquake clusters using rescaled nearest neighbour distance networks, *Geophysical Journal International*, *217*(1), 487–503, https://doi.org/10.1093/gji/ggz034.

Bell, M. L., and A. Nur (1978), Strength changes due to reservoir-induced pore pressure and stresses and application to Lake Oroville, *Journal of Geophysical Research: Solid Earth*, *83*(B9), 4469–4483, https://doi.org/10.1029/JB083iB09p04469.

Board, M., T. Rorke, G. Williams, and N. Gay (1992), Fluid injection for rockburst control in deep mining, in *33rd U.S. Rock Mechanics/Geomechanics Symposium*, pp. 111–120, A. A. Balkema, Rotterdam.

Cocco, M., S. Hainzl, F. Catalli, B. Enescu, A. M. Lombardi, and J. Woessner (2010), Sensitivity study of forecasted aftershock seismicity based on Coulomb stress calculation and rate- and state-dependent frictional response, *Journal of Geophysical Research: Solid Earth*, *115*(B5), https://doi.org/10.1029/2009jb006838.

Dieterich, J. (1994), A constitutive law for rate of earthquake production and its application to earthquake clustering, *Journal of Geophysical Research: Solid Earth*, *99*(B2), 2601–2618, https://doi.org/10.1029/93JB02581.

Dieterich, J. H. (2007), Applications of Rate- and State-Dependent Friction to Models of Fault-Slip and Earthquake Occurrence, in *Treatise on Geophysics (Second Edition)*, edited by G. Schubert, second edition ed., pp. 93–110, Elsevier, Oxford, https://doi.org/10.1016/B978-0-444-53802-4.00075-0.

Gimmelfarb, B. M., G. M. Virovlyansky, and A. A. Shugin (Eds.) (1965), *Proceedings of the State Research Institute of Mining Chemical Raw Materials, issue 10. Khibiny Apatite Deposits. Issues of Structure, Hydrogeology and Exploration Methods*, 315 pp., Nedra (in Russian).

Gupta, H. K. (2002), A review of recent studies of triggered earthquakes by artificial water reservoirs with special emphasis on earthquakes in Koyna, India, *Earth-Science Reviews*, *58*(3–4), 279–310, https://doi.org/10.1016/S0012-8252(02)00063-6.

Gutenberg, B., and C. F. Richter (1944), Frequency of Earthquakes in California, *Bulletin of the Seismological Society of America*, *34*, 185–188.

Hainzl, S., T. Kraft, J. Wassermann, H. Igel, and E. Schmedes (2006), Evidence for rainfall-triggered earthquake activity, *Geophysical Research Letters*, *33*(19), https://doi.org/10.1029/2006GL027642.

Hainzl, S., Y. Ben-Zion, C. Cattania, and J. Wassermann (2013), Testing atmospheric and tidal earthquake triggering at Mt. Hochstaufen, Germany, *Journal of Geophysical Research: Solid Earth*, *118*(10), 5442–5452, https://doi.org/10.1002/jgrb.50387.

Heinicke, J., H. Woith, C. Alexandrakis, S. Buske, and L. Telesca (2017), Can hydroseismicity explain recurring earthquake swarms in NW-Bohemia?, *Geophysical Journal International*, *212*(1), 211–228, https://doi.org/10.1093/gji/ggx412.

Holschneider, M., C. Narteau, P. Shebalin, Z. Peng, and D. Schorlemmer (2012), Bayesian analysis of the modified Omori law, *Journal of Geophysical Research: Solid Earth*, *117*(B6), https://doi.org/10.1029/2011JB009054.

Kartseva, T. I., V. B. Smirnov, A. V. Patonin, D. S. Sergeev, N. M. Shikhova, A. V. Ponomarev, S. M. Stroganova, and V. O. Mikhailov (2022), Initiation of Rock Fracture by Fluids of Different Viscosities, *Izvestiya, Physics of the Solid Earth*, *58*(4), 576–590, https://doi.org/10.1134/S106935132204005X.

Korchak, P. A., S. A. Zhukova, and P. Y. Menshikov (2014), Formation and Development of the System of Monitoring Seismic Processes in the Zone of Production Activities of JSC Apatit, *Gornyi Zhurnal*, pp. 42–46 (in Russian).

Kozyrev, A. A., S. A. Zhukova, and A. S. Batugin (2021), Influence of water content on seismic activity of rocks mass in apatite mining in Khibiny, *Gornyi Zhurnal*, (1), 31–36, https://doi.org/10.17580/gzh.2021.01.06.

Kozyrev, A. A., I. E. Semenova, S. A. Zhukova, and O. G. Zhuravleva (2022), Factors of seismic behavior change and localization of hazardous zones under a large-scale mining-induced impact, *Russian Mining Industry*, (6), 95–102, https://doi.org/10.30686/1609-9192-2022-6-95-102.

Kremenetskaya, E. O., and V. M. Trjapitsin (1995), Induced seismicity in the Khibiny Massif (Kola Peninsula), *Pure and Applied Geophysics PAGEOPH*, *145*(1), 29–37, https://doi.org/10.1007/BF00879481.

Lazarevich, T. I., V. P. Mazikin, I. A. Malyi, V. A. Kovalev, A. N. Polyakov, A. S. Kharkevich, and A. N. Shabarov (2006), *Geodynamic Zoning of Southern Kuzbass*, 181 pp., Kemerovo (in Russian).

Manga, M., and C.-Y. Wang (2015), Earthquake Hydrology, in *Treatise on Geophysics, 2nd edition*, vol. 4, edited by G. Schubert, chap. 4.12, pp. 305–328, Elsevier, Oxford.

Marzocchi, W., and L. Sandri (2009), A review and new insights on the estimation of the b-valueand its uncertainty, *Annals of Geophysics*, *46*(6), https://doi.org/10.4401/ag-3472.

Maystrenko, Y. P., M. Brönner, O. Olesen, T. M. Saloranta, and T. Slagstad (2020), Atmospheric Precipitation and Anomalous Upper Mantle in Relation to Intraplate Seismicity in Norway, *Tectonics*, *39*(9), https://doi.org/10.1029/2020TC006070.

Mekkawi, M. (2004), A Long-Lasting Relaxation of Seismicity at Aswan Reservoir, Egypt, 1982-2001, *Bulletin of the Seismological Society of America*, *94*(2), 479–492, https://doi.org/10.1785/0120030067.

Miller, S. A. (2020), Aftershocks are fluid-driven and decay rates controlled by permeability dynamics, *Nature Communications*, *11*(1), https://doi.org/10.1038/s41467-020-19590-3.

Molchan, G. M., and O. E. Dmitrieva (1992), Aftershock identification: methods and new approaches, *Geophysical Journal International*, *109*(3), 501–516, https://doi.org/10.1111/j.1365-246x.1992.tb00113.x.

Motorin, A., and S. Baranov (2022), Distribution of strongest aftershock magnitudes in mining-induced seismicity, *Frontiers in Earth Science*, *10*, https://doi.org/10.3389/feart.2022.902812.

Narteau, C., S. Byrdina, P. Shebalin, and D. Schorlemmer (2009), Common dependence on stress for the two fundamental laws of statistical seismology, *Nature*, *462*(7273), 642–645, https://doi.org/10.1038/nature08553.

Nikolaev, N. I. (1988), *Newest Tectonics and Geodynamics of the Lithosphere*, 491 pp., Nedra, Moscow (in Russian).

Onokhin, F. M. (1975), *Features of the Structures of the Khibiny Massif and Apatite-Nepheline Deposits*, 105 pp., Nauka, Leningrad (in Russian).

Pisarenko, V. F., and M. V. Rodkin (2019), Declustering of Seismicity Flow: Statistical Analysis, *Izvestiya, Physics of the Solid Earth*, https://doi.org/10.31857/S0002-33372019538-52 (in Russian).

Rastogi, B. K., P. Mandal, and N. Kumar (1997), Seismicity around Dhamni Dam, Maharashtra, India, in *Seismicity Associated with Mines, Reservoirs and Fluid Injections*, pp. 493–509, Birkhäuser Basel, https://doi.org/10.1007/978-3-0348-8814-1_9.

Reasenberg, P. A., and L. M. Jones (1989), Earthquake Hazard After a Mainshock in California, *Science*, *243*(4895), 1173–1176, https://doi.org/10.1126/science.243.4895.1173.

Rebetskiy, Y. L. (2007), *Tectonic Tensions and Strength of Natural Massifs*, 406 pp., IKC "Akademkniga", Moscow (in Russian).

Shabarov, A. N., A. D. Kuranov, and V. A. Kiselev (2021), Assessing the Zones of Tectonic Fault Influence on Dynamic Rock Pressure Manifestation at Khibiny Deposits of Apatite-Nepheline Ores, *Eurasian Mining*, pp. 3–7, https://doi.org/10.17580/em.2021.02.01.

Shapiro, S. A. (2015), *Fluid-Induced Seismicity*, 276 pp., Cambridge University Press.

Sharma, S., S. Hainzl, and G. Zöller (2023), Seismicity Parameters Dependence on Main Shock-Induced Co-seismic Stress, *Geophysical Journal International*, *235*(1), 509–517, https://doi.org/10.1093/gji/ggad201.

Shebalin, P., and C. Narteau (2017), Depth Dependent Stress Revealed by Aftershocks, *Nature Communications*, *8*(1), https://doi.org/10.1038/s41467-017-01446-y.

Shebalin, P. N., C. Narteau, and S. V. Baranov (2020), Earthquake Productivity Law, *Geophysical Journal International*, *222*(2), 1264–1269, https://doi.org/10.1093/gji/ggaa252.

Simpson, D. W. (1986), Triggered Earthquakes, *Annual Review of Earth and Planetary Sciences*, *14*(1), 21–42, https://doi.org/10.1146/annurev.ea.14.050186.000321.

Smirnov, V., A. Ponomarev, P. Bernard, and S. Bourouis (2013), Field Experiment in Soultz-Sous-Forêts, 1993: Changes of the Pattern of Induced Seismicity, *Acta Geophysica*, *61*(6), 1598–1625, https://doi.org/10.2478/s11600-013-0150-0.

Smirnov, V. B., and A. V. Ponomarev (2020), *Physics of Transient Seismicity Regimes*, 412 pp., RAS, Moscow (in Russian).

Smirnov, V. B., A. V. Ponomarev, P. Benard, and A. V. Patonin (2010), Regularities in Transient Modes in the Seismic Process According to the Laboratory and Natural Modeling, *Izvestiya, Physics of the Solid Earth*, *46*(2), 104–135, https://doi.org/10.1134/S1069351310020023.

Smirnov, V. B., A. V. Ponomarev, S. A. Stanchits, M. G. Potanina, A. V. Patonin, G. Dresen, C. Narteau, P. Bernard, and S. M. Stroganova (2019), Laboratory Modeling of Aftershock Sequences: Stress Dependences of the Omori and Gutenberg–Richter Parameters, *Izvestiya, Physics of the Solid Earth*, *55*(1), 124–137, https://doi.org/10.1134/S1069351319010105.

Smirnov, V. B., T. I. Kartseva, A. V. Ponomarev, A. V. Patonin, P. Bernard, V. O. Mikhailov, and M. G. Potanina (2020), On the Relationship between the Omori and Gutenberg–Richter Parameters in Aftershock Sequences, *Izvestiya, Physics of the Solid Earth*, *56*(5), 605–622, https://doi.org/10.1134/S1069351320050110.

Smirnov, V. B., M. G. Potanina, T. I. Kartseva, A. V. Ponomarev, A. V. Patonin, V. O. Mikhailov, and D. S. Sergeev (2022), Seasonal Variations in the b-Value of the Reservoir-Triggered Seismicity in the Koyna–Warna Region, Western India, *Izvestiya, Physics of the Solid Earth*, *58*(3), 364–378, https://doi.org/10.1134/S1069351322030077.

Talwani, P. (1997), On the Nature of Reservoir-induced Seismicity, *Pure and Applied Geophysics*, *150*(3–4), 473–492, https://doi.org/10.1007/s000240050089.

Utsu, T., Y. Ogata, and S. R. Matsu'ura (1995), The Centenary of the Omori Formula for a Decay Law of Aftershock Activity, *Journal of Physics of the Earth*, *43*(1), 1–33, https://doi.org/10.4294/jpe1952.43.1.

Vorobieva, I., P. Shebalin, and C. Narteau (2016), Break of slope in earthquake size distribution and creep rate along the San Andreas Fault system, *Geophysical Research Letters*, *43*(13), 6869–6875, https://doi.org/10.1002/2016GL069636.

Vorobieva, I., P. Shebalin, and C. Narteau (2020), Condition of Occurrence of Large Man-Made Earthquakes in the Zone of Oil Production, Oklahoma, *Izvestiya, Physics of the Solid Earth*, *56*(6), 911–919, https://doi.org/10.1134/S1069351320060130.

Zaliapin, I., and Y. Ben-Zion (2016), A global classification and characterization of earthquake clusters, *Geophysical Journal International*, *207*(1), 608–634, https://doi.org/10.1093/gji/ggw300.

Zhukova, S. (2015), The Relationship of Hydrogeological Situation and Activization of Seismic Activity on Apatite Circus Deposit and Rasvumchorr Deposit, *Mining Informational and Analytical Bulletin (Scientific and Technical Journal)*, pp. 319–329 (in Russian).

Zhukova, S., A. Motorin, and S. Baranov (2023), Influence of Watering of Khibiny Mountains on the Earthquake-Size Distribution, in *Problems of Geocosmos—2022*, pp. 171–182, Springer International Publishing, https://doi.org/10.1007/978-3-031-40728-4_12.

Zoback, M. D., and H.-P. Harjes (1997), Injection-Induced Earthquakes and Crustal Stress at 9 km Depth at the KKTBDeep Drilling Site, Germany, *Journal of Geophysical Research: Solid Earth*, *102*(B8), 18,477–18,491, https://doi.org/10.1029/96JB02814.

Улучшение точности прогноза состояния Мирового океана за счет оптимального расположения измерителей

Н. А. Турко*,[1], А. А. Лобашев[2], К. В. Ушаков[1,3], М. Н. Кауркин[1], Л. Ю. Кальницкий[4], С. В. Семин[5], и Р. А. Ибраев[1,3,6]

[1]Институт океанологии им. П. П. Ширшова РАН, Москва, Россия
[2]Сколковский институт науки и технологий, Сколково, Россия
[3]Московский физико-технический институт, Долгопрудный, Россия
[4]Арктический и антарктический научно-исследовательский институт, Санкт-Петербург, Россия
[5]Институт проблем безопасного развития атомной энергетики РАН, Москва, Россия
[6]Институт вычислительной математики имени Г. И. Марчука РАН, Москва, Россия
* **Контакт:** Никита Андреевич Турко, nikitaturko@yandex.ru

В работе демонстрируется влияние расположения измерителей на точность оперативного прогноза состояния Мирового океана. Проводится сравнение различных методов расстановки измерителей, в том числе расстановка, полученная методом Concrete Autoencoder (CA). Для оценки влияния расположения датчиков на точность прогноза проводилось моделирование, имитирующее ситуацию, когда начальное состояние Мирового океана заметно отличается от реального. В эксперименте заменялись начальные условия для модели океана и льда, при этом атмосферный форсинг сохранялся из контрольного эксперимента. Затем производилось интегрирование модели с усвоением данных об «истинном» состоянии в точках расположения сенсоров. Результаты показали, что расстановка сенсоров, полученная при помощи методов глубокого обучения, превосходит в точности прогноза другие рассмотренные расстановки при сопоставимом числе сенсоров.

Ключевые слова: оперативный прогноз, Мировой океан, оптимальная расстановка измерителей, Concrete Autoencoder, усвоение данных

Цитирование: Турко, Н. А., А. А. Лобашев, К. В. Ушаков, М. Н. Кауркин, Л. Ю. Кальницкий, С. В. Семин, и Р. А. Ибраев Улучшение точности прогноза состояния Мирового океана за счет оптимального расположения измерителей // Russian Journal of Earth Sciences. — 2023. — Т. 23. — ES6005. — DOI: 10.2205/2023es000883 — EDN: UOMRDC

https://elibrary.ru/uomrdc

Получено: 25 августа 2023 г.
Принято: 15 декабря 2023 г.
Опубликовано: 30 декабря 2023 г.

1. Введение

Увеличение точности прогнозирования состояния Мирового океана является критически важной задачей, которая во многом зависит от количества наблюдательных станций и их расположения. В рамках исследований по улучшению прогностических моделей понимание влияния числа измерителей и их расположения на точность прогноза имеет первостепенное значение. В данной работе мы исследуем влияние количества сенсоров и их расположения на точность прогноза состояния океана с использованием системы усвоения данных наблюдений. Задачей данного исследования является поиск оптимальной стратегии размещения датчиков, что будет способствовать эффективному планированию океанических станций сбора данных.

Актуальность данного исследования обусловлена двумя факторами. Во-первых, эффективное размещение датчиков позволяет ускорить обработку данных и вычисления при усвоении данных. Во-вторых, это сокращает необходимость в проведении обширных и затратных по времени наблюдений с большим числом измерительных станций. Как ранее было показано в работе [*Кауркин и Ибраев*, 2019], сокращение объема усваиваемых данных наблюдений проекта АРГО [*Wong et al.*, 2020] на 50–75 процентов не оказывает значительного влияния на точность прогноза при использовании метода оптимальной ансамблевой интерполяции. Аналогичные выводы были получены в работе [*Turpin et al.*, 2016], где было показано, что усвоение только половины доступных наблюдений буев проекта АРГО приводит к незначительной деградации точности прогноза.

Классические методы размещения датчиков основаны на линейных приближениях и, обычно, используют информационную матрицу Фишера для количественной оценки ошибки между истинными и реконструированными полями [*Nakai et al.*, 2021]. Данный класс методов использует сингулярное разложение матрицы ковариаций данных [*Alonso et al.*, 2004; *Krause et al.*, 2008; *Kumar et al.*, 2014; *Nagata et al.*, 2021; *Nguyen et al.*, 2020; *Saito et al.*, 2021], которое для вектора данных размера n масштабируется по количеству операций как $\mathcal{O}(n^3)$ для полного Singular Value Decomposition (SVD) разложения или как $\mathcal{O}(n^2)$ для поиска только первых нескольких сингулярных векторов [*Li et al.*, 2019]. Однако эти методы сталкиваются с ограничениями при работе с многомерными данными, страдают от вычислительной неэффективности, и восстановленные физические поля часто не удовлетворяют физическим ограничениям.

В последние годы методы глубокого обучения стали чаще применяться в анализе климатических данных и системах оперативного прогнозирования, что позволяет проводить анализ с высоким разрешением и улучшать краткосрочные (с заблаговременностью до 3 суток) прогнозы состояния атмосферы. В то время как модели глубокого обучения с архитектурой трансформера демонстрируют многообещающие результаты для краткосрочного прогнозирования погоды [*Pathak et al.*, 2022], классические численные модели по-прежнему превосходят их для среднесрочных (3–7 суток) и долгосрочных (от 8 суток до сезона) прогнозов.

Появление распределения Gumbel-softmax и континуально-дискретного (concrete) распределения [*Jang et al.*, 2016; *Maddison et al.*, 2016] облегчило оптимизацию параметров дискретных распределений вероятностей благодаря возможности использования более эффективных методов на основе градиентного спуска. Вскоре было предложено несколько методов, применяющих распределение Gumbel-softmax для оптимального размещения датчиков, таких как Concrete Autoencoder (CA) [*Abid et al.*, 2019], глубокое вероятностное семплирование [*Huijben et al.*, 2020] и динамический выбор признаков с максимизацией взаимной информации [*Covert et al.*, 2023]. Эти методы продемонстрировали преимущества по сравнению с классическими методами на основе сингулярного разложения, а именно: повышенную эффективность использования памяти и отсутствие необходимости в дорогостоящем вычислении ковариационной матрицы данных.

В то же время исследования по оценке качества размещения датчиков с использованием статистических моделей ограничивались относительно простыми системами с сетками низкого разрешения [*Clark et al.*, 2019; *Manohar et al.*, 2018; *Sun et al.*, 2019]. В этих исследованиях качество расположения датчиков оценивалось по норме ошибки восстановления мгновенного поля по данным наблюдений на тестовой выборке. Наше исследование выходит за эти ограничения, рассматривая более сложную систему океан–лед и используя более продвинутый метод оценки качества расположения сенсоров, в котором восстановленные поля удовлетворяют законам сохранения и термогидродинамическим уравнениям. Качество расстановки оценивается по результатам численного эксперимента с усвоением данных синтетических наблюдений методом оптимальной ансамблевой интерполяции в процессе интегрирования модели глобальной циркуляции океана с пространственным разрешением $0,25 \times 0,25$ градуса. Данный подход позволяет нам существенно углубить и уточнить анализ оптимальности размещения датчиков.

Предыдущие исследования [*Abbasi et al.*, 2018; *Turpin et al.*, 2016] показали, что усвоение данных о температуре, даже с одного горизонтального слоя, может улучшить точность прогноза. Таким образом, наш подход включает усвоение измерений только из одного горизонта океана, а именно в приповерхностном слое, чтобы минимизировать влияние атмосферного воздействия.

Использование исключительно модели Мирового океана высокого разрешения для решения задачи размещения датчиков методом прямого комбинаторного поиска нецелесообразно из-за высокой вычислительной мощности и большой продолжительности одного эксперимента. Методы же глубокого обучения сами по себе не позволяют во всех деталях учесть особенности физических процессов, законы сохранения и соответствие предсказаний уравнениям гидродинамики. В отличие от методов глубокого обучения, в процессе восстановления поля по разреженным измерениям с использованием модели океана и системы усвоения, мы получаем удовлетворяющие уравнениям гидродинамики полные трехмерные поля температуры и солености, трехмерные поля горизонтальных компонент скорости, а также двумерные поля сплоченности и толщины льда. Эта работа представляет новый, более глубокий взгляд на вопрос оптимального размещения датчиков для улучшения точности прогноза состояния океана.

Чтобы снизить вычислительную нагрузку, связанную с прямым комбинаторным поиском при моделировании Мирового океана с высоким разрешением, мы предлагаем гибридный подход. Наша методология сочетает статистическую обработку данных ретроспективного гидродинамического моделирования с использованием моделей нейронных сетей для захвата нелинейных зависимостей и последующую оценку эффективности расположения датчиков в ходе прогноза по модели общей циркуляции океана. Этот гибридный подход дает физически обоснованные оптимальные координаты датчика в пределах практических временных рамок. Кроме того, он демонстрирует линейную масштабируемость с размером вычислительной области и устраняет необходимость вычисления ковариационной матрицы численного решения. Таким образом, это оказывается выгодным для таких приложений, как модели глобальной циркуляции океана при разрешении $0{,}25$ или $0{,}1$ градуса, где ковариационная матрица может иметь векторные размеры порядка от 10^{12} до 10^{16}.

В контексте данного исследования мы оцениваем эффективность размещения датчиков, применяя процедуру усвоения данных в глобальной модели океана. Одним из основных вопросов, которым мы стремимся уделить внимание, является возможность экстраполяции расположения датчиков, определенного в процессе обучения нейронной сети на исторических данных [*Lobashev et al.*, 2023], на глобальную модель прогноза океанской циркуляции [*Ushakov and Ibrayev*, 2018]. В частности, мы рассматриваем вопрос о том, будет ли конфигурация датчиков, обеспечивающая минимальную ошибку восстановления поля нейронной сетью, также оптимальной для прогнозирования состояния океана путем интегрирования модели с усвоением данных, полученных от этих датчиков.

В данном исследовании проводится сравнение метода Concrete Autoencoder с несколькими базовыми методами расстановки измерителей. Рассматриваемый вариант метода CA [*Lobashev et al.*, 2023; *Turko et al.*, 2022] включает в себя два этапа. На первом этапе проводится оценка пространственной вариабельности физического поля, аппроксимируя его информационную энтропию с использованием нейронной сети Conditional Pixel CNN. На втором этапе полученная энтропия применяется для инициализации начального расположения датчиков. Затем это расположение оптимизируется с помощью архитектуры CA, которая позволяет одновременно минимизировать количество датчиков и максимизировать точность восстановления. Мы исследуем расположение сенсоров, полученное в работе [*Lobashev et al.*, 2023]. После исключения сенсоров, попадающих на сушу, мы усваиваем показания 1160 сенсоров. Сравнение производится с фиксированными расстановками, взятыми от свободно дрейфующих станций проекта АРГО за первые сутки и за первые четверо суток с момента начала эксперимента, а также с расстановкой в соответствии с расположением буев проекта АРГО, меняющимся каждый день. Число сенсоров равняется соответственно 302, 1299 и ~280–380. Также для сравнения производится регулярная расстановка по трехполярной локально-ортогональной решетке [*Murray*, 1996]. Всего рассматриваются четыре варианта регулярной расстановки с 1301, 3379, 6792 и 13 582 сенсорами.

В разд. 1 содержится введение и обзор литературы. В разд. 2 мы описываем постановку эксперимента. В разд. 3 приводятся результаты. Наконец, разд. 4 содержит обсуждение результатов и выводы.

2. Постановка численных экспериментов

Идея эксперимента. Для оценки влияния расположения датчиков на точность прогноза проводилось моделирование, имитирующее ситуацию, когда начальное состояние Мирового океана заметно отличается от реального. В эксперименте заменялись начальные условия для модели океана и льда, при этом атмосферный форсинг сохранялся из контрольного эксперимента. Затем производилось интегрирование модели с усвоением данных об истинном (взятом из контрольного эксперимента) состоянии поля температуры в приповерхностном слое в точках расположения сенсоров. Основная идея заключается в выборе такого расположения датчиков, которое позволит достичь максимального совпадения с состоянием контрольного эксперимента за минимальное число итераций усвоения. По скорости приближения текущего состояния модели океана к целевому и уменьшению ошибки можно будет сделать вывод о влиянии способа расстановки и количества измерителей на точность прогноза. Таким образом, в качестве основной метрики, характеризующей качество расстановки измерителей, мы используем среднюю точность прогноза состояния Мирового океана в приповерхностном слое. Модель океана совместно с системой усвоения выступают в таком случае как метод восстановления трехмерного поля температуры по пространственно разреженным данным измерений.

Способы расстановки измерителей. В большинстве современных систем прогнозирования, таких как участники проекта OceanPredict, ежедневно используются данные наблюдений, полученные с помощью измерительных буев проекта АРГО. Общее количество буев достигает приблизительно четырех тысяч. При этом ежедневно передается около 280–380 профилей температуры. В качестве базового варианта расстановки мы использовали координаты буев проекта АРГО за один день (эксперимент s23) и за четыре последовательных дня (эксперимент s24) для получения синтетических данных наблюдений. Также был проведен эксперимент с реальным положением буев проекта АРГО (эксперимент s25). Для оценки влияния количества датчиков на точность прогноза мы также исследовали расположение на равномерной (трехполярной локально-ортогональной) сетке из одной (эксперимент s36), трех (эксперимент s37), шести (эксперимент s38) и тринадцати тысяч (эксперимент s39) датчиков.

Основной метод размещения датчиков, который мы исследовали, состоит из двух этапов. На первом этапе проводится оценка пространственной вариабельности физического поля, аппроксимируя его информационную энтропию с помощью нейросети Conditional PixelCNN. На втором этапе энтропия используется для инициализации начального расположения датчиков, которое далее оптимизируется с помощью архитектуры Concrete Autoencoder, позволяющей одновременно минимизировать количество датчиков и максимизировать точность восстановления поля. Этот эксперимент обозначен как s44.

Для сравнения был проведен эксперимент s00 без усвоения данных, чтобы оценить влияние атмосферного форсинга на точность прогноза. Список проведенных экспериментов и их описания представлены в табл. 1.

Постановка эксперимента. В данном исследовании мы использовали совместную модель Мирового океана с ледовым покровом. Модель океана разработана Институтом вычислительной математики РАН и Институтом океанологии РАН [*Кальницкий и др.*, 2020; *Ushakov and Ibrayev*, 2018], в качестве модели льда используется CICE 5.1 [*Hunke et al.*, 2015]. Совмещение моделей (каплинг) выполнено с помощью платформы CMF [*Fadeev et al.*, 2018; *Kalmykov et al.*, 2018]. Атмосферное воздействие осуществлялось с использованием данных реанализа ERA5 [*Hersbach et al.*, 2020]. Усвоение данных

Таблица 1. Список экспериментов и соответствующее число сенсоров

Эксперимент	Метод расположения	Измерений в день
s00	без измерений	0
s23	АРГО, 1 день	302
s24	АРГО, 4 дня	1299
s25	АРГО, динамическое размещение	~ 280–380
s36	Регулярно – $5{,}25° \times 6{,}25°$	1301
s37	Регулярно – $5° \times 2{,}5°$	3379
s38	Регулярно – $2{,}5° \times 2{,}5°$	6792
s39	Регулярно – $2{,}5° \times 1{,}5°$	13 581
s44	Concrete Autoencoder	1160
a01	Реанализ с усвоением TS профилей, сплоченности льда, аномалии уровня поверхности океана	~11 200

проводилось методом оптимальной ансамблевой интерполяции EnOI [*Kaurkin et al.*, 2016a,b] один раз в модельные сутки в 12:00. Параметры усвоения были подобраны так, чтобы корректировка модельного решения была максимально допустимой по соображениям устойчивости. Здесь требуется пояснение. Усвоение можно рассматривать как корректировку модельного решения в соответствии с данными наблюдений. В рассматриваемых экспериментах при усвоении корректировалось только поле температуры, а остальные физические поля не изменялись (соленость, компоненты скорости, уровень поверхности океана, сплоченность и толщина льда). Другими словами, при усвоении возмущалось исключительно поле температуры, что приводило к физическому несоответствию с остальными полями. Адаптация к возмущениям происходила в процессе дальнейшего интегрирования модели океана. Возмущение, внесенное при усвоении, можно воспринимать как шоковое изменение состояния, которое при слишком больших амплитудах может приводить к численной нестабильности и развалу модели. Таким образом, максимизация возмущения при усвоении позволила сократить время выхода точности на квазистационарный режим в экспериментах. Но, с другой стороны, из условия численной стабильности работы модели океана после процедуры усвоения мы получили ограничение на количество измерителей снизу. Так, в экспериментах (не представленных в работе) с усвоением данных менее чем с ~ 250 измерителей модель разваливалась из-за шоков при усвоении. Более подробное описание использованной конфигурации приведено в работе [*Lobashev et al.*, 2023].

Контрольный эксперимент a01 проводился с моделью Мирового океана, интегрированной в период с 2019-01-01 по 2020-12-01, начиная с климатических значений температуры и солености WOA2013 [*Boyer et al.*, 2013]. С 2020-01-01 мы начали усвоение данных наблюдений: аномалии уровенной поверхности океана [*Desai*, 2016], сплоченности льда [*Lavergne et al.*, 2019] и профилей буев проекта АРГО [*Wong et al.*, 2020], с использованием метода EnOI.

Для исследования влияния расположения датчиков на точность прогноза Мирового океана мы провели серию экспериментов (серия s**), в которых были одинаковы начальные и граничные условия. При этом начальное состояние отличалось от начального состояния в контрольном эксперименте, а именно, было возмущено за счет сдвига по времени на один год назад. В экспериментах варьировались количество датчиков и метод их расположения. В табл. 1 представлены названия экспериментов с указанием способов расположения датчиков и количества усваиваемых измерений.

В экспериментах серии s** в качестве начальных условий было выбрано состояние океана на 11 сентября 2019 года. Эксперименты выполнялись с атмосферным форсингом, начавшимся 11 сентября 2020 года и взятым из контрольного эксперимента a01.

Последующее усвоение данных производилось один раз в сутки, с дальнейшим интегрированием модели на 24 часа вперед, после этого вычислялась точность прогноза по сравнению с контрольным экспериментом. Для усвоения использовались синтетические данные наблюдений температуры в приповерхностном слое океана, полученные без добавления погрешностей из текущих полей температуры контрольного эксперимента a01, начиная также с 11 сентября 2020, года без усвоения альтиметрии и сплоченности льда. Точность суточного прогноза температурных полей Мирового океана оценивалась по сравнению с данными контрольного эксперимента a01 во всей трехмерной расчетной области, при этом использовались расчеты средней и среднеквадратичной ошибок [*Ryan et al.*, 2015] по формулам, представленным в работах [*Lobashev et al.*, 2023; *Turko et al.*, 2022].

3. Результаты

Результаты проведенных экспериментов представлены в табл. 2. Оценка точности прогноза проводилась на основе двух основных метрик: смещения, или средней ошибки (Bias), и среднеквадратичной ошибки (Root Mean Square Error, RMSE). Bias является мерой систематической ошибки, присутствующей в прогнозе, в то время как RMSE является стандартной мерой различия между предсказанными и наблюдаемыми значениями, т.е. мерой точности, учитывающей как систематическую, так и случайную погрешности. Данные получены из десяти различных экспериментов, каждый из которых обозначен от s00 до s44, и количество используемых датчиков варьируется от 0 до 13 582. Значения Bias и RMSE представлены для каждого эксперимента за три последовательных дня (День 0, День 1 и День 2), начиная со дня старта, а также указаны средние значения за первые 20 дней для обеих метрик. Усреднение за 20 дней выбрано исходя из того, что после этого периода значения средней и среднеквадратичной ошибок выходят на квазистационарный уровень. Расчет ошибок проводился для слоя Мирового океана от поверхности до глубины 100 метров. В этом слое наиболее выражен эффект усвоения данных (рис. 10–14). С другой стороны, этот слой представляет интерес с точки зрения восстановления динамики Мирового океана. Верхний перемешанный слой, определяющий взаимодействие океана с атмосферой, летом характеризуется толщинами до 100 метров и возрастает в зимний период [*Кошляков и Тараканов*, 2014; *Sallée et al.*, 2021]. Значения ошибок указаны до 3-го знака после запятой. При этом были проведены повторные эксперименты с одними и теми же условиями, которые показали, что численная ошибка модели океана и системы усвоения не влияет на значения точности прогноза вплоть до 4-го знака после запятой.

Таблица 2. Точность прогноза, усредненная по верхним 100 метрам, по сравнению с контрольным экспериментом a01 за первые 20 дней

Эксперимент	Сенсоры	Bias, °C				RMSE, °C			
		День 0	День 1	День 2	Среднее	День 0	День 1	День 2	Среднее
s00	0	−0,195	−0,224	−0,180	−0,222	1,139	1,173	1,197	1,128
s23	302	−0,195	−0,280	−0,192	−0,213	1,139	1,203	1,240	1,175
s24	1299	−0,195	−0,288	−0,217	−0,223	1,139	1,221	1,227	1,170
s25	~280–380	−0,195	−0,280	−0,262	−0,146	1,139	1,203	1,253	1,226
s36	1306	−0,195	−0,144	−0,053	−0,078	1,139	1,162	1,222	1,149
s37	3379	−0,195	−0,164	−0,065	−0,102	1,139	1,132	1,217	1,138
s38	6792	−0,195	−0,164	−0,071	−0,106	1,139	1,135	1,206	1,127
s39	13 581	−0,195	−0,160	−0,066	−0,100	1,139	1,136	1,210	1,127
s44	1160	−0,195	−0,162	−0,070	−0,100	1,139	1,160	1,194	1,139

Эксперимент s00, в котором не проводилось усвоение данных синтетических наблюдений, имеет большую среднюю ошибку (Bias) и одно из наименьших значений RMSE. Это объясняется отсутствием характерных для работы системы усвоения «шоков», которые присутствовали во всех остальных экспериментах серии s**, в силу настройки «агрессивного» усвоения.

Результаты численного моделирования в серии экспериментов s3* указывают на то, что при достижении порога в примерно три тысячи сенсоров дальнейшее увеличение числа измерительных устройств не влечет за собой существенного улучшения точности прогноза. Например, эксперименты, включающие усвоение данных с тремя, шестью и тринадцатью тысячами измерений в день, показывают минимальные различия в точности прогноза, с точки зрения как средней, так и среднеквадратичной ошибок. Эти данные подкрепляют гипотезу о возможности удаления примерно половины датчиков из набора s38 без ущерба для систематической и среднеквадратичной ошибок, что согласуется с результатами работ [*Кауркин и Ибраев*, 2019; *Turpin et al.*, 2016], в которых было показано, что удаление примерно половины данных проекта АРГО при усвоении не приводит к существенной деградации точности прогноза.

Интересно, что при использовании метода Concrete Autoencoder для расположения 1160 сенсоров эксперименты демонстрируют аналогичное снижение средней ошибки прогноза, как и в случае регулярного расположения сенсоров в 3, 6 и 13 раз большим количеством. По значениям средней ошибки и RMSE расстановка s44 (Bias −0,100 и RMSE 1,139) наиболее близка к регулярной расстановке 3379 сенсоров в эксперименте s37 (Bias −0,102 и RMSE 1,138). При этом среднеквадратичная ошибка оказывается заметно ниже по сравнению с использованием регулярной или АРГО схемы расположения тысячи измерителей. Эти результаты говорят о том, что при оптимальном расположении сенсоров можно добиться увеличения точности прогноза без увеличения числа сенсоров.

При сравнении экспериментов s24, s36 и s44 с приблизительно одной тысячей сенсоров наибольшее значение как средней, так и среднеквадратичной ошибок имеет расположение буев проекта АРГО. В экспериментах s36 и s44 значение средней ошибки снижается уже после второго усвоения и остается низким в течение следующих 20 дней. Наименьшее значение RMSE имеет расстановка s44, полученная методом CA.

В серии экспериментов s2* наибольшее значение RMSE имеет динамическая расстановка, соответствующая реальному положению буев проекта АРГО. При этом динамическая расстановка имеет наименьшее значение Bias за счет того, что в среднем за 10 дней всплывает около четырех тысяч буев, приблизительно равномерно распределенных по Мировому океану, за исключением Арктики. Сравнивая между собой статические расстановки s23 и s24, можно заметить, что несмотря на более чем четырехкратное увеличение числа датчиков (с 302 до 1299) в эксперименте s24, средние значения Bias и RMSE демонстрируют незначительные изменения по сравнению с экспериментом s23.

Данные указывают на улучшение точности прогноза с увеличением количества датчиков, хотя эта связь не всегда строго линейна. Также они показывают, что расстановка Concrete Autoencoder может обеспечить низкое значение как Bias, так и RMSE по сравнению с другими вариантами расстановки с близким числом сенсоров.

Графики точности от времени. На рис. 1–8 представлены графики точности прогноза на 1 сутки по сравнению с контрольным экспериментом на разных горизонтах для экспериментов серии s** с усвоением. Можно заметить, что расположение сенсоров оказывает наибольшее влияние на точность прогноза в течение первых 20–30 итераций усвоения.

Анализ рис. 1–3 показывает, что все три эксперимента имеют схожую скорость сходимости RMSE в первые 20 дней. Однако в случае реального расположения АРГО средняя ошибка уменьшается быстрее, чем в сценариях s23 и s24 со статической расстановкой. Кроме того, наибольший эффект от увеличения числа датчиков с 302 до

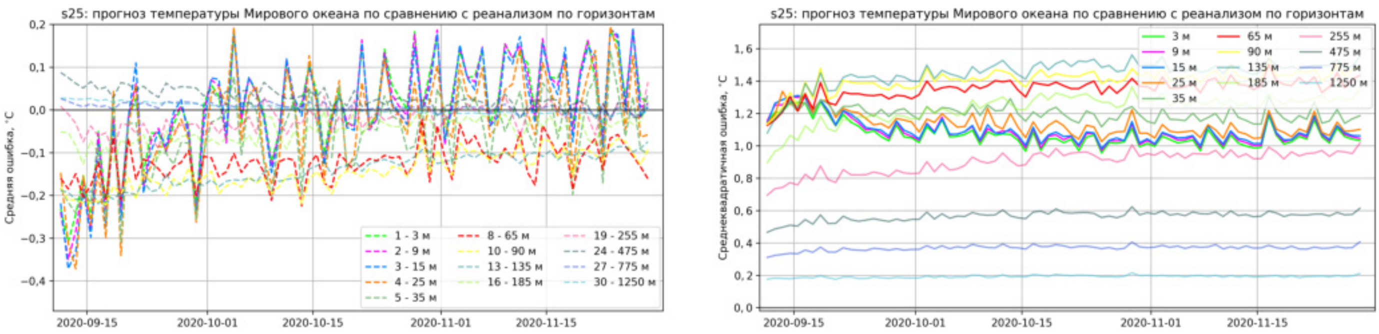

Рис. 1. Точность прогноза на 1 сутки для реального расположения ~280–380 сенсоров проекта АРГО на различных уровнях по сравнению с контрольным экспериментом. Пунктирные линии показывают Bias (слева), сплошные линии соответствуют RMSE (справа).

1299 наблюдается при рассмотрении графика RMSE через 20–25 дней после старта эксперимента. В то время как в эксперименте s23 наблюдаются признаки небольшого увеличения RMSE ближе к концу симуляции, график RMSE в эксперименте s24 достигает квазистационарных значений.

Анализ графиков, представленных на рис. 3 и 4, подтверждает важность использования алгоритмов оптимального размещения датчиков. В частности, сравнение сценариев s24 и s44 демонстрирует, что среднее значение ошибки (Bias) может быть улучшено с использованием меньшего количества датчиков при оптимальном размещении. Заметным является более быстрое уменьшение средней ошибки в эксперименте s44

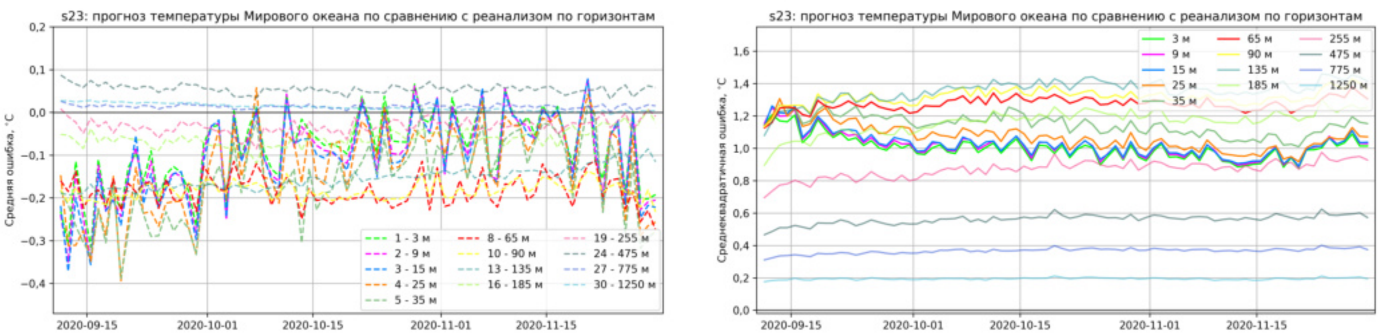

Рис. 2. Точность прогноза на 1 сутки для фиксированного расположения 302 сенсоров проекта АРГО на различных уровнях по сравнению с контрольным экспериментом. Пунктирные линии показывают Bias (слева), сплошные линии соответствуют RMSE (справа).

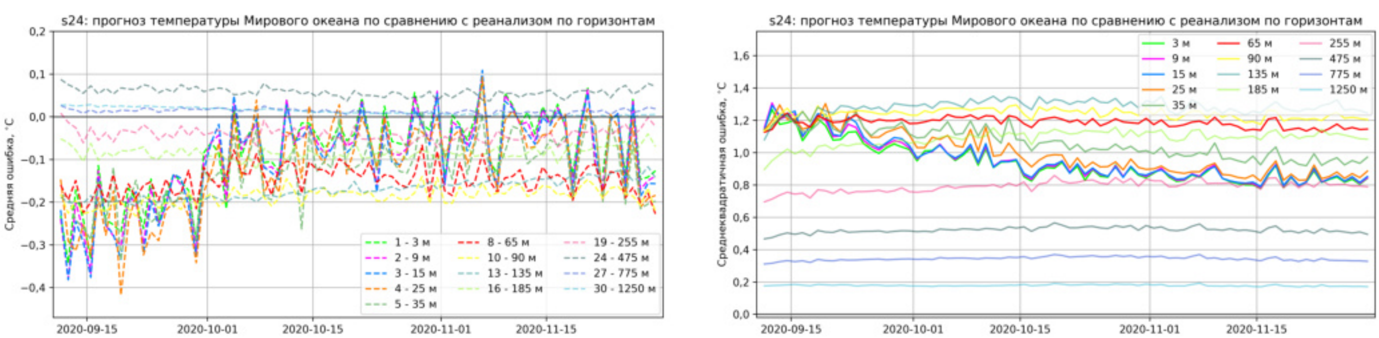

Рис. 3. Точность прогноза на 1 сутки для фиксированного расположения 1299 сенсоров проекта АРГО на различных уровнях по сравнению с контрольным экспериментом. Пунктирные линии показывают Bias (слева), сплошные линии соответствуют RMSE (справа).

по сравнению с s24. При сравнении рис. 4 и 5 можно видеть в целом схожую скорость сходимости как средней, так и среднеквадратичной ошибки в сценариях s44 и s36.

Анализ графиков на рис. 6–8 подчеркивает, что разница между использованием трех тысяч, семи тысяч и тринадцати тысяч сенсоров не является существенной. Графики ошибок в сценариях s36 и s37 указывают на то, что увеличение числа датчиков до 3 тысяч способствует значительному снижению среднеквадратичной ошибки по сравнению с 1 тысячей датчиков. С другой стороны, согласно сравнению s37 и s44, такого же снижения можно достичь без увеличения числа датчиков, за счет их грамотного расположения.

На рис. 9 приведено сравнение динамики ошибок в верхних 100 метрах в течение первых 20 суток для экспериментов s24 (фиксированное расположение измерителей проекта АРГО за 4 суток), s25 (сценарий с динамическим изменением расположения датчиков в соответствии с реальным положением буев проекта АРГО), s36 (регулярное распределение тысячи измерителей) и s44 (расстановка методом Concrete Autoencoder).

Bias, полученный при регулярной расстановке тысячи сенсоров, показывает несколько лучшие результаты в сравнении с s44. Это может быть связано с тем, что в эксперименте с регулярной расстановкой больше сенсоров попало в акваторию Северного Ледовитого океана. В отношении RMSE эксперимент s44 выделяется наилучшими показателями как сразу после старта моделирования, так и в течение всего 20-дневного периода. Также средняя ошибка (Bias) для реального расположения АРГО s25 через неделю после старта сходится к значениям, характерным для регулярной расстановки тысячи измерителей s36 и для расстановки Concrete Autoencoder s44. При этом реальная расстановка АРГО заметно хуже по показателю RMSE, чем другие рассматриваемые расстановки с большим числом сенсоров.

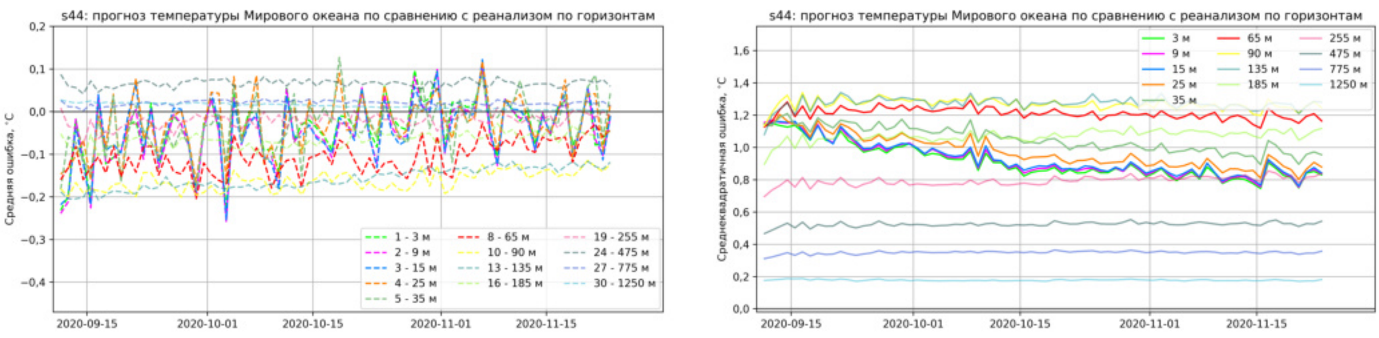

Рис. 4. Точность прогноза на 1 сутки для фиксированного расположения 1160 сенсоров, расставленных методом Concrete Autoencoder, на различных уровнях по сравнению с контрольным экспериментом. Пунктирные линии показывают Bias (слева), сплошные линии соответствуют RMSE (справа).

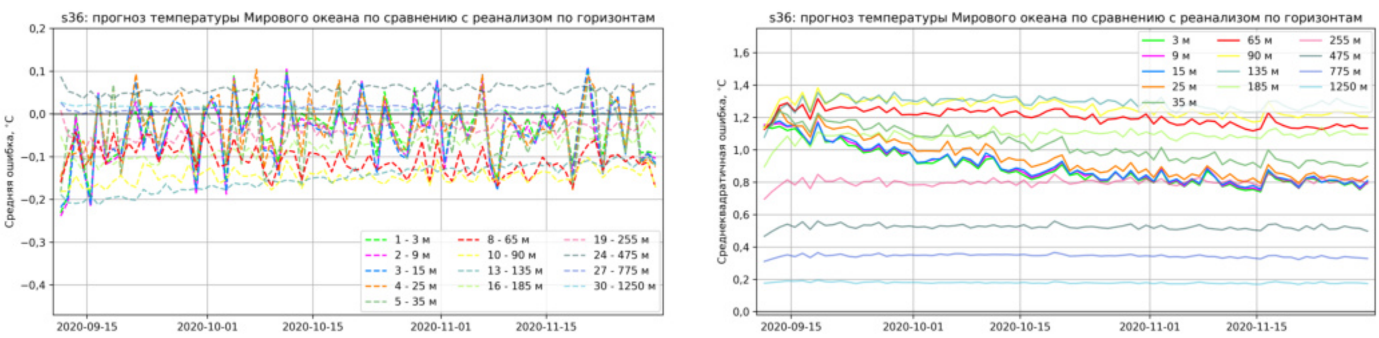

Рис. 5. Точность прогноза на 1 сутки по сравнению с контрольным экспериментом на различных уровнях для фиксированного расположения 1306 сенсоров, расставленных по равномерной решетке с шагом 5,25° по долготе и 6,25° по широте. Пунктирные линии показывают Bias (слева), сплошные линии соответствуют RMSE (справа).

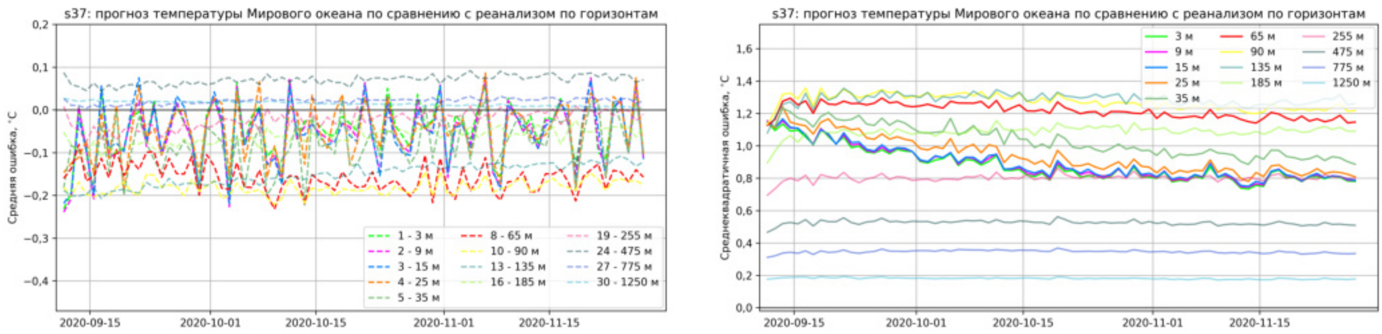

Рис. 6. Точность прогноза на 1 сутки по сравнению с контрольным экспериментом на различных уровнях для фиксированного расположения 3379 сенсоров, расставленных по равномерной решетке с шагом 5° по долготе и 2.5° по широте. Пунктирные линии показывают Bias (слева), сплошные линии соответствуют RMSE (справа).

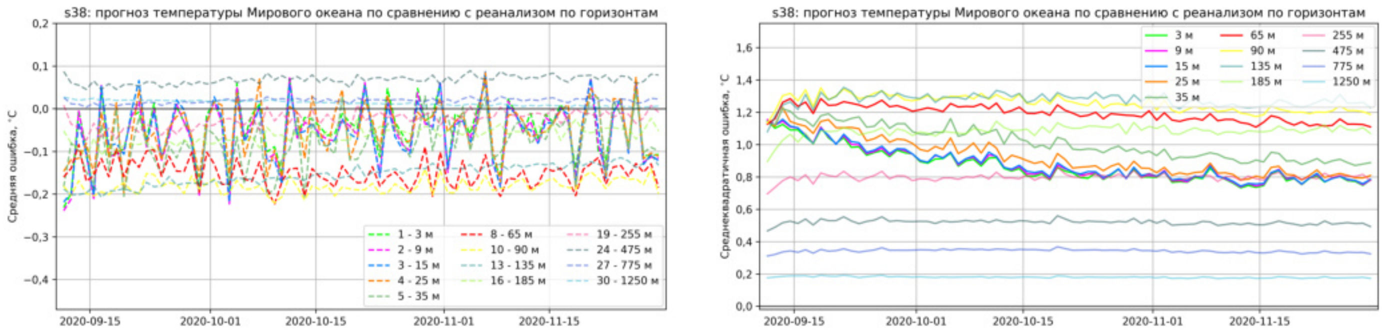

Рис. 7. Точность прогноза на 1 сутки по сравнению с контрольным экспериментом на различных уровнях для фиксированного расположения 6792 сенсоров, расставленных по равномерной решетке с шагом 2,5° по долготе и 2,5° по широте. Пунктирные линии показывают Bias (слева), сплошные линии соответствуют RMSE (справа).

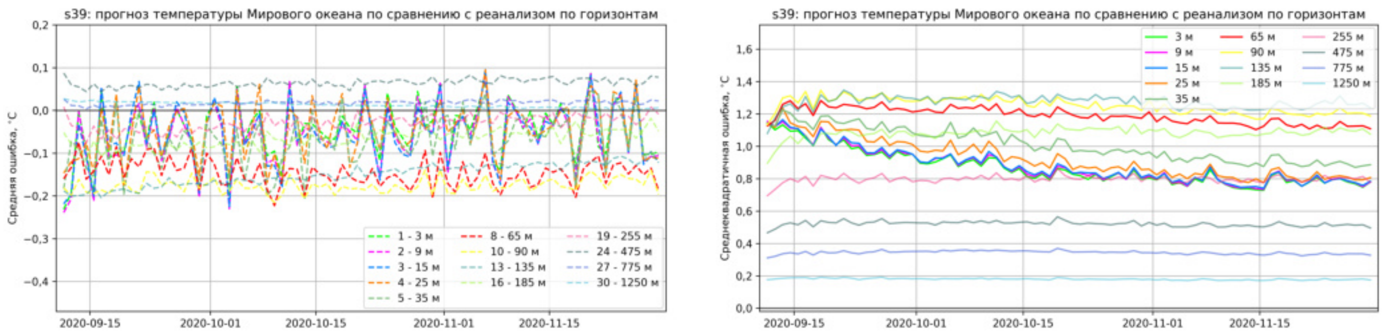

Рис. 8. Точность прогноза на 1 сутки по сравнению с контрольным экспериментом на различных уровнях для фиксированного расположения 13 581 сенсоров, расставленных по равномерной решетке с шагом 2,5° по долготе и 1,5° по широте. Пунктирные линии показывают Bias (слева), сплошные линии соответствуют RMSE (справа).

Профили от времени. Отдельно следует обратить внимание на представленные ниже средние суточные профили по 13 уровням для проведенных экспериментов с усвоением, а также для контрольного эксперимента. Эти данные позволяют наблюдать динамику профилей различных экспериментов и детальнее оценить влияние различных методов расстановки.

Как можно видеть на рис. 10 и 11, в сценариях s44, s36, s37, s38 и s39 средний профиль в верхних 60 метрах уже в течение 2–3 дней становится близким к среднему профилю в контрольном эксперименте a01. С другой стороны, при сравнении динамики в первые дни для экспериментов с тысячей сенсоров (s24, s36 и s44) мы обнаруживаем, что в сценарии s24 профиль адаптируется не так быстро, как в s36 и s44.

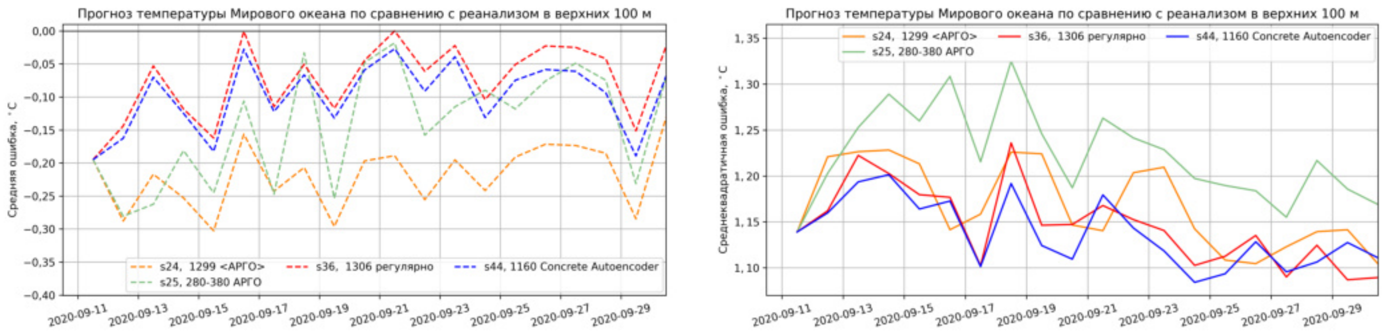

Рис. 9. Точность прогноза на 1 сутки по сравнению с контрольным экспериментом для экспериментов s24, s25, s36 и s44. Пунктирные линии показывают Bias (слева), сплошные линии соответствуют RMSE (справа).

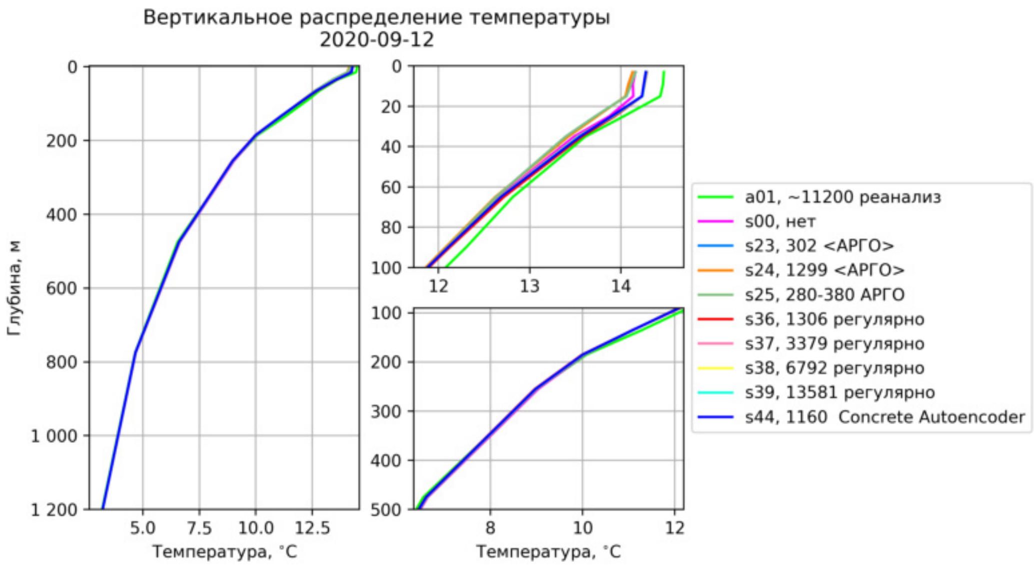

Рис. 10. Профили температуры 2020-09-12 после первой итерации усвоения.

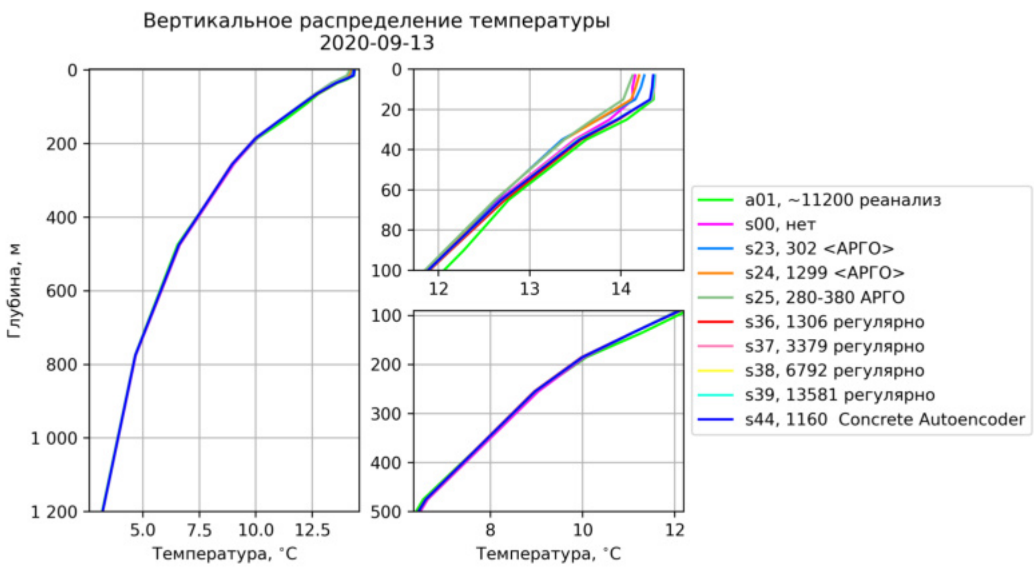

Рис. 11. Профили температуры 2020-09-13 после второй итерации усвоения.

Графики на рис. 12–14 иллюстрируют, что примерно после 20 дней всех экспериментов результаты всех применяемых методов сходятся, показывая схожую динамику.

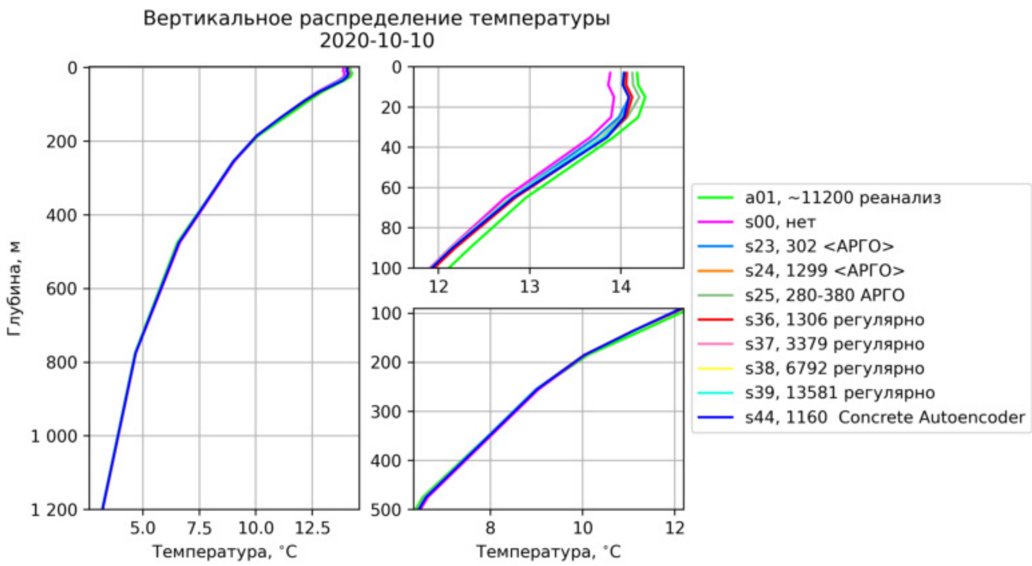

Рис. 12. Профили температуры 2020-10-10 после 29 дней работы усвоения.

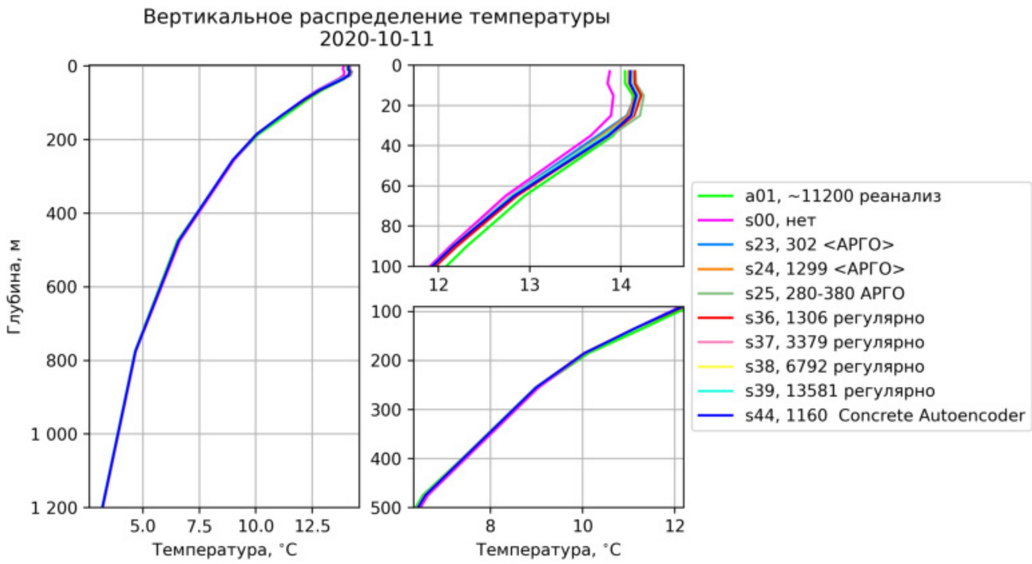

Рис. 13. Профили температуры 2020-10-11 после 30 дней работы усвоения.

Это подтверждает наше предположение о том, что продолжение эксперимента более чем на 30–40 дней не принесет дополнительной информации.

В установившемся через приблизительно 30 дней после старта моделирования квазистационарном режиме профили температур, полученные с использованием метода Concrete Autoencoder, регулярной расстановки на трех, шести и тринадцати тысячах сенсорах, совпадают с целевыми полями, с задержкой около одних суток.

Пространственное распределение ошибок. На рис. 15–18 показано пространственное распределение среднеквадратичной ошибки в верхних 100 метрах за первые 20 дней моделирования для сценариев s25, s24, s36 и s44 соответственно. В Баренцевом море и в Арктике было замечено, что ошибка прогноза при использовании метода CA и регулярной расстановки значительно меньше по сравнению с расстановкой АРГО s25 и s24. При этом регулярная расстановка (s36) имеет больше всего сенсоров по сравнению с другими способами в этом регионе. В других регионах ошибки прогноза для всех методов примерно одинаковы.

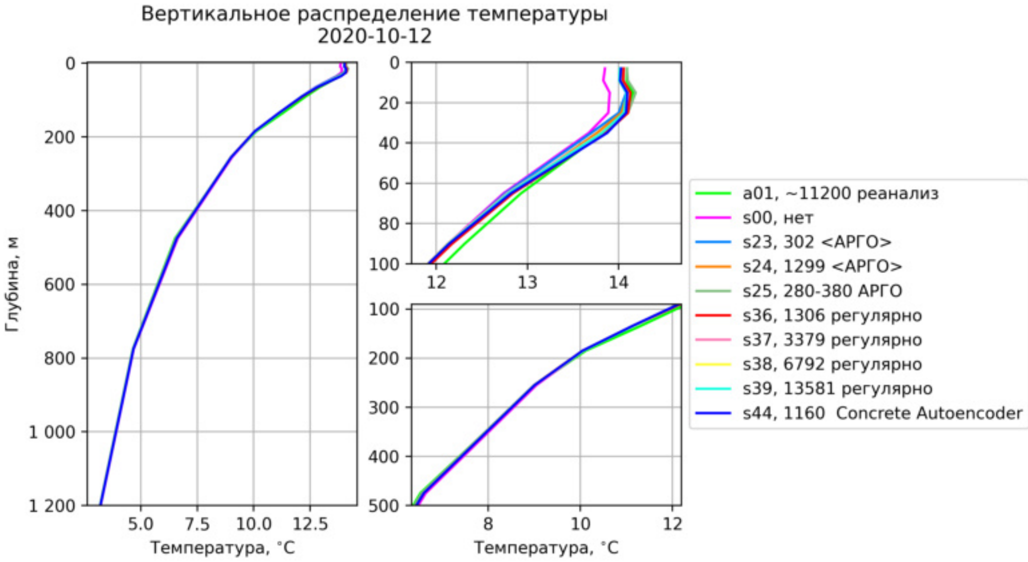

Рис. 14. Профили температуры 2020-10-12 после 31 дня работы усвоения.

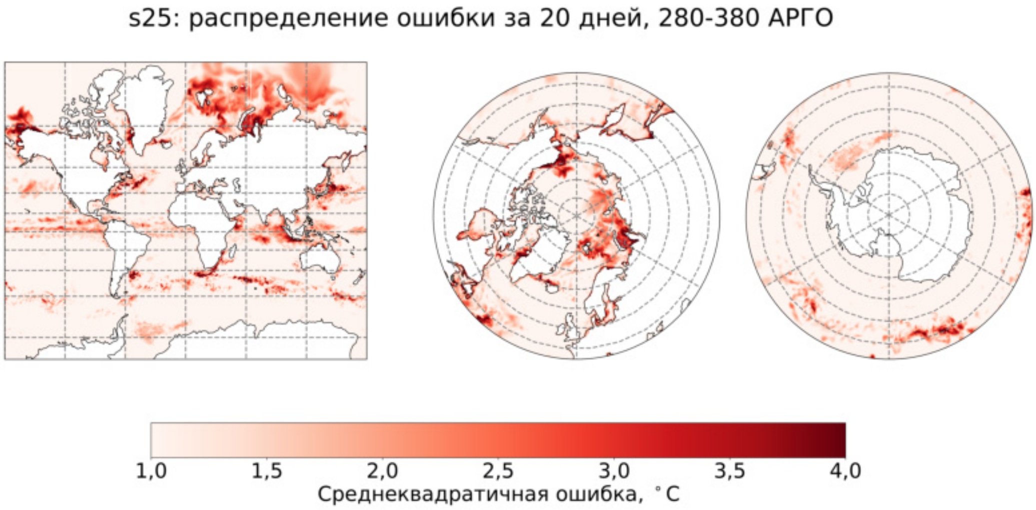

Рис. 15. Пространственное распределение ошибок температуры для изменяющейся расстановки в соответствии с реальными координатами буев проекта АРГО, 280–380 сенсоров.

Следует отметить, что паттерны ошибок в целом одинаковы для всех расстановок, но при этом варьируется амплитуда значений ошибки. Из этого можно сделать вывод, что мы заранее можем утверждать, в каких регионах прогноз получится более достоверным.

На рис. 19–21 представлены координаты сенсоров, которые использовались для наблюдений в проведенных экспериментах s44, s36 и s24 соответственно. Так как регулярное распределение и расстановка методом Concrete Autoencoder имеют большее число сенсоров в Арктике, мы можем также сделать вывод о том, что увеличение числа сенсоров в некотором регионе может значительно повысить точность прогноза.

4. Заключение

Экспериментальный анализ сценариев s00, s23, s24, s25, s36, s37, s38, s39 и s44 раскрыл ряд значимых наблюдений, улучшающих наше понимание влияния расположения и количества датчиков на значения средней (Bias) и среднеквадратичной (RMSE) ошибки.

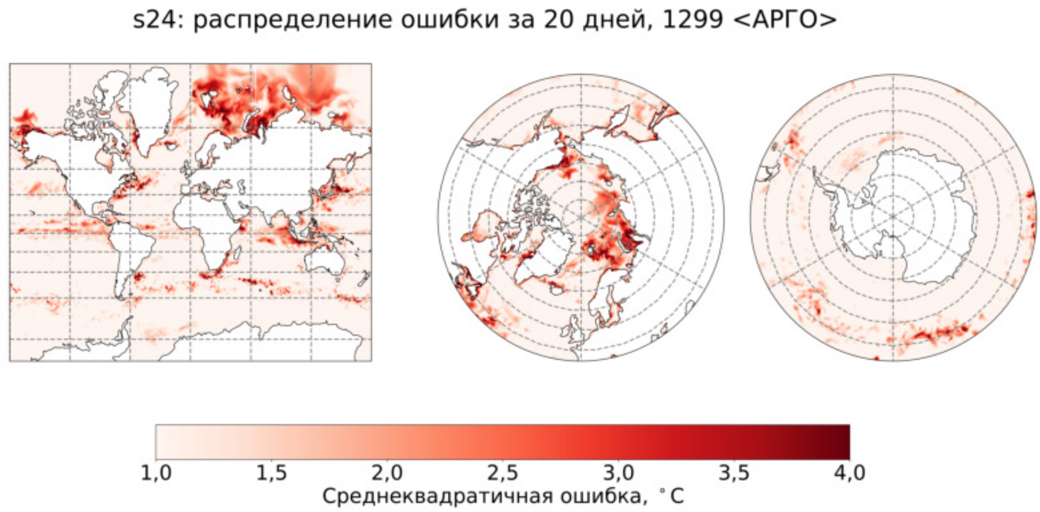

Рис. 16. Пространственное распределение ошибок температуры для фиксированной расстановки АРГО, 1299 сенсоров.

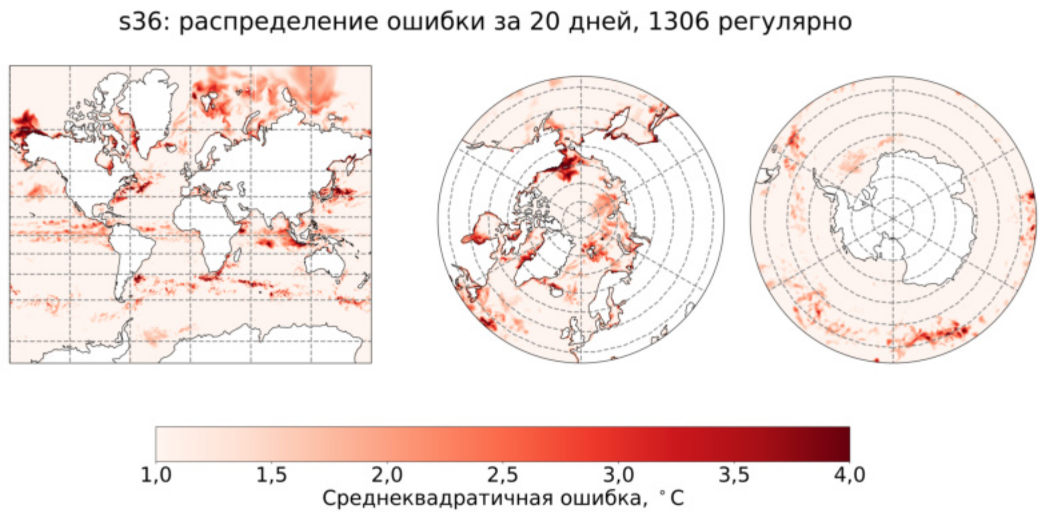

Рис. 17. Пространственное распределение ошибок температуры для фиксированной регулярной расстановки, 1306 сенсоров.

Первое наблюдение, основанное на сценариях s36 и s37 с регулярной расстановкой на 1306 и 3379 сенсоров соответственно, показывает, что увеличение числа датчиков может значительно улучшить показатели среднеквадратичной ошибки. Это подчеркивает, что при реализации сетей датчиков следует тщательно рассматривать возможность увеличения плотности расстановки датчиков, учитывая при этом другие факторы, такие как стоимость и энергопотребление. При этом, как показывает анализ экспериментов s37, s38 и s39, дальнейшее увеличение числа сенсоров более трех тысяч не приводит к заметному уменьшению средней и среднеквадратичной ошибок.

Второе наблюдение получается при сравнении сценариев s36 и s44: применение методов оптимизации при размещении датчиков может обеспечить улучшение показателя систематической ошибки при меньшем числе датчиков. Расстановка, полученная методом Concrete Autoencoder, имеет значительно меньшее значение средней ошибки, чем при регулярной расстановке. Результаты также подтверждают гипотезу, согласно которой примерно половина датчиков из сценария s38 может быть потенциально удалена без существенного ухудшения показателя систематической ошибки. Кроме того, расстановка, полученная методом Concrete Autoencoder с одной тысячей сенсоров,

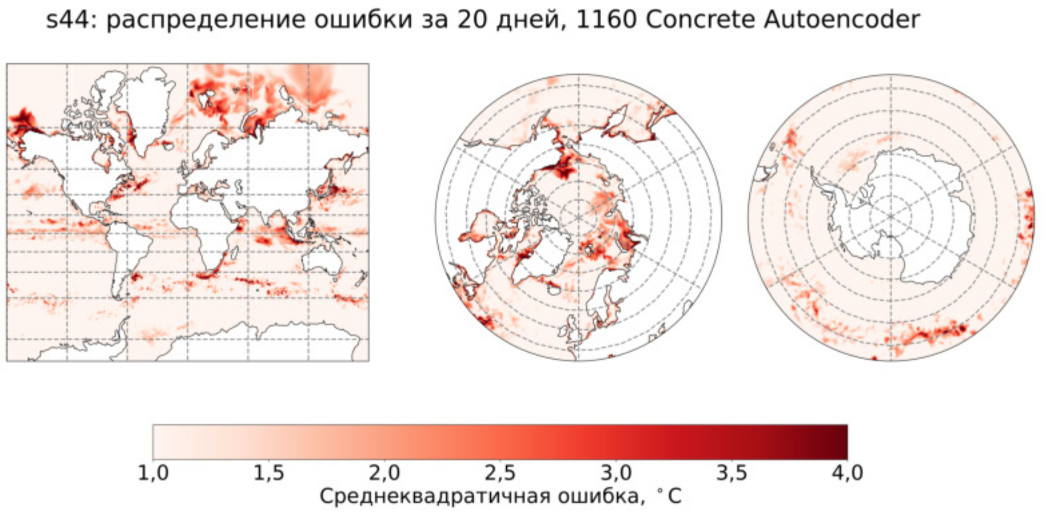

Рис. 18. Пространственное распределение ошибок температуры для фиксированной расстановки CA, 1160 сенсоров.

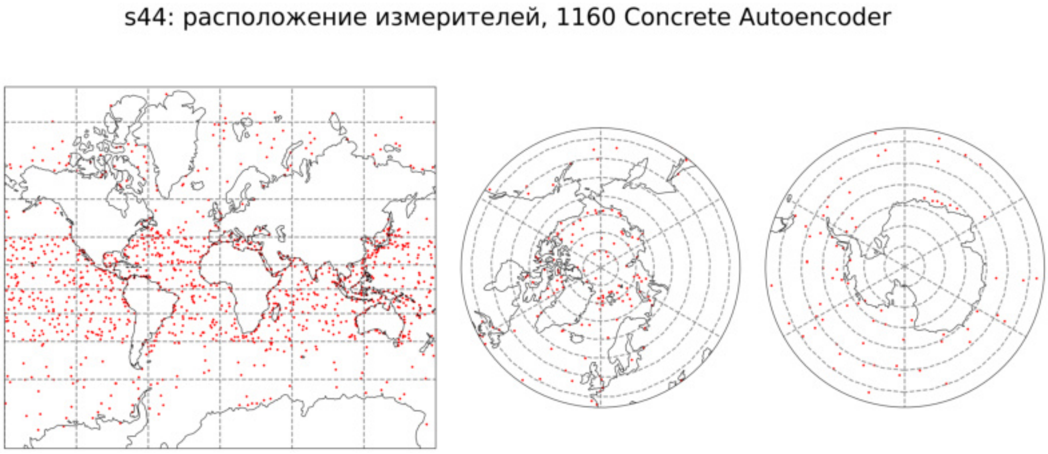

Рис. 19. Расположение 1160 сенсоров, полученное методом Concrete Autoencoder.

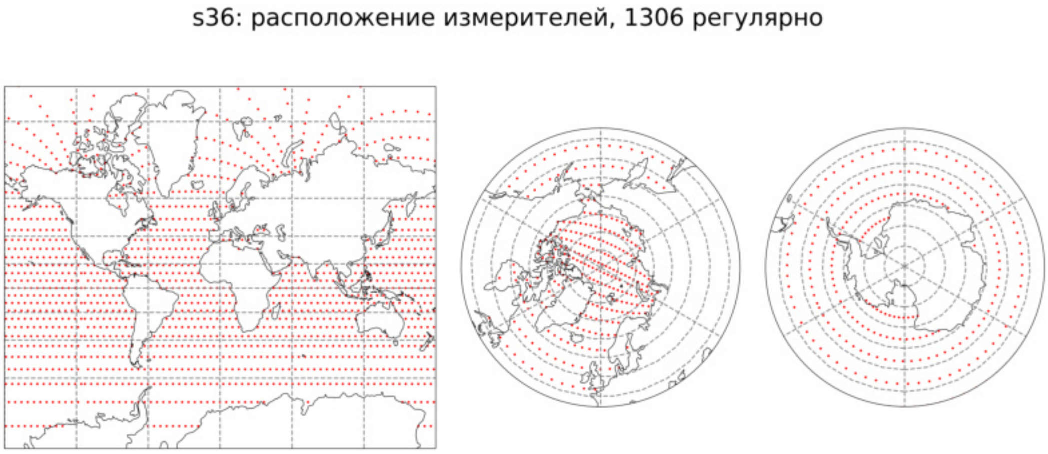

Рис. 20. Расположение 1306 сенсоров, расставленных регулярно с шагом 5,25° по долготе и 6,25° по широте.

незначительно уступает по RMSE регулярной расстановке с тремя тысячами сенсоров при сопоставимой средней ошибке.

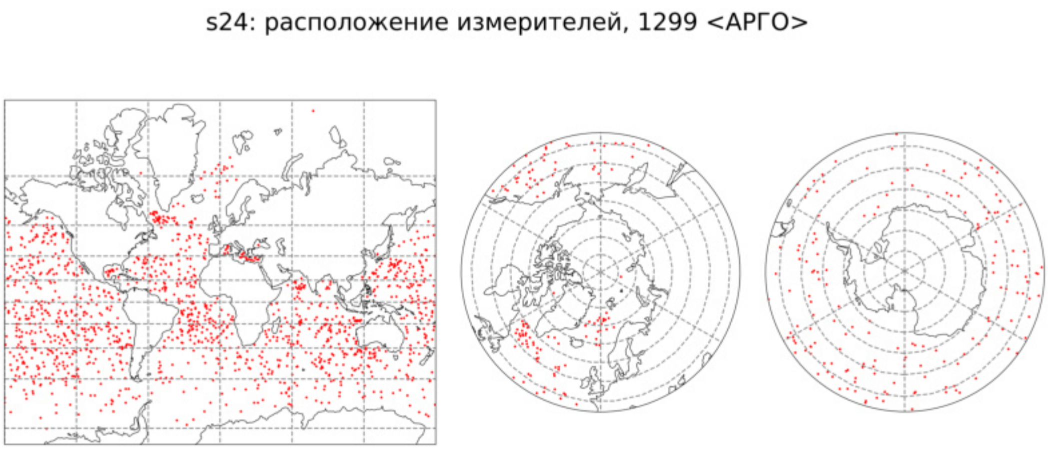

Рис. 21. Расположение 1299 сенсоров, расставленных в соответствии с координатами буев проекта АРГО, проводивших измерения в течение 4 суток, начиная с 2020-09-11.

Анализируя динамику средней ошибки в сценарии s38, мы видим, что примерно за 2–3 итерации усвоения средняя ошибка (Bias) достигает квазистационарных значений. За 20 дней все методы приближаются к одной и той же динамике профилей температуры, и значения среднеквадратичной ошибки выходят на квазистационарный уровень. Это подтверждает наше предположение о том, что продление эксперимента на более чем 30–40 дней не приводит к новым результатам.

В результате детального анализа пространственного распределения среднеквадратичных ошибок в проведенных экспериментах (выше приведены результаты для s24, s25, s36 и s44) было установлено, что, несмотря на различия в абсолютных значениях ошибок, их форма и пространственные паттерны остаются стабильными в различных конфигурациях. Это наблюдение позволяет сделать вывод о том, что в некоторых регионах достоверность прогноза будет систематически выше, в то время как в других она может быть снижена.

Следует отметить, что Concrete Autoencoder был обучен восстанавливать поле температуры в тот же момент времени, в котором проводились измерения, что несколько отличается от рассматриваемой постановки, где измерялась точность прогноза на одни сутки. Несмотря на это, из трех сценариев s24, s36 и s44 с приблизительно одинаковым числом сенсоров, расстановка s44, полученная методом Concrete Autoencoder, приводит к самой быстрой сходимости физических полей к состоянию контрольного эксперимента и наименьшему значению RMSE.

Полученные результаты подчеркивают важность оптимальной расстановки измерительных устройств при планировании наблюдательной сети, так как за счет правильного расположения можно максимизировать точность прогнозирования при одновременном снижении затрат в процессе сбора данных наблюдений.

Благодарности. Работа выполнена в рамках государственного задания ИВМ РАН (тема №075-01132-23-01 – настройка системы усвоения данных, эксперименты на устойчивость), государственного задания ИО РАН (тема №FMWE-2021-0003 – построение модельной конфигурации океана и морского льда, проведение основной серии экспериментов на точность прогноза, обработка и анализ их результатов) и при финансовой поддержке гранта Российского научного фонда (проект №20-19-00615 – построение динамического размещения измерителей, анализ восстановленных полей в Арктике, анализ профилей). Расчет численных экспериментов проводился с использованием ресурсов суперкомпьютера Межведомственного суперкомпьютерного центра РАН (МСЦ РАН, https://www.jscc.ru/).

Список литературы

Кальницкий Л. Ю., Кауркин М. Н., Ушаков К. В. *и др.* Сезонная изменчивость циркуляции вод и морского льда в Северном Ледовитом океане в модели высокого разрешения // Известия Российской академии наук. Физика атмосферы и океана. — 2020. — Т. 56, № 5. — С. 598—610. — DOI: 10.31857/S0002351520050065.

Кауркин М. Н., Ибраев Р. А. Исследование чувствительности алгоритма усвоения малочисленных данных наблюдений в модели динамики океана // Морской гидрофизический журнал. — 2019. — Т. 35, № 2. — DOI: 10.22449/0233-7584-2019-2-105-113.

Кошляков М. Н., Тараканов Р. Ю. Введение в физическую океанографию. — Москва : МФТИ, 2014. — 142 с.

Abbasi M. R., Chegini V., Sadrinasab M., *et al.* Correcting the Sea Surface Temperature by Data Assimilation Over the Persian Gulf // Iranian Journal of Science and Technology, Transactions A: Science. — 2018. — Vol. 43, no. 1. — P. 141–149. — DOI: 10.1007/s40995-017-0357-z.

Abid A., Balin M. F., Zou J. Concrete Autoencoders for Differentiable Feature Selection and Reconstruction // Cornell University. — 2019. — Vol. abs/1901.09346. — DOI: 10.48550/ARXIV.1901.09346.

Alonso A. A., Frouzakis C. E., Kevrekidis I. G. Optimal sensor placement for state reconstruction of distributed process systems // AIChE Journal. — 2004. — Vol. 50, no. 7. — P. 1438–1452. — DOI: 10.1002/aic.10121.

Boyer T. P., Antonov J. I., Baranova O. K., *et al.* World ocean database 2013. — U. S. Department of Commerce, National Oceanic, Atmospheric Administration, National Environmental Satellite, Data, Information Service, National Oceanographic Data Center, Ocean Climate Laboratory, 2013. — DOI: 10.7289/V5NZ85MT.

Clark E., Askham T., Brunton S. L., *et al.* Greedy Sensor Placement With Cost Constraints // IEEE Sensors Journal. — 2019. — Vol. 19, no. 7. — P. 2642–2656. — DOI: 10.1109/JSEN.2018.2887044.

Covert I., Qiu W., Lu M., *et al.* Learning to Maximize Mutual Information for Dynamic Feature Selection // Proceedings of the 40th International Conference on Machine Learning. — Honolulu, Hawaii, USA : PMLR 202, 2023. — DOI: 10.48550/arXiv.2301.00557.

Desai S. Jason-3 GPS based orbit and SSHA OGDR. — 2016. — DOI: 10.5067/J3L2G-OGDRF.

Fadeev R. Y., Ushakov K. V., Tolstykh M. A., *et al.* Design and development of the SLAV-INMIO-CICE coupled model for seasonal prediction and climate research // Russian Journal of Numerical Analysis and Mathematical Modelling. — 2018. — Vol. 33, no. 6. — P. 333–340. — DOI: 10.1515/rnam-2018-0028.

Hersbach H., Bell B., Berrisford P., *et al.* The ERA5 global reanalysis // Quarterly Journal of the Royal Meteorological Society. — 2020. — Vol. 146, no. 730. — P. 1999–2049. — DOI: 10.1002/qj.3803.

Huijben I. A. M., Veeling B. S., Sloun R. J. G. van. Deep probabilistic subsampling for taskadaptivecompressed sensing // International Conference on Learning Representations 2020. — ICLR, 2020.

Hunke E. C., Lipscomb W. H., Turner A. K., *et al.* CICE: The Los Alamos Sea ice Model Documentation and Software User's Manual Version 5 (Tech. Rep. LA-CC-06-012). — Los Alamos National Laboratory, 2015.

Jang E., Gu S., Poole B. Categorical Reparameterization with Gumbel-Softmax // Cornell University. — 2016. — Vol. abs/1611.01144. — DOI: 10.48550/arXiv.1611.01144.

Kalmykov V. V., Ibrayev R. A., Kaurkin M. N., *et al.* Compact Modeling Framework v3.0 for high-resolution global ocean-ice-atmosphere models // Geoscientific Model Development. — 2018. — Vol. 11, no. 10. — P. 3983–3997. — DOI: 10.5194/gmd-11-3983-2018.

Kaurkin M. N., Ibrayev R. A., Belyaev K. P. Data assimilation in the ocean circulation model of high spatial resolution using the methods of parallel programming // Russian Meteorology and Hydrology. — 2016a. — Vol. 41, no. 7. — P. 479–486. — DOI: 10.3103/S1068373916070050.

Kaurkin M. N., Ibrayev R. A., Koromyslov A. EnOI-Based Data Assimilation Technology for Satellite Observations and ARGO Float Measurements in a High Resolution Global Ocean Model Using the CMF Platform // Supercomputing. — Springer International Publishing, 2016b. — P. 57–66. — DOI: 10.1007/978-3-319-55669-7_5.

Krause A., Singh A., Guestrin C. Near-optimal sensor placements inGaussian processes: Theory, efficient algorithms and empirical studies // Journal of Machine Learning Research. — 2008. — Vol. 9, no. 2.

Kumar P., El Sayed Y. M., Semaan R. Optimized sensor placement using stochastic estimation for a flow over a 2D airfoil with Coanda blowing // 7th AIAA Flow Control Conference. — American Institute of Aeronautics, Astronautics, 2014. — DOI: 10.2514/6.2014-2101.

Lavergne T., Sørensen A. M., Kern S., *et al.* Version 2 of the EUMETSAT OSI SAF and ESA CCI sea-ice concentration climate data records // The Cryosphere. — 2019. — Vol. 13, no. 1. — P. 49–78. — DOI: 10.5194/tc-13-49-2019.

Li X., Wang S., Cai Y. Tutorial: Complexity analysis of Singular Value Decomposition and its variants // Cornell University. — 2019. — Vol. abs/1906.12085. — DOI: 10.48550/arXiv.1906.12085.

Lobashev A. A., Turko N. A., Ushakov K. V., *et al.* Concrete Autoencoder for the Reconstruction of Sea Temperature Field from Sparse Measurements // Journal of Marine Science and Engineering. — 2023. — Vol. 11, no. 2. — P. 404. — DOI: 10.3390/jmse11020404.

Maddison C. J., Mnih A., Teh Y. W. The Concrete Distribution: A Continuous Relaxation of Discrete Random Variables // Cornell University. — 2016. — Vol. abs/1611.00712. — DOI: 10.48550/arXiv.1611.00712.

Manohar K., Brunton B. W., Kutz J. N., *et al.* Data-Driven Sparse Sensor Placement for Reconstruction: Demonstrating the Benefits of Exploiting Known Patterns // IEEE Control Systems. — 2018. — Vol. 38, no. 3. — P. 63–86. — DOI: 10.1109/MCS.2018.2810460.

Murray R. J. Explicit Generation of Orthogonal Grids for Ocean Models // Journal of Computational Physics. — 1996. — Vol. 126, no. 2. — P. 251–273. — DOI: 10.1006/jcph.1996.0136.

Nagata T., Nonomura T., Nakai K., *et al.* Data-Driven Sparse Sensor Selection Based on A-Optimal Design of Experiment With ADMM // IEEE Sensors Journal. — 2021. — Vol. 21, no. 13. — P. 15248–15257. — DOI: 10.1109/JSEN.2021.3073978.

Nakai K., Yamada K., Nagata T., *et al.* Effect of Objective Function on Data-Driven Greedy Sparse Sensor Optimization // IEEE Access. — 2021. — Vol. 9. — P. 46731–46743. — DOI: 10.1109/ACCESS.2021.3067712.

Nguyen L., Hu G., Spanos C. J. Efficient Sensor Deployments for Spatio-Temporal Environmental Monitoring // IEEE Transactions on Systems, Man, and Cybernetics: Systems. — 2020. — Vol. 50, no. 12. — P. 5306–5316. — DOI: 10.1109/TSMC.2018.2872041.

Pathak J., Subramanian S., Harrington P., *et al.* FourCastNet: A Global Data-driven High-resolution Weather Model using Adaptive Fourier Neural Operators // Cornell University. — 2022. — Vol. abs/2202.11214. — DOI: 10.48550/arXiv.2202.11214.

Ryan A. G., Regnier C., Divakaran P., *et al.* GODAE OceanView Class 4 forecast verification framework: global ocean inter-comparison // Journal of Operational Oceanography. — 2015. — Vol. 8, sup1. — s98–s111. — DOI: 10.1080/1755876X.2015.1022330.

Saito Y., Nonomura T., Yamada K., *et al.* Determinant-Based Fast Greedy Sensor Selection Algorithm // IEEE Access. — 2021. — Vol. 9. — P. 68535–68551. — DOI: 10.1109/ACCESS.2021.3076186.

Sallée J.-B., Pellichero V., Akhoudas C., *et al.* Summertime increases in upper-ocean stratification and mixed-layer depth // Nature. — 2021. — Vol. 591, no. 7851. — P. 592–598. — DOI: 10.1038/s41586-021-03303-x.

Sun S., Liu S., Liu J., *et al.* Wind Field Reconstruction Using Inverse Process With Optimal Sensor Placement // IEEE Transactions on Sustainable Energy. — 2019. — Vol. 10, no. 3. — P. 1290–1299. — DOI: 10.1109/TSTE.2018.2865512.

Turko N., Lobashev A., Ushakov K., *et al.* Information Entropy Initialized Concrete Autoencoder for Optimal Sensor Placement and Reconstruction of Geophysical Fields // Supercomputing. — Springer International Publishing, 2022. — P. 167–184. — DOI: 10.1007/978-3-031-22941-1_12.

Turpin V., Remy E., Traon P. Y. L. How essential are Argo observations to constrain a global ocean data assimilation system? // Ocean Science. — 2016. — Vol. 12, no. 1. — P. 257–274. — DOI: 10.5194/os-12-257-2016.

Ushakov K. V., Ibrayev R. A. Assessment of mean world ocean meridional heat transport characteristics by a high-resolution model // Russian Journal of Earth Sciences. — 2018. — Vol. 18, no. 1. — DOI: 10.2205/2018ES000616.

Wong A. P. S., Wijffels S. E., Riser S. C., *et al.* Argo Data 1999–2019: Two Million Temperature-Salinity Profiles and Subsurface Velocity Observations From a Global Array of Profiling Floats // Frontiers in Marine Science. — 2020. — Vol. 7. — DOI: 10.3389/fmars.2020.00700.

Russian Journal of Earth Sciences

Global Ocean Forecast Accuracy Improvement Due to Optimal Sensor Placement

Nikita Turko[**,1], **Alexander Lobashev**[2], **Konstantin Ushakov**[1,3], **Maxim Kaurkin**[1], **Leonid Kalnitskii**[4], **Sergey Semin**[5], **Rashit Ibrayev**[1,3,6]

[1]Shirshov Institute of Oceanology, Russian Academy of Sciences, Moscow, Russia
[2]Skolkovo Institute of Science and Technology, Moscow, Russia
[3]Moscow Institute of Physics and Technology, Dolgoprudny, Russia
[4]Arctic and Antarctic Research Institute, Saint Petersburg, Russia
[5]Nuclear Safety Institute, Russian Academy of Sciences, Moscow, Russia
[6]Marchuk Institute of Numerical Mathematics, Russian Academy of Sciences, Moscow, Russia
**Correspondence to: Nikita A. Turko, NikitaTurko@yandex.ru

The paper examines the impact of sensor placement on the accuracy of the Global ocean state forecasting. A comparison is made between various sensor placement methods, including the arrangement obtained by the Concrete Autoencoder method. To evaluate how sensor placement affects forecast accuracy, a simulation was conducted that emulates a scenario where the initial state of the global ocean significantly deviates from the ground truth. In the experiment, initial conditions for the ocean and ice model were altered, while atmospheric forcing was retained from the control experiment. Subsequently, the model was integrated with the assimilation of data about the ground truth state at the sensor locations. The results showed that the sensor placement obtained using deep learning methods is superior in forecast accuracy to other considered arrays with a comparable number of sensors.

Keywords: operational forecast, Global ocean, optimal sensor placement, Concrete Autoencoder, data assimilation

Recieved: 25 August 2023
Accepted: 15 December 2023
Published: 30 December 2023

Citation: Turko, N., A. Lobashev, K. Ushakov, L. Kalnitsckii, M. Kaurkin, S. Semin, and R. Ibrayev (2023), Global Ocean Forecast Accuracy Improvement Due to Optimal Sensor Placement, *Russian Journal of Earth Sciences*, 23, ES6005, https://doi.org/10.2205/2023ES000883 EDN: UOMRDC

References

Abbasi M. R., Chegini V., Sadrinasab M., *et al.* Correcting the Sea Surface Temperature by Data Assimilation Over the Persian Gulf // Iranian Journal of Science and Technology, Transactions A: Science. — 2018. — Vol. 43, no. 1. — P. 141–149. — DOI: 10.1007/s40995-017-0357-z.

Abid A., Balin M. F., Zou J. Concrete Autoencoders for Differentiable Feature Selection and Reconstruction // Cornell University. — 2019. — Vol. 1. — DOI: 10.48550/ARXIV.1901.09346.

Alonso A. A., Frouzakis C. E., Kevrekidis I. G. Optimal sensor placement for state reconstruction of distributed process systems // AIChE Journal. — 2004. — Vol. 50, no. 7. — P. 1438–1452. — DOI: 10.1002/aic.10121.

Boyer T. P., Antonov J. I., Baranova O. K., *et al.* World ocean database 2013. — U. S. Department of Commerce, National Oceanic, Atmospheric Administration, National Environmental Satellite, Data, Information Service, National Oceanographic Data Center, Ocean Climate Laboratory, 2013. — DOI: 10.7289/V5NZ85MT.

Clark E., Askham T., Brunton S. L., *et al.* Greedy Sensor Placement With Cost Constraints // IEEE Sensors Journal. — 2019. — Vol. 19, no. 7. — P. 2642–2656. — DOI: 10.1109/JSEN.2018.2887044.

Covert I., Qiu W., Lu M., *et al.* Learning to Maximize Mutual Information for Dynamic Feature Selection // Proceedings of the 40 th International Conference on Machine Learning. — Honolulu, Hawaii, USA : PMLR 202, 2023. — DOI: 10.48550/arXiv.2301.00557.

Desai S. Jason-3 GPS based orbit and SSHA OGDR. — 2016. — DOI: 10.5067/J3L2G-OGDRF. — URL: https://podaac.jpl.nasa.gov/dataset/JASON_3_L2_OST_OGDR_GPS.

Fadeev R. Y., Ushakov K. V., Tolstykh M. A., *et al.* Design and development of the SLAV-INMIO-CICE coupled model for seasonal prediction and climate research // Russian Journal of Numerical Analysis and Mathematical Modelling. — 2018. — Vol. 33, no. 6. — P. 333–340. — DOI: 10.1515/rnam-2018-0028.

Hersbach H., Bell B., Berrisford P., *et al.* The ERA5 global reanalysis // Quarterly Journal of the Royal Meteorological Society. — 2020. — Vol. 146, no. 730. — P. 1999–2049. — DOI: 10.1002/qj.3803.

Huijben I. A. M., Veeling B. S., Sloun R. J. G. van. Deep probabilistic subsampling for taskadaptivecompressed sensing // International Conference on Learning Representations 2020. — ICLR, 2020.

Hunke E. C., Lipscomb W. H., Turner A. K., *et al.* CICE: The Los Alamos Sea ice Model Documentation and Software User's Manual Version 5 (Tech. Rep. LA-CC-06-012). — Los Alamos National Laboratory, 2015.

Jang E., Gu S., Poole B. Categorical Reparameterization with Gumbel-Softmax // Cornell University. — 2016. — Vol. abs/1611.01144. — DOI: 10.48550/arXiv.1611.01144.

Kalmykov V. V., Ibrayev R. A., Kaurkin M. N., *et al.* Compact Modeling Framework v3.0 for high-resolution global ocean-ice-atmosphere models // Geoscientific Model Development. — 2018. — Vol. 11, no. 10. — P. 3983–3997. — DOI: 10.5194/gmd-11-3983-2018.

Kalnitskii L. Y., Kaurkin M. N., Ushakov K. V., *et al.* Seasonal Variability of Water and Sea-Ice Circulation in the Arctic Ocean in a High-Resolution Model // Izvestiya, Atmospheric and Oceanic Physics. — 2020. — Vol. 56, no. 5. — P. 522–533. — DOI: 10.1134/S0001433820050060. — URL: https://doi.org/10.1134/S0001433820050060.

Kaurkin M., Ibrayev R., Koromyslov A. EnOI-Based Data Assimilation Technology for Satellite Observations and ARGO Float Measurements in a High Resolution Global Ocean Model Using the CMF Platform // Supercomputing. — Springer International Publishing, 2016a. — P. 57–66. — DOI: 10.1007/978-3-319-55669-7_5.

Kaurkin M. N., Ibrayev R. A. Study of Sensitivity of the Algorithm for Assimilating Small Amount of Data in the Ocean Dynamics Model // Morskoy gidrofizicheskiy zhurnal. — 2019. — Vol. 35, no. 2. — DOI: 10.22449/0233-7584-2019-2-105-113.

Kaurkin M. N., Ibrayev R. A., Belyaev K. P. Data assimilation in the ocean circulation model of high spatial resolution using the methods of parallel programming // Russian Meteorology and Hydrology. — 2016b. — Vol. 41, no. 7. — P. 479–486. — DOI: 10.3103/S1068373916070050.

Koshlyakov M. N., Tarakanov R. Y. Introduction to Physical Oceanography. — Moscow : MIPT, 2014. — 142 p.

Krause A., Singh A., Guestrin C. Near-optimal sensor placements inGaussian processes: Theory, efficient algorithms and empirical studies // Journal of Machine Learning Research. — 2008. — Vol. 9, no. 2.

Kumar P., El Sayed Y. M., Semaan R. Optimized sensor placement using stochastic estimation for a flow over a 2D airfoil with Coanda blowing // 7th AIAA Flow Control Conference. — American Institute of Aeronautics, Astronautics, 2014. — DOI: 10.2514/6.2014-2101.

Lavergne T., Sørensen A. M., Kern S., *et al.* Version 2 of the EUMETSAT OSI SAF and ESA CCI sea-ice concentration climate data records // The Cryosphere. — 2019. — Vol. 13, no. 1. — P. 49–78. — DOI: 10.5194/tc-13-49-2019.

Li X., Wang S., Cai Y. Tutorial: Complexity analysis of Singular Value Decomposition and its variants // Cornell University. — 2019. — Vol. abs/1906.12085. — DOI: 10.48550/arXiv.1906.12085.

Lobashev A. A., Turko N. A., Ushakov K. V., *et al.* Concrete Autoencoder for the Reconstruction of Sea Temperature Field from Sparse Measurements // Journal of Marine Science and Engineering. — 2023. — Vol. 11, no. 2. — P. 404. — DOI: 10.3390/jmse11020404.

Maddison C. J., Mnih A., Teh Y. W. The Concrete Distribution: A Continuous Relaxation of Discrete Random Variables // Cornell University. — 2016. — Vol. abs/1611.00712. — DOI: 10.48550/arXiv.1611.00712.

Manohar K., Brunton B. W., Kutz J. N., *et al.* Data-Driven Sparse Sensor Placement for Reconstruction: Demonstrating the Benefits of Exploiting Known Patterns // IEEE Control Systems. — 2018. — Vol. 38, no. 3. — P. 63–86. — DOI: 10.1109/MCS.2018.2810460.

Murray R. J. Explicit Generation of Orthogonal Grids for Ocean Models // Journal of Computational Physics. — 1996. — Vol. 126, no. 2. — P. 251–273. — DOI: 10.1006/jcph.1996.0136.

Nagata T., Nonomura T., Nakai K., *et al.* Data-Driven Sparse Sensor Selection Based on A-Optimal Design of Experiment With ADMM // IEEE Sensors Journal. — 2021. — Vol. 21, no. 13. — P. 15248–15257. — DOI: 10.1109/JSEN.2021.3073978.

Nakai K., Yamada K., Nagata T., *et al.* Effect of Objective Function on Data-Driven Greedy Sparse Sensor Optimization // IEEE Access. — 2021. — Vol. 9. — P. 46731–46743. — DOI: 10.1109/ACCESS.2021.3067712.

Nguyen L., Hu G., Spanos C. J. Efficient Sensor Deployments for Spatio-Temporal Environmental Monitoring // IEEE Transactions on Systems, Man, and Cybernetics: Systems. — 2020. — Vol. 50, no. 12. — P. 5306–5316. — DOI: 10.1109/TSMC.2018.2872041.

Pathak J., Subramanian S., Harrington P., *et al.* FourCastNet: A Global Data-driven High-resolution Weather Model using Adaptive Fourier Neural Operators // Cornell University. — 2022. — Vol. abs/2202.11214. — DOI: 10.48550/arXiv.2202.11214.

Ryan A. G., Regnier C., Divakaran P., *et al.* GODAE OceanView Class 4 forecast verification framework: global ocean inter-comparison // Journal of Operational Oceanography. — 2015. — Vol. 8, sup1. — s98–s111. — DOI: 10.1080/1755876X.2015.1022330.

Saito Y., Nonomura T., Yamada K., *et al.* Determinant-Based Fast Greedy Sensor Selection Algorithm // IEEE Access. — 2021. — Vol. 9. — P. 68535–68551. — DOI: 10.1109/ACCESS.2021.3076186.

Sallée J.-B., Pellichero V., Akhoudas C., *et al.* Summertime increases in upper-ocean stratification and mixed-layer depth // Nature. — 2021. — Vol. 591, no. 7851. — P. 592–598. — DOI: 10.1038/s41586-021-03303-x.

Sun S., Liu S., Liu J., *et al.* Wind Field Reconstruction Using Inverse Process With Optimal Sensor Placement // IEEE Transactions on Sustainable Energy. — 2019. — Vol. 10, no. 3. — P. 1290–1299. — DOI: 10.1109/TSTE.2018.2865512.

Turko N., Lobashev A., Ushakov K., *et al.* Information Entropy Initialized Concrete Autoencoder for Optimal Sensor Placement and Reconstruction of Geophysical Fields // Supercomputing. — Springer International Publishing, 2022. — P. 167–184. — DOI: 10.1007/978-3-031-22941-1_12.

Turpin V., Remy E., Traon P. Y. L. How essential are Argo observations to constrain a global ocean data assimilation system? // Ocean Science. — 2016. — Vol. 12, no. 1. — P. 257–274. — DOI: 10.5194/os-12-257-2016.

Ushakov K. V., Ibrayev R. A. Assessment of mean world ocean meridional heat transport characteristics by a high-resolution model // Russian Journal of Earth Sciences. — 2018. — Vol. 18, no. 1. — DOI: 10.2205/2018ES000616.

Wong A. P. S., Wijffels S. E., Riser S. C., *et al.* Argo Data 1999–2019: Two Million Temperature-Salinity Profiles and Subsurface Velocity Observations From a Global Array of Profiling Floats // Frontiers in Marine Science. — 2020. — Vol. 7. — DOI: 10.3389/fmars.2020.00700.

Russian Journal of Earth Sciences

Динамика оседания и осадконакопления приозерной части дельты р. Риты в зоне разрывов на северо-западном побережье оз. Байкал

О. В. Лунина[*,1] **и А. А. Гладков**[1,2]

[1]Институт земной коры СО РАН, Иркутск, Россия
[2]ГАУ ДО ИО «Центр развития дополнительного образования детей», Иркутск, Россия
* **Контакт:** Оксана Викторовна Лунина, lounina@crust.irk.ru

В связи с активным освоением речных дельт их оседание является одной из ключевых проблем жизнедеятельности человека. Процесс закономерный и зависит от многих факторов, влияние которых еще недостаточно изучено. Нами проведено исследование, цель которого заключалась в выявлении изменений земной поверхности приозерной части дельты р. Риты в зоне ранее выявленных разрывов на северо-западном побережье оз. Байкал. Оценка топографических изменений выполнялась путем расчета разницы между разновременными цифровыми моделями местности (ЦММ), полученными на двух локальных участках по данным беспилотной аэрофотосъемки сверхвысокого разрешения в 2020 и 2021 гг. В результате установлено, что оседание приозерной части дельты за 11 месяцев и 19 дней произошло в среднем на 5–10 см. Эти значения ассоциируются с естественным уплотнением осадков. В местах их накопления аградация происходит на аналогичные величины, уравновешивая баланс отложений. В выходах сейсмогравитационных нарушений в отсутствии наносов просадки достигли 33–37 см, что указывает на активные эндогенные и экзогенные процессы в зоне Кочериковского разлома. Наибольшие отрицательные и положительные вертикальные изменения рельефа до 40 см произошли в пределах пляжа и связаны с волноприбойной деятельностью. Самая крайняя заболоченная часть мыса Рытого испытала максимальное опускание за год. Наибольшее накопление аллювия произошло на южном участке дельты р. Риты в понижении, выраженном в рельефе местности и совпадающим с зоной современных разрывов, а также в аккумулятивном потоке, перекрывающем зону поверхностных нарушений. За исключением этой части, несмотря на интенсивные наносы, разрывы хорошо проявлены на ЦММ, а значит, продолжают развиваться. Сравнение разновременных ЦММ путем вычитания высотных отметок для каждого узла (пикселя) модели является перспективным и недорогим методом для целей мониторинга деформаций земной поверхности.

Ключевые слова: зона разрывов, дельта, оседание, беспилотная аэрофотосъемка, цифровая модель местности, Байкал

Цитирование: Лунина, О. В. и А. А. Гладков Динамика оседания и осадконакопления приозерной части дельты р. Риты в зоне разрывов на северо-западном побережье оз. Байкал // Russian Journal of Earth Sciences. — 2023. — Т. 23. — ES6006. — DOI: 10.2205/2023es000874 — EDN: HTCABO

https://elibrary.ru/htcabo

Получено: 30 июня 2023 г.
Принято: 22 сентября 2023 г.
Опубликовано: 30 декабря 2023 г.

1. Введение

Многие крупные речные дельты Земли сильно заселены и при этом испытывают интенсивное оседание, достигающее 5–10 см в год [*Schmidt*, 2015]. Оседание является закономерным и зависит от многих факторов, включающих накопление наносов, уплотнение осадков, их нагрузку на нижележащие толщи, уровень воды в водоеме, тектонику и антропогенную деятельность [*Higgins et al.*, 2014; *Loucks*, 2019; *Tessler et al.*, 2018]. Для изучения скорости этого процесса успешно используют технологии InSAR и LiDAR, которые позволяют оценивать изменения деформационного поля земной коры [*Hu et al.*, 2022; *Yang et al.*, 2022; *Zhong et al.*, 2022]. В указанных работах роль разрывных нарушений специально не рассматривается, хотя есть публикации, демонстрирующие выделение линейных зон активных деформаций по данным дифференциальной РСА-интерферометрии [*Лебедева и др.*, 2013]. Исходя их общих представлений, разрывы должны существенно влиять на локализацию процессов оседания и осадконакопления, что важно при оценке геологических опасностей территорий.

Учитывая остроту проблемы, связанной с жизнедеятельностью человека и поиском новых методов мониторинга окружающей среды, нами проведено исследование, цель которого заключалась в выявлении изменений земной поверхности приозерной части дельты р. Риты в зоне ранее выявленных сейсмогравитационных разрывов на северо-западном побережье оз. Байкал. Работа актуальна как в части развития побережий уникального озера, так и с точки зрения изучения особенностей современной динамики оседания и осадконакопления в дельтах горных рек.

Дельта р. Риты, образующая мыс Рытый, расположена на территории Байкало-Ленского заповедника, что исключает антропогенное воздействие на ее развитие, рассматриваемое во многих случаях ведущим фактором оседания крупных дельт. Выбор нашего объекта исследований обусловлен тем, что в 2019 г. в приозерной части дельты при ее аэрофотосъемке была случайно обнаружена зона разрывов общей протяженностью 2,9 км (рис. 1). Система нарушений четко локализована и разбивается на два сегмента – субмеридиональный и северо-восточный. Разрывы расположены в 30–150 м от берега оз. Байкал и представляют собой уступы высотой от 0,2 до 1,84 м, согласно измерениям 2019 г. Более подробную информацию о строении зоны разрывов, доказательствах ее связи с предшествующей тектонической структурой и инициирующим землетрясением 13.08.1962 г. с $M = 5{,}2$ можно найти в работе [*Лунина и Гладков*, 2022]. Здесь важно отметить, что обнаруженные деформации находятся в зоне Кочериковского разлома, активность которого подтверждается палеосейсмогенными разрывами, простирающимися в северо-восточном направлении на склонах Байкальского хребта и в тыловой части дельты р. Риты. В ~ 16 км на восток от мыса Рытого проходит предполагаемый меридиональный разлом, а в 10 км на юг в оз. Байкал фиксируется вытягивание изобат в направлении С–Ю прямо на субмеридиональный сегмент разрывов в дельте р. Риты. В связи с этим был сделан вывод, что несмотря на визуальное совпадение простирания современной зоны нарушений с береговой линией мыса, ее образование предопределено тектоникой. Существенную роль при этом несомненно сыграли гравитационные силы, усилившие процесс вторичного разрывообразования при сейсмическом сотрясении.

После неожиданной находки зоны современных разрывов в приозерной части дельты р. Риты на северо-западном побережье оз. Байкал возник новый не менее важный вопрос, а именно, как сейчас происходит развитие зоны в пространстве и времени. Отвечая на него, мы затронули более широкую проблему динамики оседания и осадконакопления приозерной части дельт горных рек.

2. Методика исследований

Для оценки топографических изменений земной поверхности в приозерной части дельты р. Риты нами использован расчет разницы между разновременными цифровыми моделями местности, полученными из данных беспилотной аэрофотосъемки сверхвысокого разрешения. Аналогичный подход использован при изучении ледников и оползней в работах [*Bearzot et al.*, 2022; *Rossini et al.*, 2018; *Valkaniotis et al.*, 2018].

Для исследований выбрано два участка в пределах субмеридионального и северо-восточного сегментов современной зоны разрывов (рис. 1), где в 2020 и 2021 гг. проведены повторные аэрофотосъемочные работы на более низкой высоте по сравнению с 2019 г. (табл. 1). В 2020 г. съемка выполнена с использованием беспилотного летательного аппарата (БПЛА) DJI Phantom 4 Pro V2.0, в 2021 г. – DJI Phantom 4 RTK. Оба коптера оснащены камерами одной модели с одинаковыми техническими характеристиками.

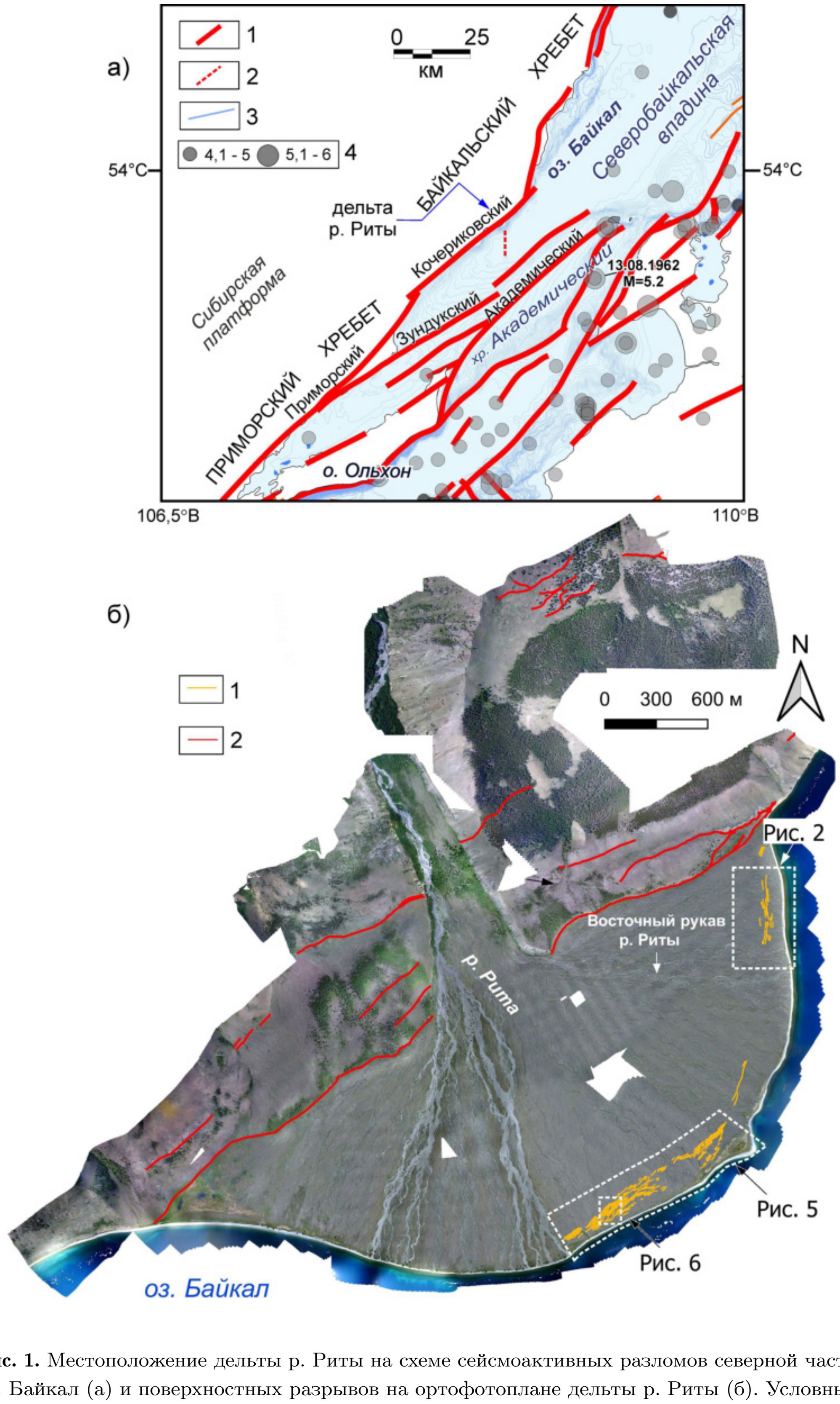

Рис. 1. Местоположение дельты р. Риты на схеме сейсмоактивных разломов северной части оз. Байкал (а) и поверхностных разрывов на ортофотоплане дельты р. Риты (б). Условные обозначения: а) 1 – сейсмоактивный разлом; 2 – упомянутый в тексте предполагаемый разлом; 3 – изобаты; 4 – землетрясения с $M > 4$; б) 1 – современный сейсмогравитационный разрыв; 2 – палеосейсмогенный разрыв.

Съемка проводилась в автоматическом режиме по полетным заданиям на одной и той же высоте (30 м), чтобы добиться идентичности пространственного разрешения, т.е. размера пикселя на местности.

По результатам работ по стандартной методике в программе «Agisoft Metashape» [*Agisoft LLC*, 2021] были построены ортофотопланы и цифровые модели местности (ЦММ), характеристики которых приведены в табл. 1. В 2021 году геодезическая привязка осуществлялась с помощью модуля RTK БПЛА и базовой станции D-RTK2, установленной в непосредственной близости от исследуемых участков. Для того, чтобы произвести сравнение ЦММ путем вычисления разницы высотных отметок, модель 2020 года была перепривязана по характерным стабильным на местности точкам (маркерам), выделенным на обеих моделях и ортофотопланах. Для проведения этой процедуры для субмеридинального участка был выделен 131 маркер, для северо-восточного – 200. В итоге геодезическая привязка ЦММ 2020 г. была скорректирована по координатам и высотам маркеров, взятым из модели 2021 г. Перед вычитанием разновременные ЦММ и ортофотопланы были приведены к одному пространственному разрешению (табл. 1). Последние использовались для визуального контроля соответствия ЦММ. После проведения процедур с помощью встроенного в программу «Agisoft Metashape» инструмента «рассчитать разницу» для каждого узла (пикселя) модели был выполнен расчет разницы между высотными отметками (из значений высотных характеристик 2021 г. были вычтены значения высотных характеристик 2020 г.). Такой подход позволил выявить относительные изменения высотных отметок внутри участка исследования и в то же время избежать проблем, связанных с погрешностью измерения координат.

Таблица 1. Характеристики ортофотопланов и ЦММ для участков аэрофотосъемки

Дата съемки	Место / высота съемки	Пространственное разрешение, см/пикс		Площадь, км^2	Количество использованных фотографий
		ортофотоплан	ЦММ		
30.06.2019 01.07.2019 05.07.2019	Дельта р. Риты и прилегающая площадь / 100–130 м	6–10	10–20	11,07	7000
03.07.2020	Субмеридиональный сегмент зоны разрывов в приозерной части дельты / 30 м	1,67	1,67	0,482	6390
22.06.2021		1,67	1,67	0,482	
03.07.2020	СВ сегмент зоны разрывов в приозерной части дельты / 30 м	3,29	3,29	0,569	7131
21.06.2021		3,29	3,29	0,569	4890

3. Результаты расчетов изменений земной поверхности

3.1. Субмеридиональный сегмент зоны разрывов

Субмеридиональный сегмент зоны разрывов простирается в северном секторе мыса Рытый, где в средней части полностью уничтожен восточным рукавом р. Риты с хорошо проработанными руслами глубиной в отдельных местах до 2,4 м (рис. 1). В северной части этого сегмента разрывы особенно отчетливо выражены на земной поверхности (рис. 2а, б и 3). Максимальные вертикальные смещения по ним колеблются от 0,33 м до 1,14 м, видимые длины разрывов – от 17,45 м до 129,6 м. В южной части субмеридионального сегмента два нарушения длиной 218 м и 43,28 м с градиентами исходных поверхностей 1,84 и 0,76 м, соответственно, плавно переходят в северо-восточный сегмент линейной зоны деформаций (рис. 1).

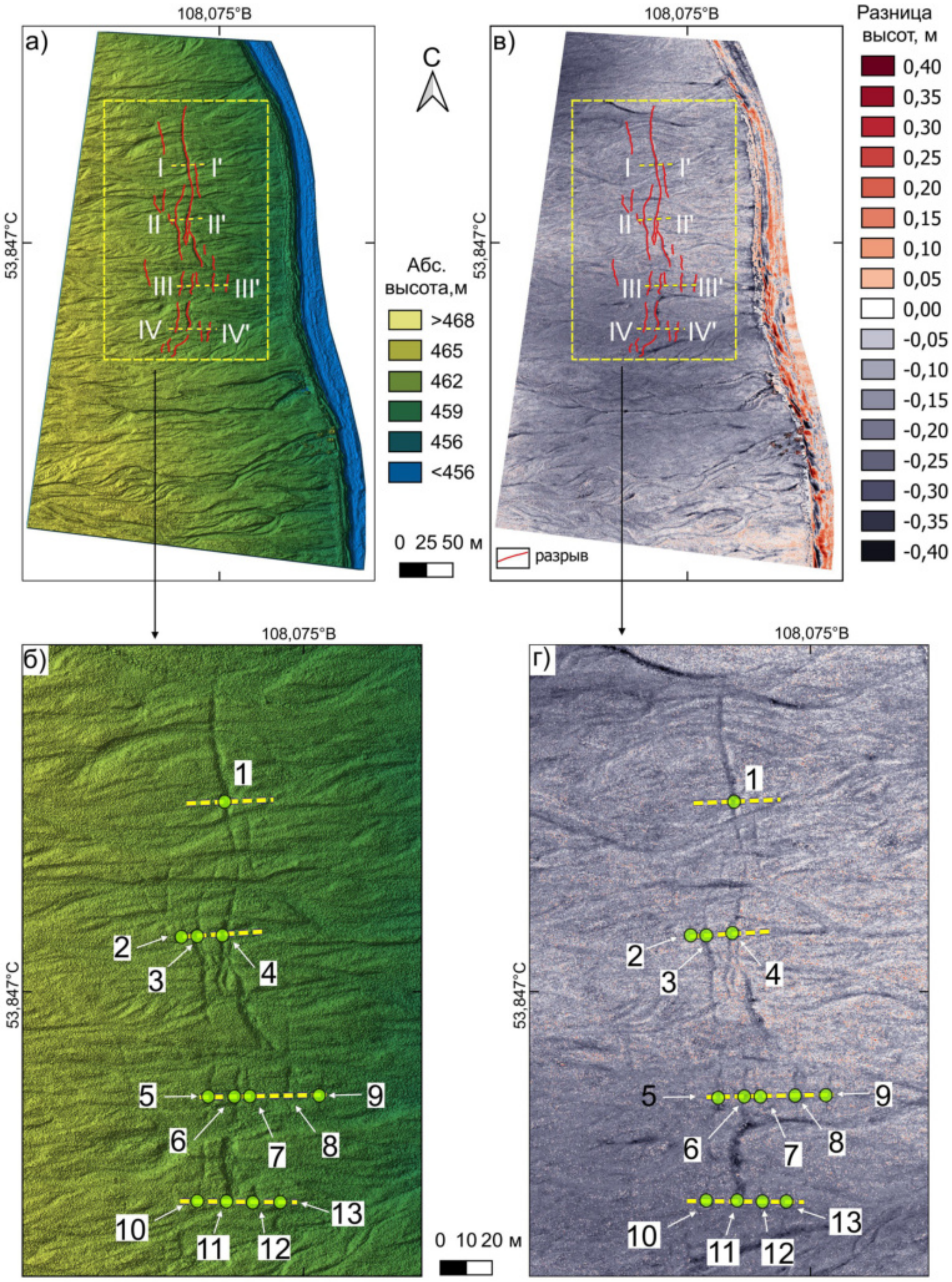

Рис. 2. ЦММ северного локального участка дельты р. Риты (а–б) и вертикальное изменение земной поверхности за период с 03.07.2020 по 22.06.2021 гг. (в–г). Римскими цифрами обозначены номера профилей, показанные на рис. 3, арабскими цифрами и зелеными кружками – выходы разрывов (показаны красными линиями на «а» и «в»).

Расчет разницы между двумя ЦММ показывает, что большая часть северной локальной площади дельты р. Риты опустилась в среднем на 5–10 см (рис. 2в, г и 3). В зоне разрывов субмеридионального простирания опускание проявилось еще больше, а просадки в линейных рвах в отдельных местах достигли 33–37 см, что позволило

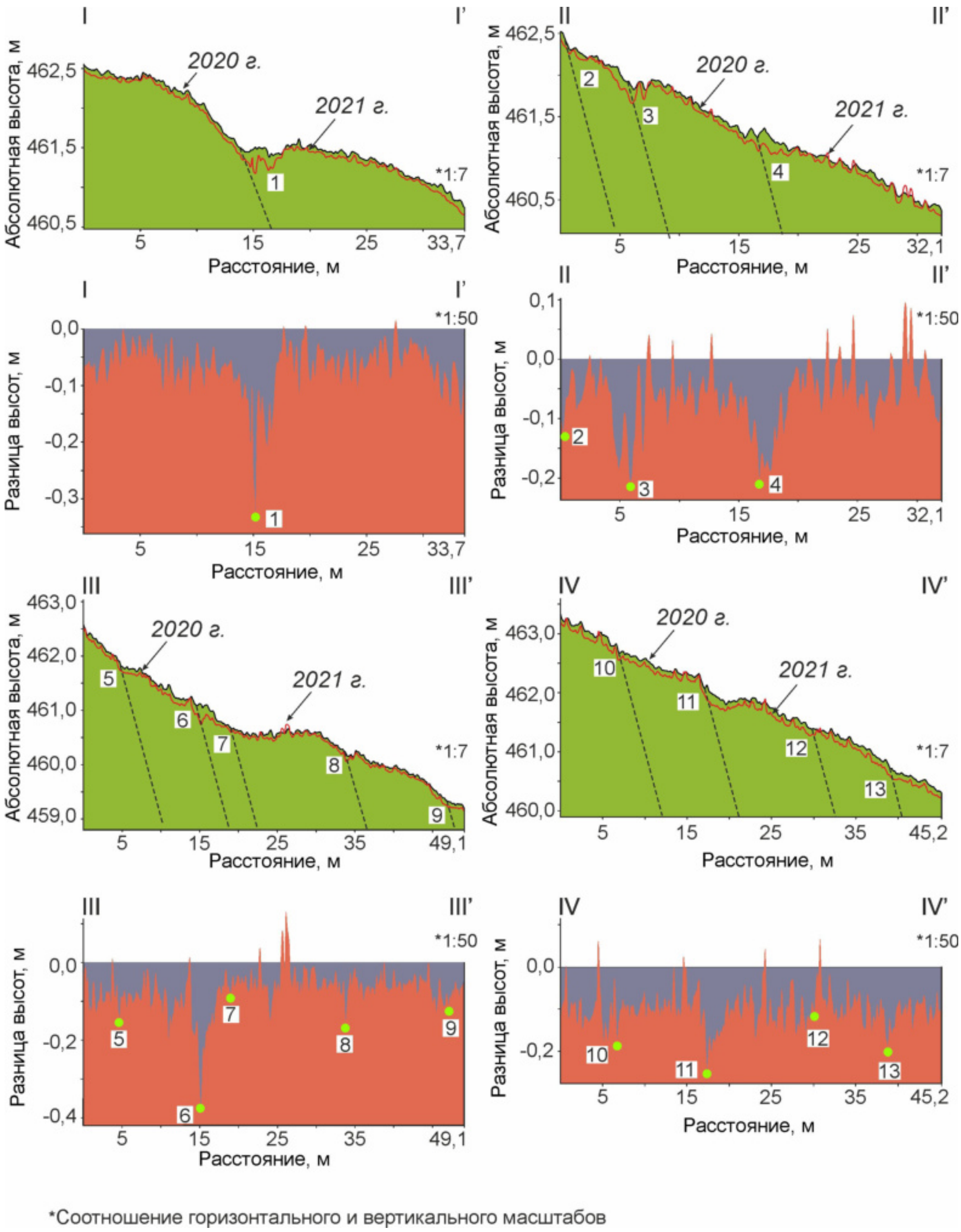

Рис. 3. Профили через современные сейсмогравитационные разрывы на северном участке, построенные по ЦММ, отражающим рельеф (зеленые) и разницу высот за период с 03.07.2020 по 22.06.2021 гг. (оранжевые). Римскими цифрами обозначены номера профилей, показанных на рис. 2, арабскими цифрами и зелеными кружками – выходы разрывов. Пунктир – условное падение разрыва.

идентифицировать нарушения даже на модели-разнице (рис. 2г). Некоторые временные, на момент съемки сухие, русла также локально углубились за счет эрозии. Отдельные аллювиальные обломки на поверхности дельты р. Риты были принесены ее водными потоками, но наибольшее накопление осадков до 40 см произошло в береговой части, что связано в основном с геологической деятельностью волн оз. Байкал.

Общее опускание и неравномерность просадок в месте выхода разрывов хорошо демонстрируются на поперечных профилях I–I′, II–II′, III–III′, IV–IV′ (рис. 2в и 3). На фоне сравнительно равномерного оседания дельты по всем разрезам, которое, вероятнее всего, обусловлено уплотнением осадков под собственным весом, в выходах разрывов на поверхность происходит скачок в разнице высот рельефа. Характерно, что одиночные разрывы, как на профиле I–I′, имеют изначально большую вертикальную амплитуду смещения (рис. 3) и тенденцию к увеличению величины просадки. Группирующиеся субпараллельные разрывы с изначально меньшими смещениями предполагают и меньшие изменения в высотах земной поверхности, хотя отдельные малоамплитудные нарушения, например, № 6 на профиле III–III′, показывают значительную разницу высот (37 см).

3.2. Северо-восточный сегмент зоны разрывов

Северо-восточный сегмент зоны представляет собой более распределенную систему нарушений длиной от 8,16 до 210 м (рис. 1 и 4). Максимально зафиксированные вертикальные смещения по ним изменяются от 0,2 до 1,14 м. На одном из участков зона частично размыта или перекрыта осадками, из-за чего там сохранились только фрагменты разрывов. В целом они представлены менее контрастно на местности из-за меньших амплитуд смещений. Многие нарушения не имеют абсолютного согласия с простиранием береговой линии. Правостороннее смещение одного из крупных сухих русел, возможно, мнимое, так как подобных сдвиговых смещений сопоставимой величины на ортофотоплане и ЦММ не наблюдается. В какой-то момент вода временного водотока могла устремиться по разрыву с большим вертикальным и раздвиговым смещением, чем на соседнем сегменте.

Величина опускания дельты р. Риты на южном участке также, как и на северном, в среднем изменилась на 5–10 см, что свидетельствует в целом о стабильной величине скорости оседания, связанной с уплотнением отложений и/или региональными тектоническими процессами (рис. 5). Однако местами она достигла 20 см, а в отдельных редких точках даже 30 см. В отличие от северного участка, здесь идет интенсивный снос осадков в пониженные части, поэтому большинство разрывов на «модели – разнице» подчеркиваются положительными значениями (рис. 5б, в), что связано с заполнением рвов. При этом, увеличение мощности грубообломочных отложений происходит примерно на те же величины (см. профиль V–V′ на рис. 5а). Поперечный разрез VI–VI′ через всю зону в наиболее широкой ее части показывает, что рвы некоторых разрывов на фоне их заполнения продуктами сноса продолжают просаживаться (рис. 6), но в целом этот процесс, как и осадконакопление, весьма неравномерный в пространстве.

Сопоставление гипсометрического профиля (рис. 6в) и профиля, демонстрирующего разницу высот за год VI–VI′ (рис. 6г), наглядно показывает, что уменьшение высоты рельефа происходит закономерно за счет переноса осадков в пониженные участки земной поверхности. При этом на графике разницы высот (рис. 6г) даже визуально видно, что отрицательных значений больше, чем положительных, что свидетельствует о том, что определенный вклад в оседание приозерной части дельты р. Риты вносит естественное уплотнение осадков и процессы разрывообразования. Это подтверждается результатами расчетов изменений земной поверхности и наблюдениями на северном участке дельты р. Риты, в месте распространения субмеридиональных разрывов, где современное осадконакопление практически отсутствует.

Профили VII–VII′ и VIII–VIII′ построены через единичные разрывы в местах отрицательных (VII–VII′) и положительных изменений (VIII–VIII′) рельефа (рис. 7). Первый из них показывает оседание дельты в месте, где не было заметного сноса осадков, что видно по следу положительных значений (рис. 7ж). Второй демонстрирует погребение висячего крыла разрыва под новыми осадками.

4. Обсуждение результатов

Изучение молодых движений берегов оз. Байкал начато более 100 лет назад *А. П. Орловым* [1870] и *И. Д. Черским* [1886], а обобщение работ их последователей было сделано в 1961 г. *Н. П. Ладохин и Е. К. Гречищев* [1961] пришли к заключению, что выводы предшественников, основанные на применении геоморфологических ме-

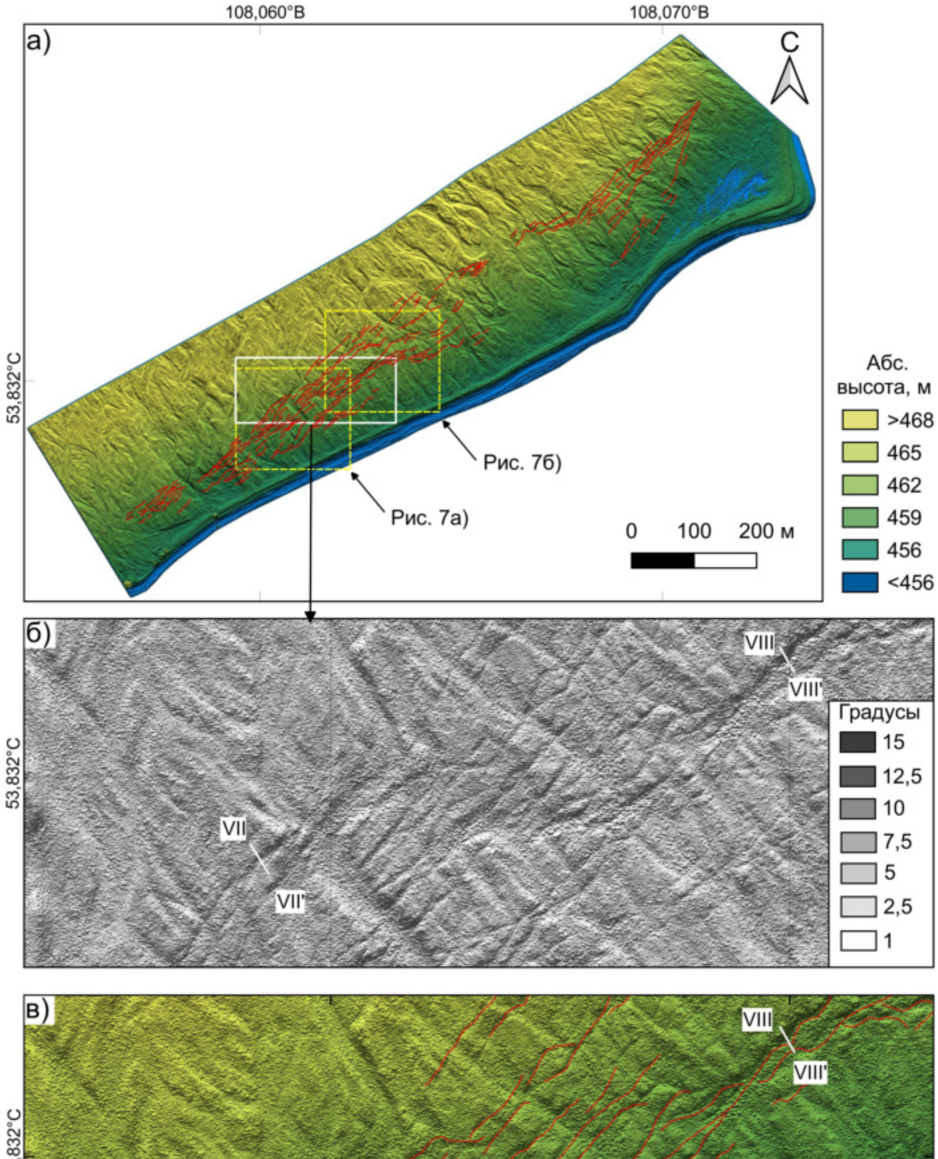

Рис. 4. ЦММ южного локального участка дельты р. Риты (а) и ее фрагменты (б–в). На «б» представлена ЦММ в виде карты углов наклона поверхности для более контрастного отображения современных разрывов. Римскими цифрами обозначены номера профилей, показанные на рис. 7, красными линиями на «а» и «в» – выходы разрывов.

тодов и инструментальных измерениях того времени имели весьма низкую точность, поэтому результаты получились весьма противоречивыми. В частности, дельта р. Риты, образующая мыс Рытый, по данным Н. В. Думитрашко и Г. Б. Пальшина относится к берегу поднятия, а по данным В. В. Ламакина она находится в нейтральном состоянии. Современные методы исследований земной поверхности, такие как GPS-геодезия, не охватывают северо-западное побережье оз. Байкал северо-восточнее пос. Онгурен,

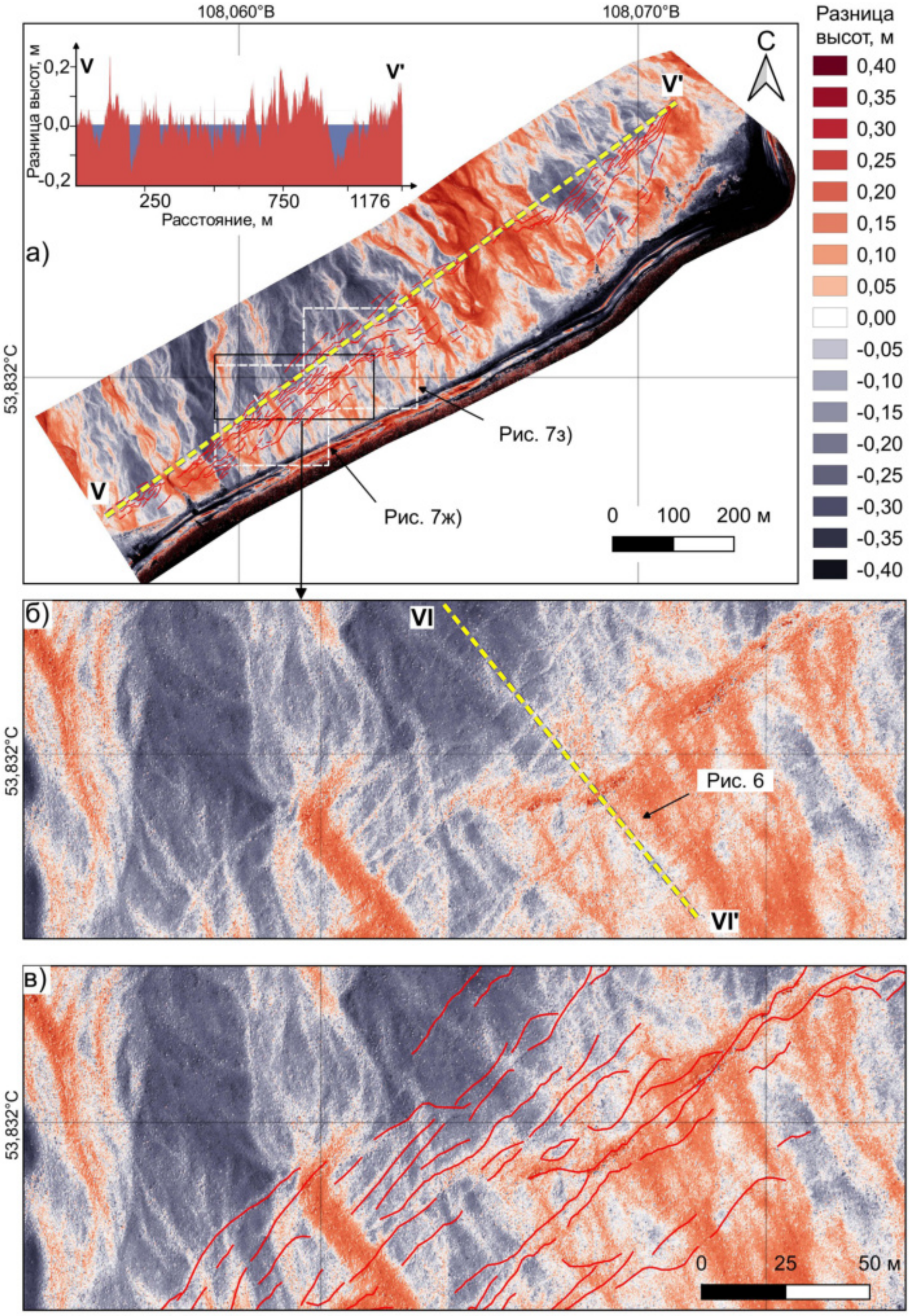

Рис. 5. Вертикальное изменение земной поверхности за период с 03.07.2020 по 22.06.2021 гг. на южном локальном участке (а) и его увеличенных фрагментах (б–в). Римскими цифрами обозначены номера профилей, показанные здесь и на рис. 6, красными линиями на «а» и «в» – современные сейсмогравитационные разрывы.

где расположен последний пункт GPS-наблюдений, показывающий горизонтальную скорость движения 2,1 мм/год на восток-юго-восток [*Lukhnev et al.*, 2013].

Наши исследования детальных участков дельты р. Риты по данным измерений земной поверхности в 2020–2021 гг. показали, что в целом ее приозерный край опускается со средней скоростью 5–10 см/год, что закономерно, так как дельта расположена в висячем крыле Кочериковского разлома, характеризующегося сбросовым типом подвижки. Наибольшие просадки происходят в зонах сейсмогравитационных разрывов

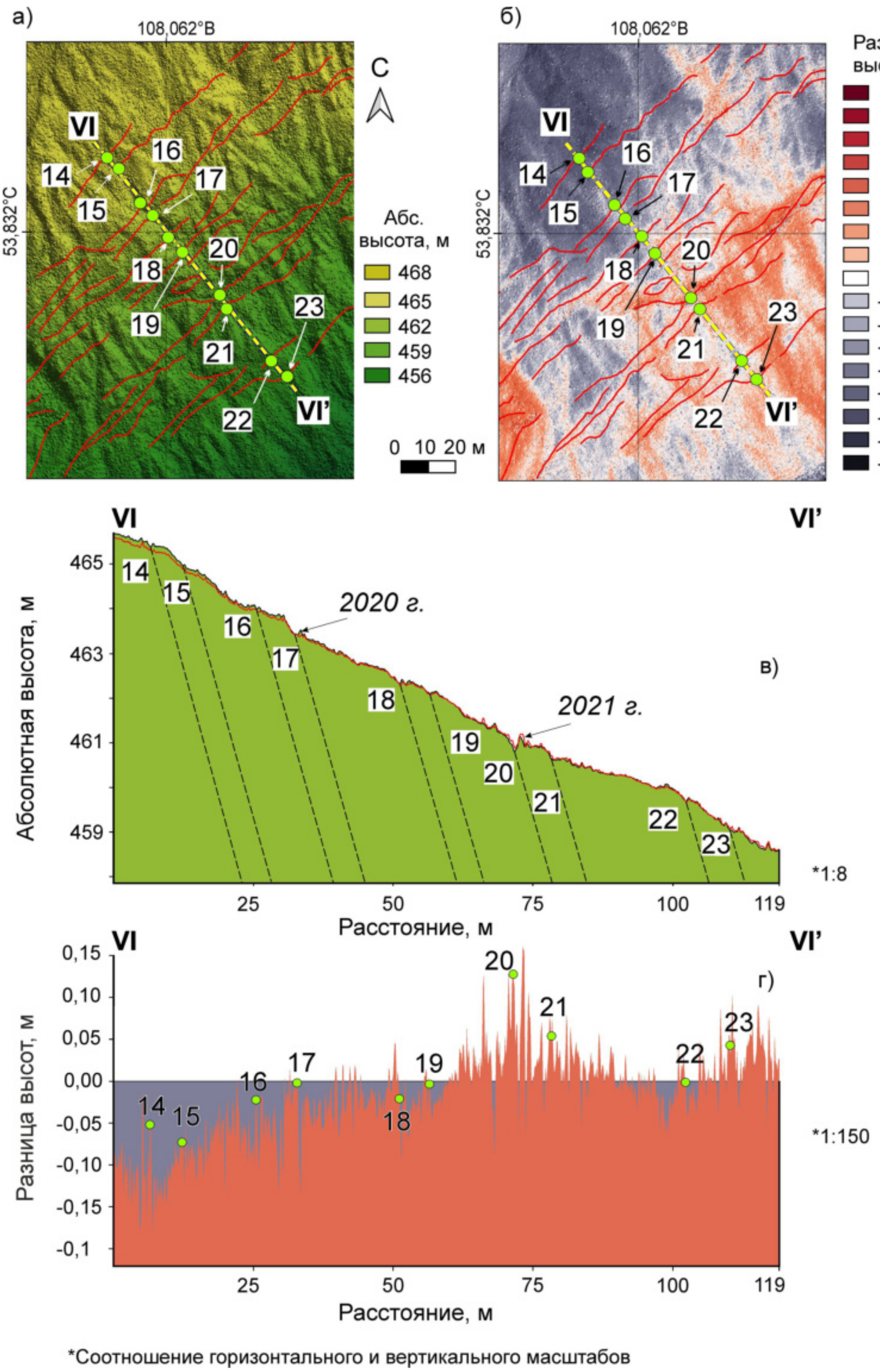

Рис. 6. Фрагмент ЦММ южного локального участка дельты р. Риты (а) и вертикальное изменение земной поверхности в его пределах за период с 03.07.2020 по 22.06.2021 гг. (б) с положением профиля VI через всю зону современных разрывов, построенного по ЦММ рельефа (в) и разнице высот (г). Арабскими цифрами и зелеными кружками обозначены выходы разрывов, показанные красными линиями на «а» и «б», пунктиром с условным падением на «в». См. положение профиля на рис. 5.

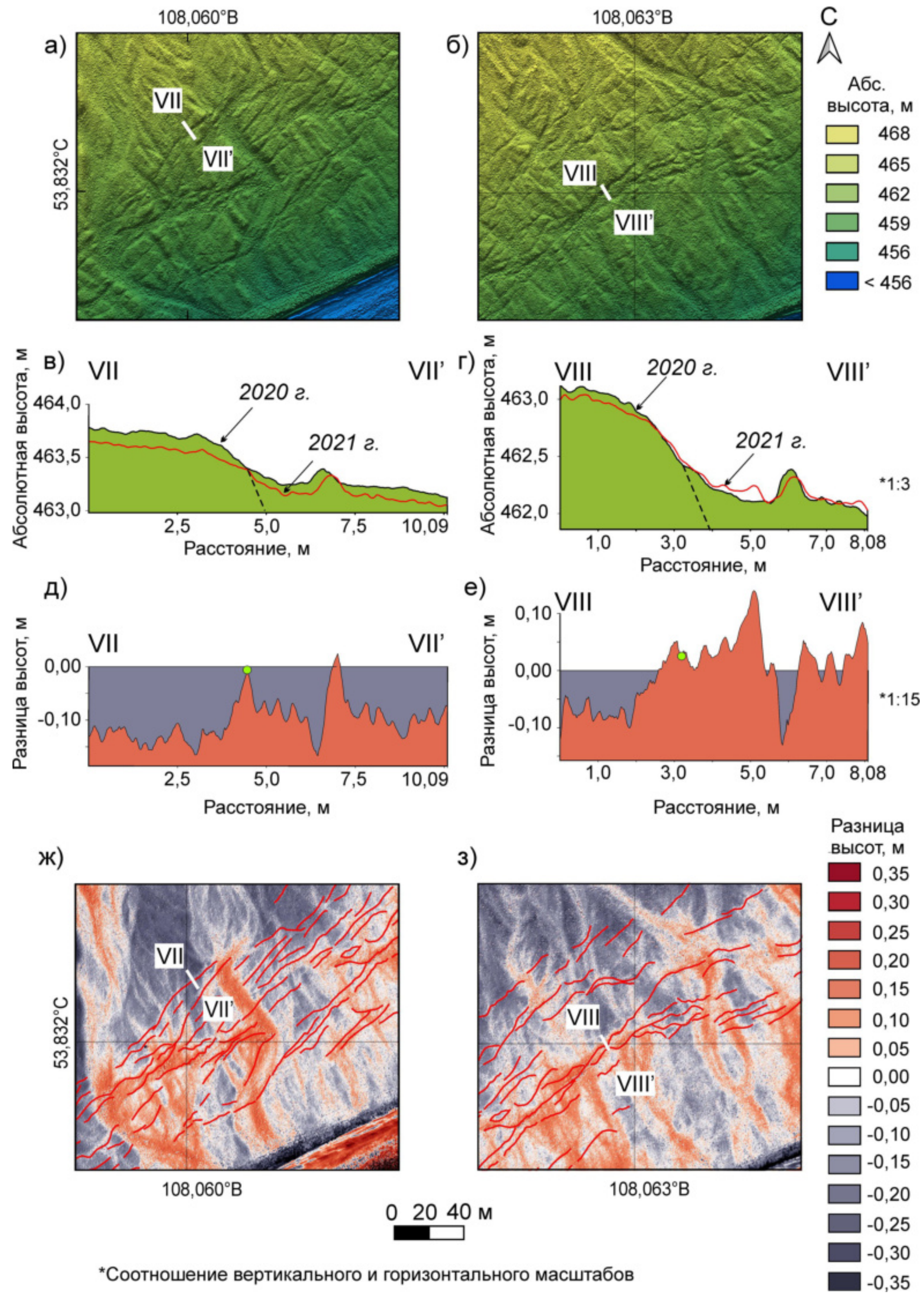

Рис. 7. Фрагменты ЦММ южного локального участка дельты р. Риты (а–б) и вертикальное изменение земной поверхности в его пределах за период с 03.07.2020 по 22.06.2021 гг. (ж–з) с положением профилей VII и VIII через отдельные разрывы, построенных по ЦММ (в–г) и разнице высот (д–е). Зелеными кружками на «д» и «е» и пунктиром с условным падением на «в» и «г» обозначены выходы разрывов, показанные красными линиями на «ж» и «з».

и могут достигать первых десятков см за год. Однако, такие высокие значения являются результатом комплекса факторов, к которым относятся оседание и уплотнение осадков под собственным весом, их перенос водными потоками с одного места на другое, эрозионная деятельность и в некоторой степени тектоника и сейсмичность. Если на северном участке практически не наблюдается новых отложений, за исключением озерных на берегу (рис. 2в), то на южном – отрицательные изменения земной поверхности в значительной мере компенсируются вновь принесенными осадками, отлагающимися в пониженных участках.

Учитывая заметную разницу в опускании на северном участке дельты р. Риты в целом и в осевых частях субмеридиональных разрывов (рис. 2г), следует признать, что тектонический и сейсмический факторы существенно увеличивают величины оседания, которые местами значительно выше значений для крупных речных дельт мира [*Tessler et al.*, 2018]. Так, среднегодовые скорости опускания дельты р. Хуанхэ составляют 0–3 см, а максимум достигает 7 см [*Liu et al.*, 2021]. Восточная часть дельты р. Ганг и р. Брахмапутра опускается в среднем со скоростью 0–1,8 см/год [*Higgins et al.*, 2014]. Проявление разрывов в рельефе северо-восточного сегмента зоны даже на фоне их заполнения осадками (рис. 5), компенсирующих в некоторой степени понижение краевой части дельты, подтверждает данный вывод. Иначе произошло бы полное выравнивание конуса выноса. Вместе с тем, разная выраженность нарушений и изменчивость величин оседания свидетельствует о пространственной неравномерности накопления напряжений и их реализации в виде медленных или быстрых смещений в гранулированной среде. Напряжения передаются от обломка к обломку через точки их соприкосновения в рыхлом осадочном грунте, а состояние контакта зерен оказывает сильное влияние на амплитуду и скорость уединенной сдвиговой волны [*Быков*, 1999], и, следовательно, на последующую деформацию.

Процессы, происходящие в устье р. Риты, могут быть характерны для других дельт и конусов выноса рек, впадающих в оз. Байкал. Так в подводной части дельты р. Селенги по батиметрическим данным и материалам многоканального сейсмического профилирования в осадочных толщах фиксируются тектонические уступы, смещения и гравитационное оседание блоков, ассоциируемое с сейсмотектонической активизацией [*Хлыстов и др.*, 2016]. Минимальные оценки оседания дельты за длительный период времени 6–8 мм/год не учитывают уплотнение осадков и могут быть существенно выше [*Dong et al.*, 2016]. Поскольку величина стока речных наносов определяется обычно в тоннах в год, нет возможности провести прямое сопоставление оценок осадконакопления в дельте р. Риты с другими реками, впадающими в оз. Байкал. Но тот факт, что величина стока наносов за последние десятилетия снизилась в среднем в 1,5–3 раза, а в сравнении с периодом до наступления потепления климата в 3–5 раз [*Потемкина и Потемкин*, 2023], свидетельствует о том, что сейсмотектонический фактор в таких условиях играет еще более значимую роль. Так, на фоне снижения величины стока наносов в период с 1980 по 2013 гг. площадь дельты р. Селенги существенно сократилась и произошло ее затопление [*Бабич и др.*, 2015].

Опубликованные примеры несейсмического разрывообразования инфраструктуры [*Howard and Zhou*, 2019; *Long et al.*, 2021; *Zervopoulou et al.*, 2007] и просадок [*Higgins*, 2015; *Liu et al.*, 2021; *Schmidt*, 2015] в городах и поселках демонстрируют насколько в целом широка проблема выявления причин деформаций в геологической среде, приводящая к экономическим потерям. Естественное уплотнение в сочетании с уменьшенной аградацией можно считать первопричиной оседания всех речных дельт. По площади его величина должна быть распределена относительно равномерно, поэтому значение оседания, равное 5–10 см для дельты р. Риты можно считать ассоциированным с этим фактором. Выкачивание флюидов в больших объемах приводит к более высоким скоростям отрицательных изменений земной поверхности, чем любой другой известный процесс [*Higgins*, 2015]. Однако в пределах дельты р. Риты и за десятки километров от нее нет никакой подобной антропогенной деятельности. Следовательно, оседание со значением меньше −10 см обусловлены эрозией или наличием разрыва, в зоне которого дезинтегрированный аллювий просаживается быстрее вследствие воздействия экзогенных и эндогенных процессов. Зная положение нарушений и направление проток нетрудно в каждом конкретном случае выделить ведущие факторы, влияющие на изменение земной поверхности.

5. Заключение

В 2019 г. в приозерной части дельты р. Риты на северо-западном побережье оз. Байкал впервые обнаружена зона сейсмогравитационных разрывов [*Лунина и Гладков*, 2022]. Повторная аэрофотосъемка локальных участков в 2020 и 2021 гг. и сравнение их ЦММ выявили оседание приозерной части дельты за 11 месяцев и 19 дней в среднем на 5–10 см. Эти значения ассоциируются с естественным уплотнением аллювия. В местах накопления осадков аградация при прочих равных условиях в среднем происходит на аналогичные величины, уравновешивая баланс отложений.

В местах выхода сейсмогравитационных нарушений в отсутствии наносов просадки достигают 33–37 см, что указывает на активные эндогенные и экзогенные процессы в зоне Кочериковского разлома. Наибольшие отрицательные и положительные вертикальные изменения земной поверхности до 40 см произошли в пределах галечного пляжа и связаны с волноприбойной деятельностью (рис. 2в и 5а). Самая крайняя, вдающаяся в озеро, заболоченная часть мыса Рытого испытала максимальное опускание за год. В местах расположения отдельных деревьев у берега положительные значения разницы высот связаны с их ростом, а локальные отрицательные значения в руслах временных проток – с интенсивной эрозией.

Наибольшее накопление аллювия произошло на южном участке дельты р. Риты в понижении, выраженном в рельефе местности (рис. 4а) и совпадающим с зоной современных разрывов, а также в аккумулятивном потоке, перекрывающем зону поверхностных нарушений (рис. 5а). За исключением этой части, разрывы хорошо проявлены на ЦММ, а значит, несмотря на интенсивные наносы, продолжают развиваться (рис. 4б, в).

Следует отметить, что изменения рельефа земной поверхности в изученной зоне разрывов следует продолжить, так как для подобных исследований необходимы многолетние наблюдения, что повышает репрезентативность данных и объективность выводов. Данная работа показывает, что сравнение разновременных ЦММ путем вычитания высотных отметок для каждого узла (пикселя) модели является перспективным методом для целей мониторинга, но необходимы коррекционные процедуры сопоставляемых ЦММ и ортофотопланов. Эффективным инструментом для сбора материала также является лидарная съемка с БПЛА.

Благодарности. Авторы благодарны Е. Б. Игнатенко за помощь при подготовке рисунков. Работы выполнены в рамках государственного задания Института земной коры Сибирского отделения Российской академии наук на 2021–2025 гг. «Современная геодинамика, механизмы деструкции литосферы и опасные геологические процессы в Центральной Азии» (проект № FWEF-2021-0009), с использованием оборудования и инфраструктуры уникальной научной установки «Южно-Байкальский инструментальный комплекс для мониторинга опасных геодинамических процессов» Центра коллективного пользования «Геодинамика и геохронология» ИЗК СО РАН по гранту № 075-15-2021-682. Работы проведены при сотрудничестве с ФГБУ «Заповедное Прибайкалье», предоставившего возможность выполнения научно-исследовательских работ на территории Байкало-Ленского заповедника в рамках договора № 43 от 30.05.2019 г.

Список литературы

Agisoft LLC. Руководство пользователя Agisoft Metashape. Standart Edition, Version 1.7. — 2021. — (дата обращения 29.06.2023). https://www.agisoft.com/pdf/metashape_1_7_ru.pdf.

Бабич Д. Б., Виноградова Н. Н., Иванов В. В. *и др.* Дельты рек, впадающих в озера: морфогенетические типы и современная динамика // Вестник Московского университета. Серия 5. География. — 2015. — Т. 4. — С. 18—26.

Быков В. Г. Уединенные сдвиговые зоны в зернистой среде // Акустический журнал. — 1999. — Т. 45, № 2. — С. 169—173.

Ладохин Н. П., Гречищев Е. К. Результаты изучения современных тектонических движений берегов оз. Байкал // Труды Восточно-Сибирского геологического института СО АН СССР. — 1961. — Т. 3. — С. 17—25.

Лебедева М. А., Саньков В. А., Захаров А. И. *и др.* Активные деформации в зоне влияния разломов Мондинской впадины по данным РСА-интерферометрии // Вестник СибГАУ. — 2013. — Т. 5, № 51. — С. 63—65.

Лунина О. В., Гладков А. А. Феномен разрывообразования в дельтовых отложениях мыса Рытый на северо-западном побережье оз. Байкал // Геология и геофизика. — 2022. — Т. 62, № 2. — С. 149—162. — DOI: 10.15372/gig2020204.

Орлов А. П. Об изменении уровня оз. Байкал // Известия Сибирского отдела Императорского РГО. — 1870. — Т. 1, № 2. — С. 6—18.

Потемкина Т. Г., Потемкин В. Л. Сток наносов озера Байкал: изменения и тенденции // Известия Иркутского государственного университета. Серия «Науки о Земле». — 2023. — Т. 43. — С. 79—90. — DOI: 10.26516/2073-3402.2023.43.79.

Хлыстов О. М., Кононов Е. Е., Хабуев А. В. *и др.* Геолого-геоморфологические особенности Посольской банки и Кукуйской гривы озера Байкал // Геология и геофизика. — 2016. — Т. 57, № 12. — С. 2229—2239. — DOI: 10.15372/GiG20161208.

Черский И. Д. О результатах исследований оз. Байкал // Записки Императорского РГО по общей географии. — 1886. — Т. 15, № 3. — С. 1—48.

Bearzot F., Garzonio R., Di Mauro B., *et al.* Kinematics of an Alpine rock glacier from multi-temporal UAV surveys and GNSS data // Geomorphology. — 2022. — Vol. 402. — P. 108116. — DOI: 10.1016/j.geomorph.2022.108116.

Dong T. Y., Nittrouer J. A., Il'icheva E., *et al.* Controls on gravel termination in seven distributary channels of the Selenga River Delta, Baikal Rift basin, Russia // Geological Society of America Bulletin. — 2016. — Vol. 128, no. 7/8. — P. 1297–1312. — DOI: 10.1130/B31427.1.

Higgins S. A. Review: Advances in delta-subsidence research using satellite methods // Hydrogeology Journal. — 2015. — Vol. 24, no. 3. — P. 587–600. — DOI: 10.1007/s10040-015-1330-6.

Higgins S. A., Overeem I., Steckler M. S., *et al.* InSAR measurements of compaction and subsidence in the Ganges-Brahmaputra Delta, Bangladesh // Journal of Geophysical Research: Earth Surface. — 2014. — Vol. 119, no. 8. — P. 1768–1781. — DOI: 10.1002/2014JF003117.

Howard K. W. F., Zhou W. Overview of ground fissure research in China // Environmental Earth Sciences. — 2019. — Vol. 78, no. 3. — DOI: 10.1007/s12665-019-8114-6.

Hu L., Navarro-Hernández M. I., Liu X., *et al.* Analysis of regional large-gradient land subsidence in the Alto Guadalentín Basin (Spain) using open-access aerial LiDAR datasets // Remote Sensing of Environment. — 2022. — Vol. 280. — P. 113218. — DOI: 10.1016/j.rse.2022.113218.

Liu Y., Liu J., Xia X., *et al.* Land subsidence of the Yellow River Delta in China driven by river sediment compaction // Science of The Total Environment. — 2021. — Vol. 750. — P. 142165. — DOI: 10.1016/j.scitotenv.2020.142165.

Long Z., Yumei L., Yong L., *et al.* An extension-dominant 9-km-long ground failure along a buried geological fault on the eastern Beijing Plain, China // Engineering Geology. — 2021. — Vol. 289. — P. 106168. — DOI: 10.1016/j.enggeo.2021.106168.

Loucks D. P. Developed river deltas: are they sustainable? // Environmental Research Letters. — 2019. — Vol. 14, no. 11. — P. 113004. — DOI: 10.1088/1748-9326/ab4165.

Lukhnev A. V., San'kov V. A., Miroshnichenko A. I., *et al.* GPS-measurements of recent crustal deformation in the junction zone of the rift segments in the central Baikal rift system // Russian Geology and Geophysics. — 2013. — Vol. 54, no. 11. — P. 1417–1426. — DOI: 10.1016/j.rgg.2013.10.010.

Rossini M., Di Mauro B., Garzonio R., *et al.* Rapid melting dynamics of an alpine glacier with repeated UAV photogrammetry // Geomorphology. — 2018. — Vol. 304. — P. 159–172. — DOI: 10.1016/j.geomorph.2017.12.039.

Schmidt C. W. Delta Subsidence: An Imminent Threat to Coastal Populations // Environmental Health Perspectives. — 2015. — Vol. 123, no. 8. — DOI: 10.1289/ehp.123-A204.

Tessler Z. D., Vörösmarty C. J., Overeem I., *et al.* A model of water and sediment balance as determinants of relative sea level rise in contemporary and future deltas // Geomorphology. — 2018. — Vol. 305. — P. 209–220. — DOI: 10.1016/j.geomorph.2017.09.040.

Valkaniotis S., Papathanassiou G., Ganas A. Mapping an earthquake-induced landslide based on UAV imagery; case study of the 2015 Okeanos landslide, Lefkada, Greece // Engineering Geology. — 2018. — Vol. 245. — P. 141–152. — DOI: 10.1016/j.enggeo.2018.08.010.

Yang Y.-H., Xu Q., Hu J.-C., *et al.* Source Model and Triggered Aseismic Faulting of the 2021 Mw 7.3 Maduo Earthquake Revealed by the UAV-Lidar/Photogrammetry, InSAR, and Field Investigation // Remote Sensing. — 2022. — Vol. 14, no. 22. — P. 5859. — DOI: 10.3390/rs14225859.

Zervopoulou A., Chatzipetros A., Tsiokos L., *et al.* Non-seismic surface faulting: the peraia fault case study (Thessaloniki, N. Greece) // 4th International Conference on Earthquake Geotechnical Engineering, Paper No. 1610. — Thessaloniki (Greece) : ISSMGE, 2007.

Zhong W., Chu T., Tissot P., *et al.* Integrated coastal subsidence analysis using InSAR, LiDAR, and land cover data // Remote Sensing of Environment. — 2022. — Vol. 282. — P. 113297. — DOI: 10.1016/j.rse.2022.113297.

Russian Journal of Earth Sciences

Subsidence and Sedimentation Dynamics of the Lakeside Part of the Rita River Delta in the Rupture Zone, the Northwestern Coast of Lake Baikal

O. V. Lunina[**,1] **and A. A. Gladkov**[1,2]

[1]Institute of the Earth's Crust, Siberian Branch of Russian Academy of Sciences, Irkutsk, Russia
[2]Center for the Development of Continuing Education of Children, Ministry of Education of Irkutsk Region, Irkutsk, Russia
**Correspondence to: Oksana V. Lunina, lounina@crust.irk.ru

Delta subsidence is one of the key problems of human life as these areas are developed quite fast. The process is natural and depends on many factors, the influence of which has not yet been sufficiently studied. This study is aimed to identify changes in the earth's surface of the lakeside part of the Rita River delta on the northwestern coast of Lake Baikal, where a zone of seismically induced gravitational ruptures were recently mapped. To assess topographic changes, we used the calculation of the difference in multi-temporal digital surface models (DSM) obtained in two local areas from ultra-high resolution unmanned aerial photography in 2020 and 2021. We established that the subsidence of the lakeside part of the delta occurred on average by 5–10 cm over 11 months and 19 days. These values are associated with natural sediment compaction. In places of their accumulation, aggradation occurs by similar values, compensating the balance of deposits. In the seismically induced gravitational failures in the absence of alluvium, subsidence reached 33–37 cm, which indicates active endogenous and exogenous processes in the Kocherikovsky fault zone. The largest negative and positive vertical topographic changes up to 40 cm occurred within the beach and were associated with wave-cutting activity. The most extreme swampy part of Cape Rytyi experienced the maximum subsidence per a year. The greatest accumulation of alluvium occurred in the southern section of the Rita River delta in a settling expressed in the surface and coinciding with the zone of recent ruptures, as well as in an accumulative flow that overlaps the zone of surface deformations. With the exception of this part, discontinuities are well exhibited on DSM that means they continue to develop despite intensive sedimentation. Comparison of multi-temporal DSM and DTM by calculating the difference in elevation for each node (pixel) of the model is a promising and inexpensive method for monitoring surface deformations.

Recieved: 30 June 2023
Accepted: 22 September 2023
Published: 30 December 2023

Keywords: rupture zone, delta, subsidence, unmanned aerial system, digital surface model, Baikal

Citation: Lunina, O. V. and A. A. Gladkov (2023), Subsidence and Sedimentation Dynamics of the Lakeside Part of the Rita River Delta in the Rupture Zone, the Northwestern Coast of Lake Baikal, *Russian Journal of Earth Sciences*, 23, ES6006, https://doi.org/10.2205/2023ES000874 EDN: HTCABO

References

Agisoft LLC. Agisoft Metashape User Guide. Standard Edition, Version 1.7. — 2021. — (access date 06.29.2023). https://www.agisoft.com/pdf/metashape_1_7_ru.pdf.

Babich D. B., Vinogradova N. N., Ivanov V. V., *et al.* Deltas of the rivers running in to lakes and reservoirs: Morphogenetic types and recent dynamics // Moscow University Bulletin. Series 5, Geography. — 2015. — Vol. 4. — P. 18–26.

Bearzot F., Garzonio R., Di Mauro B., *et al.* Kinematics of an Alpine rock glacier from multi-temporal UAV surveys and GNSS data // Geomorphology. — 2022. — Vol. 402. — P. 108116. — DOI: 10.1016/j.geomorph.2022.108116.

Bykov V. G. Isolated Shear Zones in Granular Medium // Acoustic journal. — 1999. — Vol. 45, no. 2. — P. 169–173.

Chersky I. D. About the results of research on lake Baikal // Notes of the Imperial Russian Geographical Society on general geography. — 1886. — Vol. 15, no. 3. — P. 1–48.

Dong T. Y., Nittrouer J. A., Il'icheva E., *et al.* Controls on gravel termination in seven distributary channels of the Selenga River Delta, Baikal Rift basin, Russia // Geological Society of America Bulletin. — 2016. — Vol. 128, no. 7/8. — P. 1297–1312. — DOI: 10.1130/B31427.1.

Higgins S. A. Review: Advances in delta-subsidence research using satellite methods // Hydrogeology Journal. — 2015. — Vol. 24, no. 3. — P. 587–600. — DOI: 10.1007/s10040-015-1330-6.

Higgins S. A., Overeem I., Steckler M. S., *et al.* InSAR measurements of compaction and subsidence in the Ganges-Brahmaputra Delta, Bangladesh // Journal of Geophysical Research: Earth Surface. — 2014. — Vol. 119, no. 8. — P. 1768–1781. — DOI: 10.1002/2014JF003117.

Howard K. W. F., Zhou W. Overview of ground fissure research in China // Environmental Earth Sciences. — 2019. — Vol. 78, no. 3. — DOI: 10.1007/s12665-019-8114-6.

Hu L., Navarro-Hernández M. I., Liu X., *et al.* Analysis of regional large-gradient land subsidence in the Alto Guadalentín Basin (Spain) using open-access aerial LiDAR datasets // Remote Sensing of Environment. — 2022. — Vol. 280. — P. 113218. — DOI: 10.1016/j.rse.2022.113218.

Khlystov O. M., Kononov E. E., Khabuev A. V., *et al.* Geological and geomorphological characteristics of the Posolsky Bank and the Kukuy Griva, lake Baikal // Russian Geology and Geophysics. — 2016. — Vol. 57, no. 12. — P. 2229–2239. — DOI: 10.15372/GiG20161208.

Ladokhin N. P., Grechishchev E. K. Results of studying modern tectonic movements of the shores of the lake Baikal // Proceedings of the East Siberian Geological Institute of the Siberian Branch of the USSR Academy of Sciences. — 1961. — Vol. 3. — P. 17–25.

Lebedeva M. A., Sankov V. A., Zakharov A. I., *et al.* Active deformations in the zone of influence of faults of Mondy basin by SAR interferometry data // Bulletin of SibSAU. — 2013. — Vol. 5, no. 51. — P. 63–65.

Liu Y., Liu J., Xia X., *et al.* Land subsidence of the Yellow River Delta in China driven by river sediment compaction // Science of The Total Environment. — 2021. — Vol. 750. — P. 142165. — DOI: 10.1016/j.scitotenv.2020.142165.

Long Z., Yumei L., Yong L., *et al.* An extension-dominant 9-km-long ground failure along a buried geological fault on the eastern Beijing Plain, China // Engineering Geology. — 2021. — Vol. 289. — P. 106168. — DOI: 10.1016/j.enggeo.2021.106168.

Loucks D. P. Developed river deltas: are they sustainable? // Environmental Research Letters. — 2019. — Vol. 14, no. 11. — P. 113004. — DOI: 10.1088/1748-9326/ab4165.

Lukhnev A. V., San'kov V. A., Miroshnichenko A. I., *et al.* GPS-measurements of recent crustal deformation in the junction zone of the rift segments in the central Baikal rift system // Russian Geology and Geophysics. — 2013. — Vol. 54, no. 11. — P. 1417–1426. — DOI: 10.1016/j.rgg.2013.10.010.

Lunina O. V., Gladkov A. A. The rupturing phenomena in the deltaic deposits of cape Rytyi on the northwestern shore of lake Baikal (based on aerial-photography data) // Russian Geology and Geophysics. — 2022. — Vol. 62, no. 2. — P. 149–162. — DOI: 10.15372/gig2020204.

Orlov A. P. About changes in the level of lake Baikal // News of the Siberian Department of the Imperial Russian Geographical Society. — 1870. — Vol. 1, no. 2. — P. 6–18.

Potemkina T. G., Potemkin V. L. Sediment Load Runoff of Lake Baikal Tributaries: Changes and Trends // The Bulletin of Irkutsk State University. Series Earth Sciences. — 2023. — Vol. 43. — P. 79–90. — DOI: 10.26516/2073-3402.2023.43.79.

Rossini M., Di Mauro B., Garzonio R., *et al.* Rapid melting dynamics of an alpine glacier with repeated UAV photogrammetry // Geomorphology. — 2018. — Vol. 304. — P. 159–172. — DOI: 10.1016/j.geomorph.2017.12.039.

Schmidt C. W. Delta Subsidence: An Imminent Threat to Coastal Populations // Environmental Health Perspectives. — 2015. — Vol. 123, no. 8. — DOI: 10.1289/ehp.123-A204.

Tessler Z. D., Vörösmarty C. J., Overeem I., *et al.* A model of water and sediment balance as determinants of relative sea level rise in contemporary and future deltas // Geomorphology. — 2018. — Vol. 305. — P. 209–220. — DOI: 10.1016/j.geomorph.2017.09.040.

Valkaniotis S., Papathanassiou G., Ganas A. Mapping an earthquake-induced landslide based on UAV imagery; case study of the 2015 Okeanos landslide, Lefkada, Greece // Engineering Geology. — 2018. — Vol. 245. — P. 141–152. — DOI: 10.1016/j.enggeo.2018.08.010.

Yang Y.-H., Xu Q., Hu J.-C., *et al.* Source Model and Triggered Aseismic Faulting of the 2021 Mw 7.3 Maduo Earthquake Revealed by the UAV-Lidar/Photogrammetry, InSAR, and Field Investigation // Remote Sensing. — 2022. — Vol. 14, no. 22. — P. 5859. — DOI: 10.3390/rs14225859.

Zervopoulou A., Chatzipetros A., Tsiokos L., *et al.* Non-seismic surface faulting: the peraia fault case study (Thessaloniki, N. Greece) // 4th International Conference on Earthquake Geotechnical Engineering, Paper No. 1610. — Thessaloniki (Greece) : ISSMGE, 2007.

Zhong W., Chu T., Tissot P., *et al.* Integrated coastal subsidence analysis using InSAR, LiDAR, and land cover data // Remote Sensing of Environment. — 2022. — Vol. 282. — P. 113297. — DOI: 10.1016/j.rse.2022.113297.

Russian Journal of Earth Sciences

Theoretical and Experimental Modeling of Local Scale CO_2 Flushing of Hydrous Rhyolitic Magma

A. G. Simakin[*,1], **V. N. Devyatova**[1], **and A. A. Shiryaev**[2]

[1] Korzhinskii Institute of Experimental Mineralogy, Russian Academy of Sciences, Chernogolovka, Russia
[2] Frumkin Institute of Physical Chemistry and Electrochemistry, Russian Academy of Sciences, Moscow, Russia
* **Correspondence to:** A. G. Simakin, dev@iem.ac.ru.

Abstract: Flushing of hydrous silicic magmas with crustal carbonic fluid may be an important factor controlling the dynamics of rhyolitic eruptions. We present combined theoretical and experimental study of the interaction of carbonic fluid with a hydrous silicic melt. The process of diffusional equilibration of a CO_2 bubble with a silicic melt was simulated numerically in the spherical shell approximation. The rapid water transfer from the melt to the bubble is followed by a slower diffusion of CO_2 into the melt. The water distribution in the melt becomes almost uniform over a period proportional to the diffusional unit of time $0.14\tau_w$, determined by the initial inter-bubble distance W equal the distance between neighbor bubbles centers and the water diffusion coefficient D_w in the melt ($\tau_w = W^2/D_w$), while the CO_2 distribution remains strongly contrasting and the melt remains undersaturated in CO_2. This process was modelled experimentally with a hydrous albite melt at $P = 200$ MPa and $T = 950$–$1000\,°C$. In the first series of experiments at $T = 950\,°C$, a glass powder was filled with pure CO_2 at the beginning of the experiment, forming numerous bubbles at the run temperature. Micro-FTIR measurements showed that after 40 minutes the water content in the melt decreased from 4.9 down to 1.8 wt. % with the maximum CO_2 content of 500 ppm (below saturation). After 4 hours, the crystallinity increased to 85%, and almost all of the fluid bubbles escaped. The second series of experiments CO_2 interacted with a 2 mm high column of hydrous albite melt. Diffusion profiles in the quenched glass were measured using EMPA (H_2O) and micro-FTIR (CO_2 and H_2O). The estimated diffusion coefficients in the melt for H_2O (1.1×10^{-6} cm^2/s) and CO_2 (1.5×10^{-7} cm^2/s) are consistent with published data. Scaling analysis predicts that in the nature, after the influx of CO_2 bubbles a few millimeters in size, the maximum dehydration of rhyolitic magma with viscosity near 10^5 Pa s without a significant increase in CO_2 content occurs after 1–30 days, i.e. a period compatible with the minimum duration of pre-eruption processes in the magma chamber.

Keywords: Carbon dioxide, explosive volcanic eruption, experiment in IHPV, diffusion of CO_2 and H_2O, magma flushing with CO_2.

Citation: Simakin, A. G., V. N. Devyatova, and A. A. Shiryaev (2023), Theoretical and Experimental Modeling of Local Scale CO_2 Flushing of Hydrous Rhyolitic Magma, *Russian Journal of Earth Sciences*, 23, ES6007, EDN: CTVIQU, https://doi.org/10.2205/2023es000871

Research Article

Received: 23 March 2023
Accepted: 21 September 2023
Published: 30 December 2023

Introduction

Intra-chamber degassing caused by CO_2 flushing at a mid-crustal depth can be an essential factor determining the explosive style of mafic magmas eruption [*Dallai et al.*, 2011]. Using geochemical and petrological tools, it is possible to distinguish the invasion of CO_2 into the magma from the assimilation of carbonate, causing the CO_2 generation in near-surface conditions (depth 1–3 km) by the enrichment of melt with CaO [*Mollo et al.*, 2010]. While processes involving carbonic fluid at the mid-crustal depths can only be studied indirectly, a high flux of CO_2 of deep origin is measured at the surface in mantle plume settings (Yellowstone [*Lowenstern and Hurwitz*, 2008; *Werner and Brantley*, 2003], Iceland [*Barry et al.*, 2014], Canary Islands [*Longpré et al.*, 2017] and some subduction zones (Italy [*Frezzotti et al.*, 2010]. *Frezzotti and Touret* [2014] suggested that CO_2 can be formed in the upper mantle during decarbonization reactions and can be transported to the crust either by dissolution in the mafic magma or along with it via deep tectonic dislocations (shear zones). During the upward migration, this fluid may cross magma chambers. The interaction of the carbonic fluid and water-bearing magmas can be equally important for basaltic and silicic compositions [*Caricchi et al.*, 2018]. Upon interaction with CO_2, the water undesaturated melt reaches saturation with respect to the CO_2-H_2O composite fluid. In addition to simple recharging, intra-chamber vesiculation may be a factor increasing the magma pressure in the chamber to a level sufficient to cause failure of the chamber roof and onset of an explosive eruption. The carbonic fluid transfers heat and dissolved components, thereby affecting the heat budget of the magma and its composition [*Simakin and Ghassemi*, 2018].

Fluxing of silicic magma with CO_2 of deep crustal or mantle origin or released from underplating basalts can affect the style of the eruption, increasing explosiveness, similar to mafic volcanism [*Dallai et al.*, 2011]. Melt inclusions (MIs) in quartz provide a unique opportunity to obtain direct information about the fluid regime of silicic magma.

The climatic eruptions of Yellowstone have been studied in details and analyses of MIs without water loss or corrected on water loss are available [e.g., *Befus and Gardner*, 2016; *Myers et al.*, 2016] and presented in Figure 1. Points of H_2O and CO_2 content form subvertical arrays, starting from compositions poor in CO_2 and undersaturated with water, extended vertically to solubility isobars of 200–250 MPa The Lava Creek Tuffs MIs exhibits water content variation in the range 3–4 wt. % [*Befus and Gardner*, 2016], while the Huckleberry Ridge Tuff MIs have higher water concentrations of 4–5 wt. % [*Myers et al.*, 2016].

Usually, such subvertical trends are interpreted as a manifestation of degassing due to depressurization. Figure 1 shows the calculated sequences of compositions of melts formed at pressure drops from 200 to 5 MPa in closed and open system modes [*Newman and Lowenstern*, 2002]. The interaction of CO_2-enriched fluid with magma (or flushing) also leads to degassing or dehydration of the melt, increasing the volume of the fluid phase. Assuming local equilibrium, as in modeling a pressure drop-induced degassing path, melt compositions will follow a solubility isobar as shown by the thick grey line in Figure 1, with compositions directed towards increasing CO_2 content. The same line with compositions directed towards increasing water content will characterize the process of magma crystallization with exsolution of excess fluid [*Wallace et al.*, 1995]. These trends are far from those observed for the Yellowstone eruptions data.

The interaction of a water saturated high-silica rhyolite melt with a CO_2 bearing ($X_{CO_2} = 0.4$) fluid at $T = 800$ °C and $P = 100$ MPa was experimentally studied by *Yoshimura and Nakamura* [2010]. Under the experimental conditions, the used bubble-free water-saturated glass slab was highly viscous (10^5 Pa s) and was partially dehydrated from the entire surface. In three-hour experiments, the H_2O concentration became uniform within a 0.5 mm thick melt volume, while the CO_2 distribution was still far from saturation. Disequilibrium effects were also observed during vesiculation after decompression of a melt saturated with CO_2 and H_2O, caused by slower diffusion of CO_2. Delayed saturation of the melt with CO_2 after dehydration can cause the melt compositions to follow the trend shown by the solid purple line marked by the upward arrow in Figure 1. In their vertical parts, the trends of equilibrium decompression degassing and disequilibrium CO_2 flushing are quite similar, which, at least requires not to ignore the possibility of the later process. Additional information, such as the isotopic composition (δ^7Li, δ^{11}B, δ^{34}S) [*Gurenko*, 2021; *Neukampf et al.*, 2022; *Zelenski et al.*, 2022] which is affected by isotope fractionation during degassing, could potentially help in choosing between these alternative mechanisms.

The dehydration of magma caused by CO_2 flushing leads to an increase in the liquidus temperature of magmatic minerals. This effect causes crystallization at a significant rate, exceeding the rate of quasi-equilibrium crystallization, due to the slow cooling of large volumes of magma beyond the reach of the geothermal circulation. Decompression degassing

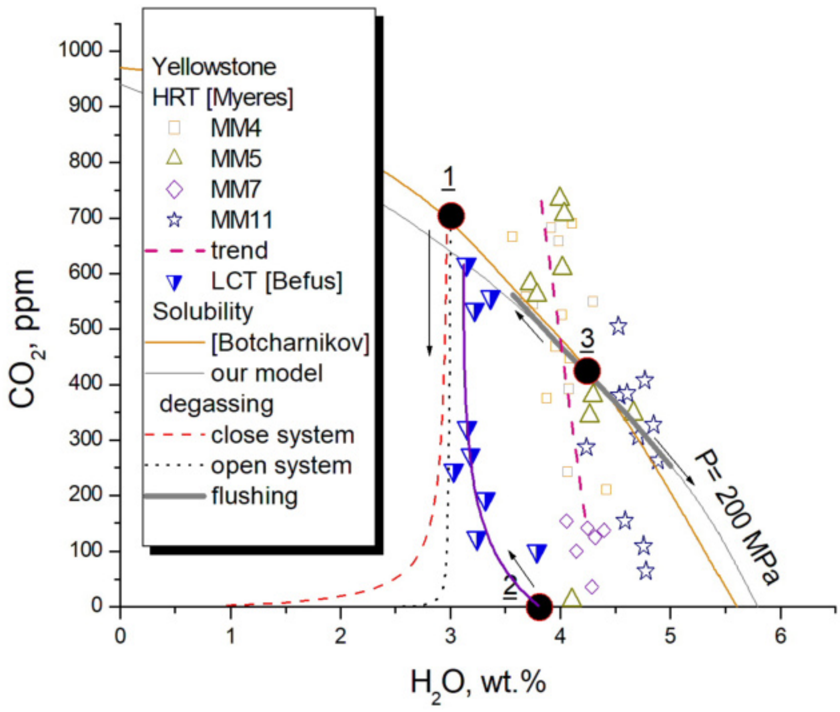

Figure 1. Compositions of melt inclusions in quartz from climatic eruptions of Yellowstone: Huckleberry Ridge Tuff (HRT), numbering of the different levels in the ash pile and analysis results from [*Myers et al.*, 2016], Lava Creek Tuff (LCT) data from [*Befus and Gardner*, 2016]. The decompression degassing lines (open and close system modes are depicted by dotted and dashed lines, respectively) were calculated and marked with an arrow pointing down. The line of flushing with CO_2 enriched fluid is shown as a solid line marked with an upward arrow, schematically. Evolution of the melt composition in equilibrium at flushing (marked with arrow directed towards increasing CO_2 content) and crystallization (marked with arrow directed to increasing H_2O content) is plotted with thick grey line as part of solubility isobar at $P = 200\,\text{MPa}$. Ideal compositions of the starting melt are marked with solid circles (1 – decompression degassing, 2 – dynamic flushing, 3 – equilibrium flushing or fluid exsolution at crystallization).

produces a similar effect of magma crystallization with an increase in undercooling, which has been well studied experimentally [*Cichy et al.*, 2010; *Couch*, 2003; *Simakin et al.*, 1999].

Here we present the results of the experiments in an internally heated high pressure vessel (IHPV) on the interaction of CO_2 with a hydrous albite melt, extending the results obtained by *Yoshimura and Nakamura* [2010]. Our experiments include studying the effect of albite crystallization caused by dehydration of the melt with CO_2 fluid. The results of numerical modeling of the growth of CO_2 bubbles during melt dehydration are also presented, which allow us to extend the experimental results to natural conditions with larger bubbles and a low fluid volume content.

Part 1. Numerical Modeling of Hydrous Melt Flushing with CO_2 on a Single Bubble Level

The Model

The interaction of a CO_2-enriched fluid with a hydrous melt (flushing) can be easily modelled theoretically in the equilibrium approach, similarly to the degassing process of a magma saturated with a two-component fluid. It is sufficient to know the mutual solubility of CO_2 and H_2O in a melt of given composition. An explosive eruption can start at a high rate on a time scale of hours or days. In this case, slow process of diffusive bubble growth can control compositions of the fluid and the adjacent melt. There are many approximate analytical and fully numerical solutions for diffusive equilibration (growth or dissolution) of a bubble in a melt [e.g., *Navon et al.*, 1998]. For clarity and consistency of consideration, we briefly describe the problem and methods of its solution.

Let us start with an analysis of the complete equation of diffusive mass transfer around a bubble growing in an infinite volume of the melt. The growing bubble expands and causes a radial flow of the melt with a rate (for the spherically symmetric case) $U(r)$. Therefore, the diffusion equation for any component of the melt can be written as:

$$\frac{\partial C}{\partial t} = -U(r)\frac{\partial C}{\partial r} + \frac{1}{r^2}\Big(\partial\big(D(C)r^2(\partial C/\partial r)\big)/\partial r\Big), \tag{1}$$

where $D(C)$ is the diffusion coefficient. The radial flow rate $U(r)$ is given by:

$$U(r) = \frac{U_0 r_0^2(t)}{r^2}$$

here $r_0(t)$ is the bubble radius at the moment t (see Table 1 for all physical parameters).

A set of bubbles of the equal size is usually [e.g., *Coumans et al.*, 2020] modeled in a spherical melt shell geometry. In this approximation, both the inner and outer (midpoint between neighboring bubbles) boundaries move as the bubble expands. The bubble growth rate is controlled by the diffusive flux of main component:

$$U_0 = \rho_{\mathrm{m}}/\rho_{\mathrm{fl}} D_{\mathrm{w}} \left.\frac{\partial C(r,t)}{\partial r}\right]_{r=r_0(t)+0}. \tag{2}$$

The influence of the flow is defined by the parameter $R_\rho = \Delta C \rho_{\mathrm{m}}$, where ΔC is the characteristic concentration difference $\Delta C = C_{r=r_0} - C_0$ (e.g., 0.01). It can be shown that for moderate values of $R_\rho < 1$ (pressures >100 MPa), the advection term can be omitted. At low pressures and fluid density, the parameter $R_\rho \gg 1$, and advection strongly affects the concentration field and transforms the solution to the type of a narrow boundary layer [*Zelenski et al.*, 2021]. Here we consider processes of the melt-fluid exchange in the magma chamber at a typical depth of about 7 km ($P = 200$ MPa) with $R_\rho \approx 0.1$ with a weak effect of advection. Our fluid consists of two main components CO_2 and H_2O, so two diffusive mass fluxes act on the bubble volume and the boundary condition (2) is replaced by:

$$\frac{\mathrm{d}V_{\mathrm{bub}}}{\mathrm{d}t} = \frac{\mathrm{dm}_{CO_2}/\mathrm{d}t + \mathrm{dm}_{H_2O}/\mathrm{d}t}{\rho_{\mathrm{fl}}(X)} + \frac{\mathrm{d}\rho_{\mathrm{fl}}/\mathrm{d}t}{\rho_{\mathrm{fl}}^2}\left(\left(1 - X_{CO_2}\right)\frac{\mathrm{dm}_{CO_2}}{\mathrm{d}t} - X_{CO_2}\frac{\mathrm{dm}_{H_2O}}{\mathrm{d}t}\right), \tag{3}$$

where m_{CO_2} and m_{H_2O} are the masses of the components in the bubble, X_{CO_2} is the mole fraction of CO_2 in the fluid, ρ_{fl} is the fluid density depending on its composition at fixed P and T. The concentrations of H_2O and CO_2 in the melt at the bubble boundary are assumed to be in equilibrium with the fluid composition:

$$C_{i,\mathrm{m}}(r = r_0) = F_i(X_{CO_2}),$$

where $i = CO_2, H_2O$, while at the outer shell boundary zero flux condition is applied

$$\frac{\partial C_{i,m}(r = r_1 - 0)}{\partial r} = 0.$$

Material Parameters.

Diffusion coefficients for CO_2 and H_2O in the melt are taken from [*Zhang and Ni*, 2010]. At T = 850–1000 °C, P = 200 MPa and C_{w} = 4–5 wt. % the ratio D_{H_2O}/D_{CO_2} is in the range 4–10.

Table 1. Physical parameters

Variable	Dimension	Value	Name
C_i	wt %, ppm	CO_2 0–1000 ppm H_2O 0–5 wt. %	concentration in the melt
P	MPa	200	pressure
D_i	m^2/s	$H_2O \approx 10^{-10}$ $CO_2 \approx 10^{-11}$	diffusion coefficient in the melt
D_x	–	4–10	diffusivities ratio ($D_x = D_{H_2O}/D_{CO_2}$)
ρ_i	kg/m^3	fl ≈500 – fluid m ≈2300 – melt	density
R_ρ	–	0.16	effective density ratio ($R_\rho = \Delta C \rho_m/\rho_{fl}$)
R_0	m	10×10^{-6}– 2000×10^{-6}	bubble radius
R_1	m	–	outer radius of the melt shell
R, r	m	–	radial coordinate
$\xi = r/r_0$	–	–	dimensionless radial coordinate ($\xi = r/r_0$)
W	m	–	model inter-bubble distance ($W = 2R_1$)
τ_w	sec	–	water diffusional unit of time ($\tau_w = W^2/D_w$)
η	Pa s	$\approx 10^5$	viscosity of the melt
$\varepsilon, \varepsilon_{fl}$	–	0–0.4	bubbles volume fraction
ε_s	–	0–0.8	crystals volume fraction
τ_H	sec	–	water homogenization time ($\tau_H = 0.55\tau_w \varepsilon_{fl}^{2/3}$)
$U(r)$	m/s	–	radial flow rate in the melt shell around bubble
U_{st}	m/s	–	Stokes rate of bubble ($U_{st} = 1/3(\rho_m - \rho_{fl}) g R_0 2/\eta$)
τ_{st}	sec	–	Stokes time scale ($\tau_{st} = 1/U_{st}$)

The CO_2-H_2O fluid density was calculated from the model from [*Kerrick and Jacobs*, 1981]. We approximated $\rho_{fl}(X_{CO_2})$ and $d\rho_{fl}(X_{CO_2})/dX_{CO_2}$ for $T = 850\,°C$ and $P = 200\,MPa$ by a second order polynomials.

The solubility of H_2O (C in wt. %, P in kbar) was approximated as:

$$C_{H_2O} = 4.1(P(1 - X_{CO_2})^{1.35})^{1/2}$$

and CO_2 (C in wt. %, T in °C):

$$C_{CO_2} = 0.0592kX_{CO_2}^{0.79},\; k = -0.54013 + 0.00164T,$$

where X_{CO_2} is the mole fraction of CO_2 in the fluid. These approximations correspond to experimental data for pressures $75\,MPa < P < 500\,MPa$, generalized for rhyolite in [*Botcharnikov et al.*, 2005], that can be illustrated by proximity of the model and experimental solubility curves in Figure 1.

Method of Solution.

For the numerical solution for the radial distributions of H_2O and CO_2 we apply the Lagrange formulation for spatial dimension, i.e. each node moves at the melt velocity [*Zelenski et al.*, 2021]. This approach was used in [*Lyakhovsky et al.*, 1996] to model bubble growth in the melt, it allows to drop advection term in (1) and avoid boundary conditions on the moving boundaries of the bubble. In Lagrangian formulation boundary conditions are set at the start and end points of the grid. In addition, for simplicity, we used the approximation of a constant diffusion coefficient at an average concentration C^*:

$$\frac{DC}{Dt} = D(C^*)\left(\frac{2\partial C/\partial r}{r} + \frac{\partial^2 C}{\partial r^2}\right), \tag{4}$$

where the Lagrangian total derivative D is applied on LHS of equation (4). The equation (4) was transformed to a dimensionless form by applying a linear scale equal to the initial bubble radius R_0 and a time scale t_0 related to the diffusion coefficient of water $t_0 = R_0^2/D_{H_2O}(C^*)$. Thus, the problem under consideration is characterized by two dimensionless parameters: R_ρ (see above) and $D_x = D_{H_2O}/D_{CO_2}$. Then Eqn. (4) was discretized using the global inverse square approximation [*Cheng et al.*, 2003]. Since the flow is weak, the nodes experience small displacements, and no new nodes were generated during the computations, as in the case of large R_ρ. Details of the algorithm first used to simulate superfast bubble growth in a lava flow are presented in [*Zelenski et al.*, 2021] and in a supplementary file to this publication. The best way to solve the complete nonlinear diffusion equation (1) is to use the control volume method [*Zelenski et al.*, 2021] However, the influence of an unexpected physical factor described in the experimental section below gives the nature of a preliminary analysis to our calculations.

Results

Our goal was to simulate the initial stage of interaction, when the process of transition of water from the melt to the bubble dominates. At a sufficiently long time, CO_2 migrates into the melt, and the molar fraction of CO_2 in the fluid decreases, so that part of the water returns to the melt. The increase in the volume of bubbles reaches a maximum at an early stage of dehydration of the melt. Here, we have estimated the minimum time required to obtain an almost uniform distribution of water in the melt around the bubble. The calculations are carried out at $D_x = 6$ (average value), $R_\rho = 0.046$ (corresponds to $\rho_m = 2.3\,g/cm^3$, $\rho_{fl} = 0.5\,g/cm^3$, $\Delta C = 0.01$) and several initial volume fractions of bubbles $\varepsilon_0 = (R_0/R_1)^3 = 0.005; 0.033; 0.053$. The time-successive radial profiles of water concentration in the melt at $\varepsilon = 0.033$ are shown in Figure 2a, 2b. Water migrates into the bubble, so its concentration in the melt decreases from 5 wt. % to 4.3 wt. %. A steep gradient of water concentration at $\tau = 0.5$ evolves almost to a flat one at $\tau = 5$. At the same time, CO_2 migrates into the melt. The concentration gradient is still steep at $\tau = 5$. In Figure 3, the distributions $CO_2(r)$ and $H_2O(r)$ are shown on the $CO_2(H_2O)$ plot. In this diagram, the distributions evolve from a steep concave curve to an almost vertical line ($\tau > 3$–4). With an order of magnitude decrease in the volume fraction of bubbles, the time of homogenization of the water content increases by ${\varepsilon_0}^{2/3}$ times, which is expected from the scaling relations. Figure 3 shows that the CO_2 content in the fluid, reflected by the maximum CO_2 content in the melt, increases with the volume fraction of the bubbles.

At short times, when the diffusion front is far from the outer boundary, the radial distribution of the ith volatile component can be described by a simple analytical solution in dimensionless coordinates $\xi = r/r_0$, $\tau = tD_i/r_0^2$. Here, we neglect the change in the boundary concentration, which depends on the composition of the fluid, and advection:

$$C(r,t) = c_0 + \frac{\Delta C}{\xi}\operatorname{erfc}\left(\frac{\xi - 1}{2\sqrt{\tau}}\right). \tag{5}$$

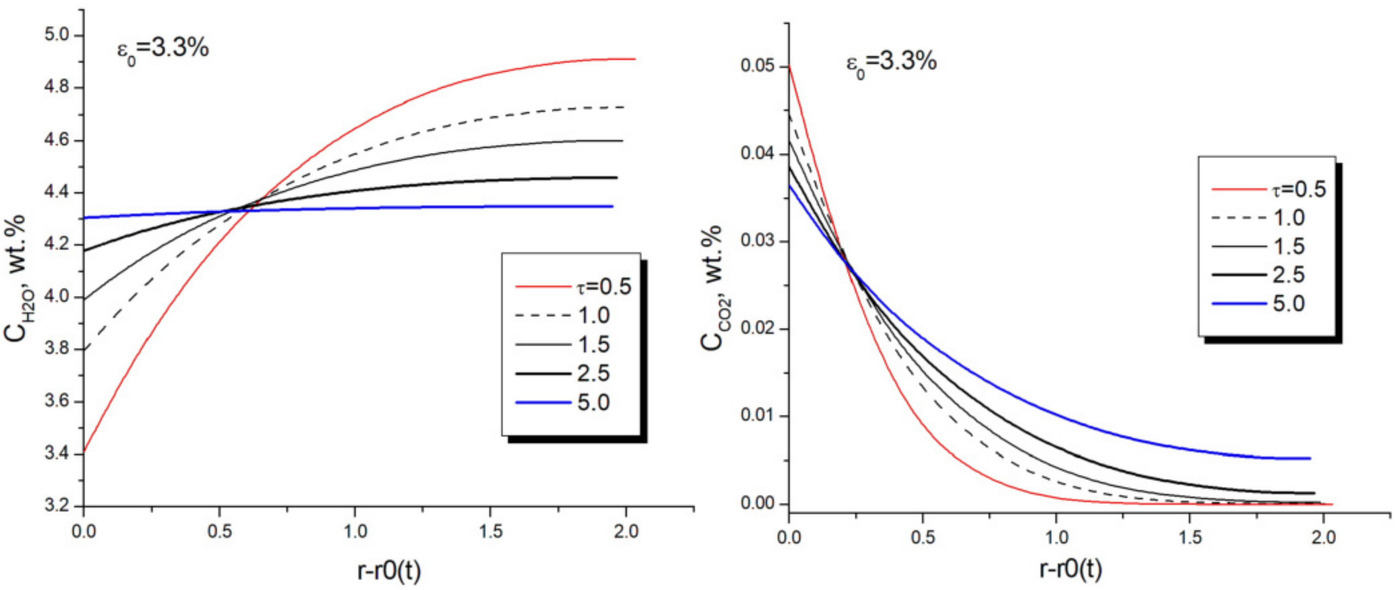

(a) (b)

Figure 2. Concentrations of CO_2 and H_2O in the melt at the contact with the a CO_2 bubble in the hydrous melt calculated at different moments of time (see legend). The distance from the contact is normalized to the initial bubble radius R_0, the time is scaled to the water diffusion time $\tau_0 = R_0^2/D_{H_2O}$, the initial water content is set at 3.3 wt. %. The linear dimensions of the bubble and melt shell correspond to the initial volumetric content of CO_2 fluid of 5 vol. %. See text for details.

Obviously, at $\tau \to \infty(\mathrm{erfc}(0) = 1)$ the distribution described by Eqn. (5) becomes a widely used stationary function $C(r,t) = \Delta C r_0/r$. Formally, the Eqn. (5) is a solution of the diffusion equation with an initial stepwise distribution: $C(r > r_0, 0) = c_0$; $C(r = r_0, 0) = \Delta C + c_0$. However, the solutions of the diffusion equation weakly depend on the initial conditions. In particular, if the boundary condition in time-dependent ($\Delta C = \Delta C(t)$), the distribution $C(r,t)$ is approximated by Eqn. (5) at a sufficiently slow change in the concentration at the boundary. As can be seen in Figure 3, the numerical and simplified theoretical dependences of $CO_2(H_2O)$ for a dimensionless time of 0.5 are quite close, which confirms the possibility of simple calculation of this dependence for various diffusion coefficients.

The ideal case of fluid exchange considered above may be far from those observed in nature, where the interaction of unevenly distributed moving bubbles with a fluid enriched in CO_2 and a hydrous melt occurs along with crystallization caused by dehydration. In the second part of the article, we report experimental results on CO_2 dehydration of albite melt, often taken as a model of silicic magmas, and consider these effects.

Part 2. Experimental Modeling of Crystallization Induced by CO_2 Flushing

Process of the bubble-magma interaction modelled above is only possible for a superheated magma. The interaction of hydrous albite melt at high temperatures with CO_2 generated *in situ* by interaction with calcite, was studied experimentally in [*Simakin et al.*, 2012]. The water content drops by 2 wt. % in several hours of flushing with CO_2 bubbles. Convection of albite melt at the millimeter scale caused by bubbles was observed. Natural melts are usually in equilibrium with one or more crystalline phases. The extraction of water by CO_2-rich bubbles induces their crystallization, since the loss of water increases the liquidus temperatures of magmatic minerals. The crystallization complicates simple process of diffusive fluid-magma interaction. We model this process in a simple albite – H_2O system at near liquidus temperature. In one series of the experiments, CO_2 bubbles with a characteristic inter-bubble distance of several tens of microns interacted with a hydrous albite melt. In the second series, the volume of albite melt interacted with the carbonic fluid via the upper interface to model the process on a larger linear scale of several millimeters.

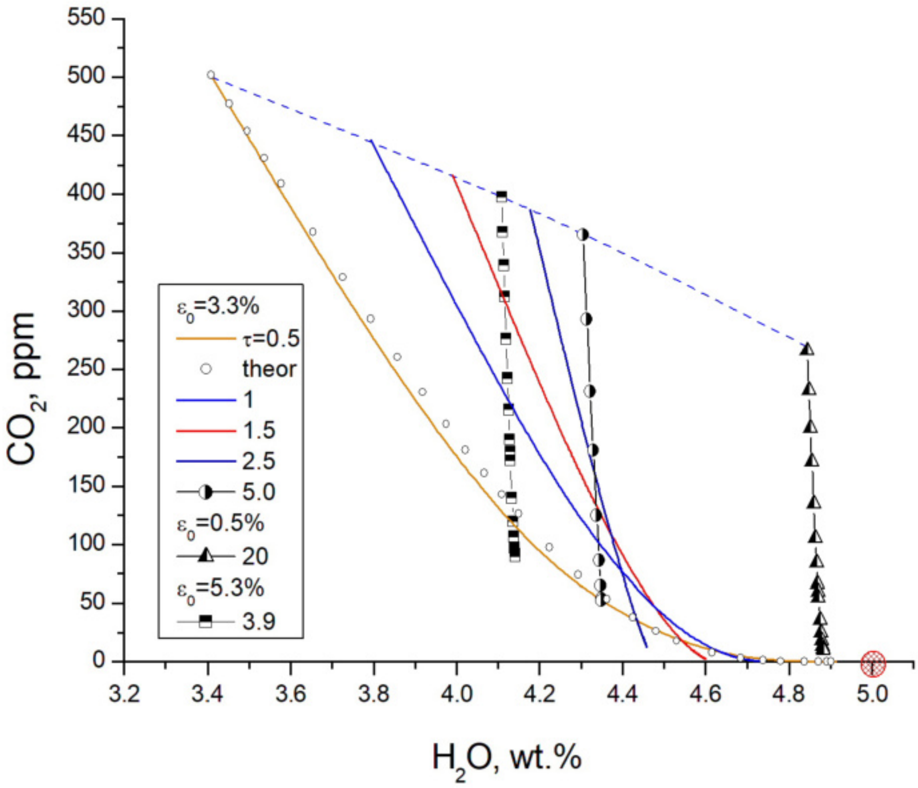

Figure 3. Calculated profiles C(R) of CO_2 and H_2O concentrations in the melt at the contact with the CO_2 bubble projected on the H_2O-CO_2 plot. The time intervals are shown in the legend (see Figure 1 for time scaling). The distributions are calculated for three volume fractions of the bubbles. The final distributions (symbols) of water and of CO_2 are, respectively, almost uniform and highly uneven. The points with the highest CO_2 content are on the fluid saturation curve (dotted line) and correspond to the fluid-melt contact. Theoretical values for the volume fraction $\varepsilon_0 = 0.033$ and dimensionless time $\tau = 0.5$ are calculated using eqn.(5). It takes more time to achieve a uniform distribution of water with a lower volume fraction of bubbles. The initial melt composition is shown by a hatched circle.

Experimental Technique and Methods

The experiments employing double capsule technique were carried out in Pt-capsules at IHPV (UHPG-10000 type) at IEM RAS and were terminated by isobaric quenching at a rate of 100–250 °C/min, and at 60 °C/s in some runs. The starting hydrous albite glass was produced from crystalline albite (natural mineral from Kalba, Kazakhstan) at $T = 1200$ °C and $P = 200$ MPa for 5 hours with the addition of a desired water content. To homogenize the water distribution, the glass was powdered and remelted at the same parameters. According to the Karl Fisher titration (KFT) data, the water content in the starting albite glass was 4.9 ± 0.1 and 5.1 ± 0.1 wt.% in the two series of experiments. Determination of the water content in the first glass by FTIR method gives a slightly lower value of 4.7 ± 0.1 wt.%.

In the first series of experiments, albite glass was a 100–200 μm powder, obtained by sieving and placed in a larger capsule. AgC_2O_4 loaded into a smaller capsule was used as a source of CO_2, in an amount providing a glass/CO_2 weight ratio of ~ 5. The small capsule (3 mm diameter) with the squeezed open end was placed in a large one (5 mm diameter), which was welded.

In the second series of experiments, glass cylinders were tightly inserted into the small capsules. The source of CO_2 was a mixture of $CaCO_3$ and quartz in an amount providing a glass/CO_2 weight ratio of $\sim 1/2.5$. To accelerate the decarbonization reaction with the formation of CO_2, a small amount of Na_2CO_3 or K_2CO_3 was added. The mixture was loaded into a large open capsule and covered with a separating platinum cap. Then a small capsule with a piece of glass was placed on the lid and the large capsule was welded. While using the cylindrical pieces of aluminosilicate glass, the fluid interacted with a melt through a sharp interface. Taking into account the curvature of the interface due to the capillary effect, this setting approximates a bubble in the melt with a size of several millimeters, which is consistent with real magmatic systems. On the contrary, in runs with the starting glass powder, due to the large number of bubbles, the reactions are complete in a short time. The experimental conditions, including temperature and duration, are shown in the Table 2 and 3.

Table 2. Series 1 of experiments with glass powder

a) Experimental data

#	time, min	ε_{fl1},%	ε_{fl2}	ε_s, %	$C_{w,gl+s}$ (EMPA)	$C_{w,gl}$*	$C_{w,max}$ (T_{run})
A21	40	9.9	3.5	8–10	2.5 ± 0.4	2.7	
A20	75	7.0	2.6	10–13	2.7 ± 0.2	3.1	3.5
A17	204	5.5	1.2	18–33	2.7 ± 0.7	3.6	
A15	242	0.7	0.1	64–76	2.5 ± 0.4	–	

Initial water content 5.1 wt. %, $T_{run} = 950\,°C$. $P = 200\,MPa$.

*$C_{w,gl}$ is an estimate of water content in the interstitial glass equal to $C_{w,gl+s}/(1-\varepsilon_s)$ (average values of parameters are used), $C_{w,max}$ (T_{run}) is liquidus water content at the run temperature, which is upper limit of $C_{w,gl}$

b) Thermodynamic constrains on the equilibrium compositions of melt and fluid

#	almost complete crystallization			no crystallization	
	fluid – $X_{CO_2,min}$	melt – $C_{w,eq}$	$T_m(C_{w,eq})$, °C	fluid – $X_{CO_2,max}$	melt – $C_{w,eq}$
A21	0.66	2.80	1008	0.77	2.15
A20	0.67	2.74	1011	0.78	2.11
A17	0.70	2.57	1021	0.79	2.00
A15	0.71	2.51	1024	0.80	1.96

$X_{CO_2,min}$ is minimal CO_2 mole fraction when practically all water is exsolved and $C_{w,eq}$ is water content in the last residual melt, $T_m(C_{w,eq}) > T_{run}$ is liquidus temperature of albite melt at $C_{w,eq}$; $X_{CO_2,max}$ fluid composition equilibrated with metastable albite melt with water content $C_{w,eq}$.

Table 3. Series 2 of experiments with single glass piece

Experimental data						Thermodynamic estimates		
#	time,min	T_{run},°C	$C_{w,0}$*, wt. %		$C_{w,max}$ (T_{run})	almost complete crystallization		
			EMPA	IR		fluid – $x_{CO_2,min}$	melt – $C_{w,eq}$	$T_m(C_{w,eq})$, °C
A57	53	1020	2.0	2.2	2.43	0.97		
A63	108	1020	1.8	2.0 (1.7)	2.43	0.98	0.2	1149
A67	239	975	2.0 ± 0.1	–	3.09	0.98		

Initial water content 4.9 wt. %, $P = 200\,MPa$,

* $C_{w,0}$ is water content in the melt on the boundary with fluid; other symbols as in Table 1.

Weighing was done in an AUW220D analytical balance (Japan), with a measurement accuracy of ±0.1 mg for the mass range used. The composition of the run products were studied by SEM-EDS on a Tescan VEGA II XMU electron scanning microscope equipped with EDX analyzer with a Si(Li) INCA Energy 450 solid-state detector. The analysis was performed at an accelerating voltage of 20 kV. The obtained data were processed using the INCA Suite ver. 4.15 software with subsequent recalculation of the obtained results for weight contents using software packages developed by A. N. Nekrasov at IEM RAS. The Tescan Atlas program was used to process the BSE images and determine the phase proportions. The water content was analyzed using the Karl Fisher titration (KFT) on an AQUQ 40 device with a heating module for solids. According to the instrument calibration data, the accuracy of water determination is 3 rel. %. The Raman spectra of fluid from bubbles in experimental glasses were measured on a RM1000 spectrometer equipped with CCD detector, rejection filter, and Leica microscope. The spectra were excited using 532 nm solid-state diode laser. The laser beam was focused on a sample with 50× objective. The measurement parameters are as follows: laser power 22 mW, slit width 50 µm, and counting time 5×10 s.

The local content of water and CO_2 was measured on a Nicolet iN10 FTIR microscope equipped with a liquid nitrogen cooled MCT detector. The microscope and sample compartment were continuously purged with high purity dry nitrogen prior to and during the acquisition of the spectra. The measurements were performed in transmission mode at room temperature; the samples were carefully cleaned in acetone and placed on a KBr plate. The microscope was focused on the top surface of the sample. For the profiles, an aperture of $50 \times 50\ \mu m^2$ the measurement spots were immediately adjacent to each other. The spectra were obtained in the spectral range 600–6000 cm^{-1}. At least 64 scans were recorded per spectrum with a spectral resolution of 2 cm^{-1}. The FTIR spectra were processed using the Origin 9.5 software. Basic nonlinear correction was performed for each region of interest.

The interpretation of IR spectra requires additional information. Water contents were calculated from the combination 4500 cm^{-1} and 5200 cm^{-1} bands for hydroxyl and molecular water, respectively. The corresponding linear extinction coefficients and density of the albite glass were taken from [*Behrens et al.*, 1996] The signal of molecular CO_2 in IR spectrum at ~2349 cm^{-1} is superposed on a gaseous CO_2 doublet present as a trace despite the purging. The rotational bands of the dissolved CO_2 are suppressed. The spectral envelope was deconvoluted into three Gaussian components. After the deconvolution the contribution of atmospheric CO_2 peaked at 2336 and 2361 cm^{-1}. Carbon dissolved in the glass is also present as a carbonate ion. An isolated symmetrical ${CO_2}^{2-}$ ion has an active IR asymmetric stretching mode ν_3 at 1415 cm^{-1}. Adsorbed ${CO_3}^{2-}$ is characterized by the splitting of this band into two with a separation $\Delta\nu_3$, reflecting interaction with the substrate: weakly monodentate and strongly adsorbed bidentate ${CO_3}^{2-}$ ions are assigned to $\Delta\nu_3 = 100$ and 300 cm^{-1}, respectively [*Coenen et al.*, 2018]. In hydrous albite glass, one band at ≈1610 cm^{-1} overlaps with OH-bending mode of molecular water at ~1636 cm^{-1}. Subsequently, another band of the ${CO_3}^{2-}$ doublet at 1375 cm^{-1} was used in the analysis. The extinction coefficients for molecular CO_2 and ${CO_3}^{2-}$ were taken from [*Stolper et al.*, 1987]. CO_2 dissolves in albite melt mainly in the form of molecular CO_2. The fraction of the carbonate form increases with cooling and in quenched glass depends on the glass formation temperature T_g. [*King and Holloway*, 2002] used $r = CO_{2,mol}/(CO_{2,mol} + CO_{2,carb}) = 0.9$ in their analysis. Application of the thermodynamic model from [*Konschak and Keppler*, 2014] to our data at $T_g = 600\,°C$ gives $r = 0.73$. At low total carbon ($CO_{2,tot}$) the carbonate band at 1375 cm^{-1} is poorly resolved and the$CO_{2,tot}$ was estimated from data on molecular CO_2 corrected with $r = 0.8$ and 0.73.

Results of Experiments

The First Set of Experiments was performed at $P = 200$ MPa and $T = 950\,°C$. AgC_2O_4 used as the fluid source decomposes 100–200 °C below softening of the Ab glass. CO_2 fills the pores and forms bubbles when the glass powder melts. BSE and optic images showed that the bubbles are 50–200 µm in diameter with a population of tiny bubbles few microns in size. Volume fractions of both types of the bubbles are shown in Table 2 in columns $\varepsilon_{\text{fl}1}$ and $\varepsilon_{\text{fl}2}$, respectively. Over time, the bubbles quickly exsolved from the melt (see Table 2), assuring CO_2 flushing.

The local water content of the vesiculated glass was estimated using EMPA. The concentrations of all elements, including oxygen (with the exception of hydrogen), were measured by focusing the electron beam on a $10 \times 10\,\mu\text{m}^2$. This method reproduces well the KFT value of 5.1 ± 1.0 wt. % in the starting glass. Minimum water content drops to 2.5–2.6 wt. % in 30 min experiment (Table 1) and to 2.7–2.8 wt. % at 40 min duration. The Table 2 shows values corrected (divided on the glass volume fraction) for crystals present in the sampled areas. The minimum water content in the glass can be estimated based on the composition of the fluid (column $X_{CO_2,\text{min}}$ in Table 2), assuming that all water has partitioned into the fluid. The values of $X_{CO_2,\text{min}}$ in different runs differ slightly due to the variation in the mass ratio of the glass and $Ag_2C_2O_4$. During the crystallization of albite glass, the water content in the melt cannot exceed $C_{\text{w,max}} = 3.5$ wt. %, at which the run temperature $T = 950\,°\text{C}$ is equal to the melting temperature of albite at $P = 200$ MPa (calculated based on the data from [*Holland*, 2001]). All values of the water content estimated with EMPA are in the range $C_\text{w}(X_{CO_2,\text{min}}) < C_\text{w} < C_{\text{w,max}}$, except for run a15. During the albite crystallization, water is released, which partially compensates its transfer to the CO_2-enriched fluid. Since the samples from the first set of experiments contain a large number of crystals and bubbles, it is difficult to use the micro-FTIR method to accurately analyze the H_2O and CO_2 content. Several measurements were performed only for glass a21 from a short run. IR spectroscopy gives a water content in the range 1.8–4.2 wt. %, which is consistent with the results of EMPA (see Table 2 and Figure 4). The lowest value of $C_\text{w} = 1.8$ wt. % corresponds to the equilibration of the water content with bulk interaction of the fluid with the melt without crystallization. In two analytical points, the content of water and carbon dioxide fall on the solubility curve within the measurement uncertainty. The melt at the other three points lost water but did not receive enough CO_2 to become saturated with fluid.

In the first series of experiments, the fluid composition in the bubbles was characterized by the Raman spectroscopy. CO_2 was identified by the characteristic Fermi dyad at 1385 and 1281 cm^{-1} (see Figure 5f). Density of the fluid (ρ_{fl}) in the bubbles was estimated from the difference of positions of these bands (the dyad splitting Δ, cm^{-1}). Since the spectral resolution of the Raman spectra is 1.5 cm^{-1}, exact positions of the bands maxima were determined from approximation of the peaks with a Lorentzian lineshape as recommended in [*Yamamoto and Kagi*, 2006]. The empirical relationship $\rho_{fl}(\Delta)$ from *Wang et al.* [2011] was used. The CO_2 density in the bubbles was evaluated in the samples a20 and a17, showing a rapid increase in the crystallization degree with an increase in the run duration from 75 to 204 minutes, respectively (see Table 2). The obtained values are 0.566 ± 0.010 g/cm^3 ($n = 3$) and 0.673 ± 0.006 g/cm^3 ($n = 3$) for a20 and a17, respectively. The CO_2 density in bubbles in the quenched glass carries information about composition (H_2O/CO_2 ratio) of the fluid at the parameters of the experiment; however, the interpretation of these data, complicated by numerous factors, is beyond the scope of our work.

In the shortest experiment (a21) the albite crystallization caused by dehydration was confined the former boundaries of glass powder chips (Figure 5a). These surfaces were exposed to CO_2 at the beginning of the experiment prior to the melting, and it is likely that microcrystals could have nucleated there and continued to grow at high temperature. The crystals possess a highly elongated morphology. The length of the crystals at 30 min is 15 µm, at 40 min – 24.3 µm. With an increase in the experiment duration to 2 hours, the crystallization degree reaches 80–85 vol. %. These observations correspond to the albite growth rate of about 1.3×10^{-8} m/s, which is almost two orders of magnitude higher than the growth rate of feldspar from rhyolite melt under similar conditions [*Rusiecka and Baker*, 2021; *Simakin and Chevychelov*, 1995], which is slowed by diffusion in the melt.

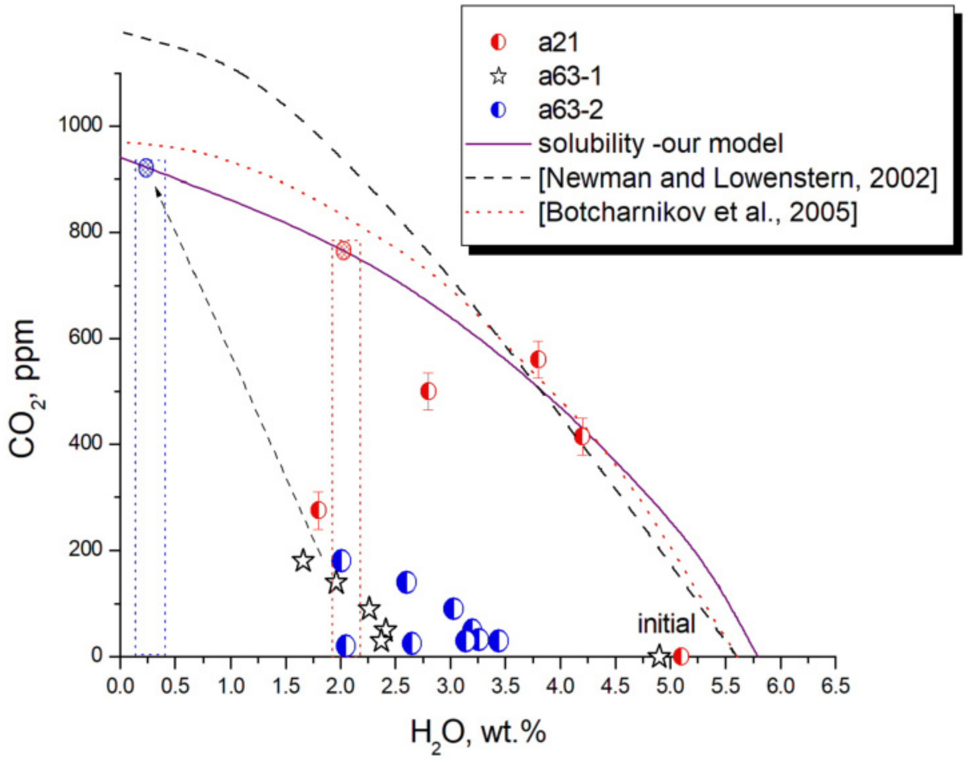

Figure 4. The results of our experiments on the composition of the fluid dissolved in the albite melt. Two profiles measured with µ-FTIR on two pieces of glass from the run a63 with frontal dehydration are represented with half-filled circles and open stars. Discreet points in the bubbly glass from the experiment a21 are marked with small red half-filled circles. The model solubility curve at 200 MPa and literature data are shown with lines. The equilibrium compositions for the exchange of the melt with CO_2 in the experiments are shown by hatched circles. The dotted boxes depict the expected locations of compositions homogenized with H_2O prior to homogenization with CO_2.

Homogeneous nucleation in albite melt is extremely difficult to achieve, making this composition ideal for glass formation [*Zanotto and Cassar*, 2017]. In our case, the glass powder with a high surface area interacted with CO_2 at temperatures below T_g, which led to the formation of numerous nucleation centers. Since the growth rate is high, the dehydrated albite glass crystallized efficiently. The volume fraction of crystals (ε_s) increases with time as indicated in Table 2 and shown in Figure 5a-d. The transformation kinetics can be approximated with Johnson – Mehl – Avrami – Kolmogorov (JMAK) equation $\varepsilon_s = 1 - a \cdot \exp(-(k \cdot t)^n)$ [e.g., *Yinnon and Uhlmann*, 1983]. The model with $n = 3$ and $a = 1$ characterizing the growth of crystals on preexisting nuclei formed on the surface of glass particles at low temperatures, does not fit the data (Figure 6). The proportion of solids extrapolated to the beginning of the experiment is non-zero (coefficient a less than 1). The best fit model has a value of $n = 10.5$, much larger than the maximum theoretical value of $n = 4$. This implies violation of the constant nucleation rate assumption underlying the JMAK equation. The extremely high rate of transformation in the time interval of 180–250 min may be associated with the rapid delayed homogeneous nucleation during this period. With more data available, the transformation kinetics can be approximated by a sum representing a set of nucleation events with different delay times [*Narine et al.*, 2006].

The Second Set of Experiments aimed to reproduce the scenario with a large inter-bubble distance and large bubbles. The carbonic fluid was in contact with a few mm thick volume

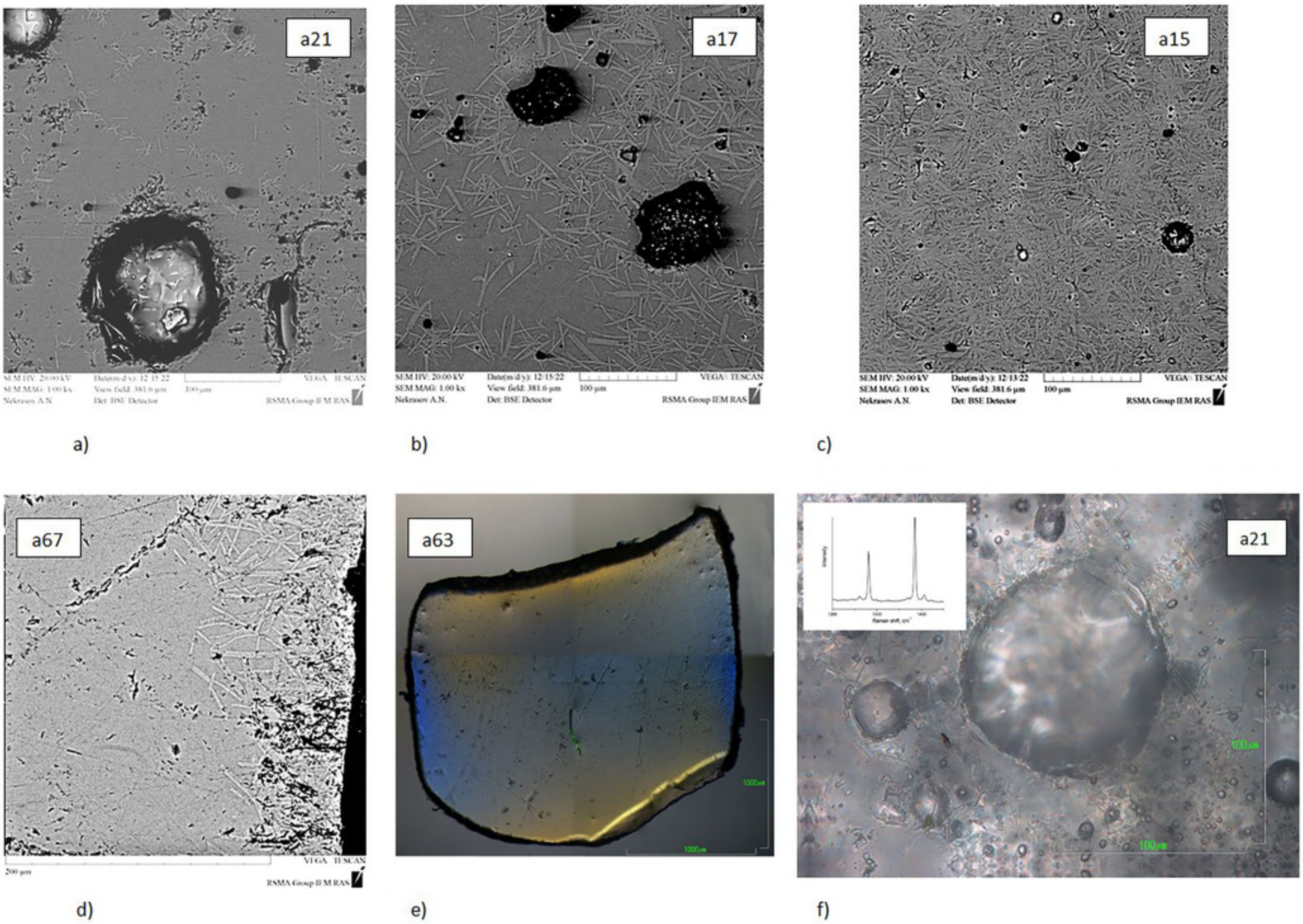

Figure 5. BSE (a–d) and optical (e,f) images of the experimental products, run numbers are indicated on the images. Images (a–c) show gradual increase in crystallinity and a decrease in the fluid bubbles fraction over time. d) In run a67 albite crystallization started from the capsule wall after dehydration of the melt near the contact. e) Double-polished glass plate used in µ-FTIR analysis. f) Optical image of the glass slice from run a21 (shortest duration 40 minutes) shows the presence of the small bubbles present in the starting imperfect glass, and larger bubbles rich in CO_2, reaching large size due to coalescence; Raman spectrum of CO_2 is in the inset.

of hydrous albite at the capsule bottom. At temperature $T = 1020\,°C$ an unexpected mechanism of the interaction between CO_2 and albite melt was observed. In a short experiment a57 (duration 53 min) the distribution of water was estimated using EMPA and is shown in Figure 7. The water concentration at the upper boundary of the profile was $C_w \approx 2$ wt.%. Since the starting glass for this experiment contains many microbubbles, only one measurement of the water content at the boundary was performed using µ-FTIR, which gives $C_w = 2.3$ wt.%. These values are much higher than $C_w \approx 0.2$ wt.%, corresponding to the equilibrium solubility in the fluid with $X_{CO_2} \geq 0.9$. More accurate data for both H_2O and CO_2 (Figure 8) were obtained using µ-FTIR for the run ab63 performed under the same PT conditions with bubble-free starting glass (see Table 3 and Figure 5e). The water contents at the boundary of 2.01 and 1.66 wt.% is close to 2–2.3 wt.% at the boundary in run a57 (Table 3). It is noteworthy that the CO_2 content near the contact is significantly smaller than the saturation level expected for a fluid with a high CO_2 mole fraction. As seen in Figure 4, the pair of concentrations (C_{H_2O}, C_{CO_2}) near the contact with the fluid for the run a63 does not approach the saturation curve for $P = 200$ MPa, in contrast to the data presented in [*Yoshimura and Nakamura*, 2010].

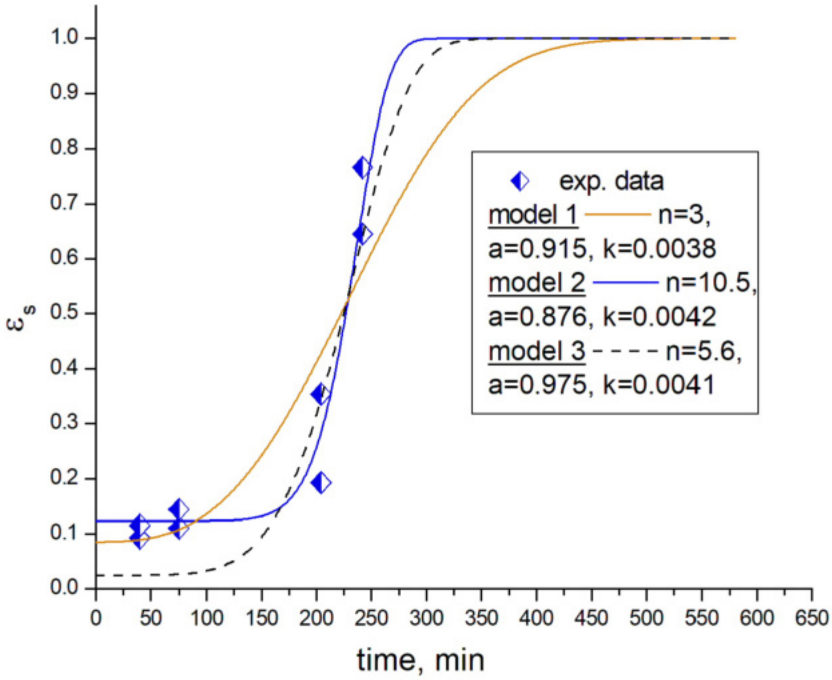

Figure 6. Time-dependence of the volume fraction of crystals in the bubble-free melt in the first series of experiments with starting albite glass powder. The experimental points (semi-filled diamonds) are approximated by the modified JMAK equation $\varepsilon_s = 1 - ae^{-kt^n}$ (see text) with the parameters indicated in the legend. The coefficient a is taken to be less than 1 to account for the rapid crystallization from the surface of glass fragments upon contact with CO_2 at the beginning of experiment. The classical model with $n = 3$, implying kinetic control without nucleation, poorly fits the observations. The preferred model 2 with $n \approx 10$ implies rapid homogeneous nucleation with large delay time.

Since there were no signs of crystallization visible on the SEM and optical images in the contact area, we assume that the dense CO_2 fluid interacted with the melt surface and extracted mainly Na and Al, enriching the upper melt film with silica. To explain the observations, the concentration gradients in this protective film must be very high, and the diffusion coefficients must be several orders of magnitude lower than in the albite melt. This hypothesis was tested using experimental data on the diffusion coefficients of CO_2 and H_2O in silica glass [*Behrens*, 2010]. It was found that a silica glass film about 2 µm thick will provide the concentrations and the diffusion fluxes observed on the melt surface in run a63.

Another unusual feature of the mechanism of interaction between albite melt and pure CO_2 at high temperatures is the decrease of the water content in the melt the near the capsule walls in the run 63. From the µ-FTIR data (Figure 8) it can be noted that the water content decreases towards the bottom and that the second, incomplete, profile is characterized by lower concentrations, since it was closer to the wall. At the same time, the CO_2 distributions follow the same dependence with a monotonously decreasing concentration with distance from the contact. These observations can only be explained by the action of some mechanism of ultrafast surface diffusion of water, but not of CO_2, along the Pt-melt interface. This mechanism equalizes the boundary concentration of water with values near the active upper contact with the fluid.

At a lower temperature of 975 °C (runs a67 and a68) crystallization began (Figure 5d) from the upper surface and, in some places, near the bottom of the capsule. In this case,

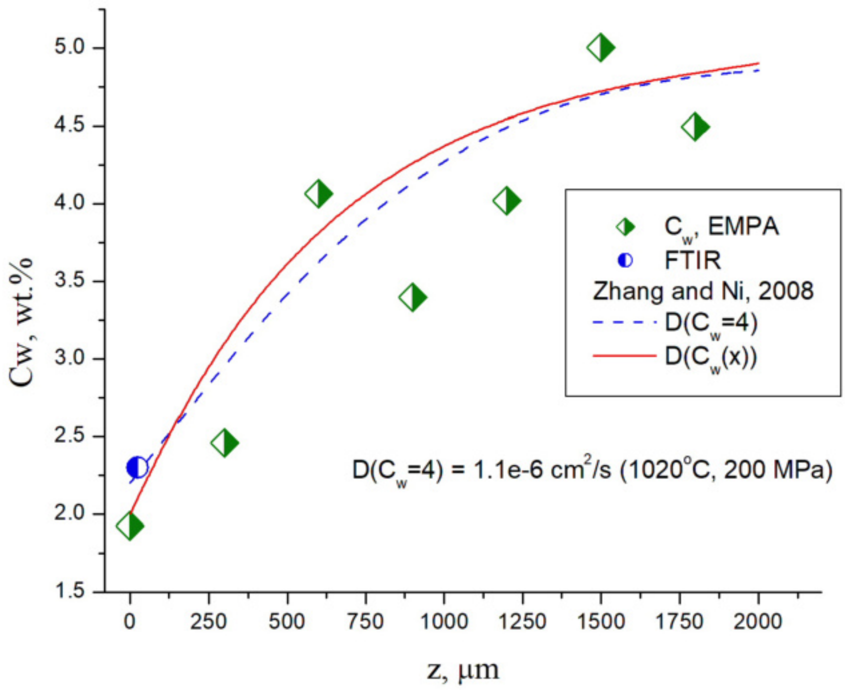

Figure 7. Water distribution in glass from experiment a57, demonstrating dehydration in contact with a CO_2-enriched fluid. Water concentrations were estimated with EMPA. Several theoretical profiles calculated with the parameters of the experiment a57 are shown; the diffusion profile at a constant boundary condition and diffusion coefficient calculated at a constant $C_w = 4$ wt. % is depicted by a dashed line; the profile shown in solid line is calculated with a diffusion coefficient dependent on water content [*Zhang and Ni*, 2010].

the concentration of water in the contact with the crystallization front was estimated only with EMPA at the level of 3.0 ± 0.5 wt. %, which is close to the water content of 3.1 wt. % in albite melt in equilibrium with crystalline albite under experimental PT conditions (see Table 3). The minimum growth rate of albite, calculated assuming zero nucleation delay time, is 0.9×10^{-8} m/s (run ab68-4) and 0.98×10^{-8} m/s (run ab67), which is somewhat lower than the estimate of 1.3×10^{-8} m/s obtained in the first series of experiments. It can be noted that the composition of alkali feldspars in the runs ab68 and ab67 slightly differ in potassium content with $K_2O = 0.35 \pm 0.10$ wt. % and 0.11 ± 0.10 wt. %, respectively. This difference is explained by the use of K_2CO_3 and Na_2CO_3 to stimulate the generation CO_2 in the reaction of $CaCO_3$ with SiO_2 in runs ab68 and ab67, respectively.

We model the distribution of water measured in run a57 by solving 1D diffusion equation with a variable diffusion coefficient:

$$\frac{\partial C(x,t)}{\partial t} = \frac{\partial D}{\partial C}\left(\frac{\partial C}{\partial x}\right)^2 + D\frac{\partial^2 C}{\partial x^2} \tag{6}$$

The diffusion front of dehydration in this run did not reach the lower boundary of the melt. Therefore, a constant water content of 4.9 wt. % at the bottom and 2 wt. % on the surface were taken as boundary conditions. The diffusion coefficient in silicic melts varies by about half an order of magnitude due to change in the water content, is a function of temperature, composition, and C_{H_2O} [*Zhang and Ni*, 2010]. Equation (6) was solved numerically using the built-in solver (FDM+Newton iterations) of the MAPLE 9.5 commercial software. EMPA measurements are relatively well reproduced both

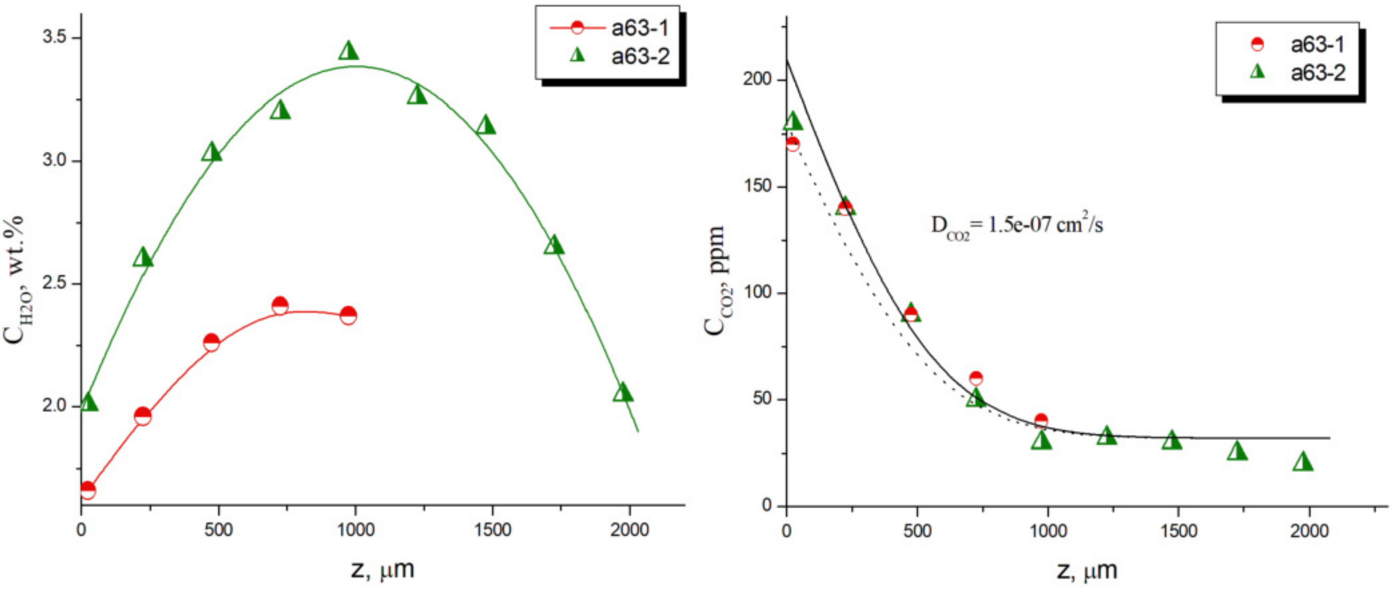

(a) **(b)**

Figure 8. The content of volatiles on two profiles across the glass from the run a63 from the top contact towards the bottom a) H_2O distributions for full (semi-filled triangles) and half (semi-filled circles) profiles b) CO_2 distributions and their approximation by a complementary error function (erfc), the value of the fitted diffusion coefficient is shown in the plot.

at concentration dependent and calculated at $C_w = 4$ wt. % values of the diffusion coefficient (Figure 7). The distribution of water in the run a63 is three-dimensional due to the loss of water from the entire surface of the melt and a large diffusion time (dimensionless $\tau > 5$). For the run a63 only the CO_2 distribution was considered due to its 1D character since the influx of CO_2 occurs only from the upper contact of the fluid with the melt (Figure 8b). The CO_2 diffusion coefficient obtained by fitting with a complementary error function (erfc), is 1.5×10^{-7} cm^2/s, which is equal to the value calculated from the model from [*Zhang and Ni*, 2010] at $C_{H_{20}} = 4$ wt. %.

The distributions of water and carbon dioxide are projected onto the graph ($C_{H_{20}}$, C_{CO_2}) in Figure 4. On this plot the studied case of extreme dehydration with pure CO_2 at a high mass ratio of CO_2/melt is characterized by a convex path that deviates significantly from the predicted series of concave trajectories evolving towards a vertical line (see Figure 3 and in [*Yoshimura and Nakamura*, 2010]. In our case, it should have a maximum CO_2 content approaching 1000 ppm and a H_2O concentration of less than 1 wt. %. As mentioned above, the influence of the protective film and ultrafast diffusion of H_2O along the Pt-melt interface leads to the observed $CO_2(H_2O)$ trajectory configuration.

Application to Rhyolitic Magma

Scaling

Schematic diagram showing principle parameters of the CO_2 flushing process in our numerical modeling, experiments with albite melt and in natural environments with initial bubble radius R_0 and inter-bubble distance $W = 2R_1$ is shown in Figure 9. Several lines of constant initial volume fraction of fluid ε_{fl} are plotted on this figure to delineate the parametric area expected in nature, encountered in experiments with albite melt and used in numerical modeling. In the process of the water migration in the melt, the water diffusion time scale is $\tau_w = R_0^2/D_w$. As demonstrated above, homogenization of the melt in H_2O takes 4–20τ_w depending on the inter-bubble distance $W = 2R_1$ or equivalent bubbles volume fraction $0.005 < \varepsilon_{fl} < 0.05$. Our modeling data correspond to a simple dependence for the homogenization time $\tau_H = 0.55\tau_w {\varepsilon_{fl}}^{2/3}$. After substituting the expression for $\varepsilon_{fl} = (R_0/R_1)^3 = 8(R_0/W)^3$ into the expression for τ_H, we get $\tau_H = 0.138W^2/D_w$. For experimental conditions water diffusion coefficient is calculated at the average C_w=1.5 and

4 wt. % and $T = 950\,°C$. In the first series of experiments with albite melt homogenization time τ_H is 3–9 minutes (see Figure 9). The residence time of bubbles in the melt in these experiments depends on their size, distance from the surface, and the local melt viscosity. The volume fraction of large bubbles rich in CO_2 over time is well described ($R^2 = 0.9995$) by the exponential function $\varepsilon_{fl} = 0.06 + 0.34\exp(-t/t_0)$ with $t_0 = 19$ minutes. This means that some bubbles may leave the melt before equilibration even in terms of water distribution. The duration of experiment a21 is comparable to the expected time of water homogenization. The duration of other experiments is several times longer, albite crystallization and diffusive migration of the exsolved water occurred on the scale of the entire sample with water loss through the surface.

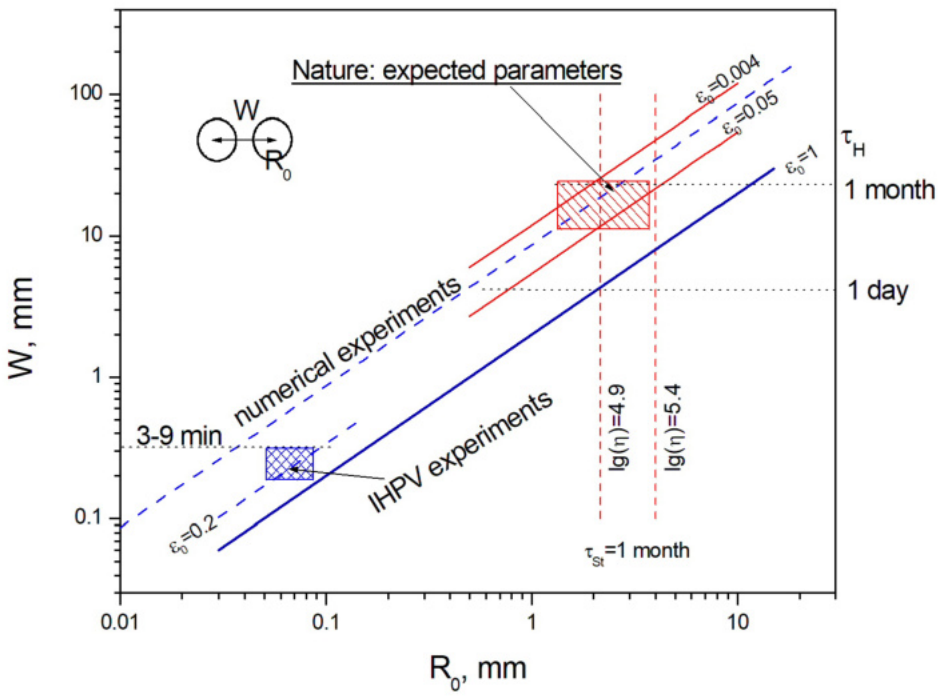

Figure 9. Schematic diagram showing the principle parameters of the CO_2 flushing process in our numerical modeling, experiments with albite melt and in nature. A homogeneous distribution of identical bubbles, the initial bubble radius R_0 and the inter-bubble distance W equal to $2R_1$ in the spherical shell model are assumed. The lines of the constant initial fraction of bubbles ε_0 are shown. The dashed lines show the average parameters of the numerical and IHPV experiments. Several values of water homogenization time $\tau_H = W^2/D_w$ are plotted near the vertical axis. For experiments with albite melt, the water diffusion coefficient D_w was calculated for $C_w = 1.5$ and 4 wt. % at $T = 950\,°C$, for natural rhyolite (τ_H values near the right axis) at $C_w = 4$ wt. % and $T = 800\,°C$. The vertical dashed lines correspond to the Stokes time $\tau_{st} = 1$ month (see text) calculated for the albite melt with $C_w = 4$ wt. % at $T = 800\,°C$ and rhyolite magma (larger values of viscosity and R_0) at the same parameters. For bubbles with $R_0 \leq 1\,\text{mm} \tau_{st} > \tau_H$ which means local equilibrium H_2O with melt and possible CO_2 unsaturation. In the experiments with albite melt, water and melt are expected to equilibrate on the scale $R_0 \approx 100\,\mu m$.

Upon reaching the homogenization of water in the melt at τ_H, dehydration reaches a maximum. Later, when CO_2 is equilibrated with the melt, the H_2O content increases to the equilibrium value following a decrease in the CO_2 concentration in the fluid. The bubbles volume also reached its maximum at τ_H. With a volume fraction of CO_2 from 0.4 vol. % to 4 vol. %, the proportion of CO_2 transferred into the melt is from approximately

0.4 to 0.06. Applying our results to nature, we can assume that after the bubbles of fluid enriched in CO_2 start at the bottom of the magma chamber, their residence time will depend on the dynamics of the magma The bubbles move relative to the melt at a rate close to the Stokes velocity (the rise of a single bubble in an infinite volume of liquid) $U_{st} = 1/3(\rho_m - \rho_{fl})gR_0^2/\eta$. Obviously, this bubbles transfer mechanism can be only local at a time scale close to τ_H. However, the density of the fluid is much less than that of the melt, and the volume of bubbly magma will induce convective flow. For a single convective cell, the convection rate will be much higher than the Stokes rate. Using the results of [*Simakin et al.*, 1997], it can be shown that at $\varepsilon_0 = 0.2$ vol. % (regardless of phase densities and melt viscosity) the convection rate will be approximately equal $U_{conv} = 0.6U_{st}(H/R_0)$, where H is cell height and R is bubble radius. At $H = 100$ m and $R_0 = 0.001$ m, the convection velocity will be approximately 6×10^4 times higher than Stokes rate. Then the minimum time for bubbles to escape from the magma due to Stokes flow τ_{st} becomes proportional to the ratio of the typical width of the convective boundary layer of 1 m [*Simakin and Bindeman*, 2022] to the Stokes bubble rise velocity U_{st}. Figure 9 shows the Stokes times equal to one month (vertical dashed lines) calculated for albite melt with $C_w = 4$ wt. % at $T = 800\,°C$ and rhyolitic magma (larger values of viscosity and R_0) with the same parameters with the model [*Hui and Zhang*, 2007]. For real values of R_0 and $\varepsilon_{fl}\tau_{st} > \tau_H$, so we expect local homogenization of water concentration corresponding to local values of ε_{fl}. Since diffusion of CO_2 is 6–10 times slower, the melt can be dehydrated, but not saturated with CO_2. Whatever the physical mechanism of bubble transport for sufficiently large bubbles in rhyolitic magma chambers, the local time of water homogenization becomes compatible with the typical time scale of pre-eruption processes, i.e. in the range of days and months.

Discussion

The unexpectedly low concentration of CO_2 and high concentration of H_2O at the contact between CO_2 and hydrous albite melt, observed in our experiments (Figure 7,8), measured with resolution of micro-FTIR method of about 50 µm and resolution of EMPA method of about 5 µm, we explained by the presence of ultrahigh concentration gradients in a narrow boundary layer, which we could not resolve. Under the PT conditions of run a63, the diffusion coefficient of H_2O decreases only by a factor of 5 when the water content in the albite melt decreases from 4 wt.% to zero [*Zhang and Ni*, 2010]. This means that the width of the diffusion zone in albite melt with a decrease in water concentration from 2 wt. % to zero should be only a few times narrower than when falling from 3.5 wt. % to 2 wt. % (≈ 1000 µm), and can be resolved using available analytical methods. The formation of a near-surface layer of a contrasting composition rich in SiO_2 with high viscosity and low diffusivities during the extraction of Na_2O and Al_2O_3 with CO_2 fluid can explain the observations. Direct experimental measurements of the solubility of the main and trace elements of the melt in supercritical CO_2 under high PT conditions have not been carried out. Observations of CO_2 fluid inclusions contained in pyroxenes indicate high solubility of Al_2O_3, Na_2O, K_2O, Rb_2O, SrO and other oxides at a pressure of about 1 GPa and a temperature of about 1000 °C [*Berkesi et al.*, 2012; *Hidas et al.*, 2010]. Our hypothesis is worth testing, since the likely effect of a protective film can significantly affect estimates of the rate of exchange of hydrous magma with pure CO_2 in nature.

The albite crystals grown in our experiments had a strongly elongated and sometimes even curved morphology (see Figure 5a–d), reflecting strong undercooling that occurs during melt dehydration. In nature, when the composition of the melt is in a quartz field, the formation of non-equilibrium morphologies of quartz crystals is expected in a dehydrated melt. As established experimentally, the transition from flat faceted to skeletal morphology of quartz occurs at $DT \approx 55\,°C$ [*Swanson and Fenn*, 1986]. Quartz crystals from the large (climatic) explosive eruptions (LCT, Yellowstone; Toba Tuff, Indonesia; Oruanui Tuff, New Zealand) of rhyolitic magma have reentrants, i.e., deep glass embayments open towards the edge of the crystal [*Befus and Manga*, 2019; *Ruefer et al.*, 2021]. Their origin may be related to the non-equilibrium growth stage of quartz with skeletal morphology.

The experiments did not confirm the hypothesis that reentrants can be formed during the dissolution of quartz in a magmatic melt, since the experimental dissolution front is flat [e.g., *Acosta-Vigil et al.*, 2005]. Some of reentrants were partially or completely filled with fluid, raising the question of how the magma became bubbly at the storage depth before the eruption [*Befus and Manga*, 2019]. Flushing with CO_2 can saturate the magma with the H_2O-CO_2 fluid and make it bubbly. An alternative mechanism is slow fractional crystallization caused by cooling of the magma, when excess fluid is exsolved [*Wallace et al.*, 1995].

Pichavant et al. [2013] extended the study of *Yoshimura and Nakamura* [2010] by experimental modelling the degassing of a basaltic melt initially saturated with CO_2 and water at $P = 200$ MPa. They found that when the pressure is reduced to 25–50 MPa at the fixed rate at a sufficiently low bubble number density (large inter bubble distance), a high supersaturation of CO_2 develops in the melt, while the water content follows equilibrium solubility (Figure 9). As with flushing, CO_2 and H_2O are decoupled due to their contrasting diffusivities. The control of the inter-bubble distance on CO_2 equilibration is very similar to the condition of disequilibrium Cpx growth in the Ab-Di-H_2O system [*Simakin et al.*, 2020]. Non-equilibrium hopper morphology of the crystal rim develops during quenching, when inter-crystalline distances exceed 5–8 µm. At a number density of crystals above $8–10 \times 10^9$ cm^{-3}, the diffusion of SiO_2 (the slowest component) homogenizes the melt composition to close to equilibrium. The diffusion coefficient of SiO_2 is many orders of magnitude lower than that of CO_2, so the threshold bubble number density is about 10^4 times lower than that of crystals. In *Pichavant et al.* [2013] study, the threshold bubble number density is determined by the time scale of experiments equal to $\tau_{\mathrm{exp}} = \Delta P/(\mathrm{d}P/\mathrm{d}t) = 1000–4000$ s. The diffusion coefficient of CO_2 in basalt melt at $T = 1150\,^\circ$C is 1.3×10^{-7} cm^2/s, and the homogenization time $\tau_{CO_2} = W^2/D_{CO_2}$. The condition $\tau_{exp} \ll \tau_{D_{CO_2}}$ (compare with Figure 8) requires the bubble volume number density $N \approx 1/(W/2)^3 \ll 1.4–12 \times 10^6$ cm^{-3}, which corresponds to the experimentally estimated $N < 10^6$ cm^{-3}.

Combined in Figure 10 are experimental data from our experiments, *Pichavant et al.* [2013] and *Yoshimura and Nakamura* [2010] demonstrate that the two types of dynamic dehydration differ significantly from the equilibrium predictions shown in Figure 1. As our scaling analysis showed, slower diffusion of CO_2 than H_2O may be important on realistic time scales for magma flushing. Our assumption about the same size of the spherical shell of the melt for all bubbles, used in numerical simulation, ignores the uneven distribution of bubbles in the melt volume and their possible escape. These effects are reflected in our data for run a21, where the composition point are scattered over a wide range of CO_2 and H_2O contents and do not follow a single trend.

All this makes it difficult to interpret the data on the content of CO_2 and H_2O in MIs. In general, the CO_2 flushing model can be supported by the presence of low (near zero) CO_2 and high H_2O points on the diagram, which may represent the melt composition before CO_2 influx. However, such compositions are rare, for example, in Figure 1 data for HRT MIs do not have distinct points of both low and high water with low CO_2. Almost CO_2 free and water saturated compositions can also be produced at a high degree of magma crystallization with an exsolved fluid accumulating CO_2 [*Wallace et al.*, 1995]. The interpretation of MI data is further complicated by the possible loss of water after entrainment. Taking into account the isotopic fractionation of fluid-mobile components between the fluid and the melt can be a decisive argument. A correlation between CO_2 concentration and δ^{11}B, δ^{7}Li, δ^{34}S is expected if these components are extracted from the melt by a CO_2-enriched fluid along with H_2O. If unequivocal arguments will be obtained in favor of the significance of flushing with carbonic fluid, a mechanical model of interaction can be developed, including the effects of crystallization, an increase in the volume of multiphase magma, and a probable heating caused by the recharge of the magma chamber with more primitive magma accompanying flushing.

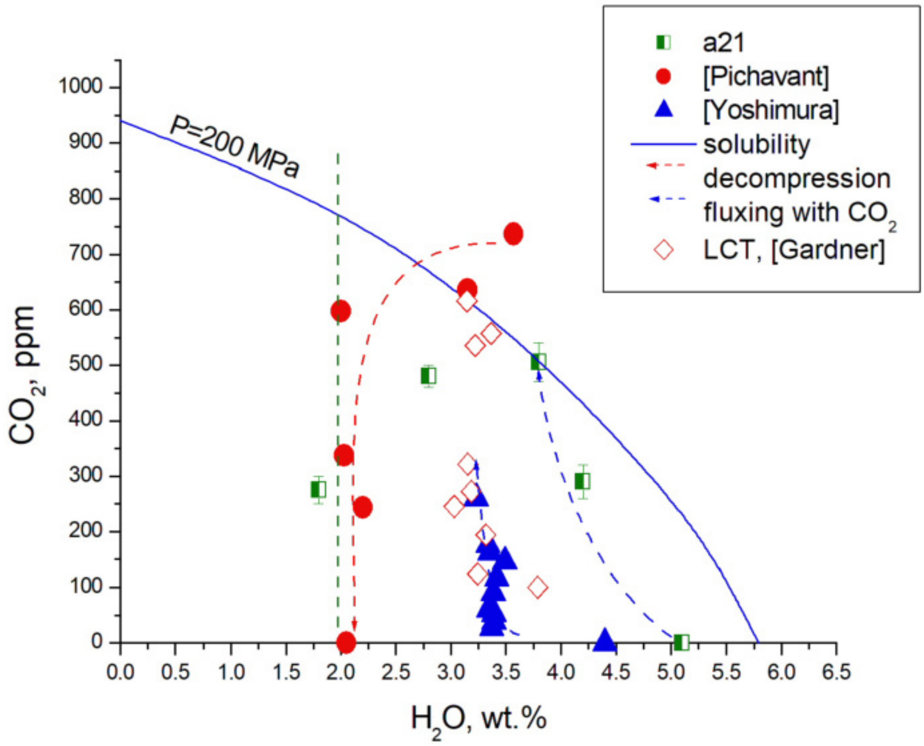

Figure 10. Diffusion-controlled trends in H_2O-CO_2 concentrations in the melt caused by CO_2 flushing and depressuration-induced vesiculation. The filled triangles display the profile distribution at the interface of the melt and CO_2 enriched fluid from [*Yoshimura and Nakamura*, 2010]. Partially filled squares refer to the experiment a21 with numerous CO_2 bubbles, the large data spread reflects uneven distribution of the bubbles in the melt with contrasting residence times. The vertical dahed line indicates the water content achieved with complete equilibration of the melt-fluid system without crystalllization. Filled circles correspond to the experiment on vesiculation during depressurization of a basaltic melt saturated with CO_2-H_2O fluid at $P = 200$ MPa from [*Pichavant et al.*, 2013].

Conclusions

1. Numerical modeling of the exchange of volatiles and the growth of a CO_2 bubble in a hydrous silicic melt is performed. It is demonstrated that water distribution between neighboring bubbles becomes uniform over a time equal to $\approx 0.14W^2/D_w$, where W is an inter-bubble distance, D_w is water diffusion coefficient and occurs when the melt is still undesaturated with CO_2.
2. Experiments with albite melt with an initial water content of about 5 wt. % at $P = 200$ MPa and $T = 950$ °C showed that the initial content of CO_2 bubbles, with characteristic radii of tens of microns, reduces from to ~ 40 to 13 vol. % in 40 minutes due to the bubble escape. Flushing of the melt with mm-size CO_2 bubbles leads to uneven dehydration with a decrease in water content to 1.8–4.1 wt. %. The CO_2 concentration measured with µ-FTIR is 200–500 ppm, in general is below the saturation.
3. In a partially dehydrated melt rapid crystallization of albite with the release of volatiles is observed after 40 min, whereas the volume fraction of crystals increases to 70 vol. % in 4 hours. The estimated concentration of water in the residual melt approaches the maximum value of 2.5–2.8 wt. % close to the limit required for melt-crystal equilibrium under the experimental PT conditions.
4. Series of experiments on the exchange of volatiles between the CO_2 fluid and the hydrous albite melt through a discrete interface were performed at $T = 1020$ °C and $P = 200$ MPa. In these experiments, the linear scale of the diffusion process increased

to several millimeters. The measured content of water and CO_2 at the interface is 2 wt. % and 200 ppm, respectively, which significantly exceeds the value imposed by fluid-melt exchange. We explain this by the formation of a SiO_2 rich protective film on the contact due to the preferential dissolution of Na_2O and Al_2O_3 in the carbonic fluid. Diffusion profiles in glass were measured using EMPA (H_2O) and µ-FTIR (H_2O and CO_2). The diffusion coefficients of H_2O (1.1×10^{-6} cm^2/s) and CO_2 (1.5×10^{-7} cm^2/s) obtained by fit of these profiles agree with the published data.

5. Possible episodes of interaction (flushing) of CO_2 enriched fluid and hydrous silicic magma will produce melts with dissolved CO_2 and H_2O contents following a dis-equilibrium distinctive trend. Due to the slow diffusion mobility of CO_2, the melt will first be dehydrated and then enriched with CO_2, which might be reflected in the composition of melt inclusions in quartz.

Acknowledgements. Authors thank for invaluable contribution of A.N. Nekrasov in EMPA analyses of our experimental samples and G. V. Bondarenko for assistance in the Raman investigation of the bubbles. The authors are also grateful to R. E. Botcharnikov and anonymous reviewer for critical comments that clarify the presentation of the results and significantly improve the MS.

References

Acosta-Vigil, A., D. London, G. B. Morgan, and T. A. Dewers (2005), Dissolution of Quartz, Albite, and Orthoclase in H_2O-Saturated Haplogranitic Melt at 800 °C and 200 MPa: Diffusive Transport Properties of Granitic Melts at Crustal Anatectic Conditions, *Journal of Petrology*, *47*(2), 231–254, https://doi.org/10.1093/petrology/egi073.

Barry, P. H., D. R. Hilton, E. Föri, S. A. Halldórsson, and K. Grönvold (2014), Carbon isotope and abundance systematics of Icelandic geothermal gases, fluids and subglacial basalts with implications for mantle plume-related CO_2 fluxes, *Geochimica et Cosmochimica Acta*, *134*, 74–99, https://doi.org/10.1016/j.gca.2014.02.038.

Befus, K. S., and J. E. Gardner (2016), Magma storage and evolution of the most recent effusive and explosive eruptions from Yellowstone Caldera, *Contributions to Mineralogy and Petrology*, *171*(4), https://doi.org/10.1007/s00410-016-1244-x.

Befus, K. S., and M. Manga (2019), Supereruption quartz crystals and the hollow reentrants, *Geology*, *47*(8), 710–714, https://doi.org/10.1130/G46275.1.

Behrens, H. (2010), Ar, CO_2 and H_2O diffusion in silica glasses at 2 kbar pressure, *Chemical Geology*, *272*(1–4), 40–48, https://doi.org/10.1016/j.chemgeo.2010.02.001.

Behrens, H., C. Romano, M. Nowak, F. Holtz, and D. B. Dingwell (1996), Near-infrared spectroscopic determination of water species in glasses of the system MAlSi3O8 (M = Li, Na, K): an interlaboratory study, *Chemical Geology*, *128*(1–4), 41–63, https://doi.org/10.1016/0009-2541(95)00162-x.

Berkesi, M., T. Guzmics, C. Szabó, J. Dubessy, R. J. Bodnar, and other (2012), The role of CO_2-rich fluids in trace element transport and metasomatism in the lithospheric mantle beneath the Central Pannonian Basin, Hungary, based on fluid inclusions in mantle xenoliths, *Earth and Planetary Science Letters*, *331–332*, 8–20, https://doi.org/10.1016/j.epsl.2012.03.012.

Botcharnikov, R., M. Freise, F. Holtz, and H. Behrens (2005), Solubility of C-O-H mixtures in natural melts: new experimental data and application range of recent models, *Annals of Geophysics*, *48*(4/5), 633–646.

Caricchi, L., T. E. Sheldrake, and J. Blundy (2018), Modulation of magmatic processes by CO_2 flushing, *Earth and Planetary Science Letters*, *491*, 160–171, https://doi.org/10.1016/j.epsl.2018.03.042.

Cheng, A. H., M. A. Golberg, E. J. Kansa, and G. Zammito (2003), Exponential Convergence and H-C Multiquadric Collocation Method for Partial Differential Equations, *Numerical Methods for Partial Differential Equations*, *19*(5), 571–594, https://doi.org/10.1002/num.10062.

Cichy, S. B., R. E. Botcharnikov, F. Holtz, and H. Behrens (2010), Vesiculation and Microlite Crystallization Induced by Decompression: a Case Study of the 1991–1995 Mt Unzen Eruption (Japan), *Journal of Petrology*, *52*(7–8), 1469–1492, https://doi.org/10.1093/petrology/egq072.

Coenen, K., F. Gallucci, B. Mezari, E. Hensen, and M. van Sint Annaland (2018), An in-situ IR study on the adsorption of CO_2 and H_2O on hydrotalcites, *Journal of CO_2 Utilization*, *24*, 228–239, https://doi.org/10.1016/j.jcou.2018.01.008.

Couch, S. (2003), The Kinetics of Degassing-Induced Crystallization at Soufriere Hills Volcano, Montserrat, *Journal of Petrology*, *44*(8), 1477–1502, https://doi.org/10.1093/petrology/44.8.1477.

Coumans, J. P., E. W. Llewellin, F. B. Wadsworth, M. C. S. Humphreys, S. A. Mathias, B. M. Yelverton, and J. E. Gardner (2020), An experimentally validated numerical model for bubble growth in magma, *Journal of Volcanology and Geothermal Research*, *402*, 107,002, https://doi.org/10.1016/j.jvolgeores.2020.107002.

Dallai, L., R. Cioni, C. Boschi, and C. D'Oriano (2011), Carbonate-derived CO_2 purging magma at depth: Influence on the eruptive activity of Somma-Vesuvius, Italy, *Earth and Planetary Science Letters*, *310*(1–2), 84–95, https://doi.org/10.1016/j.epsl.2011.07.013.

Frezzotti, M.-L., and J. L. R. Touret (2014), CO_2, carbonate-rich melts, and brines in the mantle, *Geoscience Frontiers*, *5*(5), 697–710, https://doi.org/10.1016/j.gsf.2014.03.014.

Frezzotti, M. L., A. Peccerillo, and G. Panza (2010), Earth's CO_2 degassing in Italy, *Journal of the Virtual Explorer*, *36*, https://doi.org/10.3809/jvirtex.2010.00227.

Gurenko, A. A. (2021), Origin of sulphur in relation to silicate-sulphide immiscibility in Tolbachik primitive arc magma (Kamchatka, Russia): Insights from sulphur and boron isotopes, *Chemical Geology*, *576*, 120,244, https://doi.org/10.1016/j.chemgeo.2021.120244.

Hidas, K., T. Guzmics, C. Szabó, I. Kovács, R. J. Bodnar, and other (2010), Coexisting silicate melt inclusions and H_2O-bearing, CO_2-rich fluid inclusions in mantle peridotite xenoliths from the Carpathian-Pannonian region (central Hungary), *Chemical Geology*, *274*(1–2), 1–18, https://doi.org/10.1016/j.chemgeo.2010.03.004.

Holland, T. (2001), Calculation of Phase Relations Involving Haplogranitic Melts Using an Internally Consistent Thermodynamic Dataset, *Journal of Petrology*, *42*(4), 673–683, https://doi.org/10.1093/petrology/42.4.673.

Hui, H., and Y. Zhang (2007), Toward a general viscosity equation for natural anhydrous and hydrous silicate melts, *Geochimica et Cosmochimica Acta*, *71*(2), 403–416, https://doi.org/10.1016/j.gca.2006.09.003.

Kerrick, D. M., and G. K. Jacobs (1981), A modified Redlich-Kwong equation for H_2O, CO_2 , and H_2O–CO_2 mixtures at elevated pressures and temperatures, *American Journal of Science*, *281*, 735–767.

King, P. L., and J. R. Holloway (2002), CO_2 solubility and speciation in intermediate (andesitic) melts: the role of H_2O and composition, *Geochimica et Cosmochimica Acta*, *66*(9), 1627–1640, https://doi.org/10.1016/S0016-7037(01)00872-9.

Konschak, A., and H. Keppler (2014), The speciation of carbon dioxide in silicate melts, *Contributions to Mineralogy and Petrology*, *167*(5), https://doi.org/10.1007/s00410-014-0998-2.

Longpré, M.-A., J. Stix, A. Klügel, and N. Shimizu (2017), Mantle to surface degassing of carbon- and sulphur-rich alkaline magma at El Hierro, Canary Islands, *Earth and Planetary Science Letters*, *460*, 268–280, https://doi.org/10.1016/j.epsl.2016.11.043.

Lowenstern, J. B., and S. Hurwitz (2008), Monitoring a Supervolcano in Repose: Heat and Volatile Flux at the Yellowstone Caldera, *Elements*, *4*(1), 35–40, https://doi.org/10.2113/gselements.4.1.35.

Lyakhovsky, V., S. Hurwitz, and O. Navon (1996), Bubble growth in rhyolitic melts: experimental and numerical investigation, *Bulletin of Volcanology*, *58*(1), 19–32, https://doi.org/10.1007/s004450050122.

Mollo, S., M. Gaeta, C. Freda, T. D. Rocco, V. Misiti, and P. Scarlato (2010), Carbonate assimilation in magmas: A reappraisal based on experimental petrology, *Lithos*, *114*(3–4), 503–514, https://doi.org/10.1016/j.lithos.2009.10.013.

Myers, M. L., P. J. Wallace, C. J. N. Wilson, B. K. Morter, and E. J. Swallow (2016), Prolonged ascent and episodic venting of discrete magma batches at the onset of the Huckleberry Ridge supereruption, Yellowstone, *Earth and Planetary Science Letters*, *451*, 285–297, https://doi.org/10.1016/j.epsl.2016.07.023.

Narine, S. S., K. L. Humphrey, and L. Bouzidi (2006), Modification of the Avrami model for application to the kinetics of the melt crystallization of lipids, *Journal of the American Oil Chemists' Society*, *83*(11), 913–921, https://doi.org/10.1007/s11746-006-5046-6.

Navon, O., A. Chekhmir, and V. Lyakhovsky (1998), Bubble growth in highly viscous melts: theory, experiments, and autoexplosivity of dome lavas, *Earth and Planetary Science Letters*, *160*(3–4), 763–776, https://doi.org/10.1016/s0012-821x(98)00126-5.

Neukampf, J., O. Laurent, P. Tollan, A.-S. Bouvier, T. Magna, and other (2022), Degassing from magma reservoir to eruption in silicic systems: The Li elemental and isotopic record from rhyolitic melt inclusions and host quartz in a Yellowstone rhyolite, *Geochimica et Cosmochimica Acta*, *326*, 56–76, https://doi.org/10.1016/j.gca.2022.03.037.

Newman, S., and J. B. Lowenstern (2002), VolatileCalc: a silicate melt-H_2O–CO_2 solution model written in Visual Basic for excel, *Computers & Geosciences*, *28*(5), 597–604, https://doi.org/10.1016/s0098-3004(01)00081-4.

Pichavant, M., I. Di Carlo, S. G. Rotolo, B. Scaillet, A. Burgisser, N. Le Gall, and C. Martel (2013), Generation of CO_2-rich melts during basalt magma ascent and degassing, *Contributions to Mineralogy and Petrology*, *166*(2), 545–561, https://doi.org/10.1007/s00410-013-0890-5.

Ruefer, A. C., K. S. Befus, J. O. Thompson, and B. J. Andrews (2021), Implications of Multiple Disequilibrium Textures in Quartz-Hosted Embayments, *Frontiers in Earth Science*, *9*, https://doi.org/10.3389/feart.2021.742895.

Rusiecka, M. K., and D. R. Baker (2021), Growth and textural evolution during crystallization of quartz and feldspar in hydrous, rhyolitic melt, *Contributions to Mineralogy and Petrology*, *176*(7), https://doi.org/10.1007/s00410-021-01809-1.

Simakin, A., H. Schmeling, and V. Trubitsyn (1997), Convection in melts due to sedimentary crystal flux from above, *Physics of the Earth and Planetary Interiors*, *102*(3–4), 185–200, https://doi.org/10.1016/S0031-9201(97)00010-1.

Simakin, A. G., and I. N. Bindeman (2022), Convective Melting and Water Behavior around Magmatic-Hydrothermal Transition: Numerical Modeling with Application to Krafla Volcano, Iceland, *Journal of Petrology*, *63*(8), https://doi.org/10.1093/petrology/egac074.

Simakin, A. G., and V. Y. Chevychelov (1995), Experimental studies of feldspar crystallization of granite melts of varied water content, *Geokhimiya*, (2), 216–237.

Simakin, A. G., and A. Ghassemi (2018), Mechanics of Magma Chamber with the Implication of the Effect of CO_2 Fluxing, in *Volcanoes - Geological and Geophysical Setting, Theoretical Aspects and Numerical Modeling, Applications to Industry and Their Impact on the Human Health*, chap. 9, pp. 175–207, InTech, https://doi.org/10.5772/intechopen.71655.

Simakin, A. G., P. Armienti, and M. B. Epelbaum (1999), Coupled degassing and crystallization: experimental study at continuous pressure drop, with application to volcanic bombs, *Bulletin of Volcanology*, *61*(5), 275–287, https://doi.org/10.1007/s004450050297.

Simakin, A. G., T. P. Salova, and G. V. Bondarenko (2012), Experimental study of magmatic melt oxidation by CO_2, *Petrology*, *20*(7), 593–606, https://doi.org/10.1134/S0869591112070053.

Simakin, A. G., V. N. Devyatova, and A. N. Nekrasov (2020), *Crystallization of Cpx in the Ab-Di System Under the Oscillating Temperature: Contrast Dynamic Modes at Different Periods of Oscillation*, pp. 97–120, Springer International Publishing, https://doi.org/10.1007/978-3-030-42859-4_5.

Stolper, E. M., G. Fine, T. Johnson, and S. Newman (1987), Solubility of carbon dioxide in albitic melt, *American Mineralogist*, (72), 1071–1085.

Swanson, S. E., and P. M. Fenn (1986), Quartz crystallization in igneous rocks, *American Mineralogist*, *71*(3-4), 331–342.

Wallace, P. J., A. T. Anderson, and A. M. Davis (1995), Quantification of pre-eruptive exsolved gas contents in silicic magmas, *Nature*, *377*(6550), 612–616, https://doi.org/10.1038/377612a0.

Wang, X., I.-M. Chou, W. Hu, R. C. Burruss, Q. Sun, and Y. Song (2011), Raman spectroscopic measurements of CO_2 density: Experimental calibration with high-pressure optical cell (HPOC) and fused silica capillary capsule (FSCC) with application to fluid inclusion observations, *Geochimica et Cosmochimica Acta*, *75*(14), 4080–4093, https://doi.org/10.1016/j.gca.2011.04.028.

Werner, C., and S. Brantley (2003), CO_2 emissions from the Yellowstone volcanic system, *Geochemistry, Geophysics, Geosystems*, *4*(7), https://doi.org/10.1029/2002gc000473.

Yamamoto, J., and H. Kagi (2006), Extended Micro-Raman Densimeter for CO_2 Applicable to Mantle-originated Fluid Inclusions, *Chemistry Letters*, *35*(6), 610–611, https://doi.org/10.1246/cl.2006.610.

Yinnon, H., and D. R. Uhlmann (1983), Applications of thermoanalytical techniques to the study of crystallization kinetics in glass-forming liquids, part I: Theory, *Journal of Non-Crystalline Solids*, *54*(3), 253–275, https://doi.org/10.1016/0022-3093(83)90069-8.

Yoshimura, S., and M. Nakamura (2010), Chemically driven growth and resorption of bubbles in a multivolatile magmatic system, *Chemical Geology*, *276*, 18–28.

Zanotto, E. D., and D. R. Cassar (2017), The microscopic origin of the extreme glass-forming ability of Albite and B2O3, *Scientific Reports*, *7*(1), https://doi.org/10.1038/srep43022.

Zelenski, M., A. Simakin, Y. Taran, V. S. Kamenetsky, and N. Malik (2021), Partitioning of elements between high-temperature, low-density aqueous fluid and silicate melt as derived from volcanic gas geochemistry, *Geochimica et Cosmochimica Acta*, *295*, 112–134, https://doi.org/10.1016/j.gca.2020.12.011.

Zelenski, M., V. S. Kamenetsky, N. Nekrylov, and A. Kontonikas-Charos (2022), High Sulfur in Primitive Arc Magmas, Its Origin and Implications, *Minerals*, *12*(1), 37, https://doi.org/10.3390/min12010037.

Zhang, Y., and H. Ni (2010), Diffusion of H, C, and O Components in Silicate Melts, *Reviews in Mineralogy and Geochemistry*, *72*(1), 171–225, https://doi.org/10.2138/rmg.2010.72.5.

Russian Journal of Earth Sciences

Особенности проявления внутренних волн в приустьевой зоне Дуная по спутниковым данным высокого разрешения

А. В. Медведева*[,1], Т. В. Михайличенко[1], С. В. Станичный[1], и В. В. Булатов[2]

[1]Морской гидрофизический институт Российской академии наук, Севастополь, Россия
[2]Институт проблем механики им. А. Ю. Ишлинского Российской академии наук, Москва, Россия
* **Контакт:** Алеся Викторовна Медведева, suomi-npp@mail.ru

Для приустьевой зоны Дуная рассмотрены механизмы проявления внутренних волн в спутниковых данных оптического диапазона. Выделены 3 основных механизма проявления внутренних волн – ранее описанные динамический (за счет изменения шероховатости морской поверхности в конвергентных зонах, создаваемых движущейся внутренней волной), сликовый – когда в зонах конвергенции скапливаются поверхностно активные вещества, и новый – за счет изменения яркости морской поверхности при модуляции внутренней волной толщины рассеивающего слоя. Для анализа были использованы данные сканера OLI Landsat-8 за 2015–2019 годы. Показано, что в различных ситуациях внутренние волны могут проявляться либо за счет различных механизмов, либо только за счет какого-то одного. Построены суммарные карты проявлений внутренних волн в исследуемом районе. Дополнительно рассмотрены ситуации с квазисинхронными данными MSI Sentinel-2 и C-SAR Sentinel-1, на которых отображались пакеты внутренних волн. Подбор таких пар позволил оценить фазовые скорости внутренних волн, которые составили от 0,05 м/с (0,19 км/ч) до 0,95 м/с (3,43 км/ч) в различных гидрометеорологических ситуациях. Представлены примеры трансформации фронта внутренних волн на субмезомасштабных вихрях.

Ключевые слова: Черное море, Дунай, устье Дуная, спектральные характеристики, внутренние волны, оптические изображения, спутниковые данные, скорости внутренних волн, OLI Landsat-8.

Цитирование: Медведева, А. В., Т. В. Михайличенко, С. В. Станичный, и В. В. Булатов Особенности проявления внутренних волн в приустьевой зоне Дуная по спутниковым данным высокого разрешения // Russian Journal of Earth Sciences. — 2023. — Т. 23. — ES6008. — DOI: 10.2205/2023es000869 — EDN: BYEYMH

Введение

В стратифицированном океане внутренние волны – достаточно типичное явление [*Eckart*, 1961]. Интерес к изучению внутренних волн определяется, в первую очередь, переносом энергии движения, а также возможным воздействием на окружающую среду за счет перемешивания и воздействия на компоненты морской экосистемы [*Sabinin et al.*, 2004]. Одним из основных источников генерации внутренних волн в Мировом океане являются приливы [*Bondur et al.*, 2015].

Черное море считается бесприливным бассейном, однако на основе контактных наблюдений внутренние волны уверенно регистрировались как у Крымского, так и у Кавказского побережий. [*Иванов и Серебряный*, 1985; *Ivanov et al.*, 2019]. В бесприливных морях генерация внутренних волн может инициироваться геострофическими течениями, взаимодействиями суб- и мезомасштабных процессов, [*Лаврова и др.*, 2008; *Митягина и Лаврова*, 2010; *Khimchenko et al.*, 2022], речными плюмами [*Nash and Moum*, 2005], процессами, связанными с развитием апвеллинга [*Митягина и Лаврова*, 2010]. В работах [*Серебряный и Иванов*, 2013; *Bondur et al.*, 2019] также указывается на инициирование внутренних волн интенсивным метеорологическим воздействием.

https://elibrary.ru/byeymh

Получено: 19 июня 2023 г.
Принято: 30 августа 2023 г.
Опубликовано: 30 декабря 2023 г.

С появлением спутниковых данных высокого пространственного разрешения появилось достаточно много работ, анализирующих проявление внутренних волн по изменениям характеристик поверхностного слоя моря. [*Митягина и Лаврова*, 2010; *Lavrova and Mityagina*, 2017]. В большинстве этих работ анализировались радиолокационные данные. Основной механизм воздействия внутренних волн на поверхность моря реализуется через создание волной системы конвергентно-дивергентных течений в верхнем слое и их воздействием на характеристики поверхности [*Alpers*, 1985]. Принято различать два типа воздействия внутренних волн на шероховатость поверхности [*Robinson*, 2004]:

- динамический, когда в конвергентных зонах изменяются характеристики мелкомасштабных волн (а, соответственно, отражение и рассеяние) или характеристики обрушений волн (доля поверхности, покрытой пеной);
- сликовый, когда в конвергентных зонах могут скапливаться поверхностно активные вещества (ПАВ).

Второй тип воздействия, как правило, реализуется при слабых ветрах.

В оптическом диапазоне излучение морской поверхности (как при активном [*Bulatov and Ponomarev*, 2023], так и при пассивном зондировании) формируется отраженной от поверхности и рассеянной в толще воды компонентами. И поэтому, кроме перечисленных выше механизмов воздействия, что изменяют отражательные свойства морской поверхности под воздействием внутренних волн [*Lavrova et al.*, 2014], можно выделить еще механизм модуляции толщины рассеивающего слоя моря. В этом случае при повышенной мутности верхнего слоя во впадинах внутренних волн рассеяние увеличивается за счет увеличения рассеивающих частиц в столбе воды. Как правило, этот механизм проявления внутренних волн обнаруживается вблизи речных плюмов и в зонах развития рассеивающего фитопланктона (кокколитофорид).

Районы вблизи речных эстуариев представляют собой отдельный интерес с точки зрения существования внутренних волн из-за формирования сложной вертикальной стратификации в связи с различием морских и пресных вод по температуре и солености. Так, в северо-западной части Черного моря мощный пресноводный вклад осуществляется рекой Дунай.

В настоящей работе на основе данных спутникового сканера OLI Landsat-8 проведен анализ различных механизмов проявления внутренних волн в приустьевой зоне Дуная, а также получен ряд характеристик внутренних волн с использованием дополнительных квазисинхронных данных MSI Sentinel-2 и C-SAR Sentinel-1.

Методы и материалы

Отобраны оптические спутниковые снимки высокого разрешения OLI Landsat-8 L1 (Источник загрузки USGS EarthExplorer – [*USGS*, 2022]) с 2015 по 2019 гг., на которых зафиксирована дельта Дуная. Сценами (маркированы номерами LC08_L1TP_180029 и LC08_L1TP_181029) охватываются две области, обусловленные полосами захвата сенсора OLI спутника Landsat-8: значительная часть дельты Дуная и прибрежная область южнее (по широте 44,85° на 21,8 км от берега) и полностью захваченная сенсором спутника дельта Дуная и мористая часть – по широте 44,85° на 143,5 км от берега (рис. 1а, 1б).

Предварительный отбор указанных данных выполнялся с помощью онлайн-сервиса Sentinelhub Playground [*Sentinelhub Playground*, 2022]) на основе таких критериев, как отсутствие или незначительный процент облачного покрова. Дополнительно к отобранным снимкам с помощью этого же сервиса проверялось наличие квазисинхронных изображений (с фиксацией района исследования в пределах одних суток) других спутниковых сенсоров – оптического MSI Sentinel-2 L1 и радиолокационного C-SAR Sentinel-1 с поляризацией VV (Источник загрузки Copernicus Open Access Hub – [*Copernicus Open Access Hub*, 2022]). Затем загруженные данные обрабатывались в среде Sentinel Application Platform (SNAP), – в частности, для выявления и оценки особенностей проявления внутренних волн составлялись как RGB-композиты в псевдонатуральных

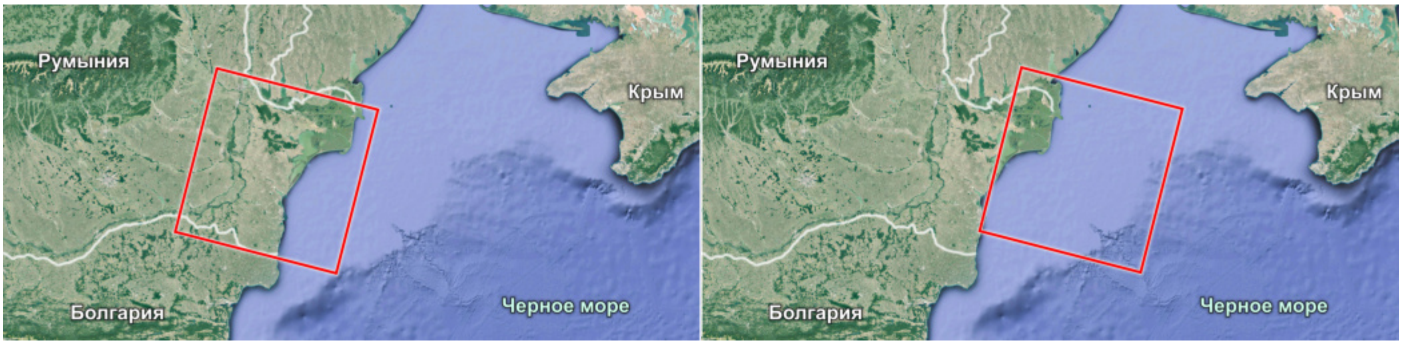

(а) (б)

Рис. 1. Положение сцен OLI Landsat-8, определяющих границы района исследования.

цветах, которые представляют собой сочетание отраженного и рассеянного излучений, так и использовались каналы и комбинации каналов с устраненным отраженным или рассеянным излучением. Для оценки отражённой компоненты излучения использовались канал OLI Landsat-8 с разрешением 30 м B05 (865 нм) и канал MSI Sentinel-2 с разрешением 10 м B08 (842 нм). Минимизация отраженного излучения (и проявление рассеянного) осуществлялась путем комбинации каналов видимого и ближнего инфракрасного диапазонов: для OLI Landsat-8 – разница каналов с разрешением 30 м Green (560 нм) и Near Infrared (865 нм), для MSI Sentinel-2 – разница каналов с разрешением 10 м B03 (560 нм) и B08 (842 нм).

Для последовательных (квазисинхронных) сцен OLI Landsat-8, MSI Sentinel-2, C-SAR Sentinel-1 с проявлением пакетов внутренних волн в пределах одних суток, дополнительно применялась опция Reprojection с целью их преобразования в изображения с одинаковыми размерами и географической сеткой для последующих пространственных и динамических расчетов в геоинформационной системе Google Earth Pro. Фрагменты пар сцен с выделенными внутренними волнами, преобразованные в формат `.kmz`, загружались в указанную ГИС, где автоматически совмещались по данным географических координат. Сдвиг первой волны в пакете внутренних волн рассчитывался путем визуального выделения наиболее контрастных пикселей (группы пикселей) на квазисинхронных изображениях с последующим измерением расстояния между ними, для каждого пакета наносилось от 5 до 27 треков. Время зондирования района исследования извлекалось из метаданных OLI Landsat-8. Для MSI Sentinel-2, метаданные которых содержат время начала периода обращения (витка), информация о времени была получена с помощью плагинов Sentinel-2A(2B) – Orbit Track & Time, включенных в систему EOSDIS Worldview [*EOSDIS*, 2022]). Время C-SAR Sentinel-1 было получено аналогичным способом – через плагины Sentinel-1A(1B) Orbit Track & Time. В связи с указанными особенностями извлечения времени при вычислении разницы фиксации района сенсорами OLI Landsat-8, MSI Sentinel-2 и C-SAR Sentinel-1 могут иметься погрешности в единицы секунд.

Обсуждение результатов

Картирование и анализ проявления внутренних волн осуществлялись на основе сцен с наиболее интенсивным и многочисленным проявлением внутренних волн, преимущественно за весенне-летний период (единично – за другие сезоны). Так, для первого района исследования (рис. 1а) было использовано 8 сцен OLI Landsat-8 L1, для второго (рис. 1б) – 12 сцен. При комплексном анализе всех отобранных сцен OLI Landsat-8 было отмечено, что в приустьевой зоне Дуная проявления внутренних волн различаются по своим спектральным характеристикам в связи с интенсивностью содержания взвешенного вещества в водах. Преимущественно обнаруживались пакеты внутренних волн с проявлением исключительно в отраженном излучении и в меньшей степени – с проявлением исключительно в рассеянном излучении, одновременным полным проявлением в отраженном и рассеянном излучении, фрагментарным проявлением в одном виде излучения и полным или фрагментарном в другом.

При проявлении внутренних волн исключительно в отраженном сигнале (рис. 2а, 2б, 2в) предполагается, что сгенерированный пакет перемещается по той части акватории, где концентрация взвешенного вещества недостаточна для обнаружения спутниковыми сенсорами процессов его модулирования или взвешенное вещество практически не включается в орбитальные течения в приповерхностном слое вод. При анализе каждой сцены выявляется, что преимущественно такого рода внутренние волны генерируются в областях с относительно низким сигналом на каналах видимого диапазона (особенно в пределах 480–560 нм), то есть, в областях с невысокими концентрациями взвешенного вещества.

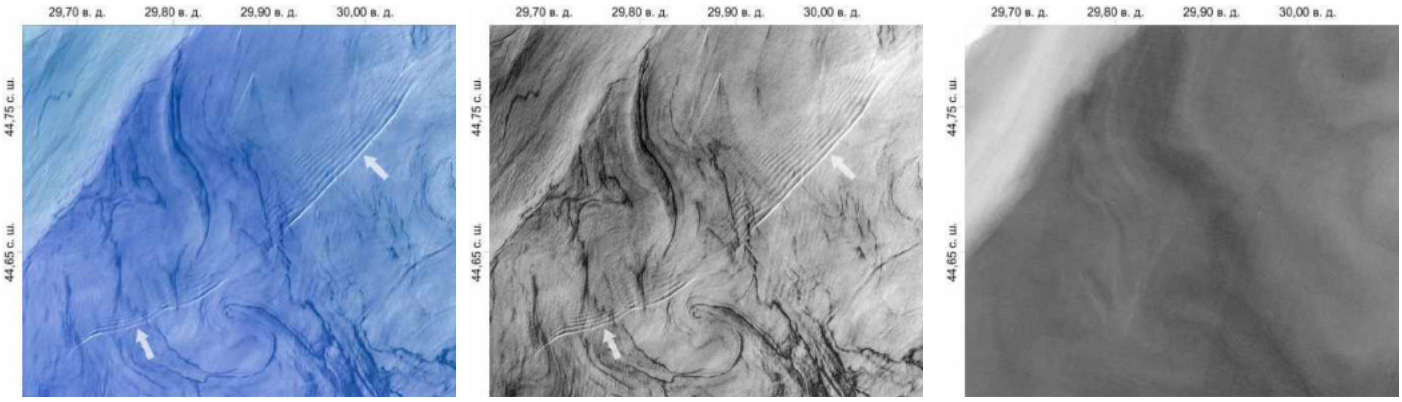

(а) (б) (в)

Рис. 2. Фрагменты сцены OLI Landsat-8 L1 от 17.05.2015 г. с разным сочетанием каналов: а – RGB-композит (внутренние волны проявляются), б – отраженное излучение (внутренние волны проявляются), в – рассеянное излучение (внутренние волны не проявляются).

Что касается внутренних волн, которые выявляются одновременно в отраженном и рассеянном излучении (рис. 3а, 3б, 3в), то их положение на момент фиксации спутниковым сенсором обычно совпадает с зонами, характеризующимися повышенными значениями сигналов видимого диапазона – то есть, с зонами с относительно средним или высоким содержанием взвешенного вещества. Зоны конвергенции фиксируются оптическими датчиками как на поверхности за счет изменений характеристик шероховатости, так и в приповерхностном слое за счет концентрирования в этих зонах взвешенного вещества.

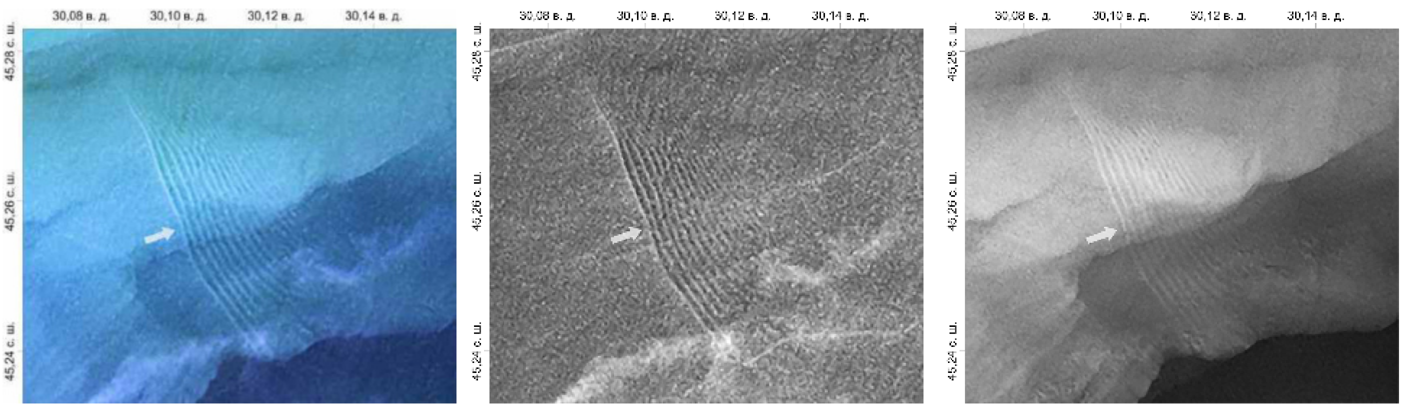

(а) (б) (в)

Рис. 3. Проявление пакета внутренних волн на фрагменте сцены OLI Landsat-8 L1 от 17.04.2016 г. при разном сочетании каналов: а – RGB-композит, б – отраженное излучение, в – рассеянное излучение.

Отдельный интерес представляют собой ситуации, при которых внутренние волны не проявляются в отраженном излучении, а регистрируются исключительно в рассеянном (рис. 4а, 4б, 4в). Предполагается, что чередование зон конвергенции и дивергенции столь слабо модулирует шероховатость, что не фиксируется оптическими сенсорами. Таким образом, источником сигнала служит изменение глубины мутного слоя.

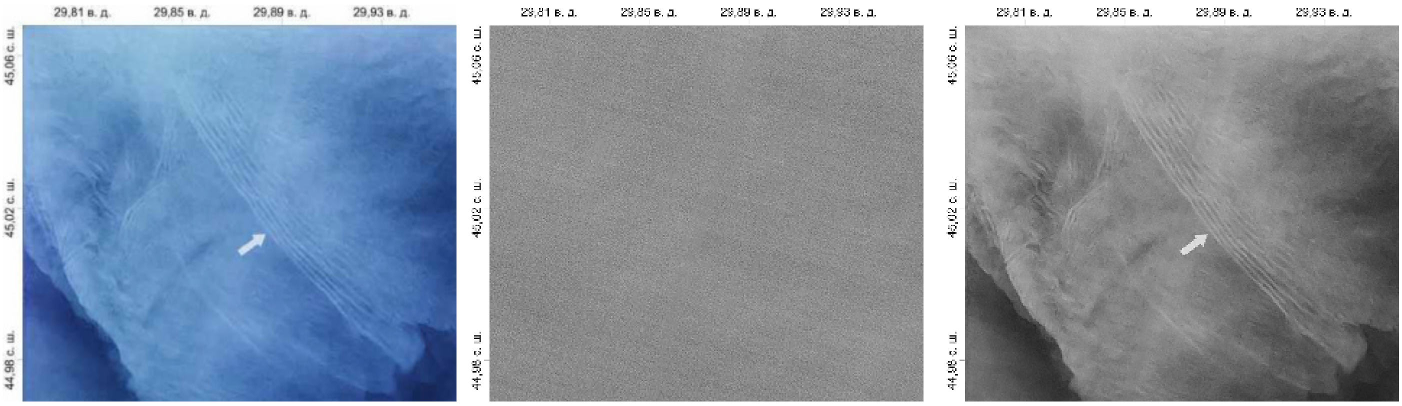

(а) (б) (в)

Рис. 4. Фрагменты сцены OLI Landsat-8 L1 от 27.12.2015 г. с разным сочетанием каналов: а – RGB-композит (внутренние волны проявляются), б – отраженное излучение (внутренние волны не проявляются), в – рассеянное излучение (внутренние волны проявляются).

Стоит отметить, что модулирование глубины мутного слоя может осуществляться не только в зонах с максимальной концентрацией взвешенного вещества. Подобная ситуация, когда пакет внутренних волн проявляется только в рассеянном излучении и не наблюдается в отраженном, продемонстрирована на изображениях ниже (рис. 5а, 5б, 5в).

Потенциально проявления за счет модуляции толщины верхнего слоя могут наблюдаться и в случае, когда нижний слой мутный, а верхний – более прозрачный.

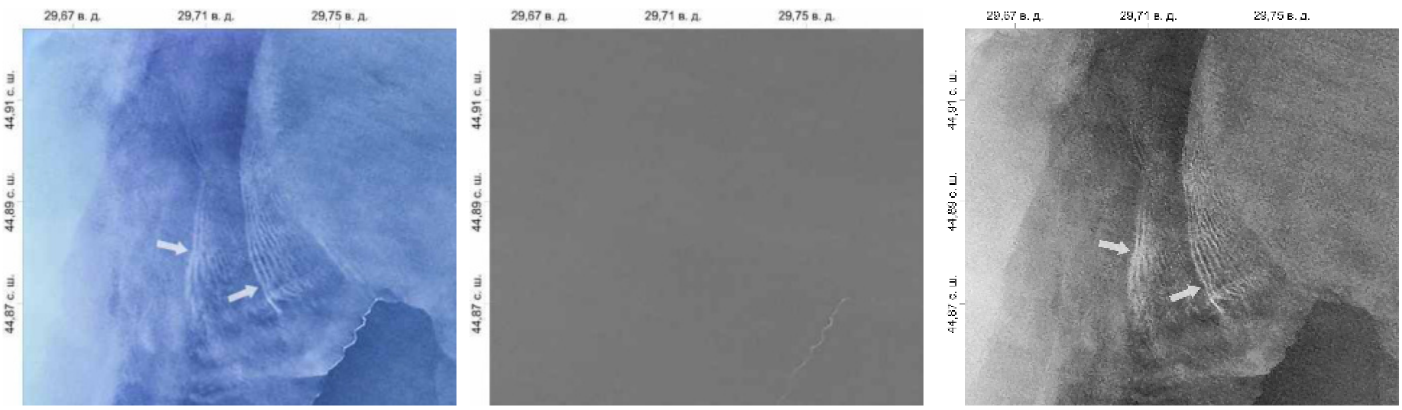

(а) (б) (в)

Рис. 5. Проявление пакетов внутренних волн за счет модулирования толщины мутного слоя, фрагмент сцены OLI Landsat-8 L1 от 27.12.2015 г. Проявление осуществляется в рассеянном излучении (а, в) и не осуществляется в отраженном излучении (б).

На оптических изображениях также обнаруживаются пакеты внутренних волн, для которых характерно фрагментарное проявление в том или ином виде излучения. В частности, периодически наблюдались пакеты внутренних волн, которые целиком проявлялись за счет изменения характеристик шероховатости поверхности и частично – за счет модуляции толщины взмученного слоя (рис. 6а, 6б, 6в). И сравнение их положения в момент регистрации спутниковым сенсором с распространением взвешенного вещества продемонстрировало, что модулирование толщины оптического слоя выявлялось в зонах с относительно более высоким содержанием взвешенного вещества.

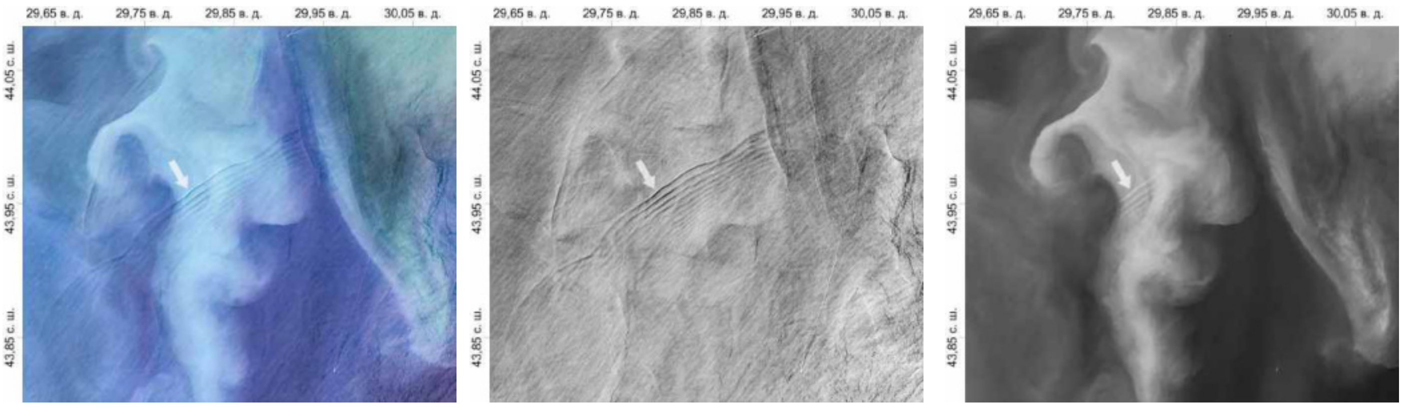

(а) (б) (в)

Рис. 6. Пример особенностей проявления пакета внутренних волн при разном сочетании оптических каналов OLI Landsat-8 L1 (фрагмент сцены от 07.06.2017 г.): а – на RGB-композите (полное проявление), б – в отраженном излучении (полное проявление), в – в рассеянном излучении (частичное проявление).

Фрагментарное проявление внутренних волн может иметь различные комбинации оптических характеристик: полное проявление в отраженном излучении, частичное – в рассеянном или одновременно в отраженном и рассеянном; полное проявление в рассеянном излучении, частичное – в отраженном или одновременно в отраженном и рассеянном; полное проявление в одновременно в отраженном и рассеянном излучении, частичное – в отраженном или рассеянном. По оптическим характеристикам ширина фронта может разбиваться обычно на 2–3 фрагмента.

Так, например, 4 августа 2018 г. наблюдался пакет внутренних волн вблизи речного выноса (рис. 7а, 7б, 7в). Он слабо, но полностью проявлен на RGB-композите, частично в отраженном излучении (преимущественно северная часть пакета) и полностью в рассеянном (более выражено – в южной части пакета). Частичное проявление пакета внутренних волн в отражённой компоненте может быть следствием увеличения амплитуды волны при выходе на мелководье (по данным батиметрических карт Navionics [*Navionics*, 2022]) и, соответственно, усилением модуляции шероховатости, определяющей контрасты на изображении.

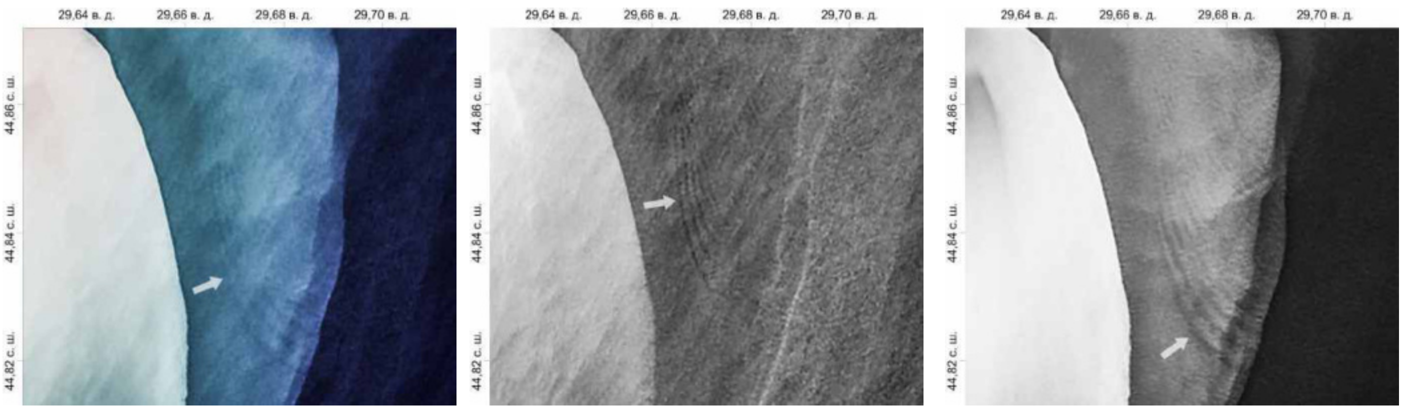

(а) (б) (в)

Рис. 7. Фрагменты сцены OLI Landsat-8 L1 от 04.08.2018 г. с разным сочетанием каналов: а – RGB-композит (внутренние волны проявляются полностью), б – отраженное излучение (внутренние волны проявляются частично), в – рассеянное излучение (внутренние волны проявляются полностью).

Стоит отметить, что хотя в данной работе рассматриваются только внутренние волны природного происхождения, различия в спектральных характеристиках (проявление в отраженном и/или рассеянном излучении), вероятно, также присущи и для внутренних волн корабельного происхождения. Внутренние волны корабельного происхождения, как правило, представляют систему из двух пакетов волн, распространяющихся под небольшим углом в разные стороны от траектории движения судна, и обычно наблюдаются при неглубоком пикноклине.

По оптическим спутниковым данным выявлялись пакеты внутренних волн с шириной фронта на уровне лидирующей волны от первых километров до первых десятков километров, с количеством волн в пакете от 2–3 до 15–16 и более, пакеты имеют различные траектории движения. При комплексном анализе пространственного распределения пакетов внутренних волн наблюдается их генерация на расстояниях до 90–120 км от берега и больших. При сопоставлении с батиметрическими данными – на расстояниях, соответствующих глубинам до 80–90 м. Полученные результаты согласуются с ранее проведенным картированием пакетов внутренних волн вблизи дельты Дуная, опубликованным в работе [*Lavrova et al.*, 2014]. Что касается пространственного распределения пакетов внутренних волн с учетом оптических характеристик (рис. 8а, 8б), то отмечается, что внутренние волны, в той или иной мере проявляющиеся в рассеянном излучении, обнаруживались преимущественно в пределах распространения взмученных вод Дуная (в районе дельты реки и прибрежной зоне города Констанца).

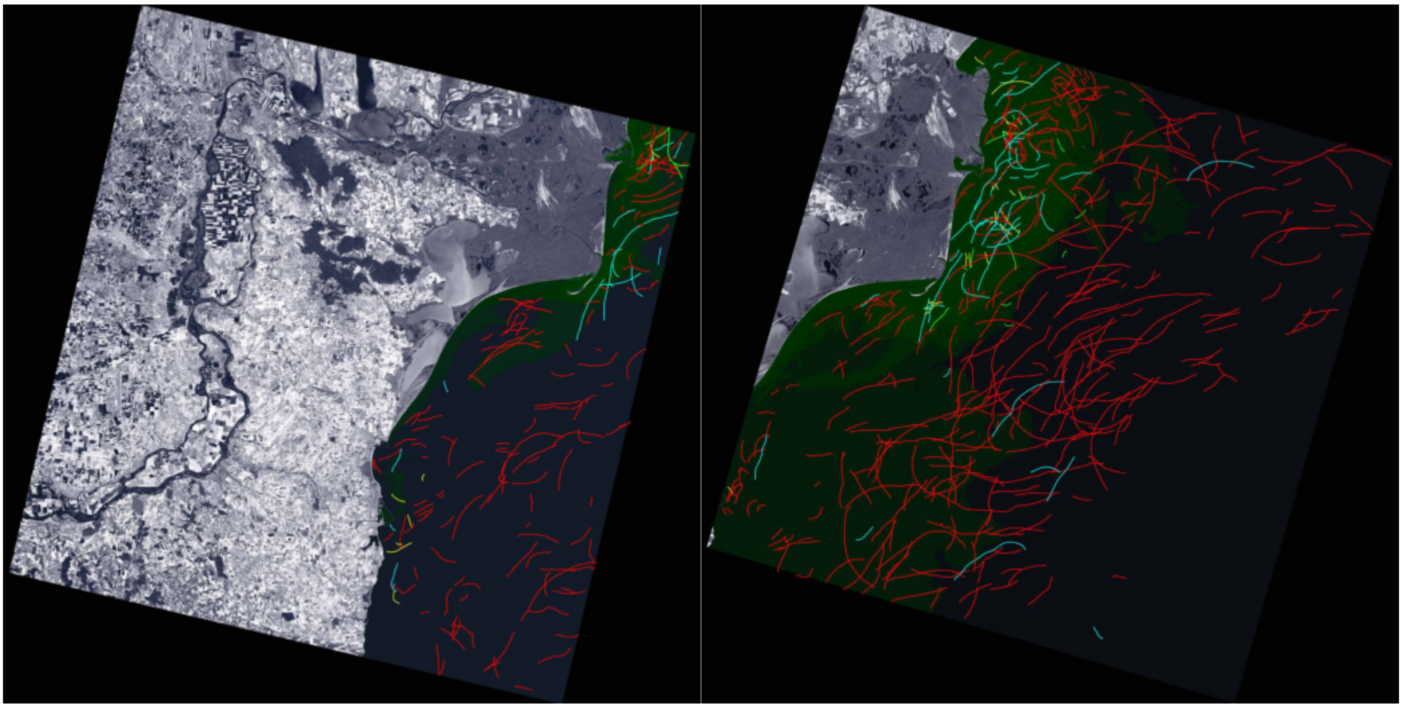

(а) (б)

Рис. 8. Пространственное распределение пакетов внутренних волн в пределах комплектов сцен OLI Landsat-8 L1, указанных на рис. 1 (1а, 1б), с учетом их оптических характеристик: красным отмечены пакеты внутренних волн, проявленные в отраженном излучении, желтым – в рассеянном излучении, светло-зеленым – одновременно в отраженном и рассеянном излучении, голубым – с частичным проявлением в том или ином виде излучения. Зеленым выделены области распространения вод Дуная (по взвешенному веществу) – чем интенсивнее цвет, тем чаще наблюдалось распространение.

Анализ каждой сцены OLI Landsat-8 L1 показывает, что генерация пакетов внутренних волн в значительной степени зависит от взаимодействий водных масс различной плотности. Так, в периоды уменьшения площади распространения речных вод внутренние волны регистрируются в малом количестве и на небольших расстояниях от берега (до 30–40 км). Напротив, в периоды интенсивного стока численность пакетов внутренних волн существенно варьирует, внутренние волны регистрируются на больших расстояниях – до 90–100 и более километров от берега. Но при этом определенный вклад вносят динамические процессы, сформированные вне связи со стоком Дуная. Например, интересное распределение пакетов внутренних волн отмечается 17 апреля 2016 г., когда внутренние волны генерировались преимущественно в зоне контакта распресненных вод и вод, вовлеченных в движение мезомасштабного антициклонического вихря со стороны открытого моря (рис. 9а, 9б). Динамические процессы меньших масштабов также в определенной мере оказывают влияние на внутренние волны – они могут как способствовать генерации пакетов, так и воздействовать на скорость их перемещения, что проявляется в виде деформации пакета (рис. 10а, 10б).

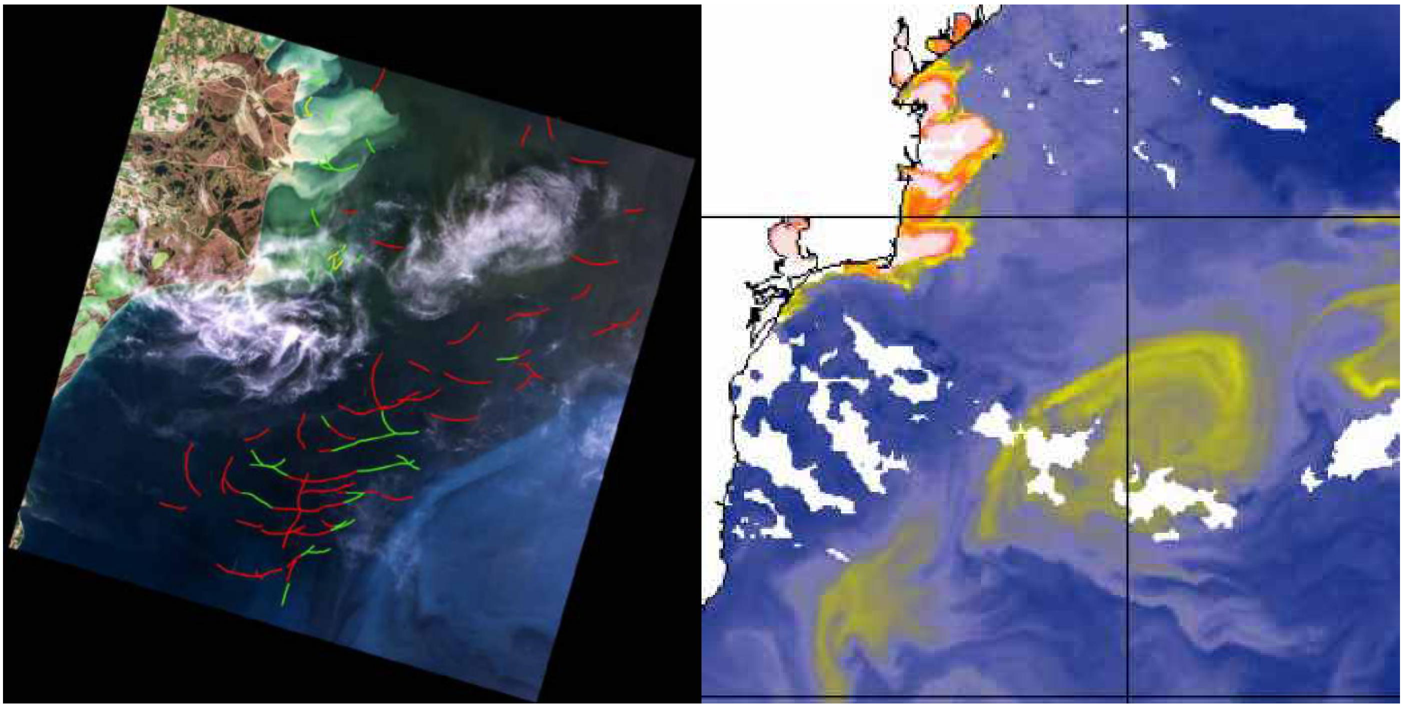

(а) **(б)**

Рис. 9. Спутниковые изображения от 17.04.2016 г.: а – пакеты внутренних волн, отмеченные на сцене OLI Landsat-8 L1 и б – мезомасштабный вихрь на фрагменте сцены VIIRS Suomi-NPP (RRS – 551 нм).

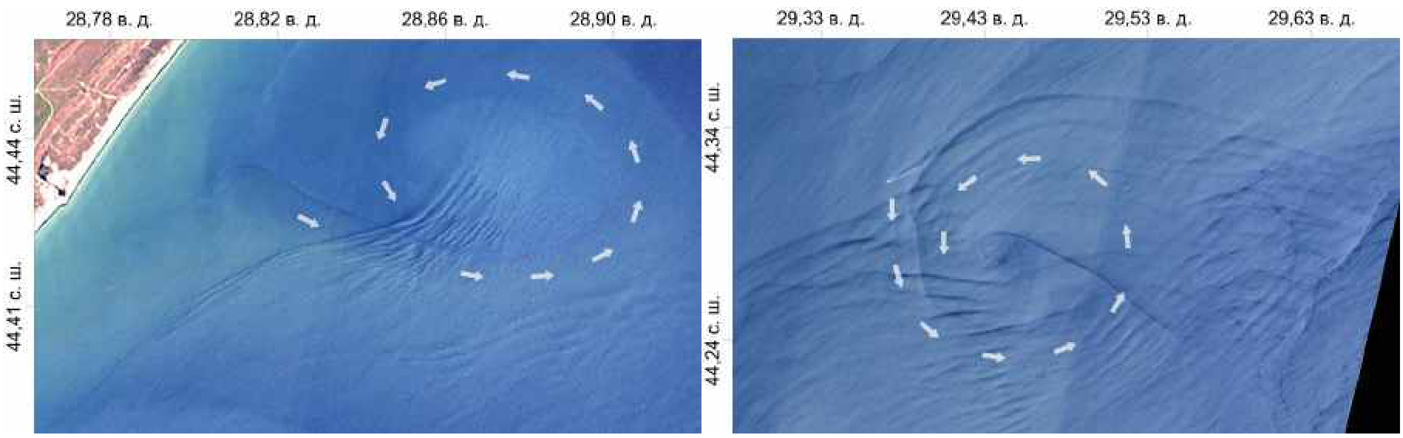

(а) **(б)**

Рис. 10. Фрагменты спутниковых изображений OLI Landsat-8 L1, на которых различима деформация внутренних волн из-за циклонического движения вихрей (направление вращения вихрей отмечено стрелками): а – от 01.08.2017 г., б – от 22.07.2019 г.

Наличие разных источников спутниковых данных позволяет подбирать последовательные (квазисинхронные) изображения с высоким разрешением для получения динамических характеристик внутренних волн. На основе таких данных выделено в сумме 19 пакетов внутренних волн, проявленных в отраженном излучении, от 01.08.2017 г., 23.04.2018 г., 03.05.2019 г. и 22.07.2019 г. в пределах районов исследования. На парах снимков OLI Landsat-8 и MSI Sentinel-2, разница которых по времени зондирования составляет от 17 мин. 15 сек. до 17 мин. 49 сек., смещение пакетов внутренних волн (расчет по первой волне) варьирует от 56 до 985 м. в зависимости от влияния динамических процессов и соответствующей деформации этих пакетов. На парах снимков C-SAR Sentinel-1 и OLI Landsat-8 (разница по времени зондирования – 4 ч. 12 мин. 11 сек.) смещение пакетов охватывает расстояния от 3897 до 7800 м. Скорости перемещения пакетов внутренних волн (в пределах нанесенных треков), с учетом, в том числе, данных C-SAR Sentinel-1, охватывают диапазон от 0,05 м/с (0,19 км/ч) до 0,95 м/с (3,43 км/ч). При оценке пакетов внутренних волн, которые были зафиксированы последовательно сенсорами C-SAR Sentinel-1, OLI Landsat-8 и затем MSI Sentinel-2, при вычислении скоростей по парам снимков наблюдается незначительное их затухание, которое, вероятнее всего, укладывается в погрешности измерений. Так, вариация скоростей (в пределах нанесенных треков) для трех пакетов внутренних волн, полученных от пар C-SAR Sentinel-1 и OLI Landsat-8, составляет от 0,33 до 0,39 м/с, от 0,28 до 0,36 м/с и от 0,26 до 0,52 м/с, тогда как расчеты по парам OLI Landsat-8 и MSI Sentinel-2 дают такие соответствующие результаты: от 0,32 до 0,37 м/с, от 0,24 до 0,35 м/с и от 0,12 до 0,49 м/с.

В общем выраженной связи между скоростью движения внутренних волн и местом их фиксации спутниковыми сенсорами не наблюдается, таковая больше обнаруживается при рассмотрении частных случаев. Так, например, 23 апреля 2018 г. (рис. 11а) наиболее высокие скорости движения внутренних волн преобладают восточнее дельты Дуная. В частности, высокая скорость перемещения отмечена для пакетов 1 (0,54–0,60 м/с), 2 (0,68–0,90 м/с), 3 (0,51–0,95 м/с) и 4 (0,64–0,82 м/с). Скорость остальных пакетов (5, 6, 7) варьирует от 26 до 42 м/с. Сопоставление выделенных внутренних волн с процессами, проявленными в рассеянном излучении, показывает, что движение пакета 3 совпадает с переносом в том же направлении в зоне влияния грибовидной структуры. Пакет 4 имеет траекторию перемещения от речного плюма, пересекает циклоническую часть вихревого диполя, которая, вероятно, на момент наблюдения не проявила тормозящего эффекта. Пакет 5 (с пониженной скоростью) зафиксирован после пересечения циклонической и центральной частей вихревого диполя, в момент движения через антициклоническую. В данном случае справедливо предположить, что грибовидная структура уже способствовала снижению скорости движения 5 пакета.

Распределение внутренних волн 3 мая 2019 г. (рис. 11б) представляет интерес тем, что скорости перемещения некоторых пакетов оценивались не только по оптическим данным, но и по радиолокационным. Хотя на сценах от сенсора C-SAR Sentinel-1 проявлено достаточное количество внутренних волн, при совмещении с оптическими данными удалось отметить только 3 пакета. Основная причина заключается в большом временном интервале (более 4 часов) между зондированием радиолокационным и оптическими сенсорами, за который большая часть внутренних волн подверглась или значительной трансформации, или диссипации. Также некоторая часть пакетов оказалась скрытой облачным покровом на оптических изображениях.

Вариация скоростей внутренних волн (по данным наложенных треков) в этой ситуации отличается меньшим диапазоном, нежели 23 апреля 2018 г., что в какой-то степени связано с районом картирования, который находится южнее дельты Дуная и отличается меньшей интенсивностью влияния динамических процессов. Так, границы скоростей для всех выделенных пакетов составляют от 0,12 до 0,52 м/с. Наибольшая разница скорости движения первой волны в пределах одного пакета отмечается для пакета 4 (от 0,18 до 0,49 м/с) из-за процессов деформации первой волны и для пакета 5 (от 0,12 до 0,49 м/с) также из-за его деформации и выраженного сдвига в северном направлении относительно геометрии и положения, зафиксированного радиолокационным сенсором. Для остальных внутренних волн разница скоростей в пределах пакета варьирует от 0,03 до 0,26 м/с.

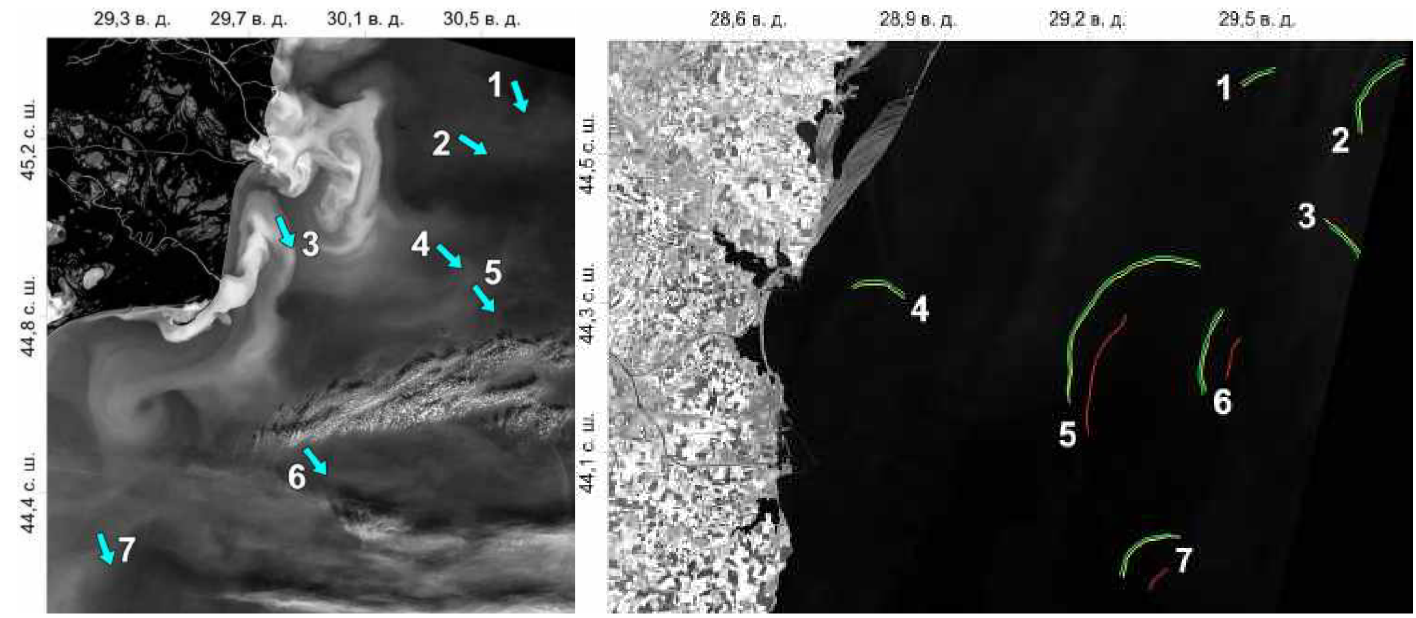

(а) (б)

Рис. 11. Внутренние волны, отмеченные с помощью последовательных изображений: а – на фрагменте сцены OLI Landsat-8 с устраненным отраженным излучением от 23.04.2018 г., стрелками отмечены траектории движения пакетов; б – на фрагменте сцены OLI Landsat-8 от 03.05.2019 г., где красным цветом отмечено положение первой волны пакетов по данным C-SAR Sentinel-1, желтым – по данным OLI Landsat-8, зеленым – по данным MSI Sentinel-2.

Заключение

По оптическим спутниковым данным высокого разрешения и радиолокационным данным проанализировано проявление внутренних волн в динамически активном районе – приустьевой зоне Дуная. Отмечено, что на распространение и интенсивность проявления внутренних волн в значительной степени влияют различные динамические процессы, источником которых являются как пресные воды Дуная, так и движение водных масс (в частности, мезомасштабные вихри) со стороны центральной части Черного моря. Определенное влияние динамических процессов на генерацию и эволюцию внутренних волн дополнительно подтверждается анализом последовательных (квазисинхронных) спутниковых изображений, также по ним определены скорости перемещения пакетов внутренних волн, которые в динамически интенсивных зонах достигают 0,8–0,9 м/с, тогда как в иных не превышают 0,5 м/с.

Внутренние волны по-разному отображаются в различных спектральных интервалах. В зависимости от концентрации взвешенных веществ и интенсивности внутренних волн они в разной степени проявляются за счет изменения шероховатости поверхности (частично или полностью) и за счет модуляции толщины взмученного слоя (также частично или полностью).

Благодарности. Работа выполнена при финансовой поддержке гранта РНФ №23-21-00194 «Аналитические методы математического моделирования волновой динамики неоднородных гидрофизических сред».

Список литературы

Иванов В. А., Серебряный А. Н. Короткопериодные внутренние волны в прибрежной зоне бесприливного моря // Известия Академии наук СССР. Физика атмосферы и океана. — 1985. — Т. 21, № 6. — С. 648—656.

Лаврова О. Ю., Митягина М. И., Сабинин К. Д. Возможные механизмы генерации внутренних волн в северо-восточной части Черного моря // Современные проблемы дистанционного зондирования Земли из космоса. — 2008. — Т. 2, № 5. — С. 128—136.

Митягина М. И., Лаврова О. Ю. Спутниковые наблюдения поверхностных проявлений внутренних волн в морях без приливов // Современные проблемы дистанционного зондирования Земли из космоса. — 2010. — Т. 7, № 1. — С. 260—272.

Серебряный А. Н., Иванов В. А. Исследования внутренних волн в Черном море с океанографической платформы МГИ // Фундаментальная и прикладная гидрофизика. — 2013. — Т. 6, № 3. — С. 34—45.

Alpers W. Theory of radar imaging of internal waves // Nature. — 1985. — Vol. 314, no. 6008. — P. 245–247. — DOI: 10.1038/314245a0.

Bondur V. G., Sabinin K. D., Grebenyuk Y. V. Generation of inertia-gravity waves on the island shelf // Izvestiya, Atmospheric and Oceanic Physics. — 2015. — Vol. 51, no. 2. — P. 208–213. — DOI: 10.1134/S0001433815020036.

Bondur V. G., Serebryany A. N., Zamshin V. V., *et al.* Intensive Internal Waves with Anomalous Heights in the Black Sea Shelf Area // Izvestiya, Atmospheric and Oceanic Physics. — 2019. — Vol. 55, no. 1. — P. 99–109. — DOI: 10.1134/S000143381901002X.

Bulatov V. V., Ponomarev A. N. About the Possibility of Improving the Image Quality of Laser Location in the Process of Remote Sensing of the Water Surface // Processes in GeoMedia-Volume VI. — Springer International Publishing, 2023. — P. 277–282. — DOI: 10.1007/978-3-031-16575-7_26.

Copernicus Open Access Hub. — URL: https://scihub.copernicus.eu/dhus/%5C#/home (visited on 2022).

Eckart C. Internal Waves in the Ocean // The Physics of Fluids. — 1961. — Vol. 4, no. 7. — P. 791–799. — DOI: 10.1063/1.1706408.

EOSDIS. Worldview. — URL: https://worldview.earthdata.nasa.gov/ (visited on 2022).

Ivanov V. A., Shul'ga T. Y., Bagaev A. V., *et al.* Internal Waves on the Black Sea Shelf near the Heracles Peninsula: Modeling and Observation // Physical Oceanography. — 2019. — Vol. 26, no. 4. — DOI: 10.22449/1573-160X-2019-4-288-304.

Khimchenko E., Ostrovskii A., Klyuvitkin A., *et al.* Seasonal Variability of Near-Inertial Internal Waves in the Deep Central Part of the Black Sea // Journal of Marine Science and Engineering. — 2022. — Vol. 10, no. 5. — P. 557. — DOI: 10.3390/jmse10050557.

Lavrova O., Mityagina M. Satellite Survey of Internal Waves in the Black and Caspian Seas // Remote Sensing. — 2017. — Vol. 9, no. 9. — P. 892. — DOI: 10.3390/rs9090892.

Lavrova O. Y., Mityagina M. I., Serebryany A. N., *et al.* Internal waves in the Black Sea: satellite observations and in-situ measurements // Remote Sensing of the Ocean, Sea Ice, Coastal Waters, and Large Water Regions 2014. — SPIE, 2014. — DOI: 10.1117/12.2067047.

Nash J. D., Moum J. N. River plumes as a source of large-amplitude internal waves in the coastal ocean // Nature. — 2005. — Vol. 437, no. 7057. — P. 400–403. — DOI: 10.1038/nature03936.

Navionics. — URL: https://www.navionics.com/ (visited on 2022).

Robinson I. S. Measuring the oceans from space: The Principles and Methods of Satellite Oceanography. — Springer, 2004. — 716 p.

Sabinin K. D., Serebryanyi A. N., Nazarov A. A. Intensive internal waves in the World Ocean // Oceanology. — 2004. — Vol. 44, no. 6. — P. 753–758.

Sentinelhub Playground. — URL: https://apps.sentinel-hub.com/sentinel-playground/ (visited on 2022).

USGS. EarthExplorer. — URL: https://earthexplorer.usgs.gov/ (visited on 2022).

Russian Journal *of* Earth Sciences

Specific Features of Internal Waves Manifestation in the Near Mouth Zone of the Danube by High-Resolution Satellite Data

A. Medvedeva,[1], T. Mikhailichenko[1], S. Stanichny[1], and V. Bulatov[2]**

[1]Marine Hydrophysical Institute, Russian Academy of Sciences, Sevastopol, Russia
[2]Ishlinsky Institute for Problems in Mechanics, Russian Academy of Sciences, Moscow, Russia
**Correspondence to: A. Medvedeva, suomi-npp@mail.ru

The mechanisms of manifestation of internal waves in satellite data of the optical range are considered for the mouth area of the Danube. Three main mechanisms for the manifestation of internal waves are identified – the previously described dynamic (due to a change in the roughness of the sea surface in convergent zones created by a moving internal wave), slick – when surfactants accumulate in convergence zones, and a new one – change in the brightness of the sea surface defined by scattering layer thickness modulation by internal waves. Data from the OLI Landsat-8 scanner for 2015–2019 were used for the analysis. It is shown that in different situations, internal waves can manifest themselves either due to various mechanisms or only due to one of them. Summary maps of manifestations of internal waves in the study area were constructed. Additionally, the situations with quasi-synchronous data of MSI Sentinel-2 and C-SAR Sentinel-1, which displayed the same packets of internal waves, are considered. The selection of such pairs made it possible to estimate the phase velocities of internal waves, which ranged from 0.05 m/s (0.19 km/h) to 0.95 m/s (3.43 km/h) in various hydrometeorological situations. Examples of internal wavefront transformation on submesoscale eddies are presented.

Keywords: Black Sea, Danube, Danube mouth, spectral characteristics, internal waves, optical images, satellite data, internal wave velocities, OLI Landsat-8.

Recieved: 19 June 2023
Accepted: 30 August 2023
Published: 30 December 2023

Citation: Medvedeva, A., T. Mikhailichenko, S. Stanichny, and V. Bulatovv (2023), Specific Features of Internal Waves Manifestation in the Near Mouth Zone of the Danube by High-Resolution Satellite Data, *Russian Journal of Earth Sciences*, 23, ES6007, https://doi.org/10.2205/2023ES000869 EDN: BYEYMH

References

Alpers W. Theory of radar imaging of internal waves // Nature. — 1985. — Vol. 314, no. 6008. — P. 245–247. — DOI: 10.1038/314245a0.

Bondur V. G., Sabinin K. D., Grebenyuk Y. V. Generation of inertia-gravity waves on the island shelf // Izvestiya, Atmospheric and Oceanic Physics. — 2015. — Vol. 51, no. 2. — P. 208–213. — DOI: 10.1134/S0001433815020036.

Bondur V. G., Serebryany A. N., Zamshin V. V., *et al.* Intensive Internal Waves with Anomalous Heights in the Black Sea Shelf Area // Izvestiya, Atmospheric and Oceanic Physics. — 2019. — Vol. 55, no. 1. — P. 99–109. — DOI: 10.1134/S000143381901002X.

Bulatov V. V., Ponomarev A. N. About the Possibility of Improving the Image Quality of Laser Location in the Process of Remote Sensing of the Water Surface // Processes in GeoMedia-Volume VI. — Springer International Publishing, 2023. — P. 277–282. — DOI: 10.1007/978-3-031-16575-7_26.

Copernicus Open Access Hub. — URL: https://scihub.copernicus.eu/dhus/%5C#/home (visited on 2022).

Eckart C. Internal Waves in the Ocean // The Physics of Fluids. — 1961. — Vol. 4, no. 7. — P. 791–799. — DOI: 10.1063/1.1706408.

EOSDIS. Worldview. — URL: https://worldview.earthdata.nasa.gov/ (visited on 2022).

Ivanov V. A., Serebryany A. N. Short-period internal waves in the coastal zone of a tidal sea // Izvestiya USSR Academy of Sciences. Physics of the atmosphere and ocean. — 1985. — Vol. 21, no. 6. — P. 648–656.

Ivanov V. A., Shul'ga T. Y., Bagaev A. V., *et al.* Internal Waves on the Black Sea Shelf near the Heracles Peninsula: Modeling and Observation // Physical Oceanography. — 2019. — Vol. 26, no. 4. — DOI: 10.22449/1573-160X-2019-4-288-304.

Khimchenko E., Ostrovskii A., Klyuvitkin A., *et al.* Seasonal Variability of Near-Inertial Internal Waves in the Deep Central Part of the Black Sea // Journal of Marine Science and Engineering. — 2022. — Vol. 10, no. 5. — P. 557. — DOI: 10.3390/jmse10050557.

Lavrova O., Mityagina M. Satellite Survey of Internal Waves in the Black and Caspian Seas // Remote Sensing. — 2017. — Vol. 9, no. 9. — P. 892. — DOI: 10.3390/rs9090892.

Lavrova O. Y., Mityagina M. I., Sabinin K. D. Possible mechanisms for generating internal waves in the northeastern part of the Black Sea // Sovremennyye problemy distantsionnogo zondirovaniya Zemli iz kosmosa. — 2008. — Vol. 2, no. 5. — P. 128–136.

Lavrova O. Y., Mityagina M. I., Serebryany A. N., *et al.* Internal waves in the Black Sea: satellite observations and in-situ measurements // Remote Sensing of the Ocean, Sea Ice, Coastal Waters, and Large Water Regions 2014. — SPIE, 2014. — DOI: 10.1117/12.2067047.

Mityagina M. I., Lavrova O. Y. Radar survey of internal waves surface manifestations in non-tidal seas // Sovremennyye problemy distantsionnogo zondirovaniya Zemli iz kosmosa. — 2010. — Vol. 7, no. 1. — P. 260–272.

Nash J. D., Moum J. N. River plumes as a source of large-amplitude internal waves in the coastal ocean // Nature. — 2005. — Vol. 437, no. 7057. — P. 400–403. — DOI: 10.1038/nature03936.

Navionics. — URL: https://www.navionics.com/ (visited on 2022).

Robinson I. S. Measuring the oceans from space: The Principles and Methods of Satellite Oceanography. — Springer, 2004. — 716 p.

Sabinin K. D., Serebryanyi A. N., Nazarov A. A. Intensive internal waves in the World Ocean // Oceanology. — 2004. — Vol. 44, no. 6. — P. 753–758.

Sentinelhub Playground. — URL: https://apps.sentinel-hub.com/sentinel-playground/ (visited on 2022).

Serebryany A. N., Ivanov V. A. Study of Internal Waves in the Black Sea from Oceanography Platform of Marine Hydrophysical Institute // Fundamental and applied hydrophysics. — 2013. — Vol. 6, no. 3. — P. 34–45.

USGS. EarthExplorer. — URL: https://earthexplorer.usgs.gov/ (visited on 2022).

Пространственные вариации коэффициента группируемости землетрясений (на примере Японии)

Е. А. Цахилова[*,1,2]

[1]Институт теории прогноза землетрясений и математической геофизики РАН, Москва, Россия
[2]Московский государственный университет имени М. В. Ломоносова, Москва, Россия
* **Контакт:** Екатерина Алексеевна Цахилова, tcakhilova.ea16@physics.msu.ru

Статья посвящена пространственному распределению средней продуктивности землетрясений основной части Японии за период 2000–2020 гг. Карты были построены с помощью инструмента The Generic Mapping Tools с использованием каталога Японского Метеорологического Агентства для землетрясений глубиной 40 км от поверхности. Речь идет о «коровых» землетрясениях сухопутной части Японии. Были построены карты для периода 2010–2020 гг., где варьировались радиус (25 км, 50 км, 100 км), полнота каталога (1 и 1,5) и ΔM-продуктивность (1 и 2). Для самой показательной карты была проверена устойчивость картины во времени. Также сделана попытка проверить влияние теплового потока на распределение средней продуктивности землетрясений.

Ключевые слова: Закон продуктивности землетрясений, метод ближайшего соседа, тепловой поток, Япония

Цитирование: Цахилова, Е. А. Пространственные вариации коэффициента группируемости землетрясений (на примере Японии) // Russian Journal of Earth Sciences. — 2023. — Т. 23. — ES6009. — DOI: 10.2205/2023es000902 — EDN: IXDUBS

https://elibrary.ru/ixdubs

Получено: 28 июня 2023 г.
Принято: 21 декабря 2023 г.
Опубликовано: 31 декабря 2023 г.

1. Введение

Исследование закономерностей сейсмичности считается ключом к решению проблемы неточности среднесрочного прогноза землетрясений. Иногда перед сильными землетрясениями бывают «рои» землетрясений, которые близки по силе и происходят чаще, чем обычно. Кроме того, перед сильными землетрясениями можно наблюдать «взрывы афтершоков» – высокоактивные серии афтершоков после землетрясений средней силы. Однако эти явления трудно было охарактеризовать с помощью небольшого числа параметров. Прогностические модели с большим количеством параметров могут давать хорошие результаты на прошлых данных, но, как правило, значительно хуже работают при взаимодействии друг с другом. Наиболее ярким примером группируемости землетрясений являются афтершоки мощных землетрясений. Для того, чтобы изучить развитие последовательности землетрясений в пространстве и времени, можно ориентироваться на продуктивность, которая представляет собой количество событий, возникших в результате возмущения напряженного состояния, вызванного другим землетрясением. Такой подход был впервые использован для разработки соответствующих моделей возникновения афтершоков с учетом эмпирического уравнения Омори-Утсу [*Utsu*, 1970].

В данной работе изучаются различия в продуктивности землетрясений на островной части Японии, где возможны землетрясения с самыми высокими магнитудами [*Pisarenko и др.*, 2023], в зависимости от их местоположения. Мы используем метод ближайшего соседа для анализа афтершоков, и для определения продуктивности землетрясений мы используем закон, основанный на единственном параметре – параметре кластеризации. Для определения этого параметра мы используем среднюю ΔM-продуктивность, которая является индивидуальной характеристикой каждого землетрясения и определяется по количеству потомков, магнитуда которых удовлетворяет условию: $M \geq M_m - \Delta M$, где M – магнитуда потомка, M_m – магнитуда родителя, а ΔM – фиксированная константа, которую мы задаем.

Продуктивность землетрясений может сильно изменяться в пространстве и времени. Она может зависеть от глубины землетрясений [*Shebalin и др.*, 2020] и от их теплового потока [*Zaliapin и Ben-Zion*, 2016]. Именно эти корреляции мы проверяем в нашей работе путем построения карт продуктивностей, глубин и теплового потока землетрясений Японии, затем сравнивая их.

2. Кластеризация землетрясений

2.1. Метрика связи между землетрясениями

Землетрясения могут проявлять сложные корреляции в разных аспектах, а именно: в пространстве, времени и магнитуде. При анализе последовательности землетрясений обычно сначала определяют основной толчок – это событие, которое является самым крупным в группе и выделяется на фоне других. Затем анализируются все остальные землетрясения, которые следуют за основным толчком в течение определенного периода времени. Если эти землетрясения имеют достаточно высокую магнитуду и находятся близко к месту основного толчка, то они могут быть отнесены к афтершокам. Однако перед этим необходимо учесть и промежуточные и более мелкие события, которые могут быть связаны с основным толчком, но не являются афтершоками. Кроме того, стоит учитывать фоновую сейсмичность в округе, чтобы правильно отличить афтершоки от других землетрясений.

Попытки идентификации и классификации афтершоков являются сложным и многогранным процессом, и требуют использования различных методов и подходов для повышения точности. Визуальное наблюдение за сейсмической ситуацией может помочь в классификации афтершоков на основе их характеристик и особенностей, но точная метка для каждого события может быть затруднительной.

В наиболее распространенном подходе афтершоки собираются с помощью подсчета всех событий в заданном пространственно-временном окне после основного события. Однако, выбор самого пространственно-временного окна важен, и может повлиять на результаты классификации. Также, возможно, что некоторые события, которые были классифицированы как афтершоки, на самом деле не связаны с рассматриваемым основным событием, что подчеркивает необходимость уточнения идентификации афтершоков.

Кроме того, никто не знает, являются ли выбранные окна большими или маленькими для минимизации ошибок в процедуре, что также важно. К тому же возникает вопрос о том, как идентифицировать афтершоки, которые могут быть связаны с несколькими крупными событиями. Эти замечания выдвигают основной вопрос: являются ли афтершоки наблюдаемыми индикаторами сейсмичности, или они могут быть определены без использования пространственно-временных окон, выбранных наблюдателем?

В работе [*Baiesi и Paczuski*, 2004] основана на временном интервале, пространственном расстоянии между землетрясениями и магнитуде первого события. Она позволяет количественно оценить корреляции между землетрясениями. С помощью этой метрики можно автоматически классифицировать события как форшоки, основные толчки или афтершоки, не прибегая к заранее заданным пространственно-временным окнам. Обычно события сильно коррелируют только с предыдущими событиями, а простейшая сетевая конструкция показывает, что каждое землетрясение связано с наиболее коррелированным предшественником. Это позволяет более точно наблюдать за сейсмической активностью и выявлять связи между различными событиями, что может быть полезно для прогнозирования и понимания землетрясений.

Степень связи между двумя землетрясениями, а также возможность рассматривать одно событие как повторное толчок другого, являются важными факторами для решения проблем, связанных с сейсмической активностью и улучшения понимания этого процесса. Этот количественный показатель должен учитывать статистические свойства сейсмической активности и быть устойчивым в пространственно-временном аспекте, в отличие от предыдущих методов идентификации афтершоков. Распределение Гутенберга-Рихтера для числа землетрясений с определенной магнитудой является одним из надежных законов, которые можно использовать в анализе и классификации землетрясений в сейсмической зоне,

$$P(m) \sim 10^{-bm},$$

где b – константа, m – магнитуда.

Ещё одним законом является фрактальный вид эпицентров землетрясений с размерностью d_f, распространяющийся на всю поверхность Земли, где данных о землетрясениях были систематически собраны. Коэффициенты b и d_f, характеризующие этот закон, могут отличаться в зависимости от исследуемого сейсмического региона и временного интервала. Совмещая эти два закона, можно установить, что среднее количество землетрясений магнитуды в пределах $(m;\ m + \Delta M)$ в радиусе r в течение временного периода t составляет

$$\bar{n} = C r^{d_f} \Delta m 10^{-bm},$$

где C – постоянная, которая зависит от общей сейсмичности в рассматриваемом регионе и в рассматриваемом временном промежутке.

Сколько землетрясений магнитудой в пределах интервала $(m;\ m + \Delta M)$ можно ожидать в течение временного интервала t и на расстоянии r от данного землетрясения j в сейсмической зоне, если рассмотреть количество землетрясений между двумя событиями i и j, произошедшими в моменты времени T_i и T_j соответственно (где $T_i < T_j$)? Путем определения магнитуды m_i i-го события, расстояния $r = r_{ij}$ между эпицентрами землетрясений и временного интервала $t_{ij} = T_j - T_i$, можно оценить ожидаемое количество событий магнитудой в пределах $(m_i;\ m_i + \Delta m)$, происходящих в определенной пространственно-временной области, ограниченной событиями j и i, равное

$$n_{ij} = C r^{d_f} \Delta m 10^{-bm_i}. \quad (1)$$

В уравнении (1) определенная область не зависит от выбора наблюдателя, а выбирается на основе исторических данных о сейсмической активности в исследуемом регионе.

Снова обратимся к уравнению (1). Среди всех зарегистрированных землетрясений, предшествующих событию j, наименее вероятно возникновение землетрясения i^*, в котором n_{ij} минимально, когда $i = i^*$. Тем не менее, землетрясение i^* все же произошло относительно события j, несмотря на низкую вероятность. Значит, между землетрясениями i^* и j имеется наиболее сильная связь. В общем случае, если значение n_{ij} мало ($\ll 1$), то существует высокая корреляция между событиями i и j, и наоборот. Следовательно, коэффициент корреляции c_{ij} между любыми двумя землетрясениями i и j обратно пропорционален значению n_{ij} в соответствии с вышеприведенным аргументом.

Получается, что уравнение (1) позволяет не только идентифицировать афтершоки, но и установить связи иерархии между ними. Это позволяет решить вопрос о том, кто является лучшим кандидатом на роль маркера, предвещающего события в количественном виде. К тому же такой метод позволяет автоматически формировать иерархически самоорганизующиеся кластеры или сети землетрясений без какого-либо предварительного анализа свойств отдельных событий или выбора пространственно-временных окон. Это делает такой подход к изучению землетрясений более универсальным по сравнению с другими методами.

2.2. Распознавание афтершоков

Кластеризация землетрясений является наиболее заметной особенностью наблюдаемой сейсмичности. Столетние всемирные наблюдения выявили широкий спектр кластеризующих явлений, которые разворачиваются в пространственно-временной области магнитуды и предоставляют наиболее надежную и полезную информацию об основных свойствах потока землетрясений. Хорошо изученные типы кластеризации включают афтершоки, форшоки, пары крупных землетрясений, рои, вспышки афтершоков, повышение сейсмической активности перед крупным региональным землетрясением, переключение глобальной сейсмической активности между различными частями Земли и т.д. Отдельные явления кластеризации и их комбинация являются важным элементом понимания перераспределения сейсмических напряжений и динамики литосферы, а также построения эмпирических методов прогнозирования землетрясений и оценки региональной сейсмической опасности [*Zaliapin и др.*, 2008].

Работа [*Zaliapin и др.*, 2008] показывает наличие двух статистически различных групп в зарегистрированной сейсмичности: первая относится к равномерному, абсолютно случайному потоку событий, а вторая – к кластеризации землетрясений. Землетрясения из последней группы подчиняются общепринятым определениям афтершоков. Таким образом, анализ дает достаточные статистические данные для выявления афтершоков, не требующие предварительно заданных параметров кластеризации, таких как вышеуказанные пространственно-временные окна для идентификации афтершоков.

Рассматривается каталог землетрясений, содержащий записи $\{t_i, \theta_i, \phi_i, h_i, m_i\}$, где каждая запись i описывает отдельное землетрясение с указанием времени возникновения t_i, θ_i, ϕ_i, h_i и магнитуды m_i. Для определения пространственно-временного расстояния по магнитуде между любыми двумя землетрясениями i и j используется формула:

$$n_{ij} = \begin{cases} C t_{ij} {r_{ij}}^{df} 10^{-b(m-m_0)}, & t_{ij} > 0 \\ +\infty, & t_{ij} < 0 \end{cases}.$$

По каждой паре землетрясений i и j из каталога вычисляются временной интервал t_{ij} и расстояние r_{ij}, а также используется фрактальная размерность d_f и наклон графика повторяемости b. События, находящиеся на расстоянии не более η, объединяются в ориентированное, по времени, дерево. Ближайший сосед j для каждого события i выбирается как событие, находящееся на минимальном расстоянии. Событие i, которое является ближайшим соседом для события j, считается его родителем. Результаты исследования Заляпина произведены на каталоге землетрясений Южной Калифорнии с магнитудой больше или равной 2. Как показано в работе [*Zaliapin и др.*, 2008], распределения имеют явную бимодальность и указывают на существование двух статистически разных групп землетрясений. Одна группа характеризуется пуассоновской сейсмичностью, а другая относится к скоплениям афтершоков.

Для обнаружения отдельных афтершоков применяется пороговое значение η_0, и все связи с $\eta_{ij} > \eta_0$ удаляются из дерева, создавая тем самым кластер – набор деревьев. Каждое дерево в кластере отражает отдельную группу землетрясений, которая может быть дополнительно изучена для решения конкретной задачи. Например, часто полагают, что афтершоки имеют меньшую магнитуду, чем соответствующие основные толчки. В таком случае, основной толчок определяется как крупнейшее землетрясение в пределах дерева T_i, а афтершоки считаются событиями, произошедшими из T_i и после основного толчка. Соответственно, форшоки считаются событиями, произошедшими в пределах дерева T_i и до нового толчка.

Имеет весомое значение наличие m_c, то есть минимального значения, по которому мы отсекаем магнитуды в каталоге при анализе афтершоков. Например, если мы анализируем землетрясения с магнитудой $m \geq m_c = 2$, то землетрясение магнитудой $m = 2$ не может иметь афтершоков меньшей магнитуды, в то время как событие магнитудой $m = 5$ может иметь афтершоки с магнитудой от 2 до 5. Чтобы выровнять диапазоны магнитуд для возможных повторных толчков основных толчков с разной магнитудой, применяется дельта-анализ, который учитывает только основные толчки с магнитудой $m \geq m_c + \Delta$ и рассматривает повторные толчки только с магнитудой в пределах $\Delta = 2$ единиц ниже, чем у основного толчка. Повторные толчки, обнаруженные с помощью этого анализа, называются Δ-повторными толчками. Анализ учитывает все события и имеет название «регулярный анализ».

2.3. Закон продуктивности землетрясений

Исследования, направленные на анализ причинно-следственных связей, возникающих внутри каскадов триггерной сейсмичности, находятся на ранней стадии развития. Несмотря на то, что механизмы триггерной сейсмичности были обнаружены уже давно, окончательной классификации этих механизмов пока не существует.

Существует несколько подходов к анализу сейсмических данных. Первый метод заключается в использовании итеративного алгоритма для отделения ветвящейся структуры последовательностей землетрясений от фоновой с помощью эпидемической модели сейсмичности [*Zhuang и др.*, 2002] Второй метод не использует априорной модели и основан на прямом и косвенном выявлении спровоцированных событий [*Marsan и Lengliné*, 2008]. Еще один подход, как выше упоминалось, заключается в идентификации кластеров землетрясений с помощью функций близости в областях время-пространство-магнитуда [*Zaliapin и др.*, 2008]. Все эти методы подтверждают зависимость продуктивности от величины m триггерного события, но меньше внимания было уделено общей изменчивости числа N инициирующих событий в сейсмических каталогах.

В исследовании [*Shebalin и др.*, 2020] уделяется особое внимание этому вопросу. Авторы исследования показали, что продуктивность землетрясений связана с количеством событий на следующем уровне иерархии, которые с ним связаны. Это позволяет использовать функцию близости и кластеры ближайших соседей землетрясений для генерации иерархических деревьев кластеризации и определения связей между уровнями иерархии. Используя относительный порог магнитуды для учета масштабной инвариантности, авторы показали, что ΔM-продуктивность каждого события следует экспоненциальному распределению, показатель экспоненты которого не зависит от магнитуды инициирующих событий и уменьшается с глубиной. Эти результаты позволяют лучше понимать активные системы разломов и улучшать эпидемические модели сейсмичности.

3. Методы решения поставленной задачи

Метод ближайшего соседа используется для определения связи между двумя землетрясениями и установления, являются ли они «родительским» и «потомком» друг относительно друга. Одним из показателей этой связи является функция близости:

$$\eta_{12} = \begin{cases} t_{12}(r_{12})^{d_f} 10^{-bm_1}, & t_{12} > 0 \\ +\infty, & t_{12} < 0 \end{cases},$$

где t_{12} – время между землетрясениями, r_{12} – расстояние между ними, d_f – фрактальная размерность, b – наклон графика повторяемости, m_1 – магнитуда первого землетрясения.

При использовании метода ближайшего соседа для анализа последовательности землетрясений, для каждого события мы ищем ближайшее к нему землетрясение с минимальным значением функции близости – η. Однако, чтобы события считались связанными, значение η между ними не должно превышать порогового значения функции близости η_0. Если значение η превышает η_0, то события не считаются связанными.

Метод, который используется для определения порогового значения η_0, описан в [*Shebalin и др.*, 2020]. В данной работе для поиска функции близости используются фрактальная размерность, наклон графика повторяемости и пороговое значение функции близости, полученные в [*Shebalin и др.*, 2022]. В настоящей работе также используется каталог Японского метеорологического агентства (JMA). Имеем: $d_f = 1{,}68$, $b = 0{,}86$ и $\eta_0 = -4{,}02$. При расчете продуктивности учитывались только прямые потомки, то есть только с уровня иерархии $N_{\text{родителя}} + 1$. ΔM-продуктивность – это количество потомков, с магнитудами удовлетворяющих неравенствам $M_{\text{потомка}} \geq M_{\text{родителя}} - \Delta M$ и $M - \Delta M \geq M_c$, где M_c – величина полноты.

Основная проблема в задаче оценки локальных значений параметров сейсмического режима заключается в необходимости анализа большого пространственного объема, где шаг регулярной сетки значительно меньше, чем размеры областей, в которых происходят события. Из-за неравномерного распределения сейсмичности результаты сильно зависят от метода сглаживания. В данной работе, мы используем так называемый «метод среднего положения» (МСП), который был предложен в работе [*Vorobieva и др.*, 2023].

Для локальных оценок параметра какого-то параметра a на сетке (i, j) регион сканируется кругами радиусом R с центрами в узлах регулярной сетки с шагом 0,1° по широте и долготе. В каждом круге подсчитывается значение параметра $\bar{a}$ (средняя продуктивность или среднее значение теплового потока). Поскольку площадь кругов значительно больше площади ячеек регулярной сетки, полученные значения необходимо привести к площади ячейки.

$$\tilde{a} = \bar{a}\frac{S_{\text{cell}}}{S_{\text{circle}}},$$

где S_{circle} и S_{cell} – площади круга и ячейки соответственно.

Если в одну ячейку попадает несколько оценок, выбирается та, что основана на наибольшем числе событий. В «пустых» ячейках значения $\tilde{a}$ определяются путем интерполяции криволинейными сплайнами с помощью встроенной процедуры «Surface» пакета Generic Mapping Tool [*Wessel и др.*, 2019]. Данный метод используется для сглаживания и сейсмичности, и значений теплового потока для обеспечения единства моделей интерполяции.

4. Результаты

Используется наиболее полный каталог Японского метеорологического агентства (JMA). Сначала рассмотрим период времени 2010–2020 гг., где варьируются следующие параметры: радиус (25 км, 50 км, 100 км), полнота каталога (1 и 1,5) и ΔM (1 и 2) (Рисунки 1, 2, 3)

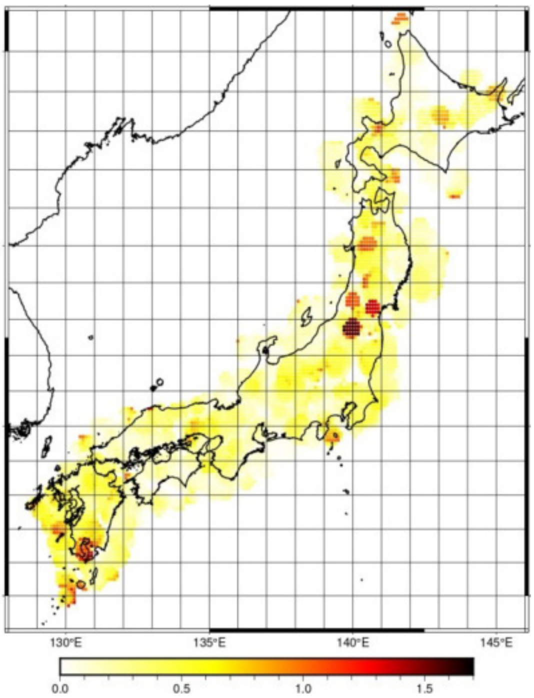

(а) $M_c = 1$, $\Delta M = 1$;

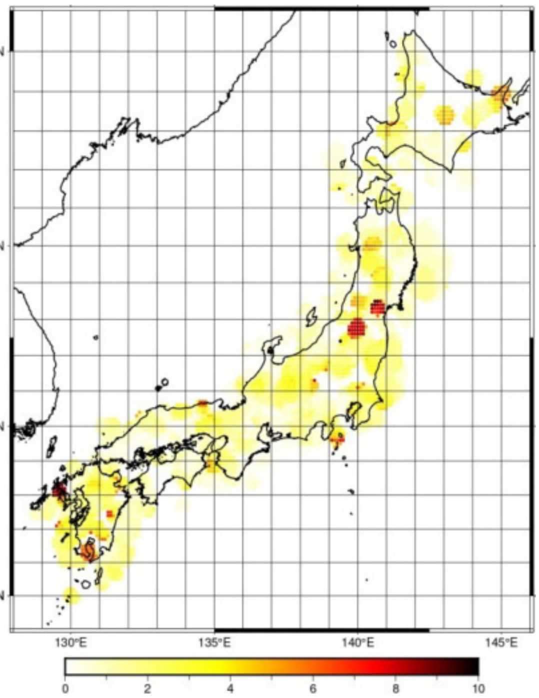

(б) $M_c = 1$, $\Delta M = 2$;

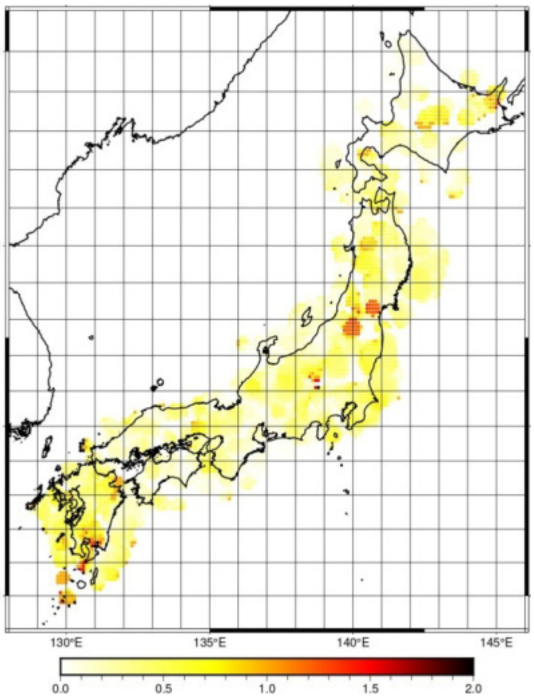

(в) $M_c = 1,5$, $\Delta M = 1$;

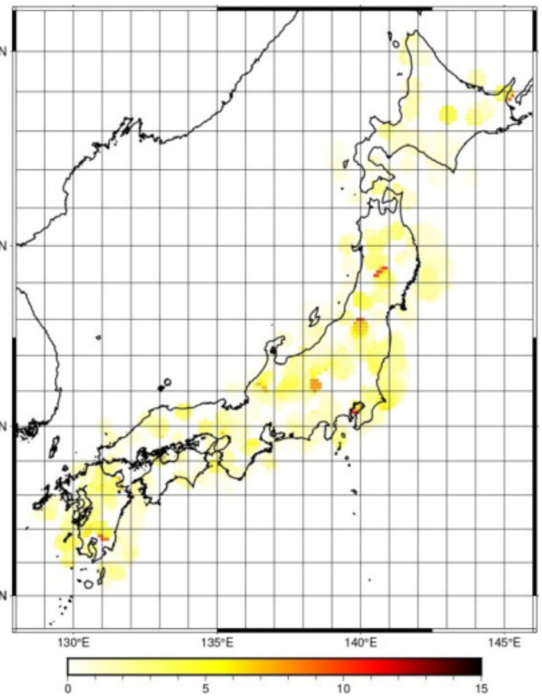

(г) $M_c = 1,5$, $\Delta M = 2$.

Рис. 1. Карты средней продуктивности Японии с $R = 25$ км.

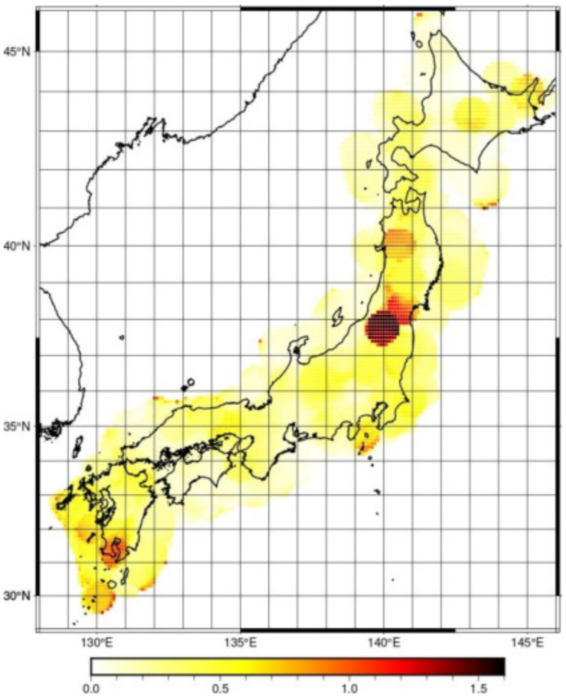

(а) $M_c = 1$, $\Delta M = 1$;

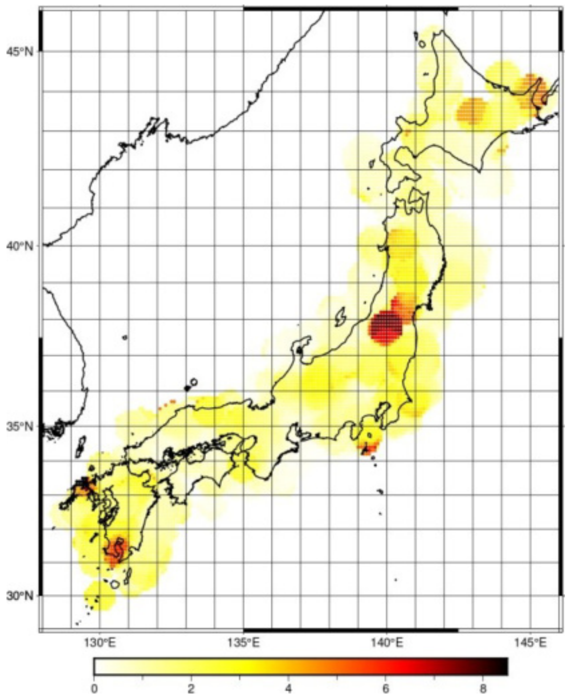

(б) $M_c = 1$, $\Delta M = 2$;

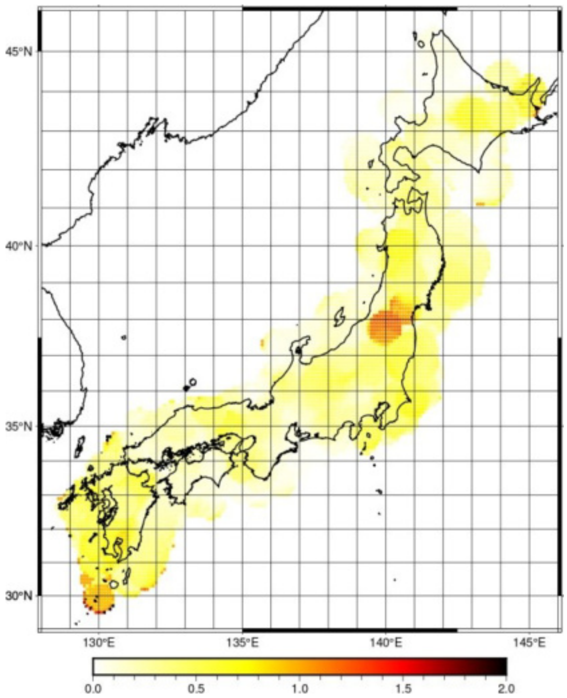

(в) $M_c = 1,5$, $\Delta M = 1$;

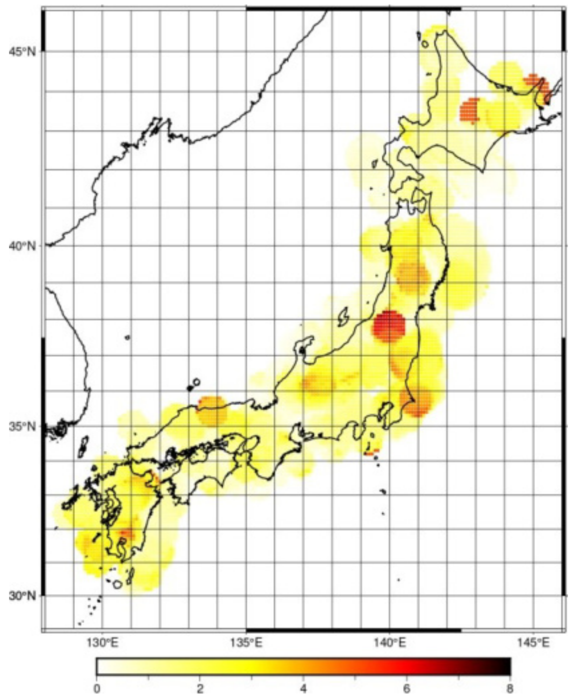

(г) $M_c = 1,5$, $\Delta M = 2$.

Рис. 2. Карты средней продуктивности Японии с $R = 50$ км.

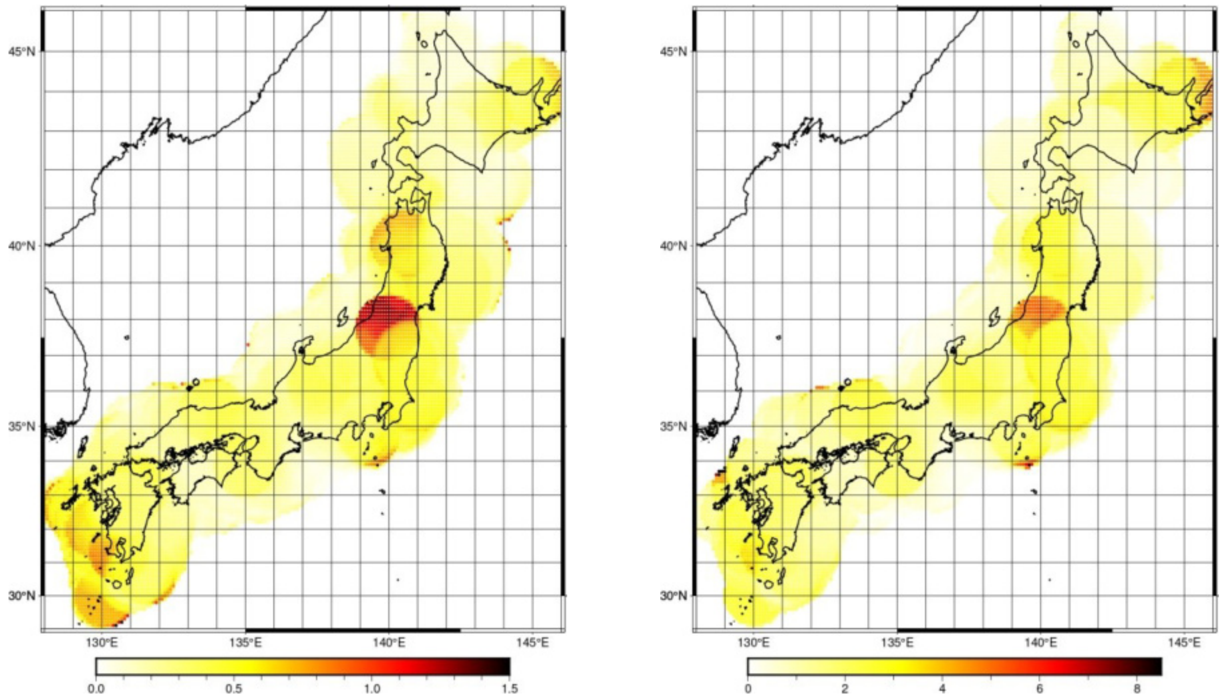

(а) $M_c = 1$, $\Delta M = 1$; **(б)** $M_c = 1$, $\Delta M = 2$;

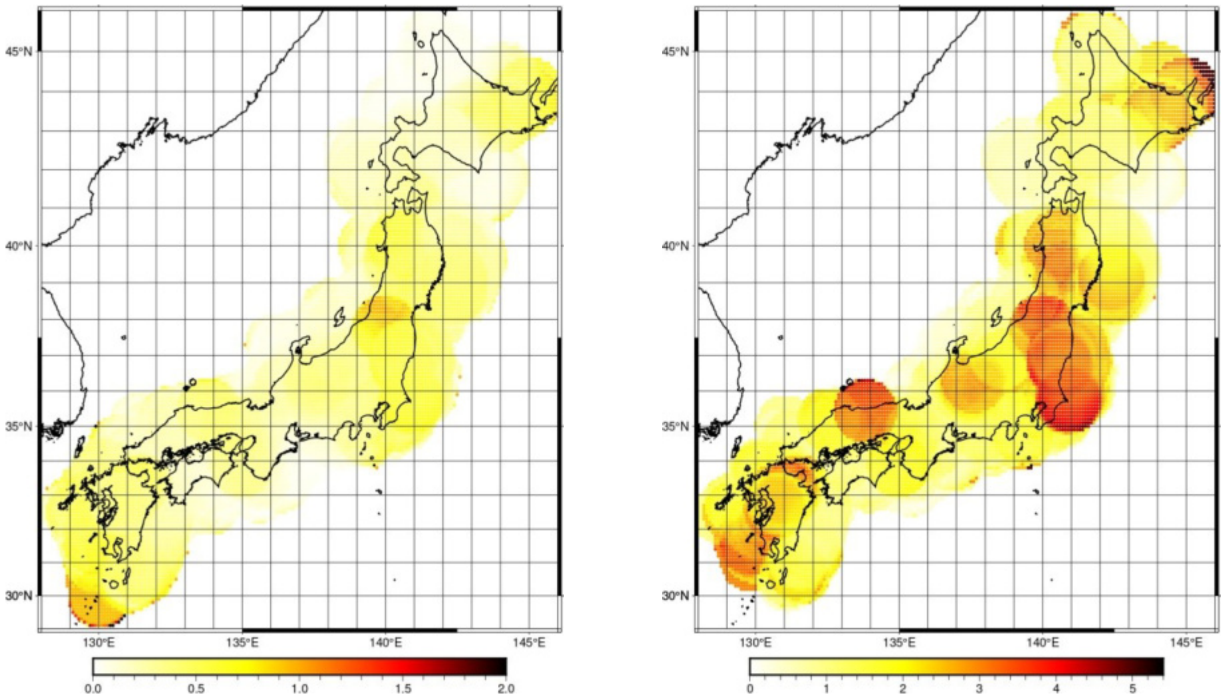

(в) $M_c = 1,5$, $\Delta M = 1$; **(г)** $M_c = 1,5$, $\Delta M = 2$.

Рис. 3. Карты средней продуктивности Японии с $R = 100$ км.

Затем фиксируем $R = 50$ км, $M_c = 1,5$ и $\Delta M = 2$, т. к. такая карта более информативная в силу большего количества событий, а так же в ней нет излишнего размытия, как, например, при $R = 100$ км. Далее проверим устойчивость картины во времени. Для этого построим карты с зафиксированными параметрами R, M_C и ΔM для разных периодов времени (рис. 4).

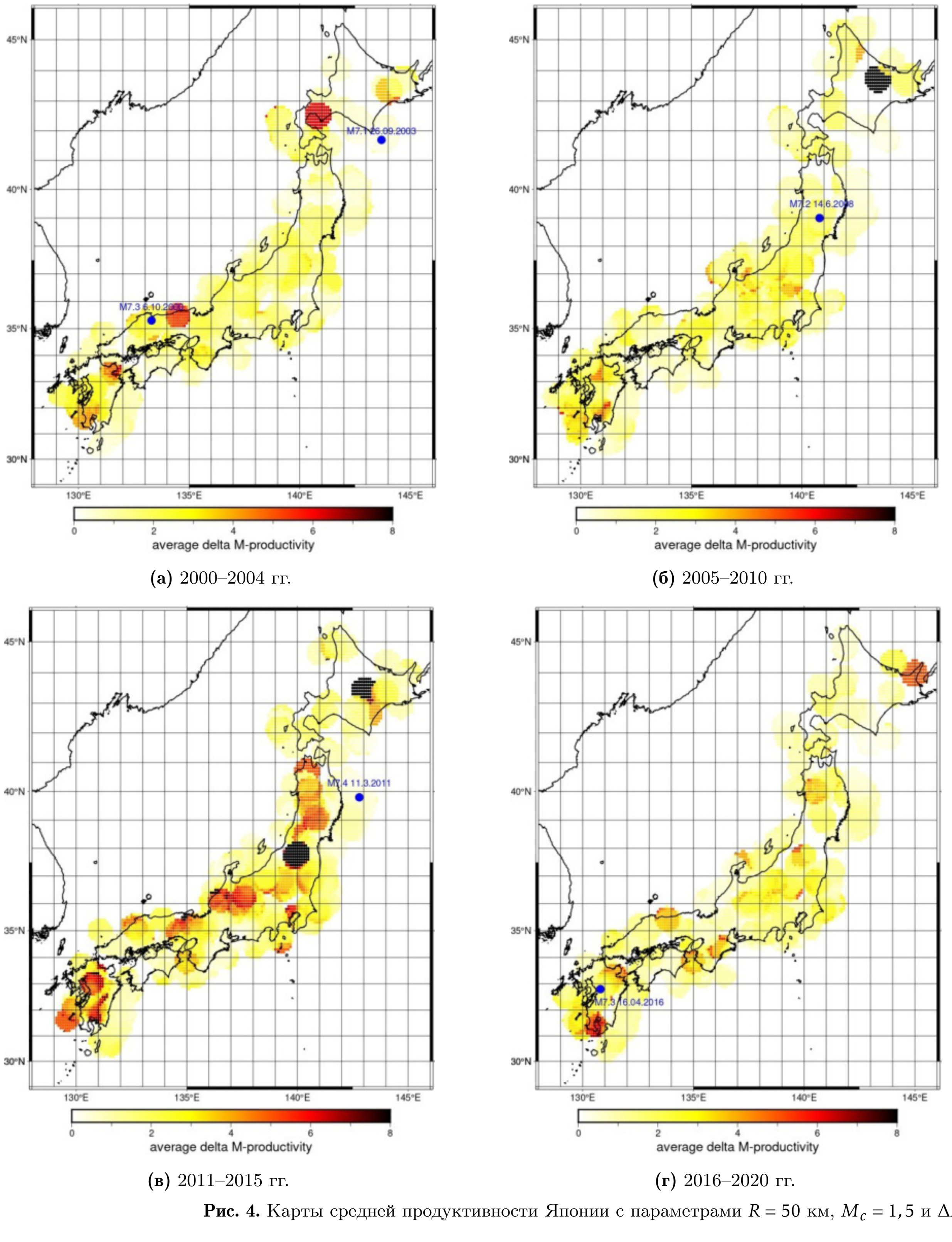

(а) 2000–2004 гг.

(б) 2005–2010 гг.

(в) 2011–2015 гг.

(г) 2016–2020 гг.

Рис. 4. Карты средней продуктивности Японии с параметрами $R = 50$ км, $M_c = 1{,}5$ и $\Delta M = 2$.

Затем мы строим карту средней продуктивности с параметрами $R = 50$ км, $M_c = 1{,}5$ и $\Delta M = 2$ для диапазона 2000–2020 гг. (рис. 5а) и сравниваем с картой поверхностного теплового потока островной части Японии (рис. 5б).

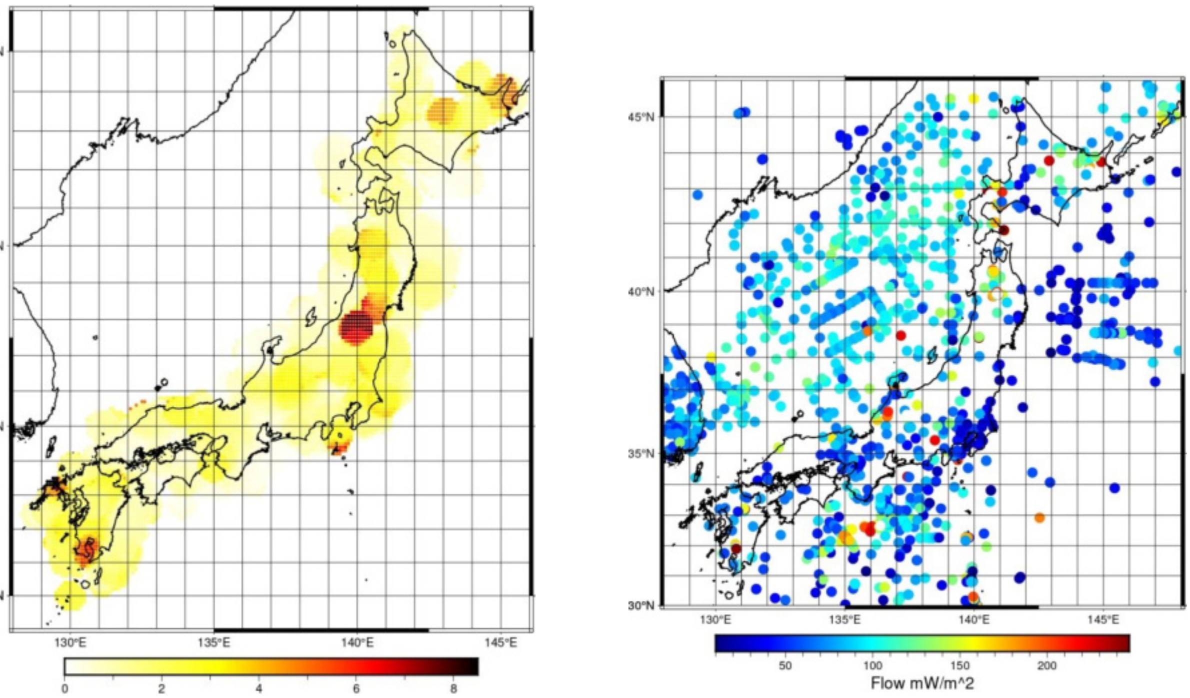

(a) (б)

Рис. 5. (a) Карта средней продуктивности Японии с параметрами $R = 50$ км, $M_c = 1{,}5$ и $\Delta M = 2$ за 2000–2020 гг.; (б) карта поверхностного теплового потока Японии.

В связи с разным порядком плотности набора данных, используемых для построения карты продуктивности и карты теплового потока были построены карты с одинаковым методом интерполяции (методом среднего положения), нормированные при этом на собственный максимум (рис. 6).

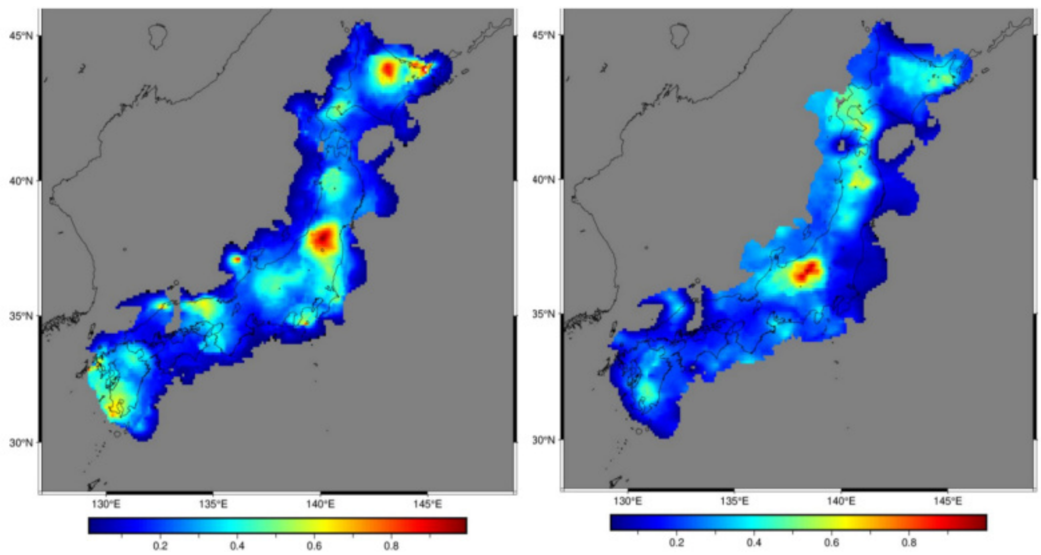

Рис. 6. Карта продуктивности и карта теплового потока, интерполированные единым методом (методом среднего положения).

Полученные результаты свидетельствуют о слабой корреляции (коэффициент корреляции 0,56) между двумя параметрами, что может свидетельствовать за ограниченное влияние теплого потока на распределение коровой сейсмичности Японии (рис. 7).

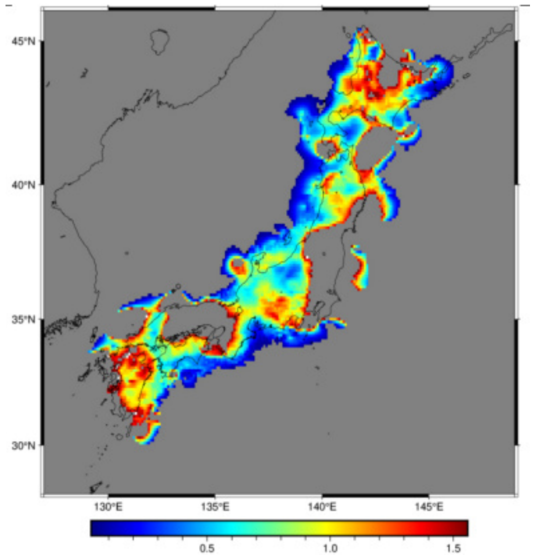

Рис. 7. Карта отношений отнормированной продуктивности к отнормированному тепловому потоку (75-й процентиль). Коэффициент корреляции 0,56.

5. Обсуждение и выводы

В данной работе исследованы характерные особенности поведения продуктивности и ее изменчивости на примере каталога коровых землетрясений Японии.

Основным выводом работы является то, что картина средней продуктивности островной части Японии устойчива во времени (карты на рис. 4).

Другим результатом является количественный определение корреляции параметров поверхностного теплового потока и средней ΔM-продуктивности, которое не показало тесной связи для коровой сейсмичности Японии за 2000–2020 гг. Положительная корреляция между сейсмичностью и тепловым потоком была исследована и показана (при тепловом потоке выше некоторого значения) в работе [*Cheng, Ch. и др.*, 2020]. Однако сейсмичность авторы определяли через параметр β – относительное распределение сейсмического момента (энергии) по размерам.

Благодарности. Работа выполнена при поддержке государственного задания ФГБУ Институт теории прогноза землетрясений и математической геофизики Российской академии наук.

Список литературы

Baiesi M., Paczuski M. Scale-free networks of earthquakes and aftershocks // Physical Review E. — 2004. — Т. 69, № 6. — С. 066106. — DOI: 10.1103/PhysRevE.69.066106.

Cheng, Ch., Hui C., Yang J. *и др.* The relationship between heat flow and seismicity in global tectonically active zones // Open Geosciences. — 2020. — Т. 12, № 1. — С. 1430—1439. — DOI: 10.1515/geo-2020-0195.

Marsan D., Lengliné O. Extending Earthquakes' Reach Through Cascading // Science. — 2008. — Т. 319, № 5866. — С. 1076—1079. — DOI: 10.1126/science.1148783.

Pisarenko V. F., Skorkina A. A., Rukavishnikova T. A. Application of New Statistical Methods to Estimation of the Seismicity Field Parameters by an Example of the Japan Region // Izvestiya, Physics of the Solid Earth. — 2023. — Т. 59, № 6. — С. 967—978. — DOI: 10.1134/S1069351323060162.

Shebalin P., Baranov S., Vorobieva I. Earthquake Productivity Law in a Wide Magnitude Range // Frontiers in Earth Science. — 2022. — Т. 10. — DOI: 10.3389/feart.2022.881425.

Shebalin P. N., Narteau C., Baranov S. V. Earthquake productivity law // Geophysical Journal International. — 2020. — Т. 222, № 2. — С. 1264—1269. — DOI: 10.1093/gji/ggaa252.

Utsu T. Aftershocks and earthquake statistics (II): Further investigation of aftershocks and other earthquake sequences based on a new classification of earthquake sequences // Journal of the Faculty of Science, Hokkaido University. Series 7, Geophysics. — 1970. — Т. 3, № 4. — С. 197—266.

Vorobieva I. A., Gvishiani A. D., Shebalin P. N. *и др.* Integrated Earthquake Catalog II: The Western Sector of the Russian Arctic // Applied Sciences. — 2023. — Т. 13, № 12. — С. 7084. — DOI: 10.3390/app13127084.

Wessel P., Luis J. F., Uieda L. *и др.* The Generic Mapping Tools Version 6 // Geochemistry, Geophysics, Geosystems. — 2019. — Т. 20, № 11. — С. 5556—5564. — DOI: 10.1029/2019gc008515.

Zaliapin I., Ben-Zion Y. A global classification and characterization of earthquake clusters // Geophysical Journal International. — 2016. — Т. 207, № 1. — С. 608—634. — DOI: 10.1093/gji/ggw300.

Zaliapin I., Gabrielov A., Keilis-Borok V. *и др.* Clustering Analysis of Seismicity and Aftershock Identification // Physical Review Letters. — 2008. — Т. 101, № 1. — С. 018501. — DOI: 10.1103/PhysRevLett.101.018501.

Zhuang J., Ogata Y., Vere-Jones D. Stochastic Declustering of Space-Time Earthquake Occurrences // Journal of the American Statistical Association. — 2002. — Т. 97, № 458. — С. 369—380. — DOI: 10.1198/016214502760046925.

Russian Journal of Earth Sciences

Spatial Variations of Earthquake Clustering Factor in Japan

E. A. Tsakhilova[1],

[1]Lomonosov Moscow State University, Moscow, Russia
[2]Institute of Earthquake Prediction Theory and Mathematical Geophysics, Russian Academy of Sciences, Moscow, Russia
**Correspondence to: E. A. Tsakhilova, tcakhilova.ea16@physics.msu.ru

The article is devoted to the spatial distribution of the average productivity of earthquakes in the main part of Japan for the period 2000–2020. The maps were generated with The Generic Mapping Tools using the Japan Meteorological Agency catalog for earthquakes 40 km below the surface. We are talking about «crustal» earthquakes on the island part of Japan. Maps were built for the period 2010–2020, where the radius (25 km, 50 km, 100 km), catalog completeness (1 and 1.5) and ΔM-productivity (1 and 2) were varied. For the most indicative map, the stability of the picture in time was checked. An attempt was also made to test the effect of surface heat flux on the distribution of average earthquake productivity.

Recieved: 28 Juny 2023
Accepted: 21 December 2023
Published: 31 December 2023

Keywords: Earthquake productivity law, nearest neighbor method, heat flow, Japan

Citation: Tsakhilova, E. A. (2023), Spatial Variations of Earthquake Clustering Factor in Japan, *Russian Journal of Earth Sciences*, 24, ES2009, https://doi.org/10.2205/2023ES000902 EDN: IXDUBS

References

Baiesi M., Paczuski M. Scale-free networks of earthquakes and aftershocks // Physical Review E. — 2004. — Vol. 69, no. 6. — P. 066106. — DOI: 10.1103/PhysRevE.69.066106.

Cheng, Ch., Hui C., Yang J., *et al.* The relationship between heat flow and seismicity in global tectonically active zones // Open Geosciences. — 2020. — Vol. 12, no. 1. — P. 1430–1439. — DOI: 10.1515/geo-2020-0195.

Marsan D., Lengliné O. Extending Earthquakes' Reach Through Cascading // Science. — 2008. — Vol. 319, no. 5866. — P. 1076–1079. — DOI: 10.1126/science.1148783.

Pisarenko V. F., Skorkina A. A., Rukavishnikova T. A. Application of New Statistical Methods to Estimation of the Seismicity Field Parameters by an Example of the Japan Region // Izvestiya, Physics of the Solid Earth. — 2023. — Vol. 59, no. 6. — P. 967–978. — DOI: 10.1134/S1069351323060162.

Shebalin P., Baranov S., Vorobieva I. Earthquake Productivity Law in a Wide Magnitude Range // Frontiers in Earth Science. — 2022. — Vol. 10. — DOI: 10.3389/feart.2022.881425.

Shebalin P. N., Narteau C., Baranov S. V. Earthquake productivity law // Geophysical Journal International. — 2020. — Vol. 222, no. 2. — P. 1264–1269. — DOI: 10.1093/gji/ggaa252.

Utsu T. Aftershocks and earthquake statistics (II): Further investigation of aftershocks and other earthquake sequences based on a new classification of earthquake sequences // Journal of the Faculty of Science, Hokkaido University. Series 7, Geophysics. — 1970. — Vol. 3, no. 4. — P. 197–266.

Vorobieva I. A., Gvishiani A. D., Shebalin P. N., *et al.* Integrated Earthquake Catalog II: The Western Sector of the Russian Arctic // Applied Sciences. — 2023. — Vol. 13, no. 12. — P. 7084. — DOI: 10.3390/app13127084.

Wessel P., Luis J. F., Uieda L., *et al.* The Generic Mapping Tools Version 6 // Geochemistry, Geophysics, Geosystems. — 2019. — Vol. 20, no. 11. — P. 5556–5564. — DOI: 10.1029/2019gc008515.

Zaliapin I., Ben-Zion Y. A global classification and characterization of earthquake clusters // Geophysical Journal International. — 2016. — Vol. 207, no. 1. — P. 608–634. — DOI: 10.1093/gji/ggw300.

Zaliapin I., Gabrielov A., Keilis-Borok V., *et al.* Clustering Analysis of Seismicity and Aftershock Identification // Physical Review Letters. — 2008. — Vol. 101, no. 1. — P. 018501. — DOI: 10.1103/PhysRevLett.101.018501.

Zhuang J., Ogata Y., Vere-Jones D. Stochastic Declustering of Space-Time Earthquake Occurrences // Journal of the American Statistical Association. — 2002. — Vol. 97, no. 458. — P. 369–380. — DOI: 10.1198/016214502760046925.

Russian Journal *of* Earth Sciences

On the Use of a Complex Indicator of the Stability of Permutation Entropy of Time Series Fragments When Analyzing Infrasound Monitoring Signals of the Altai Republic

N. G. Kudryavtsev[*,1], I. N. Frolov[1], and V. Yu. Safonova[1]

[1]Gorno-Altaisk State University, Gorno-Altaisk, Russia
* **Correspondence to:** Nikolay Kudryavtsev, ngkudr@mail.ru.

Abstract: This paper discusses one of the approaches that allows us to assess the degree of complexity or randomness of fragments of a time series in order to detect infrasound or geomagnetic signals in the results of observations of the dynamics of the natural or man-made processes under study. In our case, we are talking about monitoring the infrasound background on the territory of the Altai Republic. To solve the problem of estimating the required characteristics of a time series with minimal computational costs and in real time, a complex indicator of the stability of permutation entropy is introduced, since estimating the value of classical permutation entropy for $n = 3$ (the most commonly used version of permutation entropy) does not allow solving the problem with sufficient accuracy.

Keywords: infrasound monitoring, time series, permutation entropy, complexity assessment, stratospheric waveguide, turning points.

Citation: Kudryavtsev, N. G., I. N. Frolov, and V. Yu. Safonova (2023), On the Use of a Complex Indicator of the Stability of Permutation Entropy of Time Series Fragments When Analyzing Infrasound Monitoring Signals of the Altai Republic, *Russian Journal of Earth Sciences*, 23, ES6010, EDN: XXZEHM, https://doi.org/10.2205/2023es000887

1. Introduction

When studying the life activity of complex systems, measurement experiments are usually conducted, the result of which are time series of manifestations of certain parameters of the observed phenomena recorded at certain intervals. The results of such observations require significant effort for their interpretation, and the task of classifying fragments of the obtained data is one of the intermediate steps that allows one to come to an understanding of the processes being studied. Often, a “classifier” (classification algorithm) must determine, at a minimum, the presence or absence of a signal of a certain type, or simply a signal that differs from noise, in the fragment of a time series under study. Sometimes the task is complicated by the fact that the classification must be performed in real time.

So, for example, in the signal shown in Figure 1, there is no visually detectable signal other than noise. Although, sometimes a lot depends on the degree of “approximation” or detail of the signal being studied.

At the same time, in the fragment of the time series in Figure 2, a periodic signal is shown, although somewhat noisy, having almost the same amplitude and a slight shift to the positive area.

And the following figure (Figure 3) shows signals with different frequencies, amplitudes and varying degrees of noise.

There may also be time series where, among the predominant noise component, short-term rather implicitly determined oscillatory values of the amplitude of the fixed value are observed, corresponding, perhaps, to some fragments of the natural phenomena being examined (Figure 4). And these fragments must be found and isolated among the noise.

Research Article

Received: 6 December 2023
Accepted: 29 December 2023
Published: 31 December 2023

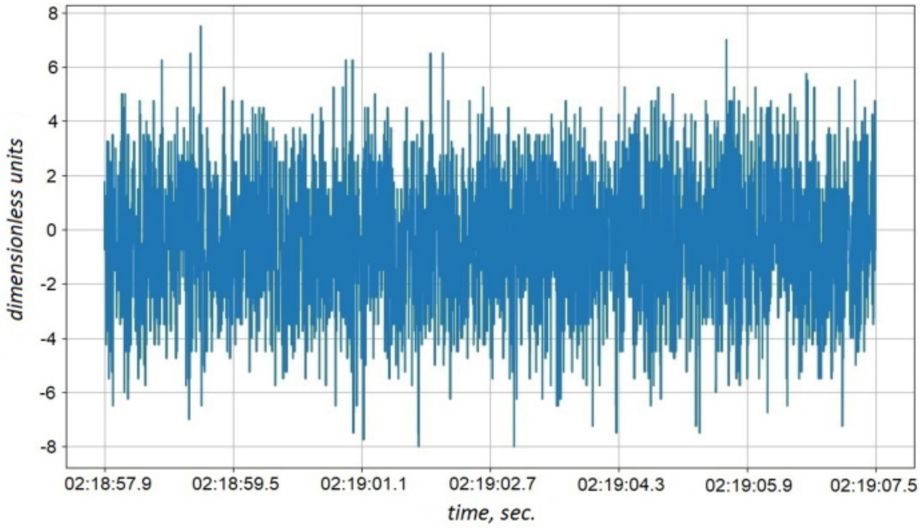

Figure 1. Noise acoustic signal. Gorno-Altaisk (03.09.2023. Ten second interval local time 02:18:57–02:19:07).

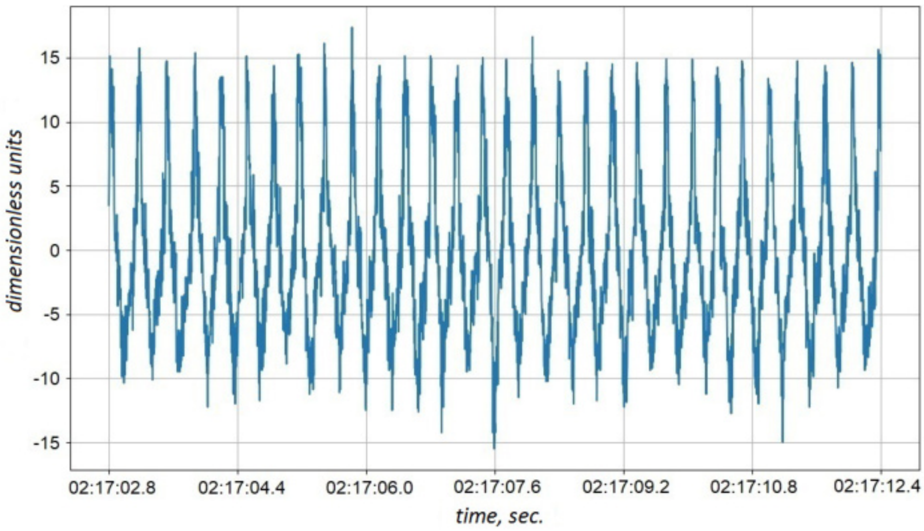

Figure 2. Periodic acoustic signal with a frequency of approximately 3 Hz. Gorno-Altaisk (03.09.2023. Ten second interval local time 02:17:02–02:17:10).

Time series that are obtained as a result of such observations can be divided into regular, stochastic and mixed; they can also be either stationary or non-stationary. For example, the study of mechanical motions that require measurements of the distance between the Moon and the Earth generates a regular time series. In this case, the results of measuring current velocities in a turbulent flow are stochastic quantities. In time series of different nature generated by non-stationary processes, there are both elements of regular data and stochastic components.

Continuing a brief excursion into the technology for processing observational results, it should be noted that when implementing long-term measurements, parameterization is used to simplify analysis procedures and reduce the amount of processed information. Parameterization is often understood as the extraction from observational data of a minimum set of the most essential parameters characterizing the system or process being studied [*Chumak*, 2012]. In fact, parameterization is a reduction of data, which, under certain conditions, allows you to restore the original data with a given accuracy based on the resulting set of parameter values and predetermined rules. The most commonly used

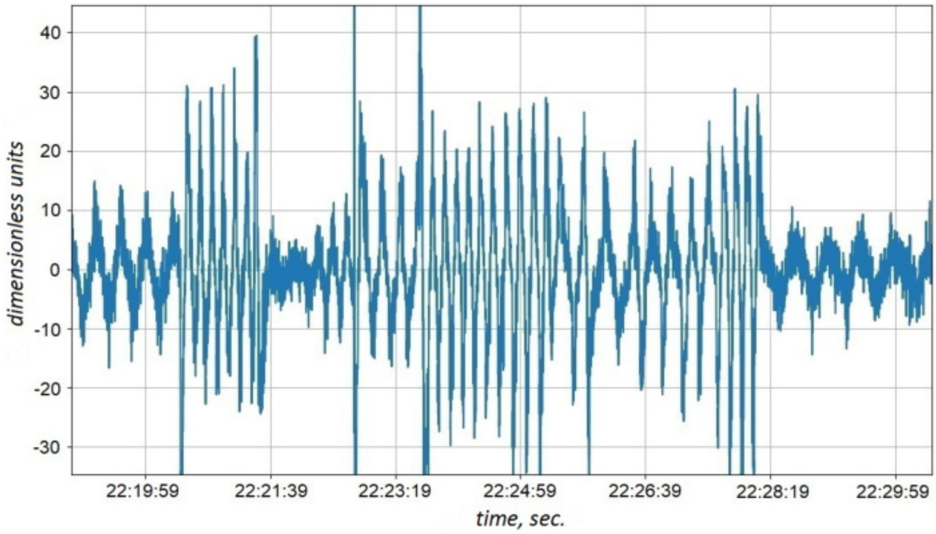

Figure 3. Mixed acoustic signal. Gorno-Altaisk (06.10.2023. Ten second interval local time 22:19:59–22:29:59).

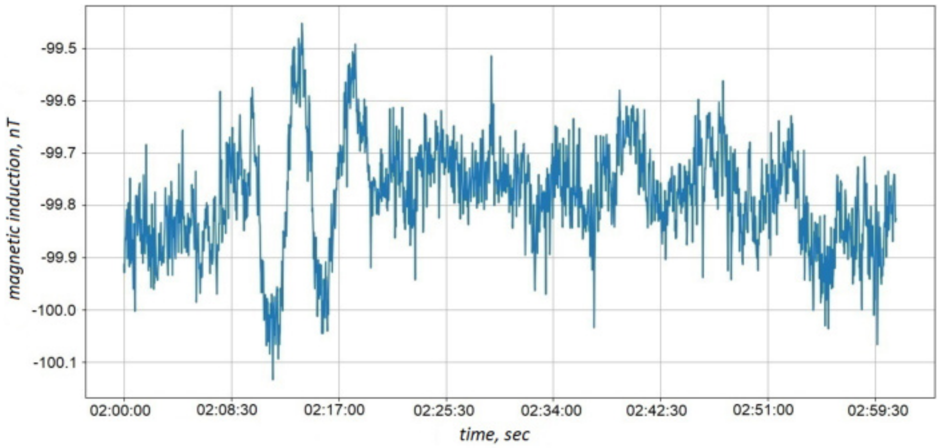

Figure 4. Difference signal between the vector sum of projections in the Euclidean metric and the magnitude of the Earth's magnetic field induction vector. Intermagnet network, SPG magnetic observatory (11.02.2024 hour interval from 2 am to 3 am GMT).

parameterization methods are integral data transformations using complete systems of orthonormal trigonometric functions (Fourier transforms) or specially selected localized functions (wavelets). In general, time series parameters are the results of applying procedures for selecting such a basic set of indicators that make it possible to quantitatively characterize the dynamics of changes in the system and understand the processes occurring in it.

Until about the middle of the last century, a naive idea of time series was used. It was believed that any series contains only a general trend, regular and random components, the numerical characteristics of which do not change over time. In this case, the trend could be considered as a fragment of change with a very long period. Time series analysis methods were reduced to extracting regular components from a data set in such a way that "white noise" remained in residuo.

The purpose of this work is to describe one of the approaches that allows us, using parameterization of measurement results, to detect a useful infrasound signal in conditions of significant interference, mainly in real time.

Generally speaking, different versions of entropies are used to act as a parameter that gives an assessment of the complexity of a certain fragment or the entire series of observations as a whole. Permutation entropies of different orders are a useful analysis tool for a large number of time series of very different nature. They make it possible to obtain important information about dynamic processes in complex systems producing non-stationary series with a significant stochastic component.

An analysis of works describing the use of permutation entropy when processing data obtained during observations of the dynamics of various natural phenomena showed that this time series parameter has been used for quite a long time and very effectively. Thus, in [*Zunino et al.*, 2012], permutation entropy was successfully used in the study of the North Atlantic Oscillation, which has a significant impact on winter weather over Western and Central Europe. In [*Liang et al.*, 2020], using permutation entropy, an indicator of the complexity of the time series of concentration of suspended solid microparticles in moisture droplets in the air was determined, on the basis of which a model was obtained and an algorithm was formulated for predicting the trend of changes in the concentration under study over time. In [*Zhu et al.*, 2016], permutation entropy was used to study the influence of climate on the dynamics of the spread of dengue fever in Southeast Asia in the period from 2004 to 2015. In [*Fu et al.*, 2019; *Lu et al.*, 2022; *Roushangar et al.*, 2021; *Silva et al.*, 2021; *Zhang et al.*, 2019] permutation entropy has been used to model and study various aspects of climate, from studying the dynamics of drought periods in northwestern Iran and northeastern Brazil, to seasonal variations in wind speed in the Ningxia and Jilin regions, and temperature throughout mainland China.

Materials and methods

Let us consider a sample $\{x_k\}$, obtained from a time series $\{x\}$. The permutation entropy of a sample of a time series of order n is usually called the Shannon entropy n! permutations defined by the relations of n consecutive sample values. Further in this work we will talk about entropy for $n = 3$. All six possible permutations for three consecutive values of the series are shown in Figure 5, published in [*Traversaro et al.*, 2018].

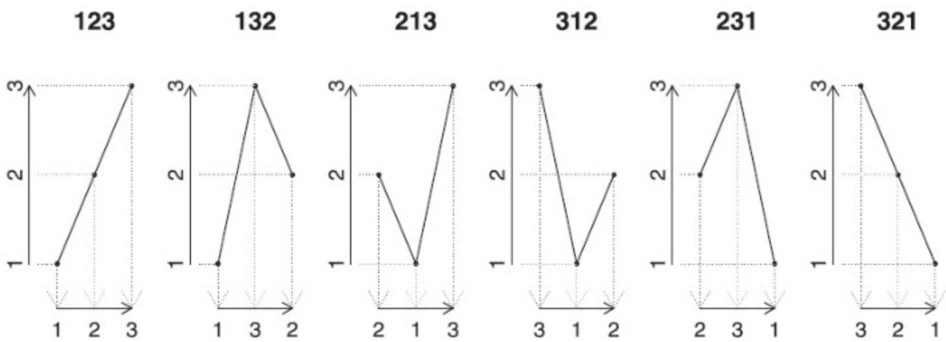

Figure 5. Permutations for $n = 3$.

The entropy itself is calculated using the classical formula (1).

$$\sum_{j=1}^{3!} m_j = N, \; p_j = m_j/N \quad and \quad H_3 = -\sum_{j=1}^{3!} p_j \log_2 p_j \tag{1}$$

Let us note that in formula (1) the letter m_j denotes the frequency of occurrence of each of the six permutations in the studied fragment of the time series. It should also be said that entropy is expressed in bits. The maximum possible value of permutation entropy will be observed when each of the permutations is uniformly distributed. Thus $\max H_3 = \log_2 3!$, which gives the result 2.584962500721156. Entropy takes its minimum value when there is only one permutation, for example (1, 2, 3). In this case, the entropy will be equal to 0.

In addition to considering the theoretical foundations of permutation entropy, we would like to dwell on the criterion proposed by *Kandal* [1981] for assessing the randomness of the sample data under study.

The method (or criterion) of turning points is one of the simplest criteria for the randomness of a fragment of an observed time series. Its essence is to count the "peaks" and "troughs" that can be formed by three neighboring points. In this case, a peak is a point that is larger than two neighboring ones, and a trough is a point that is smaller than two neighboring ones. Since out of three points, as mentioned above in the section on permutation entropy, only six permutations 123, 132, 213, 231, 312, 321 can be written, then four of them correspond to the criterion of turning points. Two permutations (132 and 231) are peaks, two more (213 and 312) are troughs. Therefore, given a random uniform distribution of time series values, the probability of encountering one of the four turning points is 4/6 or 2/3. If we do not take into account the two extreme points of the series fragment, then the mathematical expectation of the presence of a turning point at the current location is equal to $2/3(n-2)$. The value of the standard deviation for turning points is somewhat more difficult to derive. Ultimately, a sign of randomness of a time series was obtained and justified if the number of turning points in the studied fragment of the time series falls within the interval from $2 \cdot (N-2)/3 - ((16 \cdot N - 29)/90)^{0.5} \cdot 1.96$ to $2 \cdot (N-2)/3 + ((16 \cdot N - 29)/90)^{0.5} \cdot 1.96$.

The authors of this work decided to use permutation entropy to analyze the dynamics of time series representing the results of monitoring the infrasound background at an experimental site in the area of the main building of Gorno-Altaisk State University (Gorno-Altaisk, Altai Republic). To monitor the infrasound background, at the first stage of research, an acoustic sensor was used, developed on the basis of an INMP 441 MEMS microphone, the description of which is given in [*Microsin.net*, 2020]. As an undoubted advantage of the presented design, we can note the presence of a built-in 24-bit analog-to-digital converter and a special I2S bus, supported by many modern controllers for high-speed transmission of digitized audio data, synchronization of several microphones, etc. Despite the presence of a built-in bandpass filter, evaluation calibration tests have shown that with sound pressure fluctuations of the order of 0.5 Pa, an acceptable signal/noise ratio is observed starting at frequencies of the order of 2.5–3 Hz. When choosing this microphone as an acoustic sensor capturing part of the infrasound range, we proceeded from satisfactory price-quality ratios, the availability of this equipment on the market and the sufficiency of the observed part of the infrasound range to solve the assigned tasks [*Schwardt et al.*, 2022].

To increase sensitivity at low frequencies and provide protection from rain, snow, and gusts of wind, the microphone was placed in a plastic tube with a diameter of 110 mm, hermetically sealed at both ends, playing the role of a Helmholtz resonator (neck dimensions 5 mm × 20 mm). The dimensions of the pipe (620 mm) were selected taking into account a short distance from the control circuit, attachment to the mast and natural protection from the wind.

The resonant frequency for a Helmholtz resonator can be calculated using the formula (2).

$$f_H = \frac{v}{2\pi}\sqrt{\frac{S}{V_0 L}}, \tag{2}$$

where f_H – frequency, Hz; v – speed sound of a medium; S – neck section, m^2; L – neck length, m; V_0 – resonator volume, m^3. Estimated calculations showed a resonant frequency of the order of 7 Hz.

The digitization (sampling) frequency when working with a datalogger is set by the microcontroller and depends on the data transfer rate on the I2S bus. In our case, the frequency is set to about 330 Hz. At this frequency, a relatively small amount of daily data is accumulated, and at the same time it remains possible to work quite well with signals up to 100–150 Hz.

Figure 1–3 show examples of signals obtained through this acoustic sensor. The authors of this work were tasked with developing a "classifier" algorithm that allows identifying intervals of a time series containing a "noise" signal (containing only noise), a mixed signal (a periodic highly noisy signal) and a "good signal" (a periodic signal with minimal amount of noise). In this case, the duration of the interval was assumed to be equal to 3000 samples of the time series (approximately 10 seconds). In addition, the classification algorithm in the future was planned to be executed on a microcontroller in real time, which imposed requirements on a certain ease of implementation on the developed "classifier" algorithm.

The best approach, according to our preliminary estimates, for dividing fragments of a time series into "signal" or "noise" was to parameterize the analyzed data using permutation entropy (the degree of chaos of the fragment under study). To calculate this parameter, it was only necessary to "count" the number of three consecutive sample values located in a certain way in the time series stream. Even the hardware implementation of such "counters" would not be very difficult. It was assumed that a well-structured sinusoidal-like signal should show low entropy, and a noise signal should show correspondingly high entropy.

However, the calculation of entropy, performed at the preliminary stage of developing the algorithm in Python using the function `dis,cis = op.complexity\_entropy(x1)` from the `ordpy` library (corresponds to the formula (1) described above), for the signal presented in Figure 2, showed the value `dis` = 0.9992368090042947, i.e. high degree of chaos or uncertainty. At the same time, for the signal shown in Figure 1, the entropy turned out to be `dis` = 0.9863362446476029. Thus, the degree of uncertainty of the "noise" signal was estimated to be much lower than the same value for a signal resembling a sinusoidal one. A closer examination of the source data showed that the analyzed sinusoid was modulated in amplitude by a "weak" noise signal. Hence the high degree of estimated uncertainty.

To improve the classification procedure, it was decided to use the turning point criterion, which was described in the "materials and methods" section of this work.

If you look closely at the criterion of turning points, you will notice a certain "kinship" of this criterion with permutation entropy, since the turning points, the number of which is estimated when checking the required criterion, are nothing more than four of the six permutations for $n = 3$ used for calculations of permutation entropy.

Returning to the computational experiment we carried out, we note that after performing the appropriate computational procedure, the criterion of turning points was also not "able" to distinguish a noisy periodic signal from a "noisy" signal.

Of course, it was possible to filter the signal from noise before calculating the permutation entropy or turning point criterion. Even in real time this is not difficult to do. However, after "coarse" filtering using the moving average method, the turning point criterion began to "mark" both analyzed signals as periodic, i.e. the "noise" has "turned" into a "reasonably smooth" signal.

To find a solution to the problem in the current situation, the following hypothesis was put forward. Let us have a sample corresponding to a non-random noisy periodic signal, for example the one presented in Figure 2. If for this time series we calculate, for example, the normalized permutation entropy or the normalized complexity indicator or the normalized indicator of the number of turning points, first for the entire sample, then for the elements of this sample numbered 0, 2, 4, 6, 8, 10..., then for sample elements numbered 0, 3, 6, 9, 12... etc. to sample elements numbered 0, k, $2k$, $3k$..., where k is an empirically selected number depending on the sample size, then we get a sequence of values of the parameter we have defined, consisting of k elements. We call such a sequence the k-complex of the parameter under study. The assumption we accepted without proof was that for a periodic, albeit noisy time series, the obtained points of the k-complex themselves must represent some kind of "conditionally non-random series". If the original time series is random or very noisy, then the points of the k-complex must also be a "conditionally random series". Thus, we can say that by introducing its k-complex instead of a time series, we reduce the number of elements of the series without changing its degree of randomness. In this case, of course, we need to decide how we will evaluate the degree of randomness of the k-complex itself. As an assessment of the degree of randomness or regularity of a k-complex, it was proposed to use the same criterion of Kandal turning points. In addition, within the framework of the hypothesis we accepted, it was agreed that if we obtain a k1-complex of the same parameter, but for a sample not from the original time series, but from the k-complex, then we will call such a sequence a second-order k1-complex. Thus, the increase in the orders of k-complexes can be continued to a "reasonable" limit.

Note that a similar technique with "sparse" samples from the original time series was used, for example, in Higuchi's article when calculating a parameter that was called "fractal dimension" [*Higuchi*, 1988].

Results

For example, let us consider a fragment of the time series presented in Figure 2, k-complex for k = 64, and as a parameter the "normalized complexity" indicator (cis-parameter) of the time series. Essentially, the cis parameter is the one's complement of the normalized permutation entropy or dis parameter from the *ordpy* library. The desired 64-cis complex is shown in Figure 6

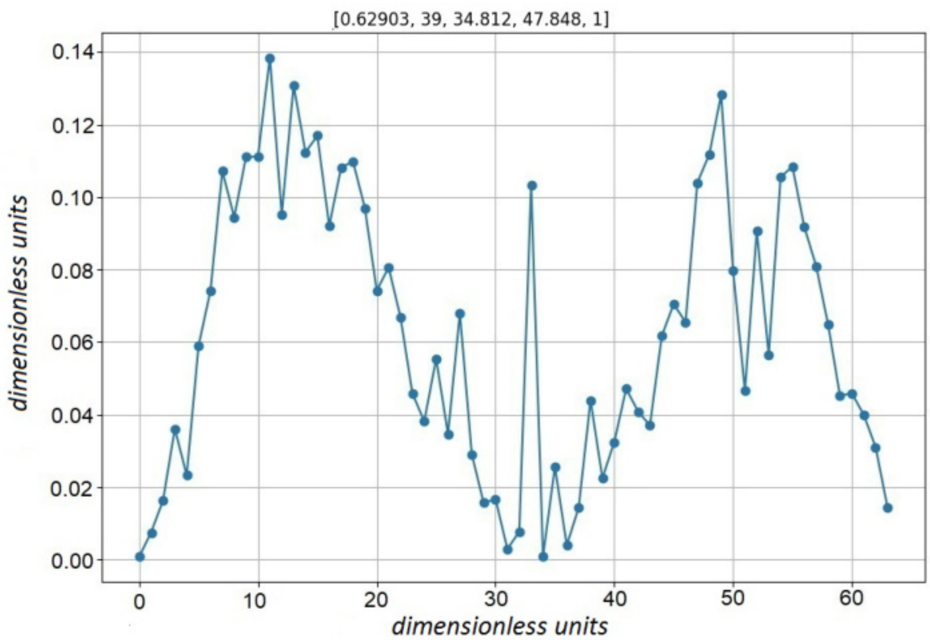

Figure 6. Sequence of values of the 64-cis complex.

The heading of Figure 6 (and other images of k-complexes) dispalys a vector in square brackets containing as the first element the normalized number of turning points of the k-complex. The second element of the vector is the absolute actual value of the number of turning points, the third and fourth elements of the vector are the left and right boundaries of the range, if the actual number of turning points fell within the range, the series would be assessed as random. A single value of the last element of the vector shows that in our case a series of 64 points (64-cis-complex) is classified as random according to the criterion of turning points, although subjectively, Figure 6 shows a fairly regular sequence.

A more reliable result, presented in Figure 7, was obtained for the 64-pnp complex, where the normalized number of turning points was used as a parameter. According to the criterion of turning points, this k-complex was assessed as regular, i.e. non-random (as

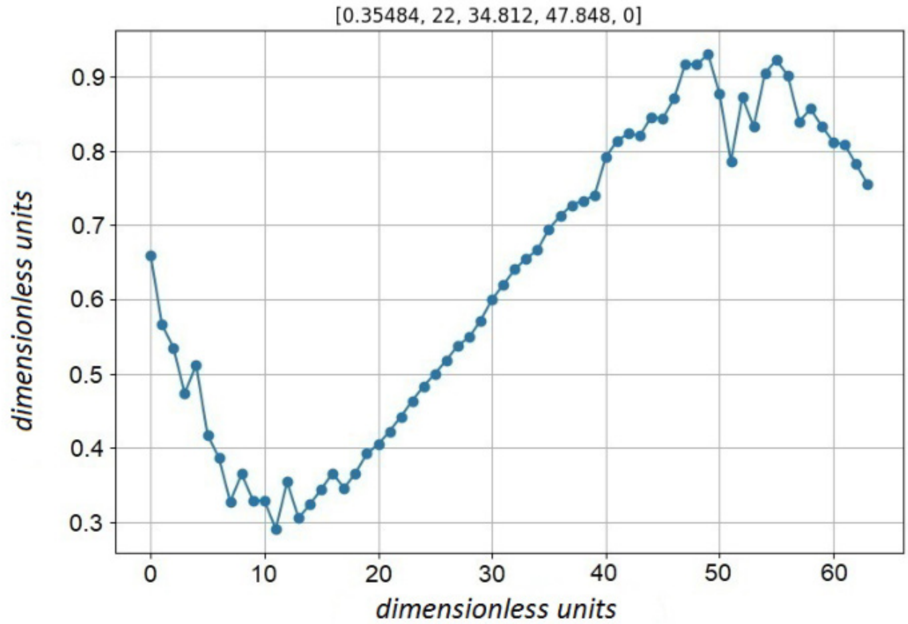

Figure 7. Sequence of values of the 64-pnp complex for the periodic signal shown in Figure 2.

expected in accordance with our accepted hypothesis). For the noise signal in Figure 1, the 64-pnp complex is shown in Figure 8. This sequence, as expected, was determined to be random by the turning point criterion.

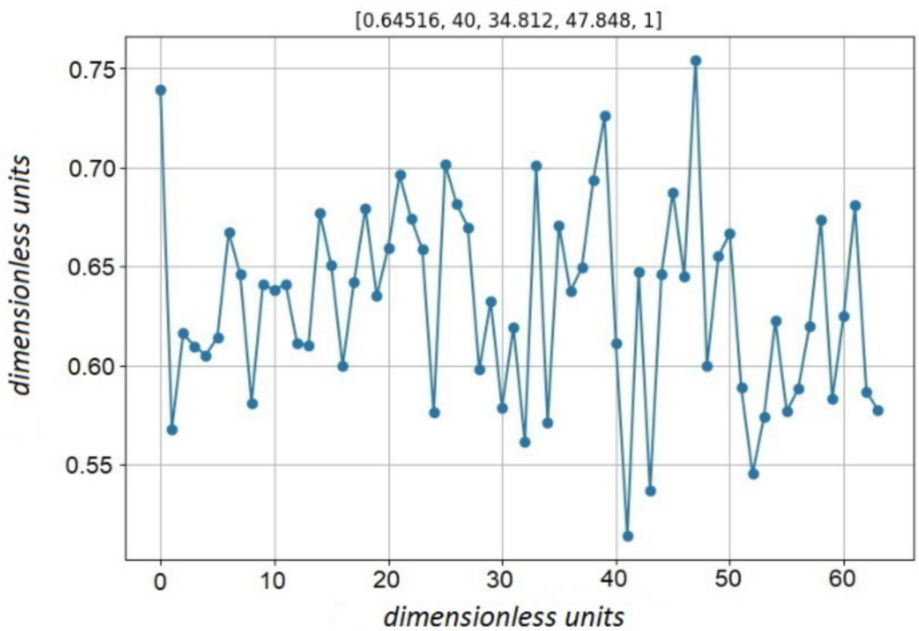

Figure 8. 64-pnp complex for the "noise" signal shown in Figure 1.

Thus, the performance of the discriminating procedure based on the k-complex was empirically tested. We could have stopped there if there had not been a need for a more complex classification of the signals under study. In fragments of the time series, it was necessary to detect a "good signal" and classify it as the "gs" class (an example of a signal is shown in Figure 2), the "noise signal" – the "nn" class (Figure 1) and the "bad signal" – the "bs" class. (Figure 9)

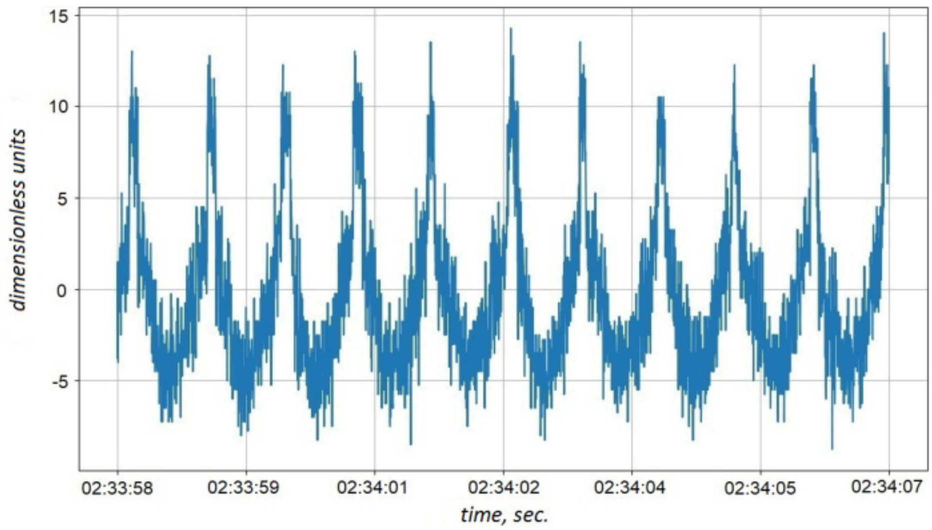

Figure 9. Example of a "bad" signal.

The 64-pnp complex for the signal presented in Figure 9 (shown in Figure 10) was assessed by the turning point criterion as random, although visually the graph (Figure 10) shows a certain regularity of the trend.

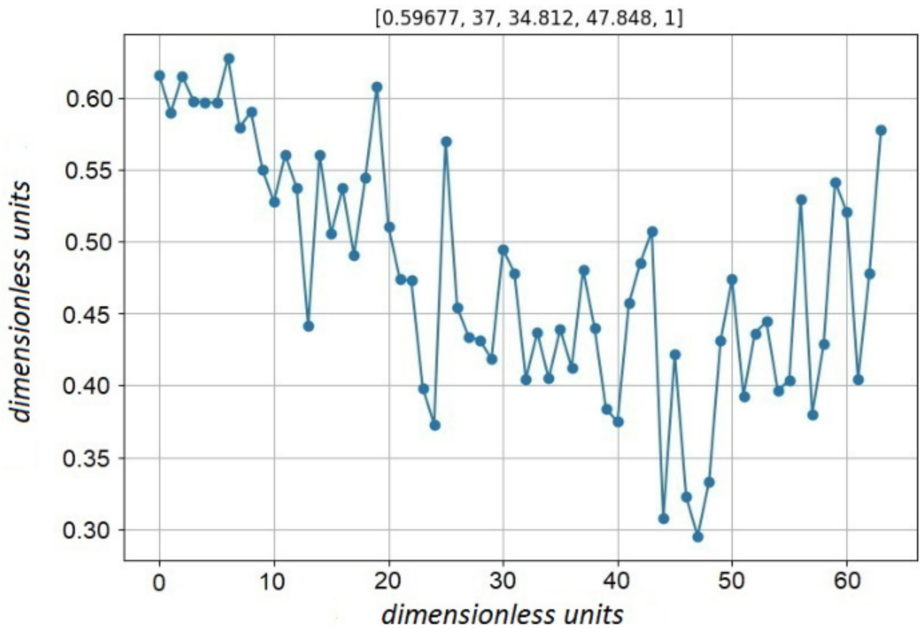

Figure 10. 64-pnp complex for the signal shown in Figure 9.

To evaluate complex signals, such as those presented in Figure 9 or 12, we decided to use a second-order k-complex. At the same time, for greater reliability, it was decided to use a 128-pnp complex as a first-order complex, and a 32-pnp complex for a second-order complex. In total we have a 128-32-pnp complex. By the way, already during the transition of the first-order pnp complex from $k = 64$ to $k = 128$ for the signal shown in Figure 9, the 128-pnp complex was assessed as regular (Figure 11).

It can be reasonably assumed that adjusting the orders of pnp complexes and selecting numbers k for each of them will allow us, if necessary, to implement quite complex classifications of signals..

Now let us give an example of more "complex" bad signals. One such signal is shown in Figure 12.

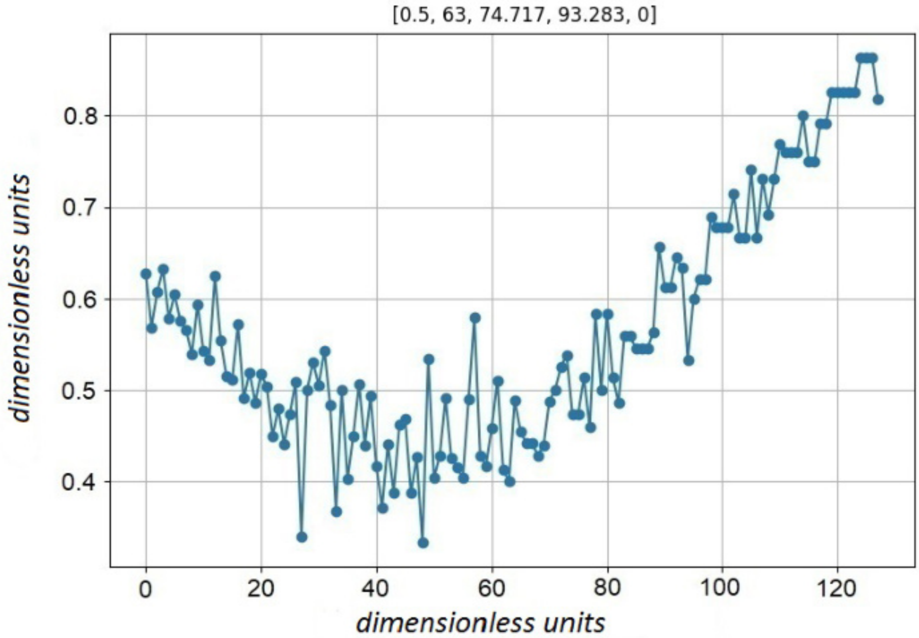

Figure 11. 128-pnp-complex for the signal (Figure 9).

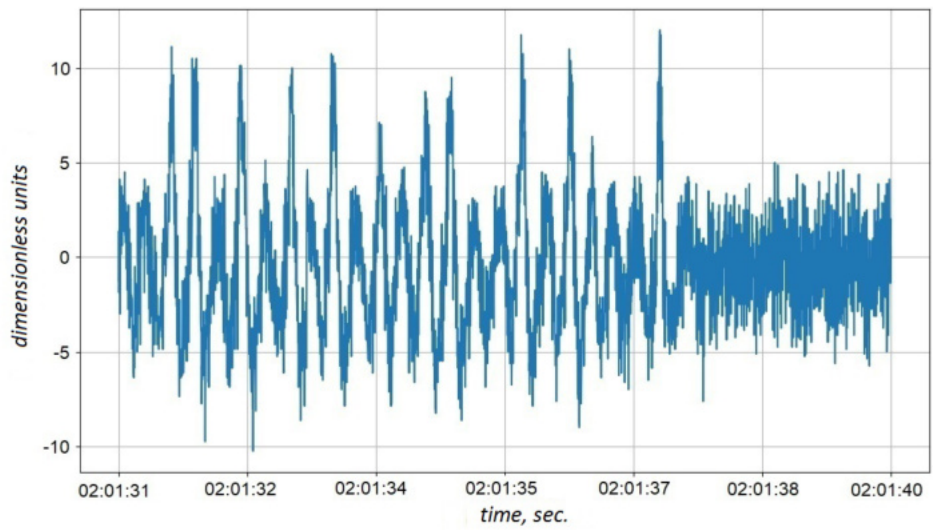

Figure 12. Example of a "bad" signal from the "bs" class.

Figure 13 shows a 128-bpn complex for this signal, which was estimated to be random.

Figure 14 shows a 128-32-pnp second-order complex. This complex was assessed as regular. Thus the signal was recognized as belonging to the "bs" (bad signal) class.

We called the above-described indicator (even to some extent a classifier) of the degree of regularity/chaoticity of the studied fragments of time series based on k-complexes of different orders a complex indicator of the stability of permutation entropy.

Now let us consider how, as a first approximation, we can organize a classifier of the studied fragments of time series, using in our case a 128-pnp complex of the first order and a 128-32-pnp complex of the second order. As already mentioned above and noted in the headings of the figures in which the above complexes are presented, each complex has a one-bit regularity indicator. If the complex is chaotic (irregular), then the bit value is equal to 1. If the complex is regular, then the bit is equal to 0. So, we have two complexes, and therefore two bits. The input for the classifier will be a two-bit binary vector, where the first bit (the left bit of the input vector) corresponds to the

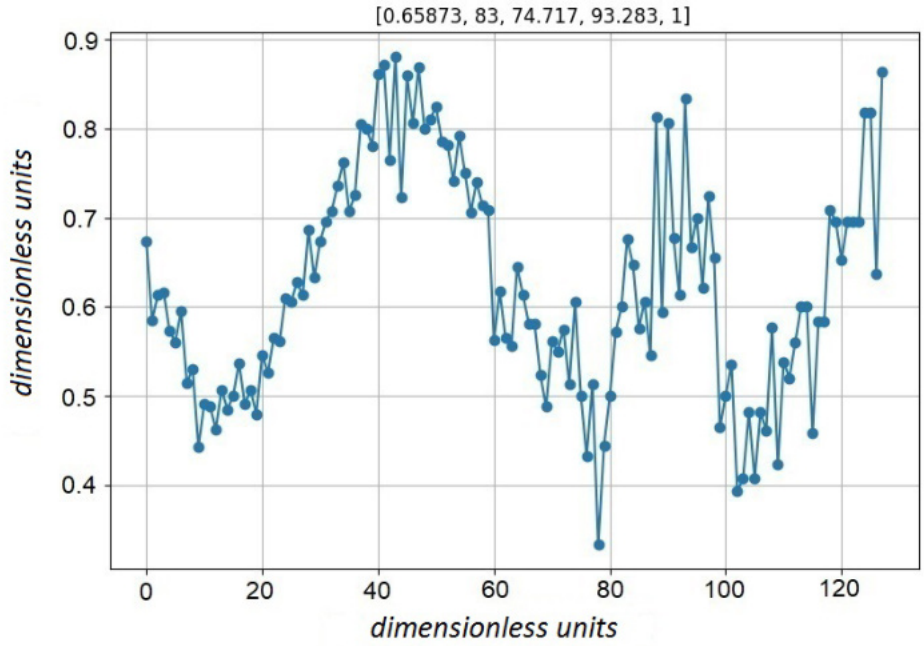

Figure 13. 128-pnp complex for the signal (Figure 12).

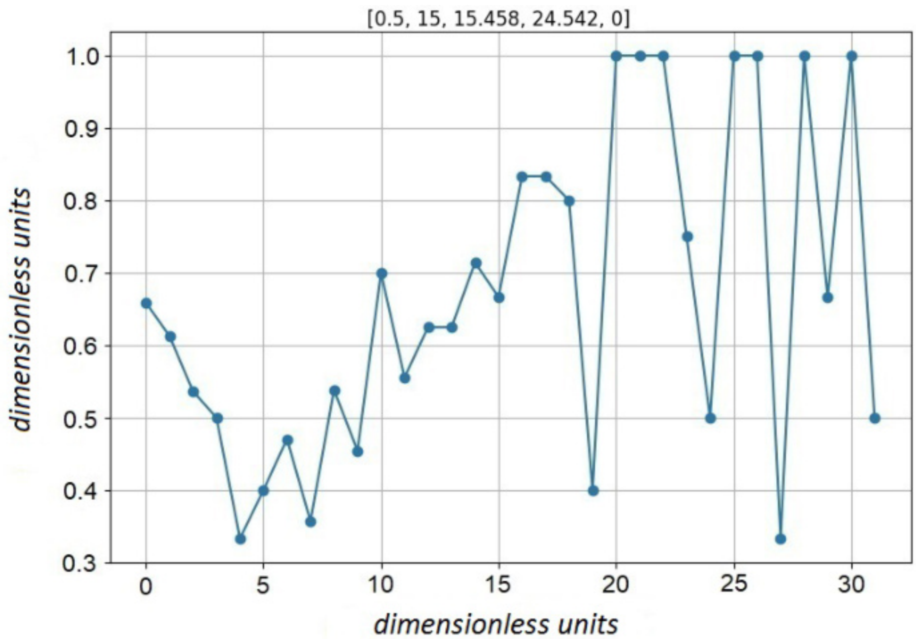

Figure 14. 128-32-pnp second order complex for the signal (Figure 12).

chaoticity index of the first-order complex, and the second bit (the right bit of the input vector) serves as an index of the chaoticity of the second-order complex. Thus we have:

(00) – class (gs) good signal,
(10) or (01) – class (bs) bad signal,
(11) – class (nn) noise signal.

Let us consider an example of the practical application of the classifier we developed. We tried to estimate the time distribution of the degree of "activity" of the observed infrasound background. At the same time, it was agreed to evaluate "activity" in proportion to the number of ten-second fragments of the time series assessed by the classifier as "gs" divided by the total number of ten-second fragments in the hourly interval. To analyze the "activity", about 390 calculations were performed for each hourly fragment of the time series. Thus, for each approximately 10-second fragment of a time series containing 3000 samples, a 128-pnp first-order complex was calculated along with an assessment of its "chaoticity" and a 128-32-pnp second-order complex, also along with an assessment of "chaoticity". Then a classification procedure was launched, assigning the current 10-second fragment to one of the three classes described above. Thus, by adding one (if the current fragment belongs to a given class) or zero, three lists of 10-second fragments were formed – members of the given classes. At the end of processing the hourly fragment of the time series, the single values of the lists were summed up, and the resulting sum was divided by the total number of 10-second fragments in the analyzed hourly interval. As a result, for each hourly fragment of the series, three numbers were obtained, the sum of which gave one. For our task in the future, we used only the "gs" list, conditionally containing information about the "activity" of the observed time series.

In a similar way, 120 hours of time series were analyzed and an array of 120 points was obtained, the value of which should, according to our hypothesis, characterize the "activity" of the infrasound background recorded at our infrasound monitoring point. The result of the analysis is shown in Figure 15 and presents information for five days from the first to the fifth of September 2023. The graph shown in Figure 15 clearly shows five peaks of infrasonic "activity" occurring during the night hours of the analyzed time series. Moreover, it should be noted that the peaks relating to the second, third and fourth of September show a significant increase in the "activity" under study.

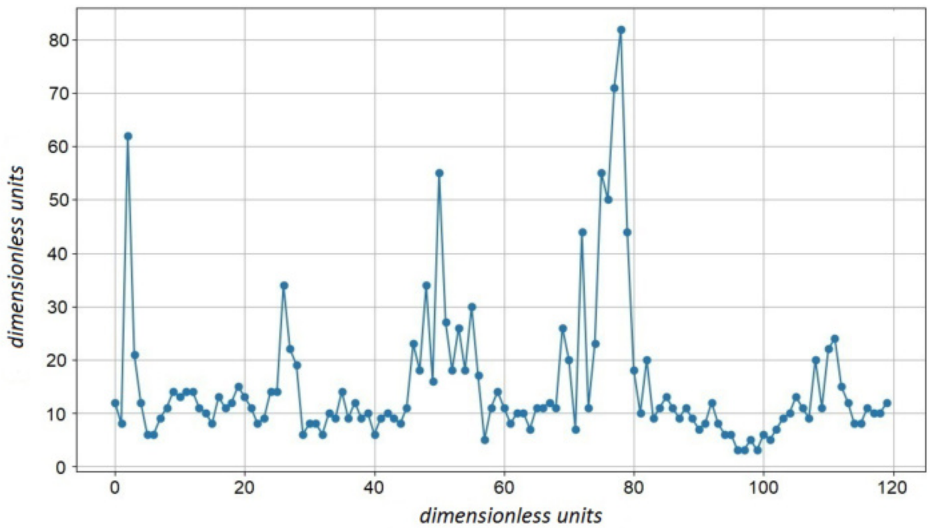

Figure 15. Infrasound activity for the period from September 1 to September 5, 2023. Gorno-Altaisk.

Further research showed that for samples containing a relatively small number of points, the k-complex randomness measure based on turning points is unstable. An alternative criterion has been developed especially for such cases.

In order to verify with sufficient reliability the adequacy of the algorithm, we take verified geomagnetic data containing noise and a useful signal, isolated using indices of geomagnetic activity or simultaneous recording of morphology at several spatially distributed observatories. Figure 4 shows a time series representing the difference signal between the vector sum of projections in the Euclidean metric and the magnitude of the Earth's magnetic field induction vector. This value is a generally accepted indicator of the quality of measurements obtained using observatory instruments, and is called Delta F (component G) [*St-Louis*, 2020]:

$$G = F(v) - F(s), \tag{3}$$

where $F(v)$ – modulus of the magnetic field strength vector, calculated from vector magnetometer data, $F(s)$ – direct measurements of the modulus on a scalar magnetometer.

The measurements were carried out at the SPG magnetic observatory [*Sidorov et al.*, 2017], part of the INTERMAGNET network, on 02/11/2024. Figure 4 itself shows the hour interval (3600 counts) from 2 am to 3 am GMT. The X axis shows time, the Y axis shows the value of magnetic induction in nT. Conventionally, the task of the "classifier" was to detect and isolate from the background noise the signal shown on the graph in the time interval approximately between 02:08:30. and 02:18:30. At the same time, the "classifier" should not have responded to any other signals.

We decided to divide the presented hourly fragment of the time series into ten-minute intervals containing 600 samples and to build for each interval a 108-pnp complex of the first order. For the desired fragment of the time series, the 108-pnp complex of the first order is presented in Figure 16. The red color in the figure shows a fourth-degree polynomial (`np.polyfit()`), which approximates the points of this complex. Below in green is a graph of the absolute values of the element-wise difference between the points of our 108-pnp complex and the approximating polynomial.

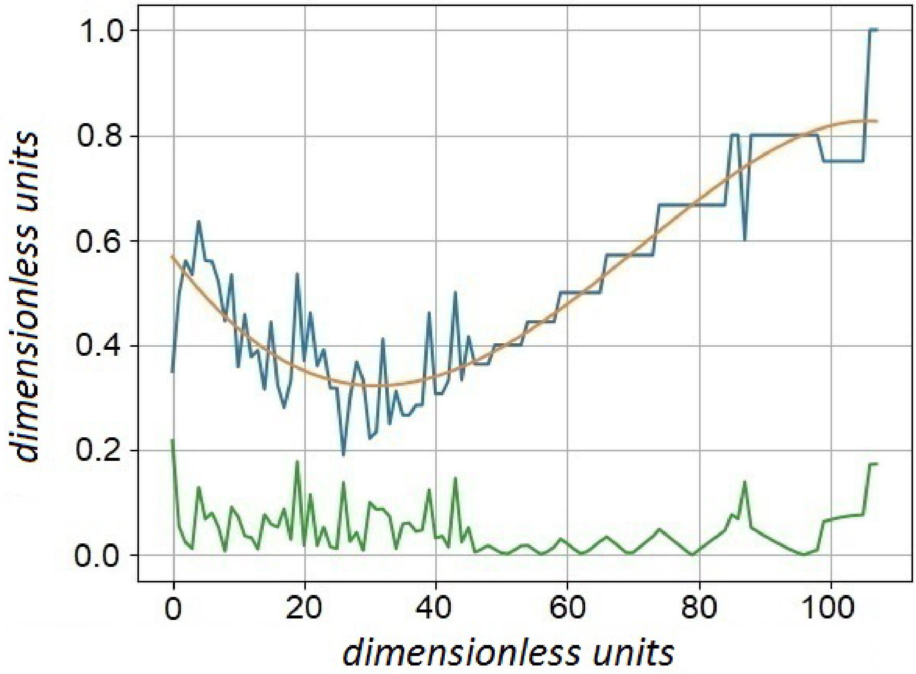

Figure 16. 108-pnp-complex of the first order.

It was hypothesized that the smaller is the standard deviation for the vector of absolute values of the element-wise difference between the points of our 108-pnp-complex and the approximating polynomial, the less random time series corresponds to the k-complex under consideration. Thus, the value of the desired standard deviation can serve as a threshold criterion for identifying more or less noisy signals.

To isolate a ten-minute fragment of the signal shown in Figure 17, the criterion STD < 0.06 was set. This criterion worked only once, because only for the k-complex presented in Figure 16, the STD value turned out to be 0.044.

As the analysis of the initial data shows (Figure 18), this interval is a natural signal and is observed at other observatories and stations of the network at the same time (Figure 19). It should be noted that isolating a useful signal using delta F analysis of one observatory is generally not an easy task that arises in the process of processing geomagnetic data [*Soloviev et al.*, 2018]. The proposed algorithm can be used to automate the selection of useful intervals when processing 1-second geomagnetic data.

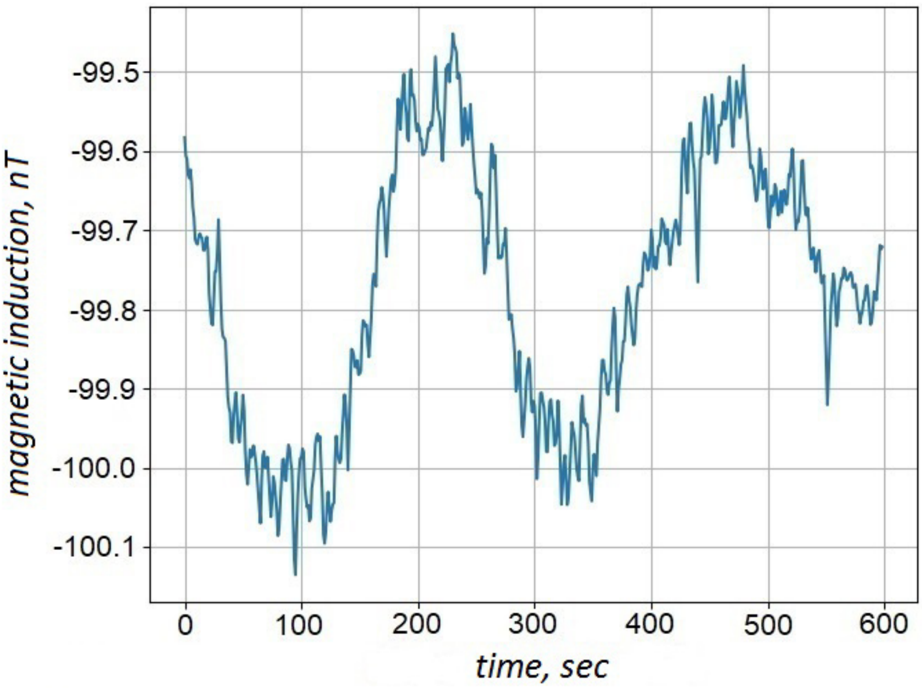

Figure 17. 108-pnp-complex of the first order.

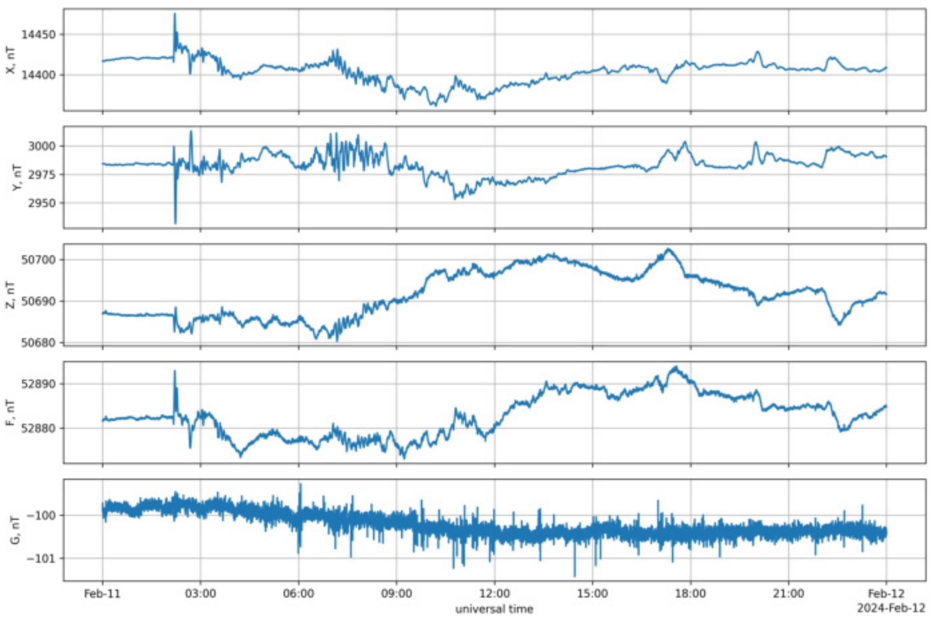

Figure 18. Fragment of data from magnetometers of the SPG observatory around 2024-02–11 02:00 UT.

Conclusion

As a result of the research presented in this work, an algorithm was proposed for detecting fragments of a time series that meet the specified "non-randomness" criteria. The proposed "classifying" algorithm is called a complex indicator of the stability of the permutation entropy of fragments of a time series. Its properties are based on reducing the number of studied points of a fragment of a time series by calculating the k-complex of some easily calculated parametric indicator of the studied fragment and subsequent assessment of the degree of randomness of the resulting k-complex. In our case, the normalized indicator of the number of turning points calculated for k sparse samples from

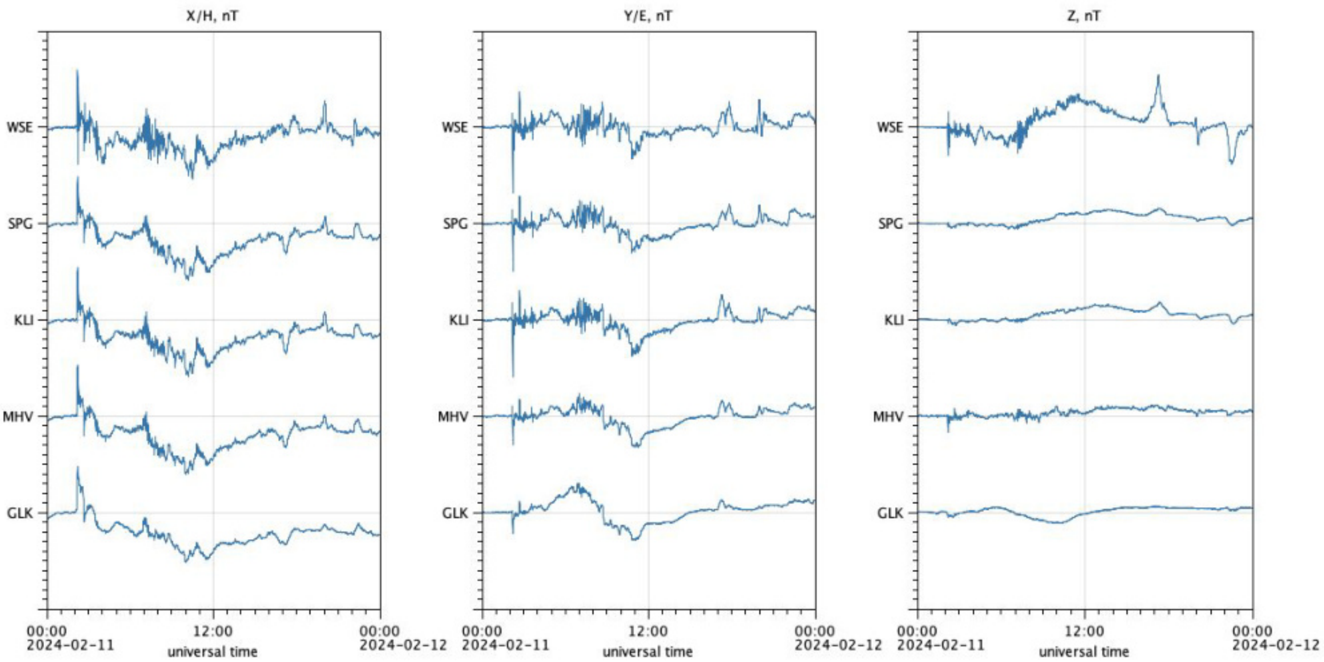

Figure 19. Comparison of vector components around 2024-02-11 UT at the magnetic observatories St. Petersburg (SPG), Klimovskaya (KLI), Mikhnevo (MHV), White Sea (WSE), Gyulagarak (GLK).

the desired fragment of the time series was used as such an indicator. For sufficiently large fragments of the time series (the first example considered was 3000 points), the degree of randomness was assessed quite well by the criterion of turning points applied to k-complexes of the first and second order. For relatively small samples (for example, 600 points), the degree of randomness was estimated by the minimum value of the standard deviation for the vector of absolute values of the element-wise difference between the points of our k-pnp-complex and the approximating polynomial of the fourth degree.

Acknowledgments. The facilities of the GC RAS Common Use Center "Analytical Center of Geomagnetic Data" (http://ckp.gcras.ru/) were used for conducting the research. The research was carried out with funds from the Russian Science Foundation (RSF) and the Ministry of Education and Science of the Altai Republic No. 23-21-10087.

References

Chumak, O. V. (2012), *Entropies and fractals in data analysis*, R&C Dynamics, https://doi.org/10.13140/2.1.4739.6800 (in Russian).

Fu, S., Y. Huang, T. Feng, D. Nian, and Z. Fu (2019), Regional contrasting DTR's predictability over China, *Physica A: Statistical Mechanics and its Applications*, *521*, 282–292, https://doi.org/10.1016/j.physa.2019.01.077.

Higuchi, T. (1988), Approach to an irregular time series on the basis of the fractal theory, *Physica D: Nonlinear Phenomena*, *31*(2), 277–283, https://doi.org/10.1016/0167-2789(88)90081-4.

Kandal, M. (1981), *Time series*, Finance and Statistics, Moscow (in Russian).

Liang, T., G. Xie, D. Mi, W. Jiang, and G. Xu (2020), PM2.5 Concentration Forecasting Based on Data Preprocessing Strategy and LSTM Neural Network, *International Journal of Machine Learning and Computing*, *10*(6), 729–734, https://doi.org/10.18178/ijmlc.2020.10.6.997.

Lu, P., L. Ye, M. Pei, Y. Zhao, B. Dai, and Z. Li (2022), Short-term wind power forecasting based on meteorological feature extraction and optimization strategy, *Renewable Energy*, *184*, 642–661, https://doi.org/10.1016/j.renene.2021.11.072.

Microsin.net (2020), INMP441: digital microphone with interface I2S, https://microsin.net/adminstuff/hardware/inmp441-i2s-omnidirectional-digital-microphone.html (in Russian), (visited on 18.02.2024).

Roushangar, K., R. Ghasempour, V. S. O. Kirca, and M. C. Demirel (2021), Hybrid point and interval prediction approaches for drought modeling using ground-based and remote sensing data, *Hydrology Research*, *52*(6), 1469–1489, https://doi.org/10.2166/nh.2021.028.

Schwardt, M., C. Pilger, P. Gaebler, P. Hupe, and L. Ceranna (2022), Natural and Anthropogenic Sources of Seismic, Hydroacoustic, and Infrasonic Waves: Waveforms and Spectral Characteristics (and Their Applicability for Sensor Calibration), *Surveys in Geophysics*, *43*(5), 1265–1361, https://doi.org/10.1007/s10712-022-09713-4.

Sidorov, R., A. Soloviev, R. Krasnoperov, D. Kudin, A. Grudnev, Y. Kopytenko, A. Kotikov, and P. Sergushin (2017), Saint Petersburg magnetic observatory: from Voeikovo subdivision to INTERMAGNET certification, *Geoscientific Instrumentation, Methods and Data Systems*, *6*(2), 473–485, https://doi.org/10.5194/gi-6-473-2017.

Silva, A. S. A., R. S. C. Menezes, O. A. Rosso, B. Stosic, and T. Stosic (2021), Complexity entropy-analysis of monthly rainfall time series in northeastern Brazil, *Chaos, Solitons & Fractals*, *143*, https://doi.org/10.1016/j.chaos.2020.110623.

Soloviev, A., V. Lesur, and D. Kudin (2018), On the feasibility of routine baseline improvement in processing of geomagnetic observatory data, *Earth, Planets and Space*, *70*(1), https://doi.org/10.1186/s40623-018-0786-8.

St-Louis, B. (Ed.) (2020), *INTERMAGNET Technical Reference Manual, Version 5.0.0*, INTERMAGNET Operations Committee and Executive Council, https://doi.org/10.48440/INTERMAGNET.2020.001.

Traversaro, F., F. O. Redelico, M. R. Risk, A. C. Frery, and O. A. Rosso (2018), Bandt-Pompe symbolization dynamics for time series with tied values: A data-driven approach, *Chaos: An Interdisciplinary Journal of Nonlinear Science*, *28*(7), https://doi.org/10.1063/1.5022021.

Zhang, T., C. Cheng, and P. Gao (2019), Permutation Entropy-Based Analysis of Temperature Complexity Spatial-Temporal Variation and Its Driving Factors in China, *Entropy*, *21*(10), 1001, https://doi.org/10.3390/e21101001.

Zhu, G., J. Hunter, and Y. Jiang (2016), Improved Prediction of Dengue Outbreak Using the Delay Permutation Entropy, in *2016 IEEE International Conference on Internet of Things (iThings) and IEEE Green Computing and Communications (GreenCom) and IEEE Cyber, Physical and Social Computing (CPSCom) and IEEE Smart Data (SmartData)*, IEEE, https://doi.org/10.1109/iThings-GreenCom-CPSCom-SmartData.2016.172.

Zunino, L., M. C. Soriano, and O. A. Rosso (2012), Distinguishing chaotic and stochastic dynamics from time series by using a multiscale symbolic approach, *Physical Review E*, *86*(4), https://doi.org/10.1103/PhysRevE.86.046210.